

# **Development of an Additively-Manufactured Slit Reactor Concept – Validation for Decentralized Fischer-Tropsch Synthesis**

Zur Erlangung des akademischen Grades eines  
DOKTORS DER INGENIEURWISSENSCHAFTEN (DR.-ING.)

von der KIT-Fakultät für Chemieingenieurwesen und Verfahrenstechnik des  
Karlsruher Instituts für Technologie (KIT)  
genehmigte

DISSERTATION

von  
M.Sc. David Fabian Metzger  
aus Karlsruhe

Tag der mündlichen Prüfung: 17.10.2024

Erstgutachter: Prof. Dr.-Ing. Roland Dittmeyer

Zweitgutachterin: Prof. Dr.-Ing. Maren Petersen





If not otherwise indicated, the content of this document is licensed under a Creative Commons Attribution-ShareAlike 4.0 International License (CC BY-SA 4.0): <https://creativecommons.org/licenses/by-sa/4.0/deed.en>

## Danksagung

Durch Unterstützung mit Fördermitteln, Feedback, konstruktiver Kritik, Materialien, Analysen, Daten, dem Fertigen von Teilen und Anlagen, Tipps, moralischem Halt oder einfach nur Geduld haben viele Menschen und Institutionen zum Gelingen dieser Dissertation beigetragen. Hierfür spreche ich meinen aufrichtigen Dank aus an:

- das Bundesministerium für Bildung und Forschung, das meine Arbeit durch das Projekt Kopernikus P2X Phase 2 (Förderkennzeichen 03SFK2Q0-2) gefördert hat,
- Prof. Roland Dittmeyer, der diese Arbeit ermöglicht hat,
- meinen Gruppenleiter Prof. Christoph Klahn für die hilfreichen Gespräche,
- Prof. Maren Petersen für die Übernahme des Zeitgutachtens und ihren wertvollen Beitrag zur Struktur der Arbeit,
- alle Mitarbeitenden des Instituts für Mikroverfahrenstechnik (IMVT), hier besonders an Manuel Hofheinz, Cornelia Schorle, Fabian Rupp, Matthias Schöffler, Dennis Scherhauser, Florian Messerschmidt, Torsten Wunsch und Conrad Grehl,
- die Doktorand\*innen des IMVT, insbesondere Fabian, Paul, Laura, Dorela und Mohanna,
- die Studierenden, die mich bei meiner Arbeit unterstützt haben: Miriam Urbansky, Marcel Kreitner, Jonas Nist, Franziska Ewert, Jennifer Schmidt, Tim Benker, Leon Hoffmann, Anselm Dreher und Joshua Fischer,
- Thi Tra My Nguyen und Dr. Mario Walter vom Institut für Angewandte Materialien (IAM),
- Bernd Fränkle und Nina Schladebeck vom Institut für Mechanische Verfahrenstechnik und Mechanik (MVM),
- meine Ansprechpartner\*innen bei der Ineratec GmbH für den Vergleich unserer Reaktoren,
- die Sasol Deutschland GmbH für das kostenlose zur Verfügung Stellen von Aluminiumoxidpulver,
- die Betreiber der Large Scale Data Facility (LSDF) (<https://www.scc.kit.edu/forschung/11843.php>, zuletzt abgerufen am 15.06.2024),
- den Publikationsfond der KIT Bibliothek,
- meine Familie und meine Freunde, hier besonders meine Eltern Friederike und Hans, meinen Bruder Constantin, Babett und
- meine Freundin Caro für ihre unglaubliche Unterstützung und ihr Verständnis während der Doktorarbeit.



# Abstract

## Motivation

Climate change poses a threat to mankind's habitat and thus human livelihood. Mitigating its consequences must include severe reduction of anthropogenic CO<sub>2</sub> and other greenhouse gas emissions. Fossil fuel combustion in medium- and long-distance flights contributes heavily to the greenhouse effect but dispensing with these liquid hydrocarbon energy carriers anytime soon or medium-term does not seem feasible. Sustainable aviation fuels (SAF) – especially those gained from renewable electrical power, CO<sub>2</sub> recaptured from the atmosphere, and water – present themselves as an alternative to the highly problematic fossil fuels. Such so-called E-fuels, or Power-to-Liquid (PtL) fuels, can be produced via Fischer-Tropsch-Synthesis (FTS) in decentralized plants: under elevated pressure and temperature and on a cobalt catalyst, CO and H<sub>2</sub> react into long-chain hydrocarbons, involving major heat release. This reaction requires reactors featuring inner channels on a millimeter scale. Such reactors can be manufactured, among other methods, from sheet metal tooled with stock-removing and/or cauterizing processes. After diffusion bonding (DB), the metal sheets are processed further, adapted via joining procedures, and standard components are then assembled into reactors. This is where additive-manufactured (AM) reactors lend themselves as an alternative requiring less manufacturing steps, materials, and components. This alternative, reactors made via '3D printing', are the subject of this thesis, which has been sponsored by the German Ministry of Education and Research (Bundesministerium für Bildung und Forschung) under the project 'Kopernikus P2X'.

## Manufacturing Method

Additive Manufacturing, i.e. powder bed-based melting of metal via laser beam (PBF-LB/M), is a suitable manufacturing procedure to produce a solid physical part from a digital 3D model. First, the 3D model is fragmented into two-dimensional layers. Then, metal powder is applied to a base plate and a laser traces the specified build areas, melting the metal powder only there and thus creating solid metal. Lowering the base plate, applying new powder, and lasering the build areas is repeated layer by layer until the complete part has been built, then to be raised and freed from any non-molten powder. Subsequent post-processing having taken place, it is adapted with joining procedures and standard parts are assembled into a reactor. The no-tool, selective, and automated procedure of additive manufacturing allows for efficient manufacturing of parts with complex inner structures. This also applies to small parts and single-copy parts with integrated functions, which can also be manufactured efficiently in one single additive-manufacturing step.

## Objective

The additive-manufacturing process comprises several advantages in the manufacture of a reactor for the examined application. However, literature offers little systematic research and no example

of a Fischer-Tropsch-Synthesis reactor in decentralized plants for the production of Power-to-Liquid (PtL) fuels. The objective is to develop a concept for an easy-to-manufacture, modular, scalable, and at the same time safe (gas-tight and pressure-resistant), cooled, controllable, easy-to-open reactor with catalyst particles. These requirements are translated into standard partial functions for procedural apparatuses: mechanical stability, local fluid permeability, particle insertion, gas distribution, heat transfer, controls integration, and detachable connection.

## Procedure

The concept was tested for all individual functions. For each function, the smallest module required for the respective function was manufactured. By use of hybrid manufacturing (a combination of metal nuts, placed into the 3D printer, on which the additive manufacturing process was performed), a large selection of modules and geometric variations could be built. Standard testing procedures, such as helium leak test, water pressure test, flow test, insertion of catalyst powder, pressure- and vacuum filtration, were applied. An automated test rig with clamping function for the tested parts was built to determine heat transfer under gas and water flow with (partial) evaporation under elevated pressure. In an apparatus with many channels, a simple literature-validated model for CO conversion was combined with a model for pressure loss-induced flow distribution, which made conclusions concerning uniform flow distribution in reactors possible.

## Verification and Scale-Up

A laboratory-scale reactor was manufactured under the proposed concept, filled with 3.3 g catalyst, and then operated. At  $p=21$  bar, temperatures between 190 and 234 °C, and under varying volume flow, CO conversion of up to 79 % was reached. Notwithstanding the demanding conditions, an almost isotherm operation and thus efficient cooling could be proven and PtL raw product of good quality could be produced. The reactor featured numerous functions (reaction, cooling, catalyst particles, temperature sensors, heating element) with few sealing surfaces and was at all times pressure resistant and gas tight despite the demanding conditions. A further step entailed the identification of scaling-up and optimization measures to improve the reactor's capacity regarding manufacturing effort and make economical manufacture of a production reactor possible. Basing calculations on an optimized, scaled-up reactor and favorable manufacturing costs results in costs lower than can be expected for such reactors. The project partner Ineratec GmbH stated that additive-manufactured reactors up to a certain reactor size be cheaper and heavier than diffusion-bonded reactors.

## Outlook

Results show that the developed reactor concept is suitable for the intended application: Fischer-Tropsch-Synthesis production of sustainable aviation fuels. In compliance with the given guidance, individual functions can be arbitrarily combined, thus reducing design and construction effort. Reactor scale-up should be implemented into manufacturing, and TÜV certification should be obtained. With the help of the developed testing methods and the fast manufacture of test components, individual functions can be examined in more detail and be compared with simulation results. Especially for FTS and other heterogeneously catalyzed reactions, the reactor is promising. Based on the conclusive

concept from manufacture to operation, small-scale reactors, e.g. for laboratory tests and smaller production plants, can be produced fast and at low cost.



# Zusammenfassung

## Motivation

Die Klimakrise gefährdet die Lebensgrundlage vieler Menschen. Um die Folgen der Klimakrise einzudämmen, müssen die menschengemachten Emissionen von CO<sub>2</sub> und anderen Treibhausgasen signifikant verringert werden. Mittel- und Langstreckenflüge tragen mit der Verbrennung von fossilem Kerosin besonders viel zum Treibhauseffekt bei, sind jedoch mittelfristig nicht ohne diese flüssigen Kohlenwasserstoffe als Energieträger möglich. Eine Alternative stellen nachhaltige Flugkraftstoffe (engl. sustainable aviation fuels (SAF)) dar, insbesondere jene, die aus erneuerbarer elektrischer Energie, CO<sub>2</sub> aus der Atmosphäre und Wasser gewonnen werden. Diese sog. E-Fuels oder Power-to-Liquid (PtL) Kraftstoffe können in dezentralen Anlagen über die Fischer-Tropsch-Syntheseroute (FTS) hergestellt werden. Dabei reagieren CO und H<sub>2</sub> bei erhöhtem Druck und Temperatur an einem Kobaltkatalysator unter großer Wärmefreisetzung zu langkettigen Kohlenwasserstoffen. Dafür werden Reaktoren benötigt, die im Inneren Kanäle mit Abmessungen im Bereich von Millimetern haben. Solche Reaktoren können unter Anderem aus Metallblechen hergestellt werden, die mit zerspanenden Verfahren oder mit Ätzen bearbeitet wurden. Nach dem Diffusionsschweißen (engl. diffusion bonding (DB)) werden die Metallbleche nachbearbeitet, mit Fügeverfahren adaptiert und mit Standardbauteilen zum Reaktor zusammengebaut. Eine Alternative hierzu sind additiv gefertigte (engl. additive manufacturing (AM)) Reaktoren, bei denen weniger Fertigungsschritte, Material und Einzelteile benötigt werden. Sie sind Gegenstand dieser Forschungsarbeit, die im Rahmen des Projektes Kopernikus P2X vom Bundesministerium für Bildung und Forschung gefördert wurde.

## Fertigungsverfahren

Das AM Verfahren, also pulverbettbasiertes Schmelzen von Metall mit Laserstrahl (PBF-LB/M), ist geeignet, um aus Metallpulver ein digitales 3D-Modell als massives physisches Bauteil herzustellen. Dazu wird das 3D-Modell in zweidimensionale Schichten zerteilt. Aus Metallpulver, das dünn auf eine Bauplatte aufgetragen wird, wird die erste Schicht erstellt, indem ein Laser die Bereiche des Bauteils in der Schicht abfährt und das Metall aufschmilzt. Das Absenken der Bauplatte, Auftragen von neuem Pulver und Belichten der Schicht wiederholen sich so lange bis das Bauteil fertig ist. Anschließend wird es nach oben gefahren und von umliegendem, nicht aufgeschmolzenem Pulver befreit. Nachdem das Bauteil nachbearbeitet wurde, wird es ebenfalls mit Fügeverfahren adaptiert und mit Standardbauteilen zum Reaktor zusammengebaut. Durch das werkzeuglose, selektive und automatische Vorgehen bei der additiven Fertigung können Bauteile mit komplexen, inneren Strukturen effizient hergestellt werden. Auch kleine Bauteile und Einzelstücke mit integrierten Funktionen können so in einem Fertigungsschritt effizient hergestellt werden.



## **Zielsetzung**

Das Fertigungsverfahren bietet zahlreiche Vorteile für einen Reaktor für die untersuchte Anwendung. In der Literatur gibt es jedoch wenige systematische Untersuchungen und kein Beispiel für einen Reaktor für die FTS in dezentralen Anlagen für die Herstellung von PtL Kraftstoffen. Es soll ein modulares, sicheres (gasdicht und druckfest), skalierbares, einfach fertigbares Konzept für einen gekühlten, offenbaren, regelbaren Reaktor mit Katalysatorpartikeln erstellt werden. Die Anforderungen werden in Standardteilkfunktionen für verfahrenstechnische Apparate übersetzt: mechanische Stabilität, lokale Fluid-Durchlässigkeit, Partikelbefüllung, Gasverteilung, Wärmeübertragung, Integration von Regelungselementen und lösbare Verbindung.

## **Vorgehensweise**

Das Konzept wurde einzeln auf die Teilkfunktionen getestet. Dazu wurde jeweils das kleinste Modul gefertigt, das für die Abbildung der Teilkfunktion benötigt wurde. Durch das effiziente, hybride Fertigungsverfahren (eine Kombination aus Mattern, die in die AM-Maschine gelegt wurden und die darauf stattfindende additive Fertigung) konnten eine Vielzahl von Modulen und Geometrievierungen gefertigt werden. Es wurden Standardtestverfahren wie Heliumleckagetest, Wasserdrucktest, Durchströmungstest, Einfüllen von Pulver, Druck- und Vakuumfiltration angewendet. Für die Bestimmung des Wärmeübergangs bei Gasströmung und Wasserströmung mit (teilweise) Verdampfung bei erhöhtem Druck wurde ein automatisierter Teststand mit Klemmfunktion für die Testteile gebaut. Mithilfe eines einfachen literaturvalidierten, Modells für den CO-Umsatz in Kombination mit einem Modell für die druckverlustbedingte Strömungsverteilung in einem Apparat mit vielen Kanälen wurden Aussagen über die Gleichverteilung der Strömung in Reaktoren möglich gemacht.

## **Demonstration und Skalierung**

Ein Reaktor im Labormaßstab wurde nach dem Konzept gefertigt, mit 3,3 g Katalysator gefüllt und betrieben. Bei  $p=21$  bara, Temperaturen von 190 bis 234 °C und mit unterschiedlichen Volumenströmen wurde ein Umsatz von CO von bis zu 79 % erreicht. Trotz der hohen Anforderungen konnte ein beinahe isothermer Betrieb und somit eine effiziente Kühlung nachgewiesen und PtL-Rohprodukt mit einer guten Qualität hergestellt werden. Der Reaktor zeichnet sich durch viele Funktionen (Reaktion, Kühlung, Katalysatorpartikeln, Temperatursensoren, Heizelement) bei wenigen Dichtflächen aus und war trotz der hohen Anforderungen zu jeder Zeit druckfest und gasdicht. In einem weiteren Schritt wurden Maßnahmen zur Skalierung und Optimierung identifiziert, die die Leistungsfähigkeit des Reaktors bezogen auf den Fertigungsaufwand verbessern und die ökonomische Fertigung eines Produktionsreaktors ermöglichen. Wenn ein optimierter, hochskalierter Reaktor und günstige Fertigungskosten zugrundegelegt werden, ergeben sich Kosten, die niedriger sind als bei solchen Reaktoren erwartet werden kann. Der Projektpartner Ineratec gab an, dass die additiv gefertigten Reaktoren bis zu einer bestimmten Reaktorgröße günstiger und schwerer seien als diffusionsgeschweißte Reaktoren.

## **Ausblick**

Die Ergebnisse zeigen, dass das entwickelte Reaktorkonzept für die Anwendung geeignet ist. Die Teilfunktionen können unter den angegebenen Hinweisen beliebig kombiniert werden. Der Konstruktionsaufwand wird damit reduziert. Die Skalierung des Reaktors sollte aus der Konstruktion in die Fertigung umgesetzt und eine Zertifizierung durch den TÜV erworben werden. Mithilfe der entwickelten Versuchsmethoden und der schnellen Erstellung von Testbauteilen können Teilfunktionen noch gründlicher untersucht und mit simulativen Ergebnissen verglichen werden. Insbesondere für die FTS und andere heterogen katalysierte Reaktionen ist der Reaktor vielversprechend. Aufgrund des schlüssigen Konzeptes von der Fertigung bis zur Anwendung können im kleinen Maßstab, etwa für Laborversuche und kleine Produktionsanlagen, günstig und schnell Reaktoren gefertigt werden.



# Contents

<b>Abstract</b>	<b>i</b>
<b>Zusammenfassung</b>	<b>v</b>
<b>List of Figures</b>	<b>xiii</b>
<b>List of Tables</b>	<b>xvii</b>
<b>1. Introduction</b>	<b>1</b>
1.1. Background and Motivation	1
1.2. Objective of this Thesis	2
<b>2. Fischer-Tropsch Synthesis (FTS)</b>	<b>5</b>
2.1. Reactor Performance and Modeling	6
2.2. Decentralized Power-to-Liquid Plants	9
2.3. Reactors	11
2.3.1. Industrial Reactors	11
2.3.1.1. Multi-Tubular Fixed Bed Reactors	12
2.3.1.2. Slurry Bubble Column Reactors	12
2.3.2. Lab-Scale Reactors	12
2.3.2.1. Lab-Scale Conventional Reactors	13
2.3.2.2. Lab-Scale Micro-Structured Reactors	13
2.3.3. Commercially Available Micro-Structured Reactors	15
2.4. Design of Packed-Slit Reactor Concept	17
2.4.1. Developing Flow	19
2.4.2. One-Phase Heat Transfer in Slits without Internal Structures	20
2.4.3. Fluid Guiding Elements (FGE)	21
2.4.4. Boiling Heat Transfer	22
2.5. Interim Summary FTS	23
<b>3. Micro-Reactor Fabrication with Laser-Based Powder Bed Fusion of Metals (PBF-LB/M)</b>	<b>25</b>
3.1. Process	27
3.1.1. Processing	27
3.1.2. Post-Processing	28
3.2. Machines	30
3.3. Materials and Properties	33
3.4. Existing PBF-LB/M Reactors and Components	35
3.4.1. AM Reactors	35
3.4.2. AM Heat Transfer Enhancement	36
3.4.3. AM Connections	37
3.5. Interim Summary PBF-LB/M	38

<b>4. Design for Reactor Subfunctions</b>	<b>39</b>
4.1. Mechanical Stability	41
4.1.1. Design and Fabrication	41
4.1.1.1. Empty Modules	42
4.1.1.2. Modules with Internal Structures	43
4.1.1.3. Connections and Fabrication	44
4.1.2. Experimental Method	46
4.1.3. Calculation Method	46
4.1.4. Simulation Method	47
4.1.5. Results	47
4.1.6. Interim Summary Mechanical Stability	52
4.2. Local Fluid Permeability	52
4.2.1. Catalyst Powders	53
4.2.2. Design and Fabrication	53
4.2.3. Method	54
4.2.3.1. Pressure Filtration	54
4.2.3.2. Vacuum Filtration	55
4.2.4. Results	56
4.2.5. Interim Summary Local Fluid Permeability	58
4.3. Particle Loading	59
4.3.1. Materials	59
4.3.2. Method	61
4.3.3. Results	61
4.3.4. Interim Summary Particle Loading	63
4.4. Uniform Gas Distribution	64
4.4.1. Model and Simulation	65
4.4.2. Results	66
4.4.3. Interim Summary Gas Distribution	68
4.5. Heat Transfer	68
4.5.1. Test Rig	72
4.5.2. Method	74
4.5.2.1. Nitrogen	75
4.5.2.2. Water	76
4.5.3. Results	77
4.5.3.1. Heat Transfer Results Water	77
4.5.3.2. Heat Transfer Results Nitrogen	82
4.5.4. Interim Summary Heat Transfer	84
4.6. Control Systems Integration	85
4.6.1. Measuring Temperature of Fluid	86
4.6.2. Measuring Temperature of Casing	87
4.6.3. Electrical Heating of Fluid	88
4.6.4. Electrical Heating of Casing	89
4.6.5. Measuring Pressure and Composition	89
4.6.6. Results	90
4.7. Removable Connection	91
4.7.1. Fully Additive Flanged Reactor	91
4.7.2. Hybrid Flanged Reactor	92
4.7.3. Results	93
4.8. Interim Summary of Design for Reactor Subfunctions	94

<b>5. Integrated Test of Packed-Slit Reactor Concept</b>	<b>97</b>
5.1. Design and Manufacturing	97
5.1.1. Design	98
5.1.2. Manufacturing	99
5.2. Experimental Procedure	100
5.2.1. Catalyst	100
5.2.2. Reactor Preparation	100
5.2.3. Test Rig and Analytics	102
5.2.4. Reduction, Activation, and Operation	103
5.3. Results	104
5.3.1. Safety Tests and Reduction	104
5.3.2. Stationary Fischer-Tropsch Synthesis	104
5.3.3. Dynamic Operation	105
5.3.4. Interim Summary Integrated Test	107
<b>6. Scalability of Reactor Concept</b>	<b>109</b>
6.1. Scale-Up Aspects	110
6.1.1. Internal Numbering Up	110
6.1.2. Scaling	111
6.1.3. External Numbering Up	111
6.2. Design Improvement	111
6.2.1. Optimized Design for Operation	111
6.2.2. Optimized Design for Fabrication	112
6.3. Energy Intensity of Fabrication	115
6.4. Fabrication Cost	116
6.5. Interim Summary of Scalability of Reactor Concept	118
<b>7. Summary</b>	<b>121</b>
<b>8. Outlook</b>	<b>123</b>
<b>Bibliography</b>	<b>125</b>
<b>List of Symbols</b>	<b>149</b>
<b>A. Sustainable Aviation Fuels (SAF)</b>	<b>157</b>
A.1. Chemical Species	157
A.2. SAF Production Routes	157
A.3. Calculations	158
<b>B. Fabrication</b>	<b>161</b>
B.1. Application of Fluid-Permeable Structures	161
B.2. Manufacturing of Micro-Structured Reactors	161
B.3. Realizer SLM125	162
B.4. CT of AM Reactor	162
B.5. TÜV Approval	163
B.6. Realizer SLM 125	164
B.6.1. Tensile Tests	164
B.6.2. Thin Walls with Discrete Thicknesses	164
B.7. Reactors	166

B.8. All Modules . . . . .	169
<b>C. Materials . . . . .</b>	<b>175</b>
C.1. Alumina Powders . . . . .	175
C.2. Controlled Permeability Materials . . . . .	179
C.3. Metal Powder . . . . .	179
C.4. Experimental Materials . . . . .	180
<b>D. Heat Transfer . . . . .</b>	<b>183</b>
D.1. Convective Heat Transfer in the Reaction Zone . . . . .	183
D.2. Evaporative Heat Transfer . . . . .	183
D.3. Heat Transfer Coefficient Error Calculation . . . . .	183
D.4. Results Heat Transfer Coefficient Water . . . . .	185
D.5. Results Heat Transfer Coefficient Nitrogen . . . . .	187
<b>E. Round Robin Test Results . . . . .</b>	<b>189</b>

# List of Figures

1.1. Energy density of Li-Ion batteries and various fuels. Adapted from [5] with additional data from [6, 7]. . . . .	1
2.1. Process chain for a decentralized Power-to-Liquid plant in project Kopernikus P2X [72]. . .	10
2.2. Images of reactor types for Fischer-Tropsch synthesis (FTS). Modified after [31, 61]. . . .	11
2.3. Typical micro-structured reactor by IMVT. . . . .	14
2.4. Micro-structured reactor by Ineratec used at IMVT [137]. . . . .	15
3.1. Manufacturing routes with conventional micro-fabrication (non-additive) and with powder-bed fusion of metals with laser-beam (PBF-LB/M) fabrication. . . . .	26
3.2. Statistics on additive manufacturing (AM) machine sales and research results. . . . .	26
3.3. Schematic of energy transport in powder bed. Inspired by [150]. . . . .	28
3.4. Local fluid permeability module: one layer of scan vectors. . . . .	30
3.5. Schematic and picture of self-made pump skid. . . . .	31
3.6. Representation of laser section and build chamber of a PBF-LB/M machine [164]. . . . .	32
3.7. Realizer SLM125 at IMVT. . . . .	32
3.8. Ishikawa (cause and effect) diagram of PBF-LB/M [164]. . . . .	34
3.9. Computer aided design (CAD) representation of fluid-guiding elements from [210]. . . . .	36
3.10. CAD representation and photo of tool made with hybrid manufacturing [212]. . . . .	37
3.11. Photo of PBF-LB/M threaded holes [217]. . . . .	37
4.1. Packed-bed reactor subfunctions. . . . .	40
4.2. Cooled packed-slit reactor concept with AM. . . . .	40
4.3. Designs for mechanical stability testing. . . . .	43
4.4. CAD images of FGE-equipped modules. . . . .	45
4.5. CAD representation of module connectors. . . . .	45
4.6. Hybrid manufacturing of modules on nuts with exemplary empty module (three-quarter cut). . .	46
4.7. Experimental procedure for testing mechanical stability. . . . .	46
4.8. Schematic of the dimensions in an hexagonal arrangement of pins and how it was abstracted to an annular disc. . . . .	47
4.9. Modules after pressure test. (a-c) $t_w=1$ mm. (d-f) $t_w=0.6$ mm. . . . .	48
4.10. Results of mechanical stability calculation and experiment for pin-equipped modules. . . .	49
4.11. Failed module <i>Pins-1-4-20</i> : cross-cut after test, calculated, and simulated deflection. . . . .	49
4.12. Calculated stability criterion for various thicknesses at constant load. . . . .	51
4.13. Calculated stability criterion for various loads at constant wall thickness. . . . .	51
4.14. CAD image of local fluid permeability module. Red=local fluid-permeable region, gray=solid region. . . . .	54
4.15. Modules and materials for local-permeability testing. . . . .	55
4.16. Particle permeation of local-permeability modules plotted over $d_{red}$ . . . . .	56
4.17. Pictures of polished modules with hatch distance $HD=170$ and $300\ \mu\text{m}$ . . . . .	57
4.18. Pressure loss over locally fluid-permeable regions as a function of volumetric flow rate. Lines signify linear fits. . . . .	58



4.19. Three quarter-cut CAD representation of metal modules with no internal structures, pins, and FGE. Red are the fluid-permeable regions. . . . .	60
4.20. CAD representation of resin module <i>FGE-8-2</i> (hidden edges visible) and the module being tested. . . . .	60
4.21. Light shining through locally fluid-permeable bottom of a module. . . . .	62
4.22. Bed porosity in PBF-LB/M samples assuming $\epsilon_{\text{bed,inf,md}}=0.36$ . All module dimensions in mm. Circles refer to calculated values. . . . .	63
4.23. Bed porosity in PBF-LB/M samples assuming $\epsilon_{\text{bed,inf,md}}$ obtained experimentally . . . . .	63
4.24. Bed porosity in PBF-LB/M and vat photo polymerization samples assuming corrected infinite porosities. All module dimensions in mm. Circles refer to calculated values. . . . .	64
4.25. Results of gas distribution simulations. . . . .	67
4.26. Schematic representation of heat transfer modules without and with internal structures. Note internal structure also reduced cross-sectional area. . . . .	69
4.27. P&ID of test rig. Meaning of symbols can be found in Ref. [261]. . . . .	73
4.28. Photos of test rig. . . . .	74
4.29. Picture of module and process flow diagram (PFD) of heat transfer testing with nitrogen. . . . .	76
4.30. Picture of module and PFD of heat transfer testing with water. . . . .	77
4.31. Module <i>Pins-1-0.42-1.4</i> with $t_w=0.6$ mm. Experimental results for heat-transfer coefficient of one-phase (closed symbols) and two-phase (open symbols) heat-transfer with $\text{H}_2\text{O}$ . . . . .	78
4.32. Module <i>Pins-1-0.42-1.4</i> with $t_w=0.6$ mm. Experimental and calculated results for heat-transfer coefficient of one-phase (closed symbols) and two-phase (open symbols) heat-transfer with $\text{H}_2\text{O}$ of selected set-points. . . . .	79
4.33. Pin-equipped modules. Experimental results for one-phase (closed symbols) and two-phase (open symbols) heat transfer with $\text{H}_2\text{O}$ . . . . .	80
4.34. Fin-equipped modules. Experimental results for one-phase (closed symbols) and two-phase heat transfer (open symbols) with $\text{H}_2\text{O}$ . . . . .	81
4.35. Module <i>Lattice-1</i> with $d_{\text{strut}}=0.2$ mm and $t_w=0.6$ mm. Experimental and calculated results for heat-transfer coefficient of one-phase (closed symbols) and two-phase (open symbols) heat-transfer with $\text{H}_2\text{O}$ . . . . .	81
4.36. Module <i>Pins-12-1-3.4</i> with $t_w=0.8$ mm. Experimental and calculated results for heat-transfer coefficient with $\text{N}_2$ without and with particles. . . . .	83
4.37. Module <i>FGE-12-4</i> with $t_w=0.8$ mm. Experimental and calculated results for heat-transfer coefficient with $\text{N}_2$ without and with particles. . . . .	83
4.38. Modules with pins and FGE. Experimental and calculated results for heat-transfer coefficient with $\text{N}_2$ at $G \approx 3.8 \text{ kg m}^{-2} \text{ s}^{-1}$ without and with particles . . . . .	84
4.39. Sheathed thermocouples used in laboratory applications. Sealing is done from left to right via: sheath, shell, and protective tube, respectively. . . . .	86
4.40. Additive manufacturing (AM) channel for thermocouples to measure fluid temperature. . . . .	87
4.41. AM channels for thermocouples to measure solid temperature. . . . .	88
4.42. Heating of a flow in laboratory settings with heating line and micro-structured heat-exchanger. . . . .	88
4.43. Conventionally manufactured diffusion-bonded micro-structured reactor with holes for heating cartridges [274]. . . . .	89
4.44. AM reactor with pre-fabricated holes for heating cartridges. . . . .	90
4.45. Micro process engineering devices with taps. . . . .	90
4.46. Fabrication of fully additive reactor. . . . .	92
4.47. Hybrid manufacturing of reactor concept. . . . .	93
4.48. Fully additive reactor during bubble-test. . . . .	93
4.49. Packed-bed reactor subfunctions. Interactions within the AM packed-slit reactor concept. . . . .	95

5.1.	CAD representation of reactor with parts cut out to show internal structure. . . . .	98
5.2.	Drawing of reactor with thermocouple holes. . . . .	99
5.3.	Reactor scan strategy. . . . .	100
5.4.	Hybrid manufacturing of reactor. . . . .	101
5.5.	Process flow diagram of test rig used for Fischer-Tropsch synthesis. . . . .	102
5.6.	Pictures of reactor and oil thermostat. . . . .	103
5.7.	Temperature field inside reactor during reduction (electrical heating) and operation (thermal oil heating/cooling). Mind the different temperature scales. . . . .	104
5.8.	Experimental and fitted results for CO conversion in the plane generated by modified space velocity and temperature. . . . .	107
6.1.	CAD representation of internal numbering-up of the reactor from chapter 5. Parts cut out to show internal structure. . . . .	110
6.2.	Schematic representation: slit depth was increased from (a) to (b). While the catalyst volume stayed constant, the required volume of walls and cooling zone relatively decreased. All dimensions in mm. . . . .	111
6.3.	Reactor with horizontal holes for heating cartridges. . . . .	112
6.4.	Schematic representation: internal structure was removed from (a) to (b). While the catalyst volume stayed constant, the required volume of walls and cooling zone relatively decreased. All dimensions in mm. . . . .	112
6.5.	Schematic representation: wall thickness was decreased from (a) to (b). While the catalyst volume stayed constant, the required volume of walls relatively decreased. All dimensions in mm. . . . .	113
6.6.	CAD representation of rectangular flange plates with external dimensions of $(124\text{ mm})^2$ for Realizer SLM125. . . . .	113
6.7.	Reactor design with $V_{\text{cat}}=130\text{ mL}$ for rectangular base plate for SLM125. . . . .	113
6.8.	CAD representation of rectangular flange plate with external dimensions of $(60\text{ cm})^2 \times 3\text{ cm}$ . . . . .	114
6.9.	Reactor design for production in a printer with a build volume of $(60\text{ cm})^3$ . . . . .	114
6.10.	CAD representation of realistic reactor models for round-robin test. . . . .	117
A.1.	Different biogenic production routes for SAF [303]. . . . .	157
B.1.	Application of porous structures in process engineering [304]. . . . .	161
B.2.	CT scan of a reactor similar to the one used in chapter 5. . . . .	163
B.3.	First page of inspection and test plan: template for the approval of AM parts by TÜV Süd [305]. . . . .	164
B.4.	Strain-stress diagram. . . . .	165
B.5.	Photos of tensile specimens and fracture surface. . . . .	165
B.6.	Schematic of part with varying wall thickness and realistic scanning vectors. . . . .	166
B.7.	Picture of reactor 'fully additive' cut open. . . . .	167
B.8.	Manufacturing drawing of a flange for the hybrid concept. . . . .	168
B.9.	Reactor designs having been gradually improved over time. . . . .	169
B.10.	Pictures of preliminary fully additive reactor. . . . .	169
C.1.	Scanning electron microscope images of alumina powders. . . . .	175
C.2.	Report from static light scattering (SLS) analysis of sieved Sasol Puralox SCCa5-150. . . . .	176
C.3.	Report from SLS analysis of sieved Sasol Puralox SCCa150-230. . . . .	177
C.4.	Schematic representation of porous particle(s) being tested with He pycnometry and Hg intrusion porosimetry. . . . .	178
C.5.	Pictures of mercury intrusion porosimetry and He pycnometry analysis. . . . .	179

D.1. Results of modules with various internal structures during heat-transfer testing with water.	186
D.2. Experimental results of heat transfer with nitrogen without and with particles. . . . .	188

# List of Tables

2.1.	Literature overview of Co catalysts and respective reactor types. . . . .	7
2.2.	Results of fit of literature data to linearized equation. . . . .	9
2.3.	Industrial GtL plants employing Co as catalyst and fixed bed or surry bubble column reactors. Modified after [47, 89, 91–97]. . . . .	13
2.4.	Literature overview of reactors employing Co catalysts. Operating conditions and catalytic performance. . . . .	16
3.1.	Scanning strategies used in this work. . . . .	29
3.2.	PBF-LB/M machines with build space and build rates. Reference from [167], if not indicated otherwise. Usually $h_1=30-80\text{ }\mu\text{m}$ . . . . .	33
4.1.	Calculated and measured values of $\varphi_{\text{FGE}}$ . . . . .	44
4.2.	Material properties of 316L at room temperature used in calculation and simulation. [237]	47
4.3.	Results for stability of empty and fin-equipped modules $l=60\text{ mm}$ . . . . .	50
4.4.	Results for stability of pin-equipped modules. $t_w=0.6\text{ mm}$ . . . . .	50
4.5.	Results for stability of FGE-equipped ( $t_w=0.8\text{ mm}$ , $t_{\text{FGE}}=0.4\text{ mm}$ ) and lattice-equipped ( $t_w=0.6\text{ mm}$ ) modules. . . . .	50
4.6.	Characteristic values of particle size distribution of alumina powders. . . . .	53
4.7.	Particle permeation through commercial sinter metal frits. . . . .	56
4.8.	Experimental results for validation of the experiment. . . . .	57
4.9.	Laminar flow pressure loss through locally permeable modules. Values for $\Psi_V$ as fitted to measurements and as calculated according to Ref. [246]. . . . .	59
4.10.	Distribution parameter of the poly-disperse alumina powders derived from SLS measurements.	59
4.11.	Particle density and apparent particle density calculated from mercury intrusion porosimetry results. . . . .	61
4.12.	Calculated and measured infinite bed porosity of the poly-disperse alumina powders. . . .	62
4.13.	Parameters for the calculation of $c_p$ of $\text{N}_2$ . . . . .	69
4.14.	Values of heat transfer coefficients for rate determining step estimation and underlying assumptions. It was assumed that the slit was without internal structures ( $\varphi=0$ ), $d_{\text{slit}}$ , $t_w=1\text{ mm}$ , and $l=55\text{ to }60\text{ mm}$ , if not otherwise mentioned. With eq. (2.15), $T=213\text{ }^\circ\text{C}$ and $SV_{\text{mod}}=6\text{ L}_\text{N g}_{\text{cat}}^{-1}\text{ h}^{-1}$ result in $X_{\text{CO}}=70\text{ }\%$ . $\lambda_p=1\text{ W m}^{-1}\text{ K}^{-1}$ [260]. . . . .	72
4.15.	Important process variables, examples of sensors, actors, and respective requirements. . . .	85
5.1.	Overview of experimental set points and results. Constant for all set points were $p = 20\text{ barg}$ ; $\text{H}_2/\text{CO} = 2$ ; $\text{N}_2/\text{CO} = 0.1$ . . . . .	106
6.1.	Calculations for scale-up of packed-slit reactor concept to a capacity of $20\text{ barrel d}^{-1}$ . . . .	115
6.2.	Energy consumption of fabrication materials. . . . .	116
6.3.	Energy consumption of powder production and PBF-LB/M manufacturing. . . . .	116
6.4.	Cost estimation for PBF . . . . .	116

6.5.	Results of a Round Robin done with realistic reactor models of different sizes. Results for the largest arrived in December 2022 and January 2023, the rest in February and March 2022. Cost excluding value-added tax. . . . .	117
6.6.	Cost and material demand of reactors up to a capacity of 20 barrel d <sup>-1</sup> that were constructed, designed, or estimated during this work. . . . .	118
A.1.	Paraffins and olefins up to carbon number of four present in Fischer-Tropsch product. . . .	157
A.2.	Additional values for calculation of reaction criteria. . . . .	159
A.3.	Evaluation of criteria. . . . .	160
B.1.	Laser power as function of laser current . . . . .	162
B.2.	Spot diameter as a function of lens position. . . . .	162
B.3.	Scanning strategies used in this work. . . . .	163
B.4.	Modules without internal structures $t_w=1$ mm, $\varphi=0$ . . . . .	170
B.5.	Pin-equipped modules with $t_w=0.6$ mm. . . . .	171
B.6.	Pin-equipped module with $t_w=0.8$ mm, $t_p=1$ mm, and $a=3.4$ mm. . . . .	172
B.7.	Pin-equipped module with $t_w=1$ mm. . . . .	172
B.8.	Fin-equipped modules. . . . .	173
B.9.	FGE-equipped modules $t_w=0.8$ mm. . . . .	173
B.10.	Lattice-equipped module. . . . .	174
C.1.	Results from Mercury intrusion porosimetry and calculation of solid density. . . . .	178
C.2.	Composition of metal powders in wt-%. Both powders conformed both ASTM A276 and DIN EN 10088. . . . .	180
C.3.	Experimental materials and equipment. . . . .	181
C.3.	Experimental materials and equipment. (Continued) . . . . .	182
D.1.	Systematic errors of measured variables. . . . .	184
D.2.	Vapor pressure as function of boiling temperature according to Antoine equation [306] and Wagner equation in the 2.5-5-form [7]. . . . .	185

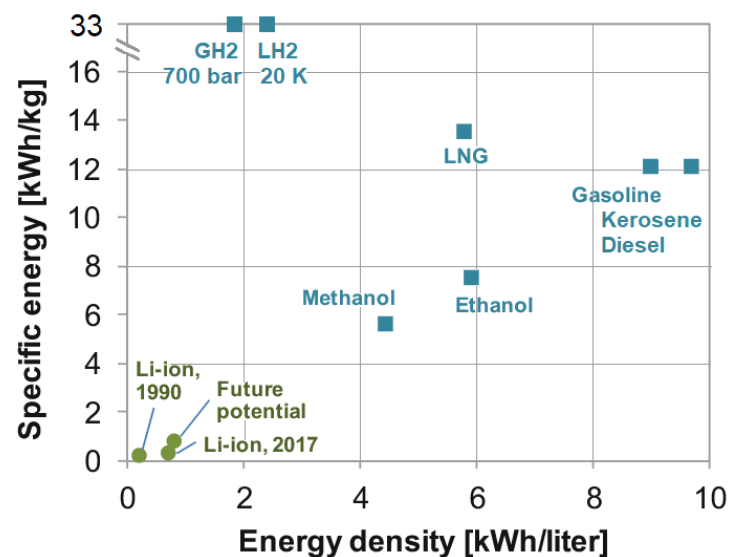
# 1. Introduction

## 1.1. Background and Motivation

Planet Earth is undergoing notable climate change, the rise in global temperature seriously endangering humanity's livelihood. By now it has been established that this climate crisis is in large part caused by anthropogenic carbon dioxide (CO<sub>2</sub>) emissions. [1]

Around 4 % of global warming are attributed to aviation [2], approximately half of which are direct effects of CO<sub>2</sub> emissions. The other half are indirect effects of nitrous oxides and contrails [3].

While battery electric vehicles are presently the most energy-efficient choice for road transport, it will be a long time until battery- or hydrogen-powered aircraft could be a viable option for future long-distance flights [4]. Until then, jet engines remain best suited for air traffic due to liquid hydrocarbons' high volumetric energy density (fig. 1.1).



**Figure 1.1.:** Energy density of Li-Ion batteries and various fuels. Adapted from [5] with additional data from [6, 7]. Reproduced with permission from SNCSC (©2018).

However, both direct and indirect effects of aviation's contribution to global warming can be significantly reduced by changing from fossil fuels to sustainable aviation fuels (SAF) [8]. SAF production can be started from two different sources: either from biogenic sources, or from renewable electricity, water, and CO<sub>2</sub> retrieved from environmental air [9]. SAF gained from the latter are so-called Power-to-Liquid (PtL) fuels or e-fuels and not only have a lower demand of water and land use, but also the highest potential for greenhouse gas reduction [9, 10]. From 2025 on, the European Union (EU) will impose mandatory quotas for SAF and subquotas for e-fuels within the aviation industry [11]. Germany plans to have 200,000 t a<sup>-1</sup> of PtL fuel by 2030 [12] (2 % of its current kerosene consumption [13]).

Within the family of Kopernikus projects funded by the German Federal Ministry of Education and Research (BMBF), Kopernikus Power-to-X (P2X) is committed to investigating the production of e-fuels and other chemical energy carriers. As part of Phase II of these studies, this PhD thesis focuses on the design, manufacture, and use of Fischer-Tropsch synthesis (FTS) reactors for decentralized production of e-fuels. Another application of hydrocarbons in the future are sustainable performance materials like lubricants, coatings, or polymers as construction materials [14].

There is no standard definition for decentralized plants. It is very likely that their thermal power (lower heating value (LHV) of products) is below 500 MW, likely below 100 MW. This is reasonable considering the decentralized nature (spatial variation) of the input renewable energy and of the output kerosene. To also cope with the temporal fluctuation of renewables, decentralized PtL plants have to be load-flexible. Current industrial FTS plants based on fossil resources are large (both in equipment size and thermal power which is  $\geq 1$  GW), which makes them inflexible [15].

Some of the advantages of decentralized PtL plants are at the same time challenges to the FTS reactor, adding up to the following requirements/challenges of the reactor: compactness, load flexibility, modularity, high efficiency, and low cost. Until now, only few reactors are suitable for application in this field [16]. They characteristically comprise complex internal channels and integration of cooling, heating and sensing. Building such miniature level reactors by conventional manufacturing methods is relatively difficult, one approach being a complex multi-step process of subtractive sheet metal manufacturing, diffusion welding, and further machining as well as adaptation [17].

### 1.2. Objective of this Thesis

The objective of this dissertation is to use additive manufacturing (AM) for producing an FTS reactor for decentralized PtL plants. One of the major benefits is that this manufacturing method provides a way to produce almost arbitrarily shaped parts efficiently in a mostly automated process. Cost per part being independent of part complexity and lot size is a notable advantage over conventional production methods [18]. It is assumed that the ramp-up of PtL is successful with the production of many decentralized plants/reactors. Therefore, AM is a promising option.

AM is a relatively new manufacturing method, especially its application to chemical reactors. There are promising laser-based powder bed fusion of metals (PBF-LB/M) solutions for isolated applications, mostly on lab-scale. They suggest performance equal or superior to diffusion-welded micro-structured reactors (MSRs) and streamlined manufacturing. To date, not many systematic investigations of AM devices for process-engineering applications have been documented.

AM is approved and recognized by industry majors such as BASF [19] and Shell [20, 21]. But small and medium-sized companies do not necessarily have the means to develop an AM reactor concept.

This doctoral research study aims to identify the technical requirements to be met by AM chemical reactors for FTS in general and propose a suitable reactor concept. With thorough investigations in fabrication, performance, and safety, the trust of chemical engineering practitioners in AM is ensured. The provided design recommendations enable industry and researchers alike to adapt the concept to their needs and decrease design and fabrication effort [22].

Both research and industry are highly interested in improved reactors, especially with shorter design and fabrication time. This work strives to facilitate this by providing pre-validated modules for designers and researchers to adapt to their requirements. Chemical engineers are interested in fabricating better

reactors faster but are also somewhat hesitant to adopt new technologies, compare history of micro-structured reactors [23]. An objective of this work is also to establish confidence in AM reactors for chemists and chemical engineers.

Incorporated into a PtL plant, FTS can be performed in an optimal way to produce a certain product or several products. Beside kerosene, this could be gasoline, diesel, or wax. The main focus of the dissertation being placed on FTS reaction, and every FTS-gained product having to undergo upgrading steps in additional (usually conventionally-manufactured) reactors, product selection remains variable. This has been shown in Kopernikus P2X Phase I with an integrated plant with a thermal power of 10 kW [24]. That plant was equipped with diffusion-welded FTS reactors which are also intended for plants with higher capacity in the project (250 kW in Phase II and several MW in Phase III). For the first time, this dissertation explores the potential of additive FTS reactors for this application.

This doctoral thesis was carried out at the Institute for Micro Process Engineering (IMVT) of Karlsruhe Institute of Technology (KIT). IMVT, under the management of Prof. Roland Dittmeyer, has a proven track record of developing novel reactors [25].

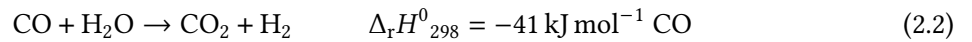
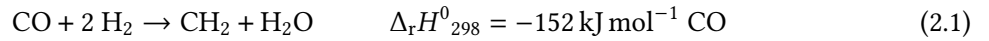




## 2. Fischer-Tropsch Synthesis (FTS)

This chapter outlines the basic principles of Fischer-Tropsch synthesis (FTS). Section 2.1 contains the definition of reaction performance for this work and a simple reactor model to assess design variants. Section 2.2 focuses on the implications of decentralized Power-to-Liquid (PtL) plants on reactor requirements. Section 2.3 presents a thorough literature review on existing FTS reactors and their performance, while section 2.4 is about the design of a micro-structured FTS reactor based on slit-shaped modules. The chapter is summarized in section 2.5.

FTS was discovered in Germany in the 1920s [26, 27]. The feed is a mixture of carbon monoxide (CO) and hydrogen (H<sub>2</sub>), referred to as synthesis gas or syngas [28]. Under low-temperature FTS, syngas reacts at  $p=20\text{--}30$  bar and  $T=200\text{--}250$  °C on a solid catalyst to various hydrocarbons and H<sub>2</sub>O as byproduct (eq. (2.1)) [29, 30]. Water-gas shift reaction might occur in parallel, depending on the catalyst and operating conditions (eq. (2.2)) [31]. FTS is very exothermal with reaction enthalpy being taken from Ref. [32].



To avoid harming the catalyst with high partial pressure of water, reactors are operated with limited conversion of CO,  $X_{\text{CO}} \leq 70\%$  [33]. Hence, at the outlet, syngas is mixed with the product and usually separated and recycled. Furthermore, inert gases can be present [34].

The syngas source is arbitrary. In industrial FTS plants, fossil resources coal and natural gas are used [28], hence the terms Coal-to-Liquid (CtL) and Gas-to-Liquid (GtL). Renewable e-fuels can only be produced with syngas from biomass or from renewable electricity, water (H<sub>2</sub>O), and carbon dioxide (CO<sub>2</sub>) [35]. Syngas is toxic and flammable, and operating pressure and temperature pose further physical risks [36].

Remarkably, during FTS, carbon atoms are linked, forming higher molecules in a polymerization-like reaction. The chain growth probability  $\alpha_{\text{ASF}}$  is the ratio between propagation and termination rate [32]. The formed products are various hydrocarbons, simply denoted as CH<sub>2</sub>. Products include mainly alkanes and olefines, and, to a lesser extent, oxygenates such as alcohols [37]. The product constitution can be described by the Anderson-Schulz-Flory (ASF) distribution with one common  $\alpha_{\text{ASF}}$  for all hydrocarbons. Product constitution can be described more thoroughly by using one common  $\alpha_{\text{ASF}}$  with deviations in methane and ethene, or with separate  $\alpha_{\text{ASF}}$  for each homologous series [38]. Dry [30] and Stadler et al. [39] found that co-fed CO<sub>2</sub> has no effect on the reaction. Higher temperatures usually lead to a shorter average chain length (lower  $\alpha_{\text{ASF}}$ ), particularly to an increase in unwanted methane (CH<sub>4</sub>) [31].

FTS is highly exothermal and thus reactor stability has to be considered. A simple calculation reveals that the adiabatic temperature rise would be  $\Delta T_{\text{ad}} \approx 1730$  K with undiluted syngas, appendix A, when Lu and Hildebrandt [15] found this number to be 1500 K. Uncontrolled temperature rise ('run-away') must be avoided due to negative effects on selectivity, catalyst lifetime, and safety. This is achieved

by diluting synthesis gas, diluting catalyst, active cooling, or a combination thereof [29], as will be discussed in section 2.3.

The possible active components of FTS catalysts are Fe, Co, and Ru [31]. On average, these metals were priced, the reference being iron, at a ratio of 1 : 163 : 35,000 between 2018 and 2022 [40–42], which is no significant change from the findings of van der Laan and Beenackers [37] valid for 1989: 1 : 230 : 31,000. Co combining the highest yield of long and linear hydrocarbons, the longest lifetime, low water-gas shift reaction activity, and good availability, it was the catalyst component chosen for the research under this thesis [37, 43].

Supported cobalt (Co) catalysts consist of the metallic active component and minor amounts of metallic promoter(s), which are both dispersed on a porous ceramic support [31]. The diameter of Co crystallites should be as small as possible for maximum yield, but  $d_{Co} > 10$  nm for oxidation resistance [31]. Wolf et al. [44] state that oxidation is more likely with high partial pressures of  $H_2O$  and  $CO$ .

Multiple combinations of Co catalyst-promoter-support are employed in research and industry. In this work, they are denoted as "Co/Re/Pt/Si/Mn@Support", with the metal being replaced by the weight fraction of reduced metal per support in wt-%, '-' if the metal was not present, and '?' if the amount was unknown. Support is replaced by the respective material.

In table 2.1, a literature overview of Co catalysts is given. The reactor type is given: N=annulus, T=tube, M=micro-structured, A=additive, S=slurry, as well as the scale of the operation: L=laboratory, P=pilot, I=industry. This literature overview is not exhaustive but it is reporting research orienting itself to either one of three criteria: 1. taking place at Institute for Micro Process Engineering (IMVT) or in cooperation therewith, 2. dealing with innovative highly active catalysts, and/or 3. dealing with innovative reactors.

Alvarado Rupflin et al. [45] investigated systems of the type: cobalt, two promoters, and support under industrially relevant conditions. They found that reduction of first promoter Rh from 0.1 % to 0.01 % is compensated for by the addition of 5 % Hf in a certain catalyst with regard to activity.

Velocys Inc. (Plain City, OH, USA) uses an organic matrix combustion catalyst with high Co loading in its commercially available micro-structured reactor (MSR) [46].

Shell plc (London, UK) utilizes a Co-Mn/ $TiO_2$  catalyst with  $d_p = 1\text{--}3$  mm in its industrial multi-tubular reactors [31, 47].

Sasol Ltd. (Johannesburg, South Africa) employs a Co-Pt/ $Al_2O_3$  catalyst with  $d_p < 100\text{ }\mu\text{m}$  in its industrial slurry bubble-column reactors [31]. Ineratec GmbH (Karlsruhe, Germany) announced that they use Sasol's catalyst in their commercially available MSR [48].

## 2.1. Reactor Performance and Modeling

Reactor performance was described in terms of the conversion of CO  $X_{CO}$  at a given temperature  $T$  and space velocity ( $SV$ ), eqs. (2.3) to (2.4). Space time yield ( $STY$ ) can be calculated from this (eq. (2.5)) but also fairly easily measured, eq. (2.6). Both  $STY$  and  $SV$  are related to the volume of catalyst. The modified versions are related to its mass, hence  $\square_{mod} = \square/\rho_{cat}$ . [32, 62]

$$X_{CO} = \frac{\dot{n}_{CO,in} - \dot{n}_{CO,out}}{\dot{n}_{CO,in}} = \frac{y_{CO,in}/y_{N_2,in} - y_{CO,out}/y_{N_2,out}}{y_{CO,in}/y_{N_2,in}} \quad (2.3)$$

**Table 2.1.:** Literature overview of Co catalysts and respective reactor types.

Ref.	Type, scale	Co/Re/Pt/Si/Mn@ Support	wt-% of	$d_p$ / $\mu\text{m}$	$m_{\text{cat}}$ / g	$d_t$ / mm	$d_{\text{slit}}$ / mm	$l_{\text{cat}}$ / mm	$V_e$ / mL	Inert material	$V_{\text{cat}}$ / mL	$\rho_{\text{bed}}$ catalyst / $\text{g mL}^{-1}$
[49]	N,L	20/0.5/-/-/-@Al <sub>2</sub> O <sub>3</sub>		50-200	0.8	12	1.5	<107	6.8	>1mL SiC	5.8	?
[50]	N,L	18.7/0.46/-/-/-@Al <sub>2</sub> O <sub>3</sub>		50-100	?	12	1.5	<107	6.8	Al <sub>2</sub> O <sub>3</sub>	?	?
[51]	T,L	21/-/0.2/-/-@Al <sub>2</sub> O <sub>3</sub>		50-150	1	9.1	-	<304.8	?	1 g SiC 50-150	?	?
[33]	T,L	21.4/-/0.2/1.6/-@Al <sub>2</sub> O <sub>3</sub>		50-150	0.5	9.1	-	<304.8	?	3 g SiC 105	?	?
[52]	T,L	10-20/-/-/-@TiO <sub>2</sub>		125-150	0.2-0.8	6	-	?	?	None	?	?
[45]	T,L	5-20/var/-/-@var		35-100	?	4.2	-	<70	?	SiC	?	?
[53]	T,L	22.8/-/0.1/-/-@Al <sub>2</sub> O <sub>3</sub>		300	7.2	27.8	-	19	11.5	0.11 PBF-LB/Al	?	0.64
										POCS, Al <sub>2</sub> O <sub>3</sub>		
[54]	M,L	20-40/0.5-1/-/-@Al <sub>2</sub> O <sub>3</sub>		53-90	1.5	-	0.8	?	?	None	2	0.75
[54]	T,L	20-40/0.5-1/-/-@Al <sub>2</sub> O <sub>3</sub>		53-90	1.5	10	-	?	?	1:20 SiC	?	0.75
[55]	M,L	20/0.5/-/-@Al <sub>2</sub> O <sub>3</sub>		50-200	-	-	0.8/1.5	?	?	None	?	?
[56]	M,L	20/0.5/-/-@Al <sub>2</sub> O <sub>3</sub>		<sup>a</sup>	0.164-0.41	-	0.7	20	?	None	?	?
[57]	A,L	61/-/-/-@ <sup>b</sup>		-	-	8	-	50	0.4-1.3	None	2.5 <sup>c</sup>	-
This work	A,L	21.4/-/0.2/1.6/-@Al <sub>2</sub> O <sub>3</sub>		50-150	3.3	-	1	60	4	None	3.3	$\approx 1$
[58]	M,L+P	20/0.5/-/-@Al <sub>2</sub> O <sub>3</sub>		50-200	2/120	-	1.5	?	2.7/163	None	2.7/163	0.74
[59]	M,P	20/0.5/-/-@Al <sub>2</sub> O <sub>3</sub>		50-200	120	-	1.5	?	163	None	163	0.74
[60]	M,I	20/0.5/-/-@Al <sub>2</sub> O <sub>3</sub> <sup>d</sup>		50-200	?	-	?	?	?	None	?	?
[23, 46, 61]	M,I	?		100-300	?	-	0.2-5	600	?	None	?	?
[29, 31]	T,I	20/-/?/-/1.66@TiO <sub>2</sub>		1000-3000	?	25.4	-	12200	?	None	?	?
[29, 31]	S,I	20/-/0.05/?/-@Al <sub>2</sub> O <sub>3</sub>		10-200	?	11000	-	?	?	1:4 liquid wax	?	?
N=annulus, T=tube, M=micro-structured, A=additive, S=slurry, L=laboratory, P=pilot, I=industry, var=various, -=not applicable, ?=unknown.												

<sup>a</sup> Catalytic washcoating with thickness 32 and 80  $\mu\text{m}$  respectively<sup>b</sup> So-called self catalytic reactor made from Co<sup>c</sup> Volume of the whole tube<sup>d</sup> Catalyst from Sasol

$$SV = \frac{\dot{V}_{N, \text{syngas}}}{V_{\text{cat}}} \quad (2.4)$$

$$STY = X_{\text{CO}} \cdot SV \cdot y_{\text{CO}, \text{in}} \cdot S_{\text{C}5+} \cdot \tilde{\rho}_N \cdot \frac{\dot{M}_{\text{C}5+}}{n_{\text{C}5+}} \quad (2.5)$$

$$STY = \frac{\dot{m}_{\text{C}5+}}{V_{\text{cat}}} \quad (2.6)$$

The inlet composition can be calculated via eqs. (2.7) to (2.9) assuming it consists of CO, H<sub>2</sub>, and N<sub>2</sub> only.

$$y_{\text{CO}, \text{in}} = \frac{1}{1 + \text{H}_2/\text{CO} + \text{N}_2/\text{CO}} \quad (2.7)$$

$$y_{\text{H}_2, \text{in}} = \frac{\text{H}_2/\text{CO}}{1 + \text{H}_2/\text{CO} + \text{N}_2/\text{CO}} \quad (2.8)$$

$$y_{\text{N}_2, \text{in}} = \frac{\text{N}_2/\text{CO}}{1 + \text{H}_2/\text{CO} + \text{N}_2/\text{CO}} \quad (2.9)$$

A more in-depth view on product constitution provide the carbon-related molar selectivities of hydrocarbons  $S$  (eqs. (2.10) to (2.11)) [58], the chain growth probability  $\alpha_{\text{ASF}}$ , and the olefin-paraffin ratio [37]. The chain growth probability  $\alpha_{\text{ASF}}$  is related to the weight fraction  $\omega_{\text{Cn}}$  of products with carbon number  $n$  according to eq. (2.12) [58]. It takes values between 0 and 1, with high numbers referring to a higher average carbon number of the products. The olefin-paraffin ratio was calculated for hydrocarbons C2 to C4 according to eq. (2.13) [37]. The weight fractions of the isomers were added.

$$S_{\text{Cn}} = \frac{\dot{n}_{\text{Cn}, \text{out}} \cdot n}{\dot{n}_{\text{CO}, \text{in}} - \dot{n}_{\text{CO}, \text{out}}} \text{ for } n \in [1; 4] \quad (2.10)$$

$$S_{\text{C}5+} = 1 - \sum_{n=1}^4 S_{\text{Cn}} \text{ for } n \geq 5 \quad (2.11)$$

$$\omega = n \cdot (1 - \alpha)^2 \cdot \alpha^{n-1} \quad (2.12)$$

$$O/P = \frac{1}{3} \cdot \left( \frac{\omega_{\text{C}2, \text{o}}}{\omega_{\text{C}2, \text{p}}} + \frac{\omega_{\text{C}3, \text{o}}}{\omega_{\text{C}3, \text{p}}} + \frac{\omega_{\text{C}4, \text{o}}}{\omega_{\text{C}4, \text{p}}} \right) \quad (2.13)$$

For modeling fixed bed reactors, which is the type investigated in the thesis in hand, most researchers assume ideal behavior of a plug-flow reactor. This is justified in most applications [49], and a one-dimensional mass- and energy balance can be set up. The differential-algebraic coupled equations can be solved as initial value problems with a numeric solver [63].

Chemical reaction kinetics are the critical factor. They can be formulated for one or more educts, or for lumps of products, or for the complete spectrum of individual product species. Dependency of kinetics can be as simple as educt concentration and temperature [64]. Dependencies can also extend to product concentrations and pressure, taking into account inhibition terms [65, 66].

Acknowledgment of pressure, stoichiometry, gas contraction, and non-trivial reaction orders makes finding an explicit formula for the dependence of  $X_{\text{CO}}$  impossible [51]. It was necessary to express  $X_{\text{CO}}$  as a function of  $T$  and  $SV_{\text{mod}}$ , hence a linearization of the former w.r.t. the latter two was made, resulting in the formula shown in eq. (2.14), which is similar to Loewert et al. [59].

$$X_{\text{CO}} = a + b \cdot SV_{\text{mod}} + c \cdot T \quad (2.14)$$

Since the proposed designs in the thesis in hand are in the realm of MSR with efficient heat transfer, isothermal performance is expected most of the time, and no energy balance has to be solved. This leads to the unique ability to model multiple reaction channels with different flow condition, without the need to solve differential equations.

If this formula describes the reaction well,  $a$  and  $b$  are supposed to be negative and  $c$  positive, respectively.  $T_I = -a/c$  can be interpreted as the ignition temperature where an infinitely small amount of syngas ( $SV_{\text{mod}} \rightarrow 0, \tau_{\text{mod}} \rightarrow \infty$ ) starts to react ( $X_{\text{CO}} \geq 0$ ).

Values for these parameters can only be compared under similar conditions of  $p$ , ratio of  $\text{H}_2/\text{CO}$ , or dilution. In table 2.2 experimental data from literature was fitted to the linearized formula, yielding good results. Each data-set was obtained with a different catalyst at  $p=20$  bar [53, 54, 67] except for the data from Loewert's pilot scale reactor, which was measured at  $p=30$  bar [59]. Coefficients of determination were above 0.95 in four out of five cases.

**Table 2.2.:** Results of fit of literature data to linearized equation.

Data	Ref.	N. of points / -	$a$ / %	$b$ / % $\frac{\text{g}_{\text{cat}}}{\text{h L}_\text{N}^{-1}}$	$c$ / % $^\circ\text{C}^{-1}$	$T_I$ / $^\circ\text{C}$	$R^2$ / -
Myrstad, A, $p=20$ bar	[54]	7	-341.9	-2.441	1.977	172.9	0.957
Myrstad, B, $p=20$ bar	[54]	5	-474.9	-2.747	2.619	181.3	0.983
Fratalocchi	[53]	11	-208.7	0.000	1.141	182.9	0.975
Loewert, pilot, $\text{H}_2/\text{CO} \in [1.93; 2.11]$	[59]	12	-556.4	-2.508	2.625	212.0	0.948
Almeida, block 2	[67]	9	-304.3	-2.114	1.581	192.4	0.734

The values of the coefficients could not be verified in reality, but their algebraic signs were as expected, and the theoretical ignition temperatures took realistic values in all cases. The formula given in eq. (2.15) was employed for simulating the reaction performance of design candidates in this work.

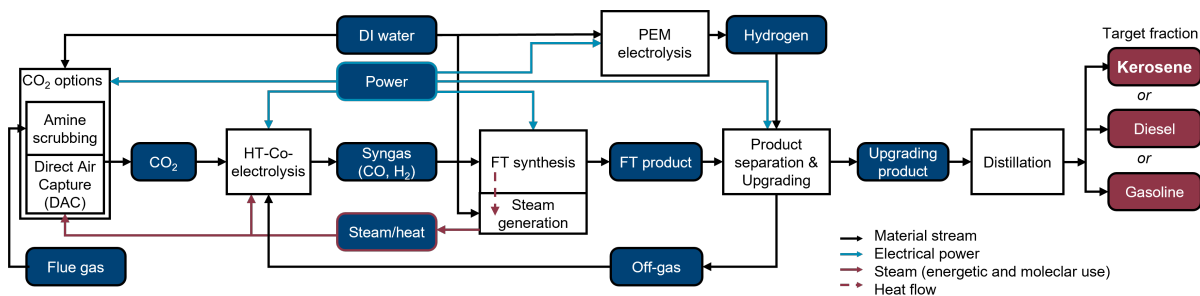
$$X_{\text{CO}} = -340 - 2.5 \cdot SV_{\text{mod}} + 2 \cdot T \quad (2.15)$$

## 2.2. Decentralized Power-to-Liquid Plants

The power output of onshore wind energy plants reaches from 40–318 MW [68], while solar power plants reach up to 605 MW [69]. The power output of offshore wind energy plants goes from 48–522 MW with power of the single turbine reaching from 2.35–9.5 MW according to [70]. It is a topic of intensive research currently to transform the renewable electricity from offshore wind energy locally to chemical energy carriers. Instead of cables, pipelines or ships would be used to transport the energy onshore or to the point of consumption [71]. The full-load hours actually amount to approximately 2000, 1000, and 4000 for the before mentioned energy sources, respectively [6]. This emphasizes why flexible decentralized Power-to-X (PtX) plants are so important.

In the project Kopernikus PtX this process is realized in an integrated plant, assembled in containers or skids in a space-saving manner. The process chain is depicted in fig. 2.1 and consists of the following steps: 1.  $\text{CO}_2$  capture, 2. syngas generation, 3. FTS, 4. upgrading, and 5. separation [72].  $\text{CO}_2$  capture is to be done with direct air capture (DAC) in order to close the carbon cycle. Low-temperature DAC from project partner Climeworks (Zürich, Switzerland) uses adsorption at ambient conditions and

desorption under vacuum and at elevated temperatures of approx. 95 °C. Syngas generation is to be done with solid-oxide electrolysis cells in co-electrolysis mode by Sunfire (Dresden, Germany) in the project. FTS is executed in an intensified reactor by Ineratec (Karlsruhe, Germany) and upgrading is done in conventional reactor vessels procured by IMVT. Separation happens in separator vessels (so-called traps) and if required at a distillation service provider. To increase efficiency, material and energy streams are exchanged throughout the plant. [72]



**Figure 2.1.:** Process chain for a decentralized Power-to-Liquid plant in project Kopernikus P2X [72]. Reproduced with permission from the authors (©2023).

The process has been realized on a demonstration scale, for instance in Kopernikus P2X Phase I with limited upgrading capabilities and with limited energy and mass streams integration [73]. While the electrolysis capacity in Phase I was 10 kW, it is 250 kW in Phase II which amounts to a product output of two barrel per day (2 barrel d<sup>-1</sup>).

Similar process chains have been investigated by means of simulation by Ausfelder and Dura [35], Schemme [74], and König [75]. They all confirm that the process chain is suitable for production of CO<sub>2</sub> neutral e-fuels. The reported energy efficiency related to the lower heating value (LHV) is  $\eta = 0.5\text{--}0.6$ , and the reported fuel cost is  $C = 1.75\text{--}3.75 \text{ € L}^{-1}$  as of 2023.

A study by Rojas-Michaga et al. [76] confirms that the global warming potential of e-fuels is lower than that of fossil kerosene. A cost of 5.16 pounds per liter in 2030 is calculated based on low-temperature DAC, off-shore wind power, alkaline electrolysis, and a connection to the UK electricity grid.

The relevant kerosene specifications are those stipulated for the American Jet A-1. Heyne et al. [77] describes the complicated process for a synthetic fuel to comply with regulations as well as a pre-screening test. The most important required fuel characteristics are dynamic viscosity  $\eta$  at  $T = -20$  and  $-40$  °C, density  $\rho$  at  $T = 15$  °C, surface tension  $\sigma$  at  $T = 22$  °C, derived cetane number (DCN), distillation curve, and flashpoint.

De Klerk [78] defines the following steps as necessary for the attainment of final products:

- upgrading,
- partial refining, and
- complete refining.

Upgrading means that obtained intermediates still need refining. Partial refining yields some final products while complete refining yields all final products.

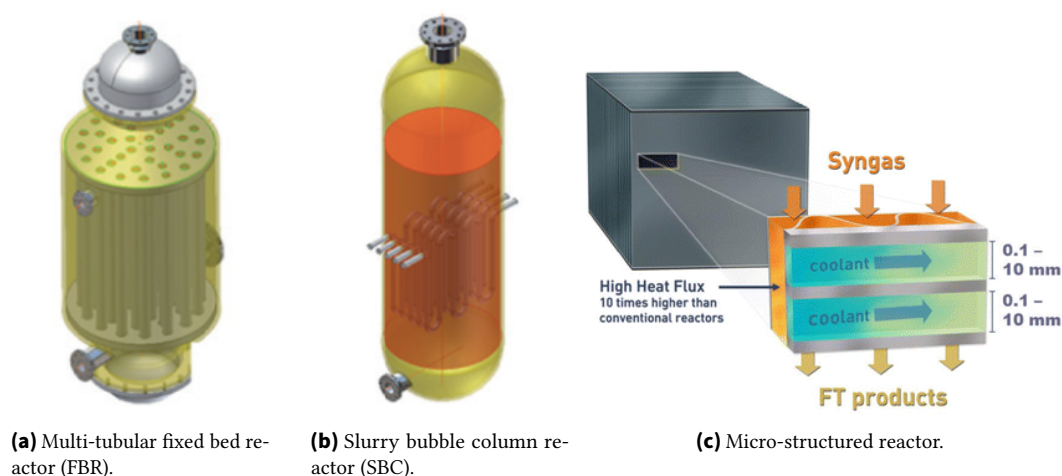
The process chain employed by Shell, the so-called Shell middle distillate synthesis (SMDS), comprises hydro-cracking and yields approx. 50 % kerosene [79]. The isomere content of a C<sub>10</sub> to C<sub>13</sub> mixture was successfully increased by Zschiesche et al. [80] with little undesired cracking by using industrial zeolite catalysts.

All studies agree that electricity cost is a significant factor of PtL product cost. Today, the lowest electricity cost is achieved by using renewable energies [81]. A production plant connected exclusively to a dedicated renewable energy facility avoids grid costs [82]. In order to be cost effective, PtL must be load-flexible and operable in small capacities to accommodate typical decentralized renewable electricity generation conditions, e.g. wind or photovoltaic. It is also beneficial for PtL plants to be space-saving and capable of being integrated into existing structures [73]. Owing to their high energy density, e-fuels from decentralized production can be transported efficiently [83].

It is well-known that by intensifying transport processes, micro-structured devices are capable of carrying out chemical reactions under harsh conditions in small spaces [16] and under fluctuating conditions [84]. The requirements of decentralized plants are also addressed by the concepts of process intensification [85] and modularization [86]. In comparison to 100 % on-site construction, the use of prefabricated, specialized-workshop-manufactured modular units allows for faster, cheaper, and cleaner erection of production plants [87]. Many studies have confirmed that MSR are compact, load-flexible, and modular [58, 82].

## 2.3. Reactors

Due to the prevailing conditions, FTS reactors must be made of steel [88]. In the following, the most common reactor types, summarized by van de Loosdrecht et al. [31], will be discussed, fig. 2.2.



**Figure 2.2.:** Images of reactor types for Fischer-Tropsch synthesis (FTS). Modified after [31, 61]. Reproduced with permissions from Elsevier (©2013) and SNCSC (©2014).

### 2.3.1. Industrial Reactors

There are two types of conventional reactors used for most industrial FTS plants employing Co as catalyst: fixed bed reactors (FBR) and slurry bubble column reactors (SBC) [89]. Packed bed reactors are a common implementation of heterogeneous catalysis in industry. The catalytic particles are packed into the reactor, its simplest form being a container with an inlet and an outlet. Such systems are also relevant for adsorption, desorption, and separation. In industrial applications, the shape of reactors is often a cylindrical vessel or a tube denoted by its length  $l$  and diameter  $d$ , with particles having various shapes and an equivalent diameter of  $d_p \approx 1-10$  mm. [32]



### **2.3.1.1. Multi-Tubular Fixed Bed Reactors**

A FBR is either called vessel, when the length to diameter ratio is close to one, or it is called tube, when this ratio is very high. In a multi-tubular reactor, many fixed bed reactor tubes are combined and surrounded by a heat transfer fluid in a common vessel. This is required for highly exothermal or endothermal processes. Multi-tubular fixed bed reactors are popular FTS to their simple design and good scalability. The catalyst is stationary, reducing wear to a minimum and eliminating the necessity to separate the catalyst from the product. [32]

Shell's multi-tubular fixed bed reactor concept uses a diluted catalyst, which improves temperature management. This is, however, still not sufficient to render the reactor isothermal and restricts catalyst effectiveness and product selectivity to below optimum. [29]

Pearl GTL in Qatar, the worldwide biggest plant of its kind, did cost around 19 B\$ and construction took three years. It produces 140,000 barrel per day ( $\text{barrel d}^{-1}$ ) of oil and 120,000  $\text{barrel d}^{-1}$  of oil equivalent in natural gas liquids and ethane [47]. Figuring in the lower heating value, this equals a thermal power of approx. 18 GW. Pearl GTL employs 24 multi-tubular fixed bed reactors with a mass of 1200 t each.

### **2.3.1.2. Slurry Bubble Column Reactors**

Within Sasol's SBC reactor concept, the product wax works as a solvent, at the same time diluting the catalyst. This helps control temperature and utilize more of the catalyst volume, but this procedure requires separation of solvent, product, and catalyst. Furthermore, FTS to hydrodynamics, scale-up of this reactor type is challenging. [29]

The Oryx GTL plant (Qatar) did cost around 1 B\$, its construction took four years, and it produces 33,000  $\text{barrel d}^{-1}$  of oil equaling a thermal power of 2 GW [90]. It employs two SBC with a mass of 2000 t each.

To date, conventional reactors employed in industry all have one restriction in common: limitation in productivity, artificially built-in to control the reaction, as is briefly highlighted in the above examples. Selected industrial GTL plants are listed in table 2.3. The capital expenses for plants of such dimensions are immense; on-site construction is complicated and takes years. They consist of huge components, exploiting the economy of scale, and are designed to run continuously at optimal operating condition. Such facilities do not adapt well to short-term performance reduction; running under half-steam renders them inefficient. [31]

### **2.3.2. Lab-Scale Reactors**

Lab-scale reactors are often miniaturized forms of large scale reactors, mostly single tubular reactors with small diameter. The other very common type are MSR.

**Table 2.3.:** Industrial GtL plants employing Co as catalyst and fixed bed or slurry bubble column reactors. Modified after [47, 89, 91–97].

Name	Country	Owner	Production / barrel d <sup>-1</sup>	Start up	Construc- tion time / a	Cost / B\$
FBR (Shell)						
Shell SMDS	Malaysia	Shell	14,700	1993	3	1
Pearl GtL	Qatar	Shell/	140,000	2012	6	19
SBC (Sasol)						
Oryx GtL	Qatar	Sasol/	34,000	2007	4	1
Escarvaros GtL	Nigeria	Chevron/NNPC	34,000	2014	9	10
Uzbekistan GtL	Uzbekistan	UNG	32,000	2022	8	2.3

### 2.3.2.1. Lab-Scale Conventional Reactors

In laboratories, tubular and annular fixed-bed reactors are employed frequently to characterize catalysts, measure data for kinetic parameter fits, or to produce FTS products for subsequent use, for sources refer to table 2.1. The following measures are taken to avoid heat and mass transfer limitations: small dimensions, dilution of feed and catalyst. They are basically smaller versions of the above described industrial reactors. Slurry-bubble column reactors are used for the same purpose, with a good heat transfer being ensured by the liquid phase [98], but not mentioned in table 2.1 due to space constraints.

In their work, Kirsch et al. [62] employed both a MSR with catalyst coating and an annular reactor with catalyst bed. The latter had an inner diameter of  $d = 12$  mm, an annulus width of  $t = 1.5$  mm, a length of  $l = 107$  mm, and contained  $m_{\text{cat}} = 0.8$  g. The maximum achieved modified  $STY$  was  $STY_{\text{mod}} = 1 \text{ g}_{\text{C5+}} \text{ g}_{\text{cat}}^{-1} \text{ h}^{-1}$ . It performed isothermally FTS to catalyst dilution and intense active cooling with thermal oil.

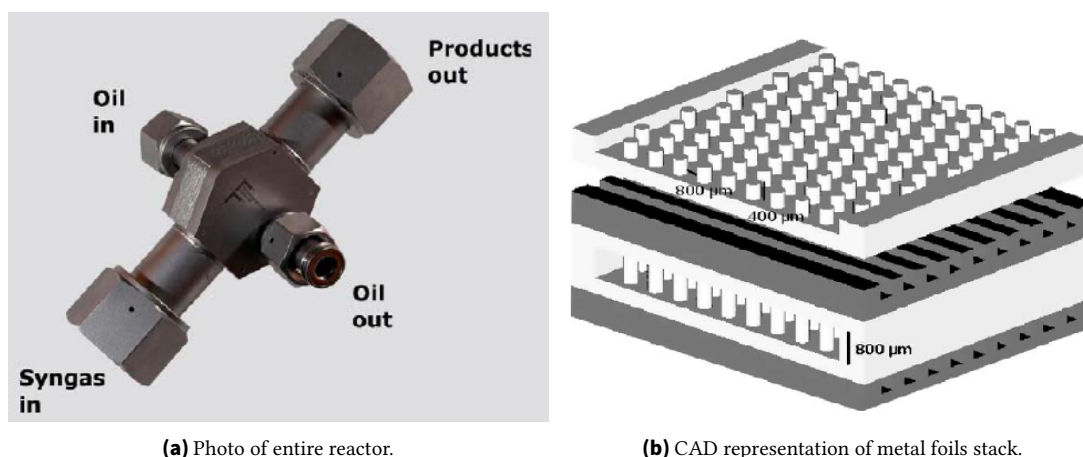
Refs. [53, 99] used a tubular reactor equipped with a periodic open cellular structure (POCS) with a solid volume fraction of  $\varphi = 0.11$ , thus proving the positive effect of POCS on heat transfer. Their reactor was non-isothermal, being operated at medium  $SV$  and an inert gas dilution of 0.24 as well as catalyst dilution.

### 2.3.2.2. Lab-Scale Micro-Structured Reactors

This standard [100] defines micro process engineering as process engineering taking place in technical apparatus having internal dimensions in the range of micrometers to a few millimeters. Consequently, the term micro-structured reactor (MSR) is used hereafter. In MSR for Fischer-Tropsch synthesis (FTS), channels are mostly rectangular with a depth in the range of  $d=0.8\text{--}1.5$  mm [49, 54, 55, 60]. Their length can be up to 300 mm. The alumina-supported Co catalyst usually has a spherical shape and a diameter of 50–200  $\mu\text{m}$  [33, 49, 51, 54, 55, 60]. Rectangular channels can be designed as individual channels with approximately square cross-section or as slit-shaped channels. In the latter case internal structures usually pins are included due to the force present during diffusion bonding [54, 101]. The other common channel shape is elliptical as consequence of the manufacturing techniques [102]. Since heat and mass transfer are inversely proportional to the characteristic length of the flow, much higher transfer rates occur in micro-structured devices. The same applies to the surface to volume ratio and the heat transfer across the thin walls of micro-structured channels. This aptitude makes MSR suitable

for process intensification. In MSR hazardous reactions can be handled safely due to two reasons: little dead volumes and dimensions below the quenching distance at which explosions can propagate [103]. In a channel with much higher heat transfer, chemical reactions can be executed with higher rates. This is realized by increasing catalyst or feed concentration and temperature. If catalyst particles of  $d_p < 100 \mu\text{m}$  (corresponding to a catalytic coating with  $t < 50 \mu\text{m}$ ) are used, pore diffusion limitation is eliminated, allowing the catalyst pore effectiveness factor to rise to near-unity. It can also be deduced that MSR show no to very little intraparticle heat transport limitations and/or interparticle heat and mass transfer limitations [49, 104]. MSR do not have a large share in the industrial production of chemicals, although successful applications exist, for instance in China and Austria [105–107].

MSR can be made conventionally from metal sheets (foils) in a manufacturing process combining milling or etching and diffusion bonding, or laser welding and adaptation [108], fig. 2.3. This figure shows on the left a picture of the complete reactor, of which the main part in the middle has around the size of a fist. In this main part layers are visible on the outside. These layers are a result of the diffusion-bonded stack of metal foils, of which parts are depicted in a computer aided design (CAD) representation on the right of fig. 2.3. A common version of such devices is made by IMVT in a procedure described in appendix B.2. Examples of such reactors for FTS can be found in research and early industrial adoption, for sources refer to table 2.1. It can be deduced that the manufacture of such a reactor is a multi-step process involving several sophisticated technological steps. When large production numbers are required, it must be doubted whether this fabrication technique is economical for laboratory and small-scale reactors. However, these reactors show excellent heat removal from the reaction zone [46, 109].



**Figure 2.3.:** Typical MSR by IMVT [54]. Reproduced with permission from Elsevier (©2009).

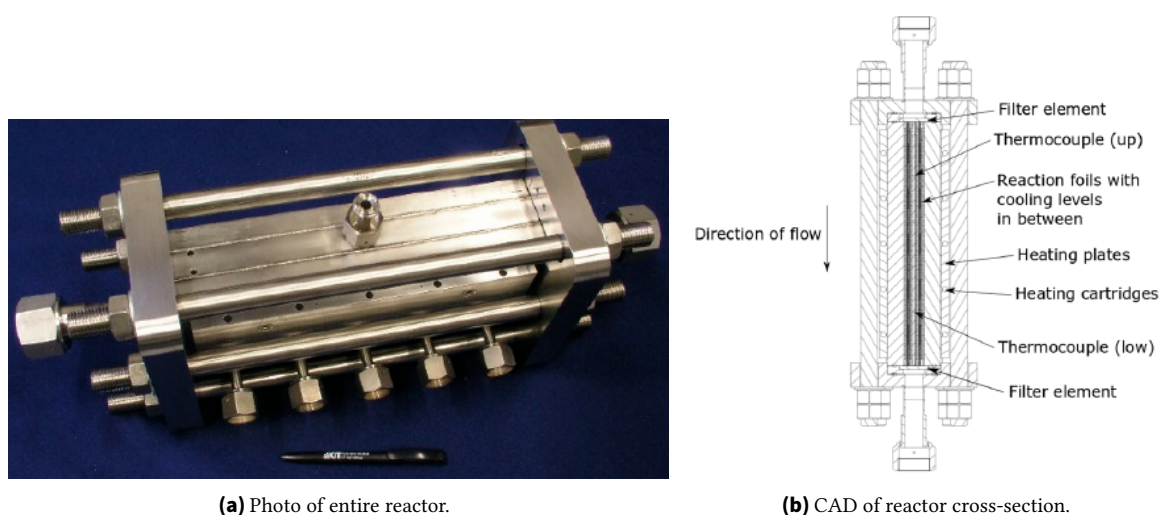
Myrstad et al. [54] operated one of the above mentioned reactors with great success. They achieved isothermal operation with little deactivation at high productivity, indicating excellent heat transfer. The maximum modified  $STY$  was  $2.6 \text{ g}_{\text{C5+}} \text{ g}_{\text{cat}}^{-1} \text{ h}^{-1}$ , being the highest found in literature. This IMVT reactor is currently designed for a maximum allowable working pressure and temperature of 50 bar and  $450^\circ\text{C}$ , respectively.

Piermartini et al. [55] tested the influence of the slit depth of two reactors of this type with Reactor I and II having  $d = 1.0$  and  $1.5 \text{ mm}$  respectively. They concluded that the reactors can still be operated almost isothermally at the higher slit depth.

The journal publication by Herz et al. [110] features an FTS reactor looking like it contains planar slits but being manufactured with conventional methods. From the dimensions visible in the photograph it is reasonable to count it as MSR.

### 2.3.3. Commercially Available Micro-Structured Reactors

The work by Loewert et al. [58] represents the first scale-up step from IMVT's lab-scale reactor to a production scale, fig. 2.4. Between [54] and [58], the catalyst volume was scaled up by factor 60. According to these authors, this reactor featured a controllable partial evaporation cooling for the first time. In a student thesis, this reactor was opened after several thousand hours of operation. Different amounts of catalyst were removed from eight identical reaction slits. Subsequently, these showed a different pressure drop, which could mean that some catalyst partially remained inside [111]. It was possible to produce a space-time yield  $STY_{\text{mod}} = 1 \text{ g}_{\text{C5+}} \text{ g}_{\text{cat}}^{-1} \text{ h}^{-1}$  with diluted syngas [58]. This scale-up was continued by spin-off company Ineratec, who are presenting their current 125 kW reactors for 1 MW plants and the next scale reactor with 1.25 MW equaling around 20 barrel  $\text{d}^{-1}$  [60]. In Phase II of the project Kopernikus P2X reactors by Ineratec are used in a plant with a syngas capacity of 250 kW. It is worth mentioning that MSR integrate a lot of functions in a small volume, such as: reaction zone, cooling zone, heating devices, and sensors.



**Figure 2.4.:** MSR by Ineratec used at IMVT [137].

Velocys developed a similar reactor concept in several scale-up steps, ultimately achieving 30 barrel  $\text{d}^{-1}$ . Their so-called laminate manufacturing is similar to the process at IMVT. Notably, they claim to have no problems filling or discharging catalyst particles from channels with a length to depth ratio  $l/d = 385$ . [23]

Ehrfeld Mikrotechnik GmbH (Wendelsheim, Germany) offers MSR concepts of different scales applying laser welding as joining technology. Their reactor 'Miprowa Produktion' has a channel with rectangular cross section with  $18 \times 3.2 \text{ mm}^2$ , which is usually inserted with static mixers. Recently, these static mixers were also covered with catalytic coating [113]. However, the reaction volume of up to 150 L could likely also be filled with catalyst particles. [114]

Table 2.4 extends table 2.1 with operating conditions and performance achieved in the respective reactors. Together these lists go beyond what is summarized by Delparish and Avci [115]. It is clear, that MSR are capable of much higher  $STY$  compared to the industrial conventional reactors. Conventional reactors miniaturized to laboratory-scale, but not to micro-structure scale show intermediate productivities.

The Fraunhofer Institute for Microengineering and Microsystems IMM (Mainz, Germany) is developing intensified micro-structured reactors. A lead application of their research are fuel processors, integrated devices that reform hydrocarbons and purify the obtained hydrogen [116].

**Table 2.4.:** Literature overview of reactors employing Co catalysts. Operating conditions and catalytic performance.

Ref.	Type, $p$ / bar Scale	$T$ / °C	H <sub>2</sub> /CO	Inert gas	$SV_{\text{mod}} / L_N$ $g_{\text{cat}}^{-1} h^{-1}$	$\dot{V}_N / L_N$ $h^{-1}$	$STY_{\text{mod,max}} /$ $g_{\text{C5+}} g_{\text{cat}}^{-1} h^{-1}$	$STY_{\text{max}} / kg_{\text{C5+}}$ $m_{\text{cat}}^{-3} h^{-1}$
[49]	N,L 20-30	225-255	1.7-2.2	N <sub>2</sub> 0.03	12-24 <sup>a</sup>	9.6-19.2	1.04	?
[50]	N,L 30	235-241	1.6-1.8	N <sub>2</sub> 0.03	12-18 <sup>a</sup>	?	0.691	?
[51]	T,L 15-30	205-230	1.06-2.11	0.04-0.36	8.8-43.2	8.8-43.2	?	?
[33]	T,L 20	200	2	0.1	13.2	6.6	?	?
[52]	T,L 20	150-233.5	1-2.5	Ar 0.1	2-8	?	1	?
[45]	T,L 20	200-230	2	Ar 0.12	?	?	2.1	?
[53]	T,L 25	190-230	2	0.24	6.41	46.2	0.43	275
[54]	M,L 20-30	215-240	2	-	14.4-20.5	21.6-30.8	2.6	1950
[54]	T,L 20-30	210-240	2	-	10.5-22.6	15.8-33.9	2.6	1950
[55]	M,L 30	215-230	1.8	-	12.6-18	?	?	?
[56]	M,L 20	220-235	2	N <sub>2</sub> <sup>b</sup>	3.05-25.0	?	0.3	?
[57]	A,L 20	260	?	?	?	1.2	?	10.5 <sup>c</sup>
This work	A,L 20	190-234	2	N <sub>2</sub> 0.03	1.85-9	6.2-30.0	1.03	≈1030
[58]	M,L+P 30	223-235	1.53-2.01	N <sub>2</sub> , CO <sub>2</sub> 0.6	13.2-20.7	?	1.10	814
[59]	M,P 30	235.5-246	1.49-2.2	<0.05	6.3-15.3 <sup>a</sup>	756-1836	?	?
[60, 109]	M,I 20	198-213	1.8-2.5	0.25-0.5	?	?	?	1785
[23, 46, 61]	M,I 25	200-235	1.8-2	0.165	?	?	1.8	1500
[23, 29, 31]	T,I ?	?	?	?	?	?	?	100
[23, 29, 31]	S,I 30	?	?	?	?	?	?	200

N=annulus, T=tube, M=micro-structured, A=additive, S=slurry, L=laboratory, P=pilot, I=industry, var=various, --not applicable, ?=unknown.

<sup>a</sup> Assuming  $\rho_N=0.5 L_N^{-1}$

<sup>b</sup> Assumed 0.03

<sup>c</sup>  $\dot{m}_{\text{C5+}}=0.0263 g h^{-1}$

The term catalyst or catalytic activity is universally used when a is working at, i.e. accelerating the desired reaction at certain conditions [117]. Catalytic activity can be related to catalyst amount and compared among catalysts at similar reaction conditions [118] but there are no absolute limits for low or high catalyst activity. Melián-Cabrera [117] explains the complex nature of the topic well and mentions volumetric efficiency as an important catalyst property. Higher volumetric efficiency means that the volume of catalyst required for a certain level of activity is lower. In the scope of this work the term high catalyst activity is used for catalysts with comparatively high activity and high volumetric efficiency. A lower limit for catalyst activity being high is set at  $STY_{\text{mod}} = 1 \text{ g}_{\text{C5+}} \text{ g}_{\text{cat}}^{-1} \text{ h}^{-1}$  which translates to  $STY_{\text{mod}} = 750 \text{ kg}_{\text{C5+}} \text{ m}_{\text{cat}}^{-3} \text{ h}^{-1}$  when assuming an bed density of  $\rho_{\text{bed}} = 0.75 \text{ g cm}^{-3}$ . The investigation of these catalyst properties is not subject of this work, but them being high is a prerequisite for highly efficient Power-to-liquid (PtL) production.

The current kerosene consumption of Germany amounts to  $10 \times 10^6 \text{ t a}^{-1}$  [13]. Germany committed itself to the use of 2 % of that amount or  $200 \times 10^3 \text{ t a}^{-1}$  ( $4300 \text{ barrel d}^{-1}$ ) of e-kerosene in 2030 [12] while the European Union (EU) mandates 28 % of that amount or  $2.8 \times 10^6 \text{ t a}^{-1}$  ( $60,300 \text{ barrel d}^{-1}$ ) in 2050 [11]. This equals a constant e-kerosene output (based on LHV) of 274 MW and 3.84 GW, respectively. Considering that PtX is only about  $\eta = 50 \%$  efficient [72] and that renewable energies are intermittent, it requires a multiple of this in reactor capacity. For the sake of simplicity a multiple of four is assumed. As stated before micro-structured reactors that are/soon will be available for decentralized PtX have a capacity of at least  $20 \text{ barrel d}^{-1}$  [60]. This would require 860 of these reactors in 2030 and 9648 in 2050. Assuming highly active catalysts as defined in this work a catalyst mass of 91.3 t with 18.3 t of active material Co would be required in 2030.

## 2.4. Design of Packed-Slit Reactor Concept

Slit-shaped devices made with conventional manufacturing are common in micro process engineering [110, 119]. Slits can be extended in width and length and can be stacked to increase capacity without significant performance loss, making them important for engineers and researchers in the disciplines of chemical engineering and flow chemistry. Mechanical integrity of slit-shaped modules is a research question in this thesis, since a pressure difference across the planar walls is continuously present. Inside the device, two neighboring slits, belonging to reaction and cooling zone respectively, have a pressure difference [58]. At the device's walls, pressure difference occurs between inside and outside. Possible tubular portions are only minor and might occur close to fluid connections.

Its name rendering the fact self-evident, a fixed-bed reactor requires the catalyst to be stationary. Both the catalyst's potentially hazardous qualities [36] and its material value demand it be hindered from being carried out by the reactants. By design, a catalyst performs best at the conditions found in its intended zone. The fluid is a gas at the inlet and usually a heterogeneous mixture of gas and liquid at the outlet of the catalyst zone. A filtering structure is to be implemented at the inlet and outlet of the catalytic zone. This can be realized with the following approaches:

**Conventional** Fluid-permeable metallic sinter metal plates are mounted to the inlet and outlet after fabrication of the reactor body.

**Additive at one end** At the same time as the solid walls are built, a fluid-permeable region is built at either inlet or outlet.

**Additive at both ends** At the same time as the solid walls are built, fluid-permeable regions are built at both inlet and outlet.

The first approach is applied per default by IMVT and other players [120]. Sinter metal plates are available in many different shapes and sizes [121]. At IMVT, they are machined without lubricoolant to avoid inserting oil permanently and with special clamping devices to avoid closing up too much area by milling. The inlet and outlet of reactors have to be accessible, often requiring bulky flanges at both ends of the reactor to mount the extra parts, including brackets and screws. Each flange, in turn, needs sealing and screws, posing the risk of leaks. The described sinter metal plates are sometimes called frits. For the last approach, it would be impossible to insert catalyst after fabrication. As a matter of fact, it is a subject of research whether a laser-based powder bed fusion of metals (PBF-LB/M) build job can be interrupted, manipulated, and then finished successfully. This has been done, for example, in order to insert sensors very close to a point of interest [122].

The bed porosity  $\epsilon_{\text{bed}}$  of a packed bed is defined in eq. (2.16) and is of utmost importance, the reason being that volumetric reactor productivity is proportional to amount of catalyst per volume. However, dense packing with catalyst results in low bed porosity. The drawback of low bed porosity is high pressure drop, which will be discussed later.

$$\epsilon_{\text{bed}} = \frac{V_e - V_p}{V_e} \quad (2.16)$$

VDI Heat Atlas [7] provides formulas for calculating bed porosity depending, among others, on tube diameter and particle size. In a rectangular slit, depth logically becomes the descriptive parameter for bed porosity under otherwise constant conditions [123, 124]. In the work in hand, ratios of slit depth to particle diameter were as low as  $N_d = 5$ , where bed porosity is relatively difficult to estimate [7, 125]. Additionally, at  $d_p < 100 \mu\text{m}$ , observed bed porosity might be higher than calculated due to electrostatic effects, Ref. [7].

Equation (2.17) describes the bed porosity of an infinite poly-disperse packing with distribution parameter  $\zeta$ , eq. (2.18), with  $Q_i$  and  $d_i$  being the volume fraction and diameter of the  $i$ -th fraction, obtained from the static light scattering (SLS) measurement [7]. The bed porosity in proximity of the confining wall was assumed constant as  $\epsilon_{\text{bed,w}} = 1.5 \cdot \epsilon_{\text{bed,\infty}}$ . This was derived from averaging the bed porosity distribution given by Winterberg and Tsotsas [124] from 0 to  $d_p/2$ . It was assumed that the bed porosity in the remaining slit was the constant infinite bed porosity. Therefore, eq. (2.19) described the bed porosity of a confined poly-disperse packing as a function of slit depth to particle diameter ratio  $N_d$  [7].

$$\frac{\epsilon_{\text{bed,pd,\infty}}}{\epsilon_{\text{bed,md,\infty}}} = -0.112\zeta^3 + 0.017\zeta^2 - 0.259\zeta + 1 \quad (2.17)$$

$$\zeta = \left( \frac{\sum Q_i/d_i^2}{(\sum Q_i/d_i)^2} - 1 \right)^{0.5} \quad (2.18)$$

$$\epsilon_{\text{bed,conf}} = \epsilon_{\text{bed,wall}} \cdot \frac{1}{N_d} + \epsilon_{\text{bed,inf}} \cdot \left( 1 - \frac{1}{N_d} \right) \quad (2.19)$$

Furthermore, there is not much literature on the influence of wall roughness on bed porosity. Von Seckendorff and Hinrichsen [126] state that half-spheres on the container walls significantly influence the bed porosity profile. Whether surface roughness occurring in PBF-LB/M parts react that way is not known to date.

Both conventional multi-tubular reactors and MSR use multiple channels to increase capacity - they are multichannel devices. The channels are connected at the inlet and outlet. For simplicity, most of the

time, this connection is a plenum (fig. 2.2 and fig. 2.4). In flow chemistry and micro-structured devices, distributors are common [127–129]. The significance of uniform flow distribution to micro-channel arrays has been pointed out by several authors, consensus being that non-uniform flow distribution leads to broadening of the residence time distribution as well as unpredictable behavior of reactions and heat transfer [130]. Reasons for maldistribution can be fabrication tolerances, uneven catalyst coatings, variation in catalyst packing, and quality of inlet flow. Especially Pfeifer and Schubert [131] point out that the inlet flow from a tube with a smaller cross-section than the micro-channel array will be imposed on the array, depending on the flow type. A known solution to this problem is a significant pressure drop in the micro-channels compared to the inlet section, which can be achieved with very narrow or long channels or a packed bed [132]. Imke and Brandner [133] suggested an artificial pressure drop, which they called "dampening", to equalize the simulated behavior of a multi-channel evaporator. General consensus is that cooling is one of the most important features of efficient reactors for FTS [16, 29]. Cooling consists of three main steps, in consecutive order [134]:

**Convection in reaction zone** The heat of the reaction is released from the catalyst particles and is transported to the wall. This forced convection is characterized by taking place in a packed bed.

**Conduction in the separating wall** The heat is conducted from the hotter reaction side to the colder cooling side of the separating wall.

**Convection in cooling zone** The heat is transferred to the bulk of the cooling medium by forced convection.

Among these consecutive steps, the slowest dictates the overall heat transfer rate. It has the lowest heat transfer coefficient, i.e. the highest heat transfer resistance. Generally speaking, transferred heat  $\dot{Q}$  depends on the conjugate heat transfer coefficient  $k$ , the heat transfer area, and the mean logarithmic temperature difference (eq. (2.20)). The conjugate or overall heat transfer coefficient  $k$  is given in eq. (2.21). For a planar system  $A_{\text{hex}}$  is constant for all heat-transfer steps. [134]

$$\dot{Q} = k \cdot A_{\text{hex}} \cdot \Delta T_{\text{LM}} \quad (2.20)$$

$$k = \left( \frac{1}{\alpha_r} + \frac{t_w}{\lambda_s} + \frac{1}{\alpha_c} \right)^{-1} \quad (2.21)$$

### 2.4.1. Developing Flow

Heat transfer is influenced by factors like flow regime and fluid properties. Beyond that, the question whether the flow is hydro-dynamically and/or thermally developed was relevant for interpretation of experimental data. Hydro-dynamically developed means that the characteristics of the flow (shape of velocity field) remain unchanged. Thermally developed means that the characteristics of heat transfer (shape of temperature field) remain unchanged. The opposite of 'developed' in this field of engineering is called 'developing'. The estimated lengths until both conditions are met in the laminar flow in a slit are given by eqs. (2.22) to (2.23), respectively [134, 135].

$$l_{\text{dev,h}} \approx 0.056 \cdot \text{Re} \cdot d \quad (2.22)$$

$$l_{\text{dev,t}} \approx 0.316 \cdot \text{Re} \cdot d \cdot \text{Pr} \quad (2.23)$$

The effects of developing flow on one-phase heat transfer without packed bed are already considered in the standard equation for calculation of heat transfer coefficient in empty pipes and slits. Nu number



for developed flow is increased for developing flow in eqs. (2.27) to (2.30) automatically. The developing velocity and temperature fields have a more uniform velocity and temperature, respectively, over the cross-section, leading to an increased temperature difference at the wall. This stands against developed laminar flow with parabolic velocity and temperature fields.

Development effects in packed circular tubes happen very fast. There is no mention of developing flow in evaporation heat transfer calculation [7]. If anything, flow subcooling can be considered. As subcooling was not significant in the experiments and accuracy limited, it was neglected [7].

#### 2.4.2. One-Phase Heat Transfer in Slits without Internal Structures

**No Packed Bed** Calculations for one-phase flow through a slit without packed bed or internal structures are taken from chap. D6.1 of Ref. [7]. All investigated modules having internal structures, this was used as an estimate and basis for calculations acknowledging internal structures. The most important formula is eq. (2.24); it states that heat transfer coefficient increases with increasing Nu number, increasing thermal conductivity, and decreasing slit depth. The Re number according to eq. (2.25) included the volume fraction of internal structures, since the superficial velocity (eq. (2.26)) was based on the full cross-sectional area.

$$\alpha = \frac{\text{Nu} \cdot \lambda}{2 \cdot d_{\text{slit}}} \quad (2.24)$$

$$\text{Re} = \frac{u_0 \cdot 2 \cdot d_{\text{slit}}}{(1 - \varphi) \cdot \nu} = \frac{u_0 \cdot 2 \cdot d_{\text{slit}} \cdot \rho}{(1 - \varphi) \cdot \eta} \quad (2.25)$$

$$u_0 = \frac{\dot{m}}{\rho \cdot A_{\text{cross}}} \quad (2.26)$$

VDI Heat Atlas (HA) Chap. G2 Sec. 2.3 deals with the case of laminar flow where both channel walls have the same uniform temperature. Equations for Nu number for laminar flow are given in eqs. (2.27) to (2.30). Laminar flow is expected for Re numbers up to 2200–3600, depending on the flow conditions at the inlet.

$$\text{Nu}_1 = 7.541 \quad (2.27)$$

$$\text{Nu}_2 = 1.841 \sqrt[3]{\text{Re} \cdot \text{Pr} \cdot 2 \cdot d_{\text{slit}}/l} \quad (2.28)$$

$$\text{Nu}_3 = \left\{ \frac{2}{1 + 22 \cdot \text{Pr}} \right\}^{1/6} \cdot (\text{Re} \cdot \text{Pr} \cdot 2 \cdot d_{\text{slit}}/l)^{1/2} \quad (2.29)$$

$$\text{Nu} = (\text{Nu}_1^3 + \text{Nu}_2^3 + \text{Nu}_3^3)^{1/3} \quad (2.30)$$

Nu number for turbulent flow is given in eqs. (2.31) to (2.32). In the transition zone of the flow, which was assumed for  $3600 < \text{Re} < 30,000$  ([7] Chap. G2 Sec. 2.4), Nu number was calculated according to eqs. (2.33) to (2.34). Nu numbers for turbulent and transitioning flow were only considered if they were higher than for laminar flow.

$$\text{Nu}_{\text{turb}} = \frac{(\xi/8) \cdot \text{Re} \cdot \text{Pr}}{1 + 12.7 \cdot \sqrt{\xi/8} \cdot (\text{Pr}^{2/3} - 1)} \cdot [1 + (2 \cdot d_{\text{slit}}/l)^{2/3}] \quad (2.31)$$

$$\xi = (1.8 \log_{10}(\text{Re}) - 1.5)^{-2} \quad (2.32)$$

$$\text{Nu}_{\text{trans}} = (1 - \Gamma) \cdot \text{Nu}|_{3600} + \Gamma \cdot \text{Nu}|_{\text{turb},30,000} \quad (2.33)$$

$$\Gamma = \frac{\text{Re} - 3600}{30,000 - 3600} \quad (2.34)$$

**Packed Bed** Forced convective heat transfer in a packed bed is a common process. It is, however, not easy to calculate in advance. One approach is given in Chap. M7 in VDI Heat Atlas [7]. In eq. (2.35) ff. the indexed "f" and "p" distinguish properties of fluid and particles, respectively.

$$\text{Nu}_W = \frac{\alpha_W \cdot d_p}{\lambda_f} \quad (2.35)$$

$$\text{Nu}_W = \text{Nu}_{W,0} + a \cdot \text{Re}_p^{m1} \cdot \text{Pr}^{m2} \quad (2.36)$$

$$\text{Re}_p = \frac{u_0 \cdot d_p}{\nu} \quad (2.37)$$

$$\text{Nu}_W = \left(1.3 + \frac{5}{d/d_p}\right) k_{\text{bed}} + 0.19 \cdot \text{Re}_p^{0.75} \cdot \text{Pr}^{1/3} \quad (2.38)$$

$$k_{\text{bed}} = \frac{\lambda_{\text{bed}}}{\lambda_f} = 1 - \sqrt{1 - \epsilon_{\text{bed}}} + \sqrt{1 - \epsilon_{\text{bed}}} \cdot k_{\text{core}} \quad (2.39)$$

$$k_{\text{core}} = \frac{\lambda_{\text{core}}}{\lambda_f} = \frac{2}{N} \left( \frac{B}{N^2} \frac{k_p - 1}{k_p} \ln \frac{k_p}{B} - \frac{B+1}{2} - \frac{B-1}{N} \right) \quad (2.40)$$

$$N = 1 - \frac{B}{k_p} \quad (2.41)$$

$$B = 1.25 \left( \frac{1 - \epsilon_{\text{bed}}}{\epsilon_{\text{bed}}} \right)^{10/9} \quad (2.42)$$

$$k_p = \frac{\lambda_p}{\lambda_f} \quad (2.43)$$

Winterberg and Tsotsas [124] confirm that this approach for heat transfer in packed beds is valid for planar slits as well. This formula is, however, not validated for  $d_{\text{slit}} \approx 1 \text{ mm}$  and  $d_p \approx 100 \mu\text{m}$ . Values for  $\alpha_W$  (hereafter called  $\alpha_I$ ) obtained from these formulas are highly dependent on  $d_p$  and  $\epsilon_{\text{bed}}$ .

### 2.4.3. Fluid Guiding Elements (FGE)

The following is based on the work by Biffar et al. [136] and discussions with the leading author. Fluid guiding elements (FGEs) improve heat transfer by increasing the effective temperature difference. This is achieved by swapping flows back and forth from core to boundary, fig. 2.5. If the swapping was perfect, the effective temperature gradient would always occur between the mean fluid temperature at the respective length and the wall temperature. This is higher, compared to the temperature field in laminar flow.

This optimal heat transfer rate could be calculated based on the flow through the outermost region of the FGE with the heat transfer coefficient  $\alpha_{\text{os}}$ . However, swapping of partial flows is not perfect and the temperature difference of the partial flow at the wall decreases inherently along the direction of flow when heat is transferred. With the help of two-dimensional simulations, a formula was derived relating the actual  $\alpha_{\text{FGE}}$  to  $\alpha_{\text{os}}$  with the application of a factor  $f$  (eq. (2.44)).  $\alpha_{\text{os}}$  is calculated as per eqs. (2.24) to (2.33) if there are no particles present, and eq. (2.35) otherwise. A description of  $f$  based on

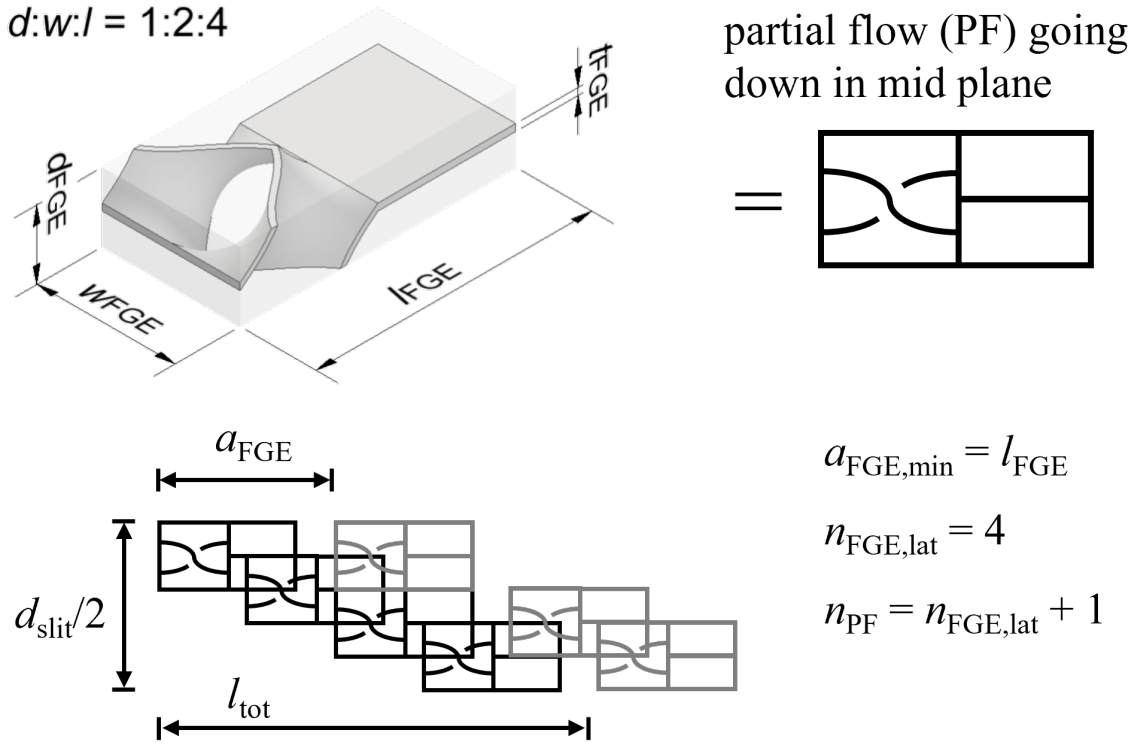


Figure 2.5.: Definitions concerning FGE.

a parameter  $\chi$  which incorporates flow properties and FGE geometry was found (eqs. (2.45) to (2.46)) by Biffar et al. [136]. Their work was done with the assumption of an empty tube, and the results of their analytical formula were in good agreement with experiments, the agreement being as good as between experiment and complex three-dimensional Computational Fluid Dynamics (CFD). In this thesis, two alterations are made: the flow happens inside a planar slit and a particle-bed can be present. It is a goal of the thesis to find out whether the approach is valid under the altered assumptions as well.

$$\alpha_{\text{FGE}} = f \cdot \alpha_{\text{os}} \quad (2.44)$$

$$f = 1 + \frac{-0.3361 - 1}{(1 - \exp(-1.7913 \cdot \chi))^{1/-0.2613}} \quad (2.45)$$

$$\chi = 1 - \exp\left(\frac{-a_{\text{FGE}} \cdot \alpha_{\text{os}} \cdot w \cdot n_{\text{PF}}}{\dot{m} \cdot c_p}\right) \quad (2.46)$$

#### 2.4.4. Boiling Heat Transfer

Until now, it was assumed a considered liquid would not evaporate under heat transfer conditions. This can be assured by setting the system pressure above the vapor pressure at the maximum temperature. Boiling heat transfer is also referred to as evaporation heat transfer. The liquid coolant is allowed to evaporate, because the system pressure is set so that the boiling temperature is below the maximum system temperature [137]. If the fluid temperature equals the heating temperature, heat is still transferred and contributes to the evaporation of available liquid. Factoring in the secondary flow and acceleration FTS to bubble formation, it is expected that the evaporation heat-transfer coefficient  $\alpha_{\text{evap}}$  is much higher than that of comparable one-phase flow [7].

Kandlikar [138] concluded that correlations for evaporation heat transfer in macroscopic systems can be employed as a first guess for microscopic systems. According to [7] Chap. H3,  $\alpha_{\text{evap}}$  consists of convective and boiling component, eq. (2.47). The convective component  $\alpha_{\text{conv}}$  figures in boiling-liquid (denoted by ') and condensing-vapor (denoted by ") quantities and has to be calculated with  $\dot{x}$ . Nucleate boiling heat-transfer coefficient  $\alpha_{\text{boil}}$  acknowledges medium, pressure, and wall properties, eq. (2.49). The as-built surface roughness of PBF-LB/M parts might be out of the range of validity of this equation, which is  $S_a=0.005\text{--}5\text{ }\mu\text{m}$  [139].  $\alpha_{\text{boil}}$  is not considered in the calculation of  $\alpha_{\text{evap}}$  (eqs. (2.47) to (2.49)), if  $\dot{q}$  is below  $\dot{q}_{\text{onb}}$ , appendix D. Since  $\dot{q}_{\text{onb}}$  is so high for the boundary conditions in this thesis (appendix D),  $\alpha_{\text{boil}}$  is never used.

$$\alpha_{\text{evap}} = \sqrt[3]{\alpha_{\text{conv}}^3 + \alpha_{\text{boil}}^3} \quad (2.47)$$

$$\frac{\alpha_{\text{conv}}}{\alpha'} = \left( (1 - \dot{x})^{0.01} \left[ (1 - \dot{x})^{1.5} + 1.9\dot{x}^{0.6} \left( \frac{\rho'}{\rho''} \right)^{0.35} \right]^{-2.2} + \dot{x}^{0.01} \left[ \frac{\alpha'}{\alpha''} \left( 1 + 8\dot{x}^{0.7} \left( \frac{\rho'}{\rho''} \right)^{0.67} \right) \right]^{-2} \right)^{-0.5} \quad (2.48)$$

$$\frac{\alpha_{\text{boil}}}{\alpha_0} = C_F \cdot \left( \frac{\dot{q}}{\dot{q}_0} \right)^{n(p^*)} \cdot \left[ 2.816p^{*0.45} + \left( 3.4 + \frac{1.7}{1 - p^{*7}} \right) p^{*3.7} \right] \cdot \left( \frac{d_0}{d} \right)^{0.4} \cdot \left( \frac{R_a}{R_{a0}} \right)^{0.133} \quad (2.49)$$

Yang et al. [140] point out the longitudinal conduction parameter (*LCP*) eq. (2.50), being relevant in micro-structured heat exchanger experiments. It relates the longitudinal thermal conductivity in the wall to the convective heat transfer in the channel subject to the same temperature difference. The higher it is, the higher the heat flow through the wall is compared to the convective heat flow.

$$LCP = \frac{\lambda_s \cdot A_w / l}{\dot{m} \cdot c_p} \quad (2.50)$$

## 2.5. Interim Summary FTS

Low temperature FTS takes place at up to  $T=250\text{ }^\circ\text{C}$  and  $p=30\text{ bar}$ . Güttel et al. [29] conclude that an ideal FTS reactor features:

- fixed bed catalyst,
- high catalyst effectiveness, and
- isothermal operation at highest possible  $T$ .

Together with the properties

- compactness, and
- load flexibility,

these are the requirements for a good FTS reactor for decentralized production of sustainable aviation fuels (SAF). It was made clear that industrial conventional reactors are not suited for this, being too large, costly, and inflexible. Micro-structured reactors are perfectly suitable; however, their fabrication is very complex and expensive in terms of time, money, and personnel. With the ability to include complex internal channels and functions, additive manufacturing (AM) in a single automated production step is a promising alternative here.



### 3. Micro-Reactor Fabrication with Laser-Based Powder Bed Fusion of Metals (PBF-LB/M)

Micro-structured reactors (MSRs) such as those described in section 2.3 can be produced via non-additive and via additive manufacturing (AM), both shown in fig. 3.1. The non-additive or conventional route is the classic micro-fabrication route used at Institute for Micro Process Engineering (IMVT) [108]. It starts from sheet metal which is transformed to micro-structured foils by milling, stamping, or wet-chemical etching. Foils are stacked and diffusion-bonded to arrive at the raw diffusion-bonded reactor body. It usually has to be post-processed, for instance by milling. Usually, connectors are adapted by means of welding. Afterwards, the diffusion bonding (DB) reactor body, together with nuts, bolts, and flanges, is assembled to the final reactor. Connectors, nuts, bolts, and flanges are manufactured with conventional (subtractive) means from pipes and semi-finished products for both reactor manufacturing routes. The additive route was created in this thesis. Gas atomization of metal powder was done by the supplier. The raw AM reactor body was directly fabricated via laser-based powder bed fusion of metals (PBF-LB/M). Just like all PBF-LB/M parts, the concept required post-processing via conventional subtractive manufacturing. However, the post-processing effort was strongly reduced since there were no support structures to be removed and the surfaces requiring milling were minimal.

The relevance of AM in both industry and research is continuously increasing. The Wohlers Report 2023 [141] shows a notable increase in metal machine sales for AM between 2002 and 2022, the sole reason for a temporary slowdown having been the Covid19 pandemic (fig. 3.2a). Yet new workflow and supply chains have to be established and agreed on with regulatory bodies as well [141]. There is also an exponential increase to be noted in research related to AM. The number of results for the search term "additive manufacturing" on [sciencedirect.com](https://www.sciencedirect.com) has been increasing exponentially since 1980 [142], signifying the highly increased number of scientific publications on this technique (fig. 3.2b).

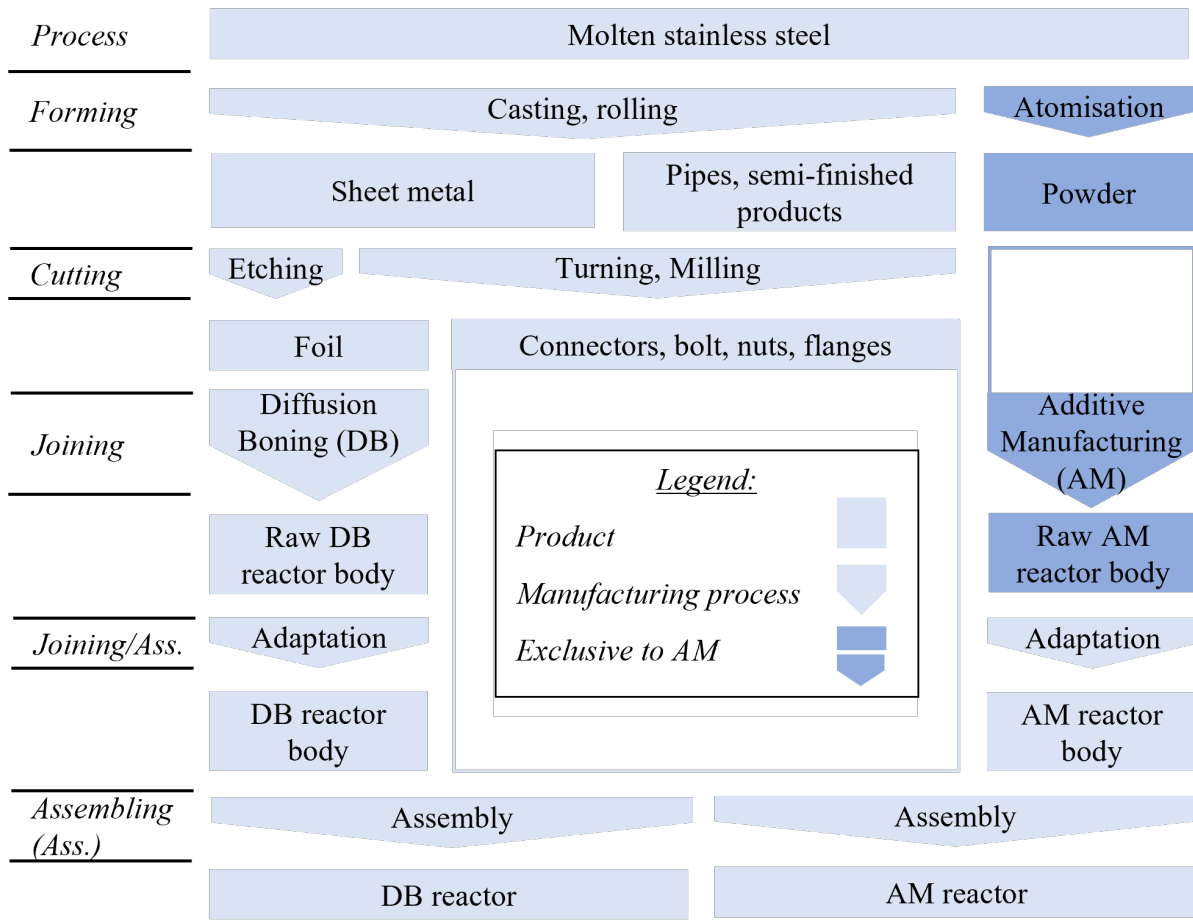
According to Gibson et al. [18] AM is

- tool-free,
- mostly automated,
- a layer-by-layer process,
- producing a physical three-dimensional model from a digital model,
- starting from a shapeless material, and
- material-efficient.

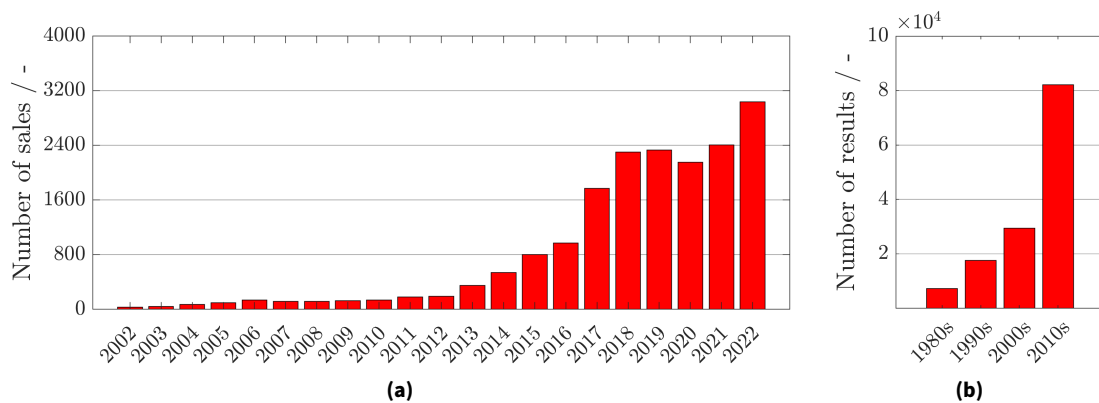
In consequence, AM cost per part is not dependent on part complexity or lot size, but rather on the part size.

This standard [143] distinguishes between seven basic AM processes. In this particular work PBF-LB/M is employed, enabling the production of complexly-shaped parts with internal channels and function integration with good quality results in a single step [144]. PBF-LB/M parts show good surface and mechanical properties, and 316L is a commonly used material [145].

This manufacturing technique is not investigated for its own sake here, but rather the relation between design, production, and function of the process engineering devices. In the following section 3.1,



**Figure 3.1.:** Manufacturing routes with conventional micro-fabrication (non-additive) and with PBF-LB/M fabrication.



**Figure 3.2.:** (a) Number of metal AM machine sales in the years of 2002 to 2022 according to Ref. [141]. (b) Number of search results for the term "additive manufacturing" on the research website sciencedirect.com between 1980 to 2019 according to [142].

the characteristics of PBF-LB/M process are explained while machines are described in section 3.2. Section 3.3 describes the material used and its properties, and, finally, in section 3.4 existing PBF-LB/M reactors and components are presented.

### 3.1. Process

This standard [143] divides the AM process into three steps: pre-processing, in-processing or just processing, and post-processing. For post-processing it is habitual to distinguish between what is required for AM versus what is required for a certain product or application thereof [146].

In the thesis in hand, the design was created with Autodesk Inventor 2020-2022 (San Rafael, CA, USA) and transferred to pre-processing software via standard tessellation language (STL) format. The STL export was executed with fine export settings (appendix B). These files could be repaired in Autodesk Netfabb prior to opening them in the printer's pre-processing software DMG MORI (Bielefeld, Germany) RDesignin. In pre-processing the part is sliced into two-dimensional layers. In this thesis each layer has a height of 50  $\mu\text{m}$  while research and industry use 30–80  $\mu\text{m}$  frequently [147, 148].

#### 3.1.1. Processing

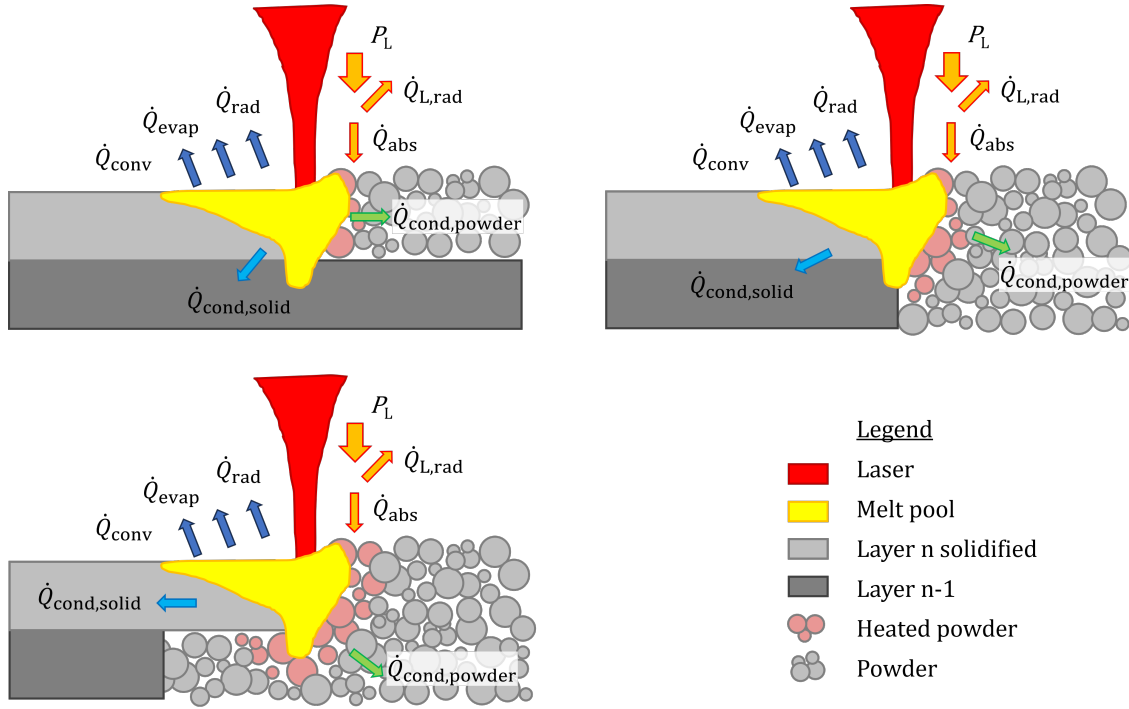
PBF-LB/M is a cyclic micro laser welding process. Each cycle begins with metal powder being fed into the build chamber and being thinly and evenly distributed on the build plate with a recoater. This procedure is followed by laser scanning; ideally, the laser energy would be perfectly absorbed and transformed into heat, melting the powder. Ideally, powder would also melt locally and selectively, and melting traces would solidify, melting with solid material on the sides and below. However, there are energy losses by reflection and due to minor partial metal evaporation. Also, the melt-pool is bigger than the laser spot and shows a complex thermo-hydraulic performance. [149]

Depending on part geometry the melting process varies as can be seen in fig. 3.3. When the bulk of a part is printed (top-left) the process-parameters are optimal; the amount of energy introduced is appropriate for powder to melt and merge with below and adjacent solid metal. In the top-right of fig. 3.3 the laser reaches the part contour; heat is conducted away by less solid metal so the melt pool will persist longer and metal powder from the outside might stick to the part contour. The bottom-left of fig. 3.3 shows a  $\beta=0^\circ$  overhang which should be avoided due to excess melt pool heat and persistence and significant powder adhesion (so-called dross formation). [150, 151]

The build chamber is continuously purged with inert gas to remove trace oxygen as well as unavoidable welding fume. The inert gas is guided through filters and partially recycled. In a well-tuned process with proper melting trace width (*MTW*) correction, the dimensional accuracy in x-y-direction is good [145]. Production problems may arise from inaccuracies in z-direction, though: when part geometry and the process of energy input are not optimal, the part may deform locally in positive z-direction. This starts a downward spiral since powder is then applied unevenly in the specific spot and energy input is disturbed, which may eventually result in the collision of part and recoater and process abortion. This phenomenon is emphasized when parts grow against the recoater movement [147].

To avoid such problems, design guidelines are readily available and recommendations on the scanning strategy exist. The scanning strategy governs how a two-dimensional area can be scanned with the non-dimensional laser spot. The movements of the laser spot are also called scan vectors [147]. Most authors agree that the contour of a part (with *MTW* correction) should be scanned first. In a next step, the bulk of the part is scanned with hatching [18, 152, 153]. The isotropy of the part can be further





**Figure 3.3.:** Schematic of energy transport in powder bed. Inspired by [150].

enhanced by varying orientation and starting points of the chessboard over each layer [154–158]. Finally, to avoid gaps or discrepancies between the two entities, a fill line should be scanned in between [150, 159]. Special care must be taken when wall thicknesses are very low [160].

The difference between solid and fluid-permeable regions in PBF-LB/M appears in the scanning strategy. For an isotropic dense solid part, the hatching in one chess board field in each layer is made to overlap  $\approx 1/3$ . The chess board is shifted across two successive layers, and the hatching rotates. According to Klahn et al. [161], for a fluid-permeable part, the scanning procedure differs; hatching scan vectors do not overlap, no chess board is required for fluid-permeable regions spanning small distances, and, most importantly, the hatching stays unaltered across successive layers.

The scan strategies employed under this thesis's work are summarized in table 3.1. Lattice was created with the scan strategy given in table B.3. Scanning strategy was changed after extensive maintenance in July, 2023. The Realizer SLM125's operating software was ROperator. Figures 3.4a to 3.4b show the scanning vectors of a layer at the part's top. The original contours of the part as computer aided design (CAD) or STL file are depicted as gray dashed line. Contours are symbolized by blue and red lines, while fill-lines are orange. Hatching (green lines) used within the contours have a narrow spacing. Hatching used for the fluid-permeable region (eight slits) has a wider spacing.

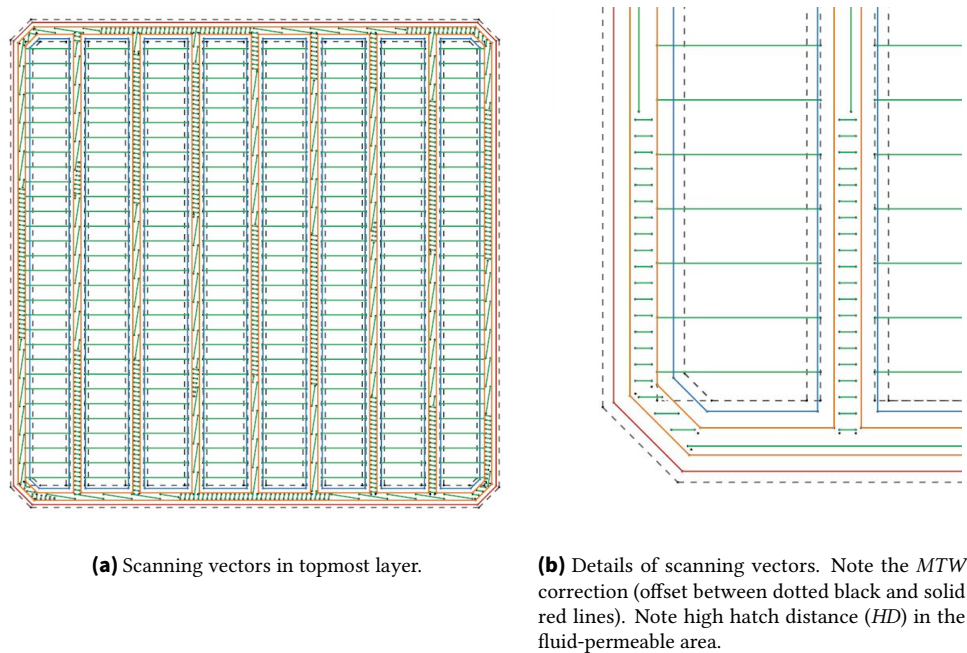
### 3.1.2. Post-Processing

After the build job, unmelted powder has to be removed. With the Realizer SLM125 de-powdering was started with the internal vacuum cleaner inside the machine, recovering most of the unmelted powder. After sieving, the larger particles were discarded, and only the finer particles were recycled. Subsequently, the part was removed from the machine and the more powerful external vacuum cleaner was used to remove residual powder. The part was then transferred into a depowdering cabinet, which

**Table 3.1.:** Scanning strategies used in this work.

Detail	Unit	chapter 4 <sup>a</sup>		chapter 5	
		solid	porous	solid	porous
Process conditions					
<i>MTW</i>	mm	0.16	0	0.199	0
Heating	°C	130	120	120	120
<i>h</i> <sub>l</sub>	mm	0.05	0.05	0.05	0.05
Heat function	-	False	False	True <sup>b</sup>	False
Support definition	-	> 10 mm <sup>2</sup> ; 0-45°		> 10 mm <sup>2</sup> ; 0-10°	
Comment	-	Delete contours		Delete contours	
Hatching					
Order		2	1	1	1
Exposure time ( <i>ET</i> )	μs	40	40	10	10
Point distance ( <i>PD</i> )	μm	40	20	10	10
Laser velocity ( <i>LV</i> )	m s <sup>-1</sup>	1	0.5	1	1
Laser current ( <i>LC</i> )	mA	2999	600	1100	1000
Laser power ( <i>P</i> <sub>L</sub> )	W	300	45	98	87
Lens position ( <i>LP</i> )	mm	-3	-1.2	0.6	0.8
To Hatching: Advanced hatch definition					
Initial offset	mm	0.16		0.12	0
Hatch distance	mm	0.12		0.08	0.18
Rotation	°	90		93	0
Shifted	-	True		True	True
Scan direction	-	Alternating		Alternating	Alternating
Multiply method	-	Random		Random	Random
Rotate by	°	9		0	0
Patch size	mm <sup>2</sup>	2x2 x 4.08x4.08		8 x 5	3 x 3
Base Offset	mm <sup>2</sup>	2x2		0	0
Fill line					
Order	-	3		2+3	
<i>ET</i>	μs	40		50	
<i>PD</i>	μm	32		10	
<i>LV</i>	m s <sup>-1</sup>	0.8		0.2	
<i>LC</i>	mA	2059		1100	
<i>P</i> <sub>L</sub>	W	200		98	
<i>LP</i>	mm	-2		0.2	
Base offset	mm	0.12		0.08	
Contour, for details see "Fill line"					
Order	-	1		4+5	

<sup>a</sup> Mechanical stability and heat transfer test modules were produced with both strategies.<sup>b</sup> Reduced  $P_L$  from 100 to 80 % at Voxel size 0.3 mm and Needed volume to absorb heat 27.0 mm<sup>3</sup>



**Figure 3.4.:** Local fluid permeability module: one layer of scan vectors. Red=outer contour, blue=inner contour, orange=fill line, green=hatching, dotted=geometry. External dimensions are 12 mm  $\times$  12 mm

contained another vacuum cleaner hose as well as a pressurized air nozzle. If applicable, manual tools like tap and countersink could also be used here, since any potentially hazardous materials were well contained.

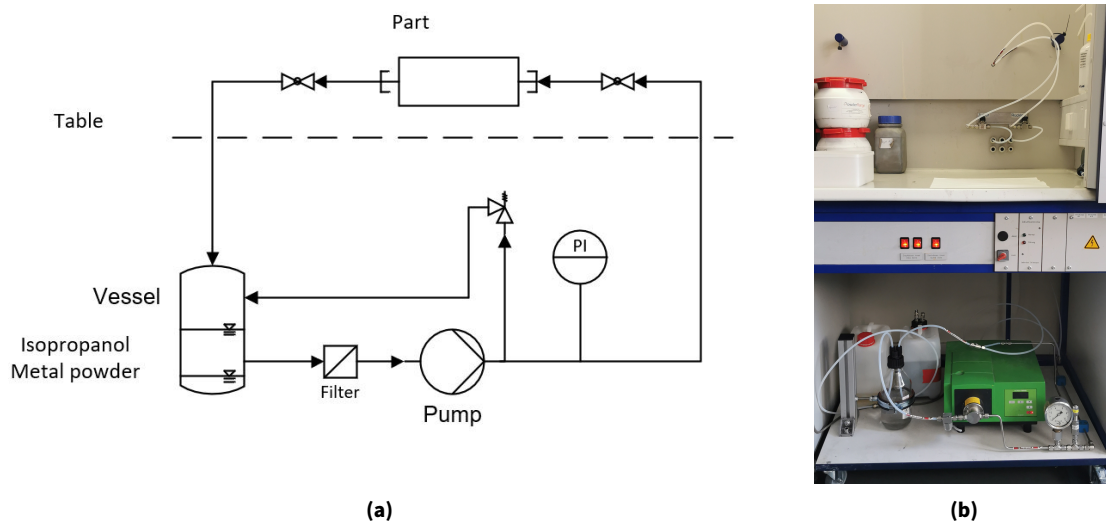
Removing powder from internal channels is a challenge [162]. This difficulty was tackled by designing and constructing a pump skid for a fume hood, fig. 3.5. The 6 mm hoses of the pump skid were connected to the part via 6 mm holes or via threaded holes according to [163]. Isopropanol was then pumped from a vessel through the leak-tight assembly, the test part, and back into the vessel. Any extracted metal powder was separated within this vessel by density difference. Afterwards, the test part was cleaned from isopropanol remains by submerging it in de-ionized water with dish detergent in an ultrasonic bath for 15 min.

Subsequently, the part could be dried in an oven. For parts with very intricate structures a vacuum oven was applied to remove trace water. If powder fell out of the part, the above described procedure was repeated.

Subtractive manufacturing is required to remove supports, reach the final contour, and to control surface quality [144].

### 3.2. Machines

The machine's build chamber contains a build platform carrying a build plate. The geometry obtained by virtually extruding the upper side of the build plate to its minimum depth is the build space. Next to the build platform, there is a device feeding powder from the powder tank into the reach of a movable recoater.



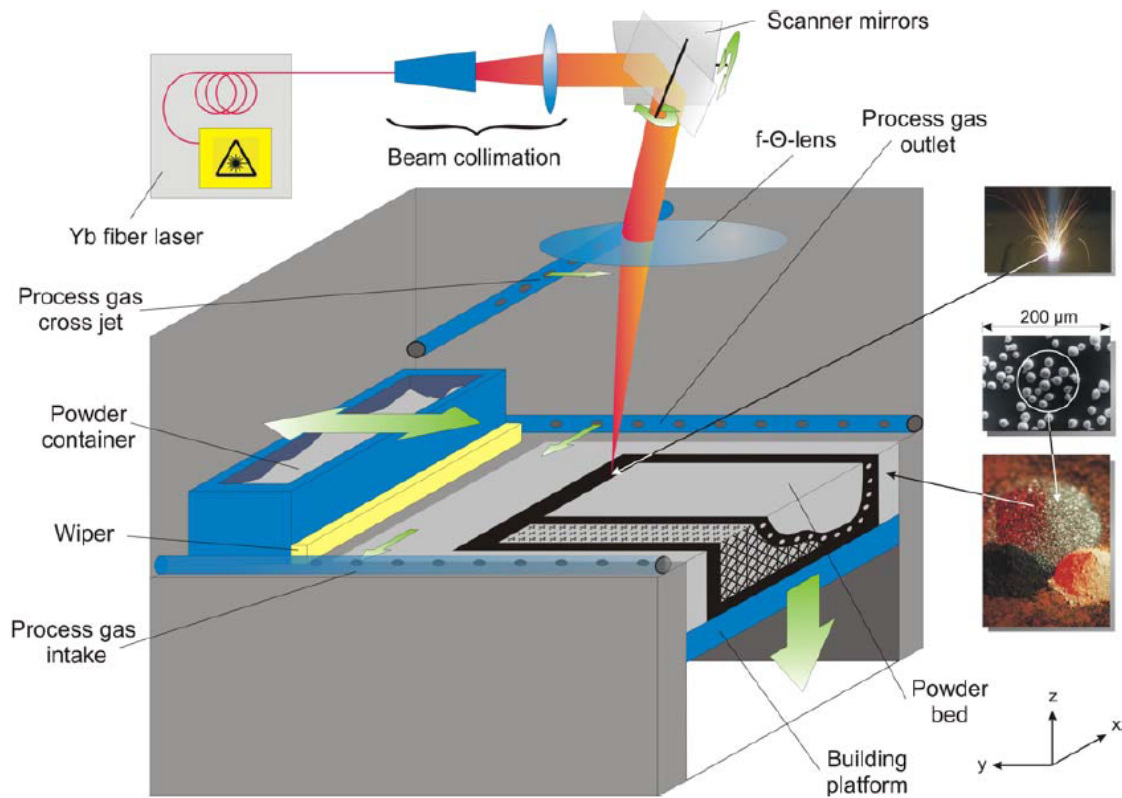
**Figure 3.5.:** Schematic and picture of self-made pump skid.

A laser is positioned outside of the build chamber. Its beam is directed over ("scanning") the working plane with the help of two galvanometers - electrically actuated mirrors - for x- and y-direction. To ensure the laser hits the working plane perpendicularly and with the intended spot size, a f- $\theta$ -lens is mounted directly below the galvanometers above the build chamber, fig. 3.6.

The build chamber is equipped with lighting, cameras, or other sensors, as well as inlets and outlets for purge gas. The chamber can usually not only be accessed through the port, but also via a glove-box. The machine may be equipped with inert gas recycling as well as a powder handling system.

For the practical stages of this work, a Realizer SLM 125 was employed, fig. 3.7. After acquisition of Realizer GmbH (Borchen, Germany) by DMG MORI AG (Bielefeld, Germany), this machine type was completely re-designed and is now called LASERTEC 12 SLM. The machine in this work was equipped with a Nd:YAG continuous wave fiber laser with a maximum power of 400 W and a wavelength of 1090  $\mu\text{m}$ . The inert gas argon (Ar) was guided above the powder bed, removing welding fumes and spatters, and through a circuit with paper and high-efficiency particulate air filters. The machine had an internal vacuum cleaning and sieving system. Parts could be de-powdered inside the machine via ports with rubber gloves. The recoaters worked with an angular motion and were equipped with silicone wipers. The printer had an Ar fire extinguishing system.

The build rate of the institute's printer was in the range of 2–3  $\text{cm}^3 \text{h}^{-1}$ . In 2016, the same year the printer was procured, Gebhardt and Hötter [165] reported 7–30  $\text{cm}^3 \text{h}^{-1}$  as an average build rate in his book. The build rate being an essential economical factor, it may well play a decisive role in future applications. Limitations in fabrication space are an issue for PBF-LB/M. PBF-LB/M machines with large fabrication space and high build rate exist for industrial production. Some examples are given in table 3.2. Karlsruhe Institute of Technology (KIT) offers a technology to build parts exceeding build space height and remove them under inert atmosphere [166]. Larger printers have multiple lasers [167], whereas the printer's price is not proportional to the number of lasers [168]. The biggest diffusion welding machine at IMVT, an apparatus by Systec Fertigungstechnik (Karlstadt, Germany), has a recipient volume of 500 × 500 × 430  $\text{mm}^3$  [169, 170]. One of the biggest diffusion welding machines in the European Union (EU) is located at PVA TePla Vacuum Processing Solutions (Wettenberg, Germany) and has a volume of 1000 × 900 × 450  $\text{mm}^3$  [171]. It can be concluded that fabrication space for a single part is limited to equal levels for conventional and additive micro-structured device manufacturing.



**Figure 3.6.:** Representation of laser section and build chamber of a PBF-LB/M machine [164]. Reproduced with permission from Cuvillier Verlag (©2010).



**Figure 3.7.:** Realizer SLM125 at IMVT.

**Table 3.2.:** PBF-LB/M machines with build space and build rates. Reference from [167], if not indicated otherwise. Usually  $h_l=30\text{--}80\text{ }\mu\text{m}$ .

Manufacturer	Model	Build space		Build rate cm <sup>3</sup> h <sup>-1</sup>	Ref.
		Dimensions / mm	Volume / dm <sup>3</sup>		
Rectangular					
3DSystems	DMP Factory 500	500 x 500 x 500	125		
Additive Industries	MetalFABG2	420 x 420 x 400	71	150	
Realizer	SLM 125	124 x 124 x 200	3	2-3	
DMG MORI	LASERTEC 30 SLM	300 x 300 x 300	27		
EOS	EOS M 270	250 x 250 x 215	13	5 <sup>1</sup>	[172]
EOS	EOS M 400-4	400 x 400 x 400	64		
E-Plus-3D	EP-M1550	1558 x 1558 x 1200	2913	650	[173]
Farsoon	FS721M	720 x 420 x 420	127		
Farsoon	FS1521M	1530 x 1530 x 1650	3862	400	[174]
GE Additive	CL XLINE 2000R	800 x 400 x 500	160	120	[175]
Renishaw	AM 500Q/S	250 x 150 x 350	13	150	
SLM Solutions	SLM 280	280 x 280 x 365	29		[172]
SLM Solutions	NXG XII 600	600 x 600 x 600	216		
SLM Solutions	SLM 800	500 x 280 x 850	119		
Xi'an BLT	BLT-S1500	1500 x 1500 x 1200	2700	900	[176]
Cylindrical					
Trumpf	TruPrint5000	∅ 300 x 400	28		
Velo3D	SapphireXC1MZ	∅ 600 x 1000	283	400	[177]

<sup>1</sup>  $h_l=30\text{ }\mu\text{m}$ 

### 3.3. Materials and Properties

PBF-LB/M is suitable for processing of light metals, tool steel, stainless steel, nickel-based super alloys, and even refractory metals [144]. Throughout this work, 316L stainless steel was used. It shows high corrosion resistance and is typically used for the construction of pressure vessels [88, 178]. Mechanical properties are influenced by a vast number of factors, some of which are interdependent [164], fig. 3.8.

Round Robin tests conducted by Jelis et al. [179] and Ahuja et al. [180] reveal that material properties of final parts can vary significantly. The former authors attribute bad material properties to non-optimal scanning strategies.

The properties of the raw material have significant influence, but can be controlled well. The powder is obtained by high pressure inert gas atomization, sieving, and drying. Important properties are chemical composition, shape, and size distribution [181]. While smaller particles promise lower surface roughness, they lower the powder's flowability [182]. Quality control concepts for metal powders are also well-established for sinter metallurgy [183].

Layer thickness is subject to a trade-off between build quality and build time, [184]. However, the most important influence on final part quality is the scanning strategy. Kamath et al. [185] found that part porosity is a function of  $P_L$  when other factors are kept constant. Porosity in turn is an indicator for low mechanical strength [186] and generally unwanted for leak-tight devices. In EU standards for conventionally manufactured pressure vessel materials, the term "porosity" is not mentioned at all [187,



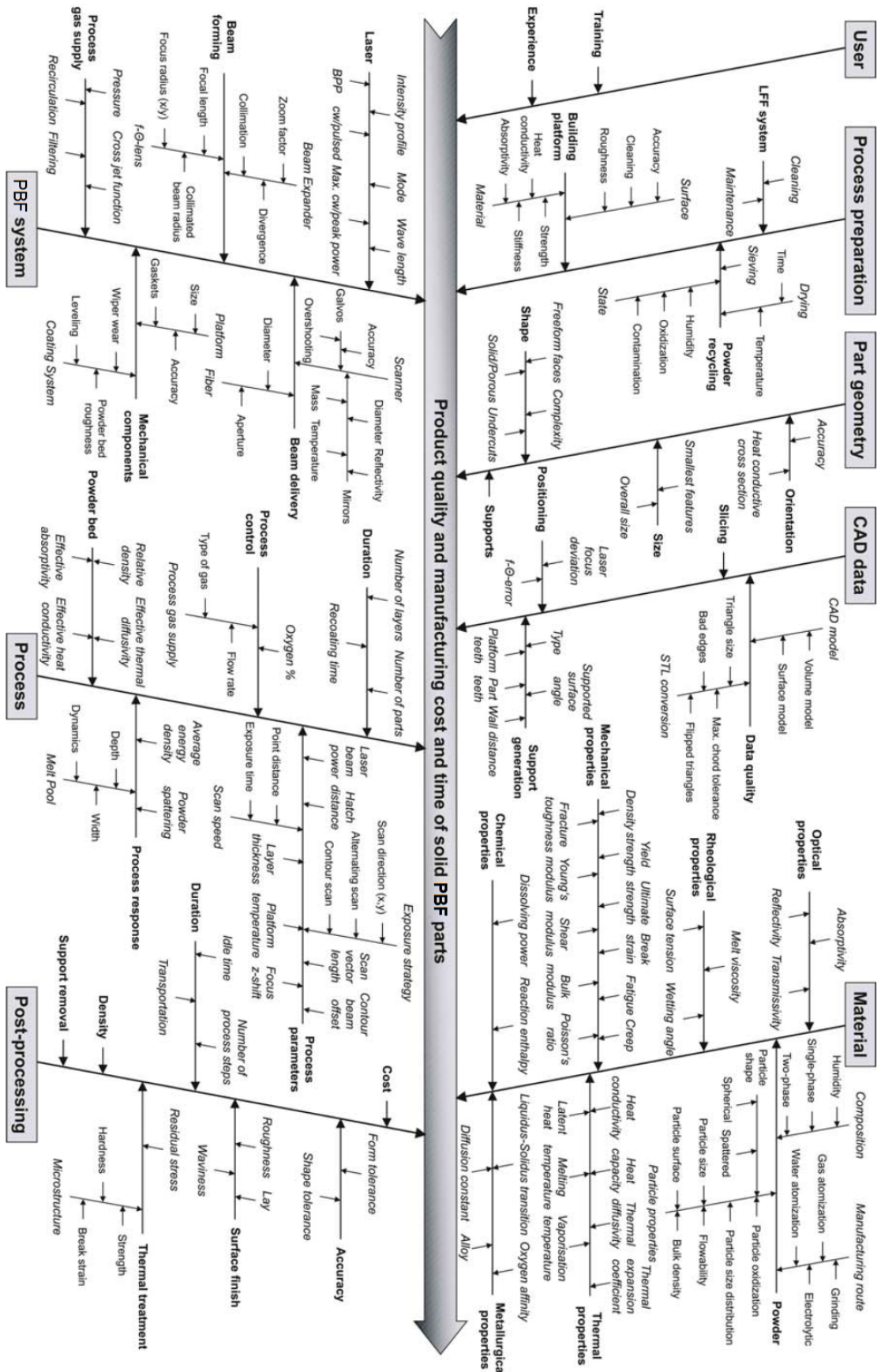


Figure 3.8.: Ishikawa (cause and effect) diagram of PBF-LB/M [164]. Reproduced with permission from Cuvillier Verlag (©2010).

188]. Ronneberg et al. [189] give a good summary on porosity in AM parts: it is generally undesired, yet there are no clear quantification or qualification methods. A degree of <0.05 % seems consensus for highly dense parts, and assessment methods are weighing (Archimedes' principle), polishing, and image processing, and computer tomography. IMVT has accumulated substantial experience with unconventional bonding methods and performs helium (He) leakage testing and water pressure testing by default. It is worth noting that German law explicitly requires leak-tightness of certain sites, especially chemical sites in its "Betriebssicherheits-Verordnung" [190].

Tolosa et al. [191] confirm that AM parts achieve the same yield strength, ultimate tensile strength, and elongation at break as wrought material. Ringel et al. [192] goes so far as to say that AM materials possess higher hardness and strength compared to conventional materials. However, isotropy and surface quality are not as good.

This leads to the conclusion that material properties can suffice in fulfilling the requirements for design and manufacturing of pressure vessels according to Pressure Equipment Directive [193]. This is proven by pre-existing parts with notified-body approval (section 3.4). TÜV Süd has created an inspection and test plan stipulating all the approval requirements for design, testing, and manufacturing, appendix B.5. It includes an initial set of strength values for the material-printer-strategy set-up by default. In virtually all cases, the final step is a pressure test with water [194].

This standard [183] covers the testing of metallic AM components. Parts made with this technology have critical-to-quality characteristics. These include in particular density, strength, hardness, surface quality, dimensional accuracy, residual stress properties, absence of cracks and structural homogeneity, which are typically tested in additively manufactured components. The quality of additively manufactured components is essential if functional components are produced on an industrial scale.

### 3.4. Existing PBF-LB/M Reactors and Components

As basis for designing and testing the AM packed-slit reactor concept (section 2.4 and chapter 4) a literature study was conducted. Laguna et al. [195] provide an excellent overview and categorization of AM in combination with catalysis. The following section examines AM parts suitable for process-engineering devices, clustering them into reactors, heat exchangers/heat transfer inserts, and connections.

#### 3.4.1. AM Reactors

One example of AM reactors is a reactor for a fast liquid-liquid reaction by Jastram et al. [196]. It features fluidic cooling and staged feed injection. Another example is a reactor for the very exothermal methanation reaction by Hauser et al. [197]. It is denoted by integrated heat-pipe functionality and a cage for catalyst particles with a size in the range of several mm. In this review by Brandner [108], first examples of PBF-LB/M slit devices at IMVT are shown.

Naudorf [19] reports an AM autoclave for BASF, reducing cycle time of batch processes significantly with conformal cooling in the wall. BASF produces and internally sells other TÜV-approved devices like the above-reported [198].

Wei et al. [57] produced catalytic reactors from the catalytically active material itself, showing good results in the lab. For Fischer-Tropsch synthesis (FTS) they used metal powder containing 61 wt-% Co. The tube-shaped part was connected to the test rig with nut-ferrule connection. It contained seven



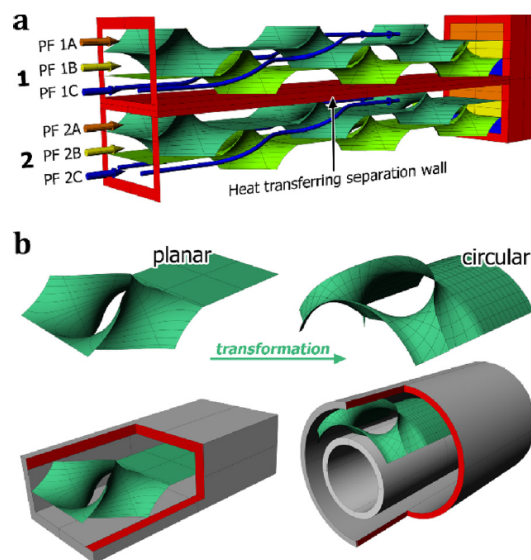
small circular channels which were in turn containing regular structures to enhance surface area. It is not known whether this is scalable or economical, though.

### 3.4.2. AM Heat Transfer Enhancement

Beyond process engineering, heat transfer is relevant in areas such as aerospace [199], automotive industry [200], and micro-electronics [201]. Scheithauer et al. [202] dedicated a review to this and found that AM technologies have the potential of increasing heat exchanging surface and compactness as well as the designing of fluidic systems and that new shapes like curved channels and fractal structures become possible. Saltzman et al. [203] present a significantly weight-reduced additive oil cooler for aircrafts; their design is still close to the conventional channel design. Another example are micro heat exchangers by Heat Cubed GmbH (Germering, Germany) [204].

Czekalla and Seibel [200] investigated the influence of triply-periodic minimal surfaces and pin-fin structures on the performance of an automotive cooler. These structures did enhance heat transfer and lower pressure drop and can only be manufactured (economically) with AM. This applies for another set of structures as well, so-called periodic open cellular structure (POCS). Fratalocchi et al. [53, 99] use these to enhance the heat transfer in an FTS reactor. The heat transfer increasing capabilities of POCS were also shown by Busse et al. [205].

Fluid guiding element (FGE) were developed at IMVT by Hansjosten et al. [206] to increase heat transfer significantly at a low pressure drop by dividing the flow into several partial flows. The partial flows are alternatingly guided smoothly towards the heat transfer area, maintaining a high temperature gradient, fig. 3.9. FGE are efficiently manufactured via PBF-LB/M since they require minimum wall-thickness. They can be custom-designed being parametrized and mathematically described via flexible splines. They were used successfully to increase heat transfer in the very exothermic methanation process. González-Castaño et al. [207] and Baena-Moreno et al. [208]. They were also used for improved physical stabilization of liquid foods [209].

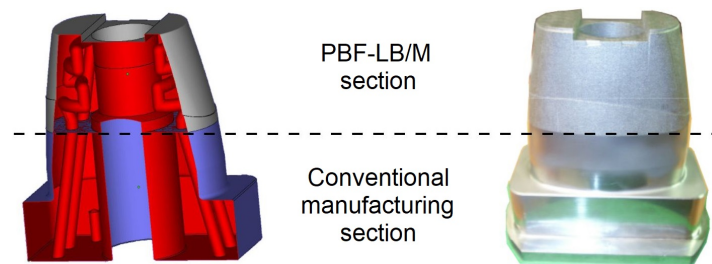


**Figure 3.9.:** CAD representation of FGE from [210]. Reproduced with permission from Elsevier (©2018).

### 3.4.3. AM Connections

Almost all parts - no matter which manufacturing technique - require connection. Of the many connections to be manufactured, two may serve as examples: 1. additive tool connecting to toolholder, and 2. additive fluidic device connecting to piping or sensors.

The method of connection in example 1 comes from a frequent application in AM. Injection molding tools can be manufactured cheaper and with included functions like conformal cooling, pressurized air ejectors, or plagiarism protection with PBF-LB/M. In a hybrid manufacturing (HM) process, the customized head of the tool is additively manufactured on its conventionally manufactured standard base, [149, 211], fig. 3.10.



**Figure 3.10.:** CAD representation and photo of tool made with hybrid manufacturing [212].

HM is also beneficial for post-processing. Ferchow et al. [213] built intricate parts on sheet metal, which was used for clamping during subtractive post-processing. They found the connection to be as strong as the additive material. Stoll et al. [214] produced parts consciously interrupting the print job. Tensile tests they performed did not reveal the layer of interruption as weak spots.

A demonstration of example 2 was presented by DeDiedrich Process Systems (Zinswiller, France) at Formnext 2022 in Frankfurt a.M., Germany. Visitors could see fluidic PBF-LB/M parts for challenging chemical reactions, featuring additive external threads with the typical Swagelok nut-ferrule connection. The rough shape had been printed and then machined [215]. As fluidic connectors female threads ([163, 216]) and pertaining of-the-shelf threaded connectors are used, as common in AM parts for hydraulic fluid ([217], fig. 3.11).



**Figure 3.11.:** Photo of PBF-LB/M threaded holes [217].

An additive burner nozzle by Biedermann et al. [218] increases the heat transfer, consolidates many single parts into one, and decreases the volume of assembly. It is welded to conventional pipes. It was

used on an industrial level by Siemens (München/Berlin, Germany). Similarly, the reactor used in the work of Hauser et al. is welded to conventional piping equipment [197].

It can be concluded that various types of permanent and temporary connections are already being made with PBF-LB/M. The feasibility and advantages of hybrid manufacturing for permanent connections merits attention.

#### **3.5. Interim Summary PBF-LB/M**

PBF-LB/M is a powerful tool with benefits surrounding customization, lightweight design, function integration, and streamlined manufacturing. It is proven on an industrial level in aerospace and the tool industry. Applications in process engineering exist with promising results in lab- and pilot-scale. Designs sought after the most are triply-periodic minimal surface structures, POCS, and fractals. However, classical designs from coolers and micro-structured devices are transferred to AM as well. The only AM reactor yet used for FTS was made by Wei et al. [57]. Compared to a packed-bed reactor with a highly active catalyst as defined in this work it would require an estimated 40-fold of the precious metal Co. No solution was found which was promising to serve as an economic and scalable concept decentralized FTS reactors. For the production of 700–10,000 reactors at 20 barrel d<sup>-1</sup> reactors have to be scaled up as much as possible and the manufacturing has to be as efficient as possible.

Provided the process is well-tuned, PBF-LB/M material properties are equivalent to other manufacturing techniques. The requirements for notified-body approval are fulfilled, confirmed by parts from BASF, Shell, Siemens, etc. It is consensus that strength and hardness of PBF-LB/M parts is equal to conventional parts while surface is rougher and anisotropy higher [149].

## 4. Design for Reactor Subfunctions

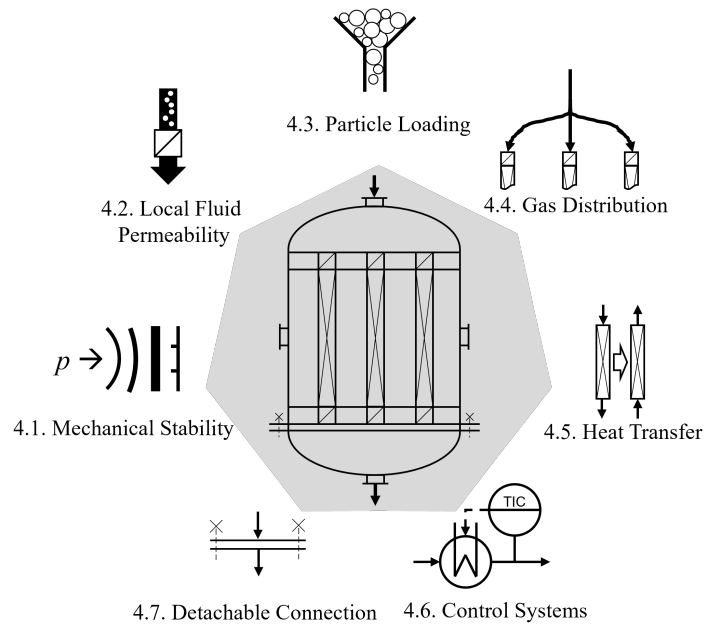
Product development strategies like the one from Ref. [219] or the Theory of Inventive Problem Solving (Russian acronym TRIZ, [220]) are not common in process engineering. Kaya and Klahn [221] proposed a systematic simulation-based design approach. Like in their work, the approach of knowledge-based engineering is taken in the thesis in hand. Knowledge-based engineering means the capture and application of engineering knowledge to automate engineering tasks [222]. To create trust in the novel fabrication route, high value has been set on safety-relevant mechanical stability and leak-tightness at high pressure and temperature; this acknowledges chemical engineers' tendency to be somewhat hesitant in adopting new reactor concepts, as is known from conventional micro-structured reactors (MSRs) [23].

The lead application of the reactor concept is Fischer-Tropsch synthesis (FTS) in decentralized Power-to-Liquid (PtL) plants, but under appropriate circumstances it can be applied for other process engineering challenges. The following subfunctions were identified as indispensable for a viable concept. Some of them are general unit operations in process engineering, e.g. heat transfer and solid/fluid separation. They all came from chemical engineering community publications and from professionals at Institute for Micro Process Engineering (IMVT) working with cooled packed-bed reactors in general and FTS reactors in particular. The following numbers of these subfunctions relates to their sections in chapter 4. A graphical representation of them can be found in fig. 4.1.

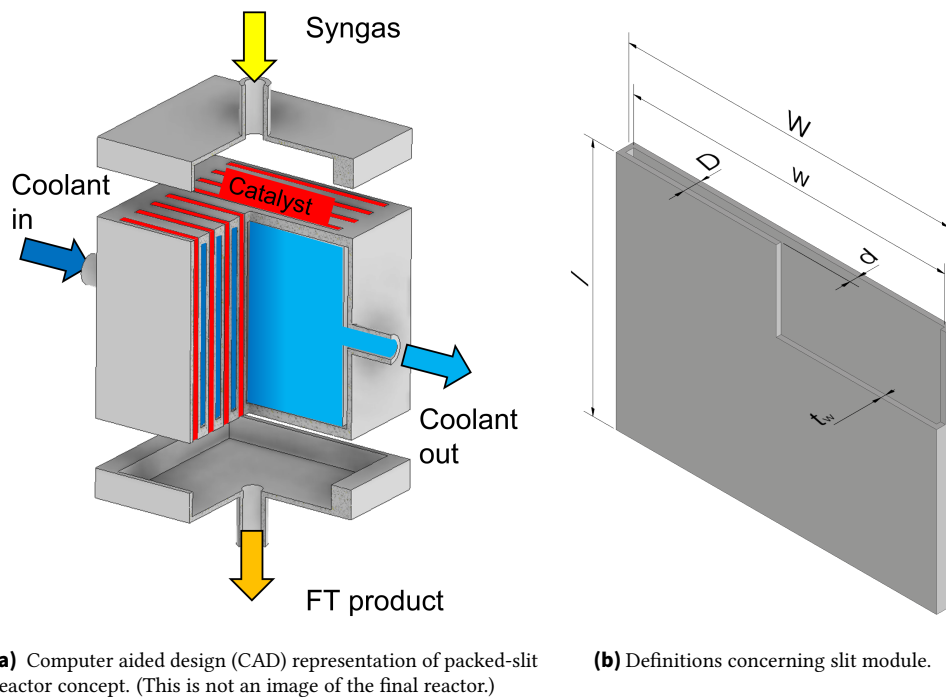
- 4.1. mechanical stability,
- 4.2. the local permeability for fluid holding particles in place,
- 4.3. particle loading,
- 4.4. gas distribution,
- 4.5. efficient heat transfer,
- 4.6. control systems integration, and
- 4.7. a detachable connection for servicing catalyst.

The proposed additive manufacturing (AM) packed-slit reactor concept is shown in fig. 4.2a. It comprises narrow planar reaction slits, holding a fixed bed of catalyst particles. The slits for reaction are placed in alternating order with those for coolant: either thermal oil, water, evaporating water, or any other fluid. The concept includes integration of a heating mechanism and sensors. The walls of the device are pressure-bearing. Manufacturing is efficient since it requires almost no post-processing. Functions being integrated, the involvement of fewer parts and steps is a clear advantage.

From a geometrical viewpoint, the concept might look simple; it might even look similar to diffusion-welded reactors. The process carried out inside it is complex, and so is the fabrication technique. The challenge was to design for optimum performance and production. The subfunctions were evaluated separately, as documented in sections 4.1 to 4.7, which not only simplifies experiments, calculations, and their interpretation, but also allows for subfunctions to be transferred to other systems as modules from a modular system. For investigation of each such module, the minimal required portion of the concept was selected. In most cases, the module was a single slit, as depicted in fig. 4.2b. Whether the combination of modules investigated separately led to unexpected results is discussed throughout the thesis. Furthermore, an integrative test of all modules was carried out as documented in chapter 5. Many



**Figure 4.1.:** Packed-bed reactor subfunctions.



**Figure 4.2.:** Cooled packed-slit reactor concept with AM.

results from the following subsection can be transferred to other heterogeneous-catalysis reactions which are involved in the production of 50 wt-% of all goods [223].

Phrases such as "Design for X" are commonly used in manufacturing engineering research. They highlight design and the fact that specialized design differs for the respective purpose. Common examples are "design for additive manufacturing (DfAM)", emphasizing the design guidelines compulsory for this technique, or "Design for Sustainability", accentuating parts that can be recycled or easily

repaired [224]. The name of this chapter comes from the fact that each section explain the design of the proposed reactor concept step by step for one particular subfunction, i.e. the relation between design and performance is examined. Obviously, DfAM is a premise in this thesis to ensure manufacturability. Each section is divided into subsections, describing several aspects: the subfunction itself, the modular segment of the complete reactor influencing this specific subfunction (hereafter called "module"), the material(s) used, the applied method(s), and the obtained results with the particular design in relation to the subfunction. Each subfunction can be distinguished from the other. Yet they have overlaps. Modules didn't have to look similar, yet they could. The most common characteristics were slit depth, type of internal structure, order of internal structures, and wall thickness. While some modules and reactors had chamfered outer edges, this is not pointed out, as it had negligible influence on the tested subfunction. For best haptics, least over-irradiation, and best stress profiles, edges would best be rounded. However, negative experience with this on the Realizer SLM125 and software led to the use of chamfers. These negative experiences were damaged meshes leading to errors in slicing and erroneous scan vectors. In some cases, especially fluid guiding elements (FGEs), meshes were repaired in Netfabb (Autodesk, San Rafael, CA, USA).

## 4.1. Mechanical Stability

The author's findings described in this section have been partially published in Ref. [225]. Some details have been slightly altered and wording has been partially revised to facilitate reading.

In Fischer-Tropsch synthesis (FTS), product formation is favored by high pressure [78], and the reactants are flammable and toxic [36]. Thus, stability is a very important reactor subfunction for safe operation. It was justifiably assumed that the construction material was corrosion resistant under the above described conditions [178].

Finite element analysis (FEA) is one option to determine stability and optimize part weight of almost arbitrary parts [226]. However, it requires re-meshing of every design and computational effort. FEA interpretation depends on the designer, especially in the presence of singularities in the analysis [227].

For fast equipment development, a reliable and user-friendly calculation model for the design with regard to stability is imperative. Such a model being accessible for the above mentioned target group who are usually no mechanical engineers is beneficial. A model that could be handled by non-mechanical engineers and directly applied to typical slit modules encountered in micro-structured devices was not found in literature.

For the comparatively simple geometries rectangle and circular disc formula for stability calculation were found in a standard reference book [228]. A subset of slit-shaped modules investigated in this article can be abstracted to simple geometries and assessed by the aforementioned formulas.

The aim of this article is to do this abstraction and validate it with FEA and experimental data. Comparing experiment, formula, and simulation of failure in AM parts helps to expand knowledge and increase trust in this promising manufacturing method [229]. The findings should be presented in a way where they can also be transferred to other operation parameters like pressure or material.

### 4.1.1. Design and Fabrication

The investigated modules consisted of parallel planar walls, forming a narrow slit with fluidic connectors at the bottom and top end. For its material, stainless steel 316L was chosen due to its strength, corrosion

resistance, and its prevalence [88, 178]. For the composition refer to table C.2. Pressure at which a module is operated could be above the outside pressure, the outside being the surroundings or another module operated at a lower pressure. Planar walls tend to buckle when submitted to a pressure difference across the two sides. Under otherwise constant conditions, buckling is more likely when the smaller of the rectangular's side's length increases or the wall thickness decreases [228]. Excess wall thickness must be avoided, but with every increase in the device's size, the walls become larger.

The following approaches were pursued to enhance mechanical stability: 1. deflection of walls in direction of  $y$ -axis, and 2. insertion of internal structures (fig. 4.3). Walls bent in three-dimensional space are expected to be more stable than planar ones [230]. Evenly distributed structures connecting neighboring walls, preventing buckling, were introduced into the design, the structures being hexagonally arranged pins, evenly distributed fins, lattice, or FGE. Topology optimization was not used mainly due to two reasons. The first reason being that process engineering devices can not be designed by only optimizing mechanical load and weight. Flow pattern and accessibility of catalyst and sensors are crucial. The second reason being that chemical industry has strong regulatory requirements especially for pressure vessels. Validation is facilitated by using well-known features such as regular pins instead of topology-optimized shapes.

Internal structures have possible downsides: reduction of the fluidic volume and addition of material to the design. The volume of internal structure per slit volume is called volume fraction  $\varphi$  and was kept as low as possible. Nevertheless, there is a physical minimum for the volume fraction of internal structures. Based on a force equilibrium (eq. (4.1)), internal structures are expected to rupture below a certain volume fraction. This resulted in  $\varphi_{\text{crit}}=0.008$  for  $p=30$  bar, a margin of error of  $S = 1.5$ , and a yield strength of  $R_{p0.2}=582$  MPa taken from [231] for vertical tensile samples.

$$p \cdot A \cdot (1 - \varphi) = S \cdot R_{p0.2} \cdot A \cdot \varphi \quad (4.1)$$

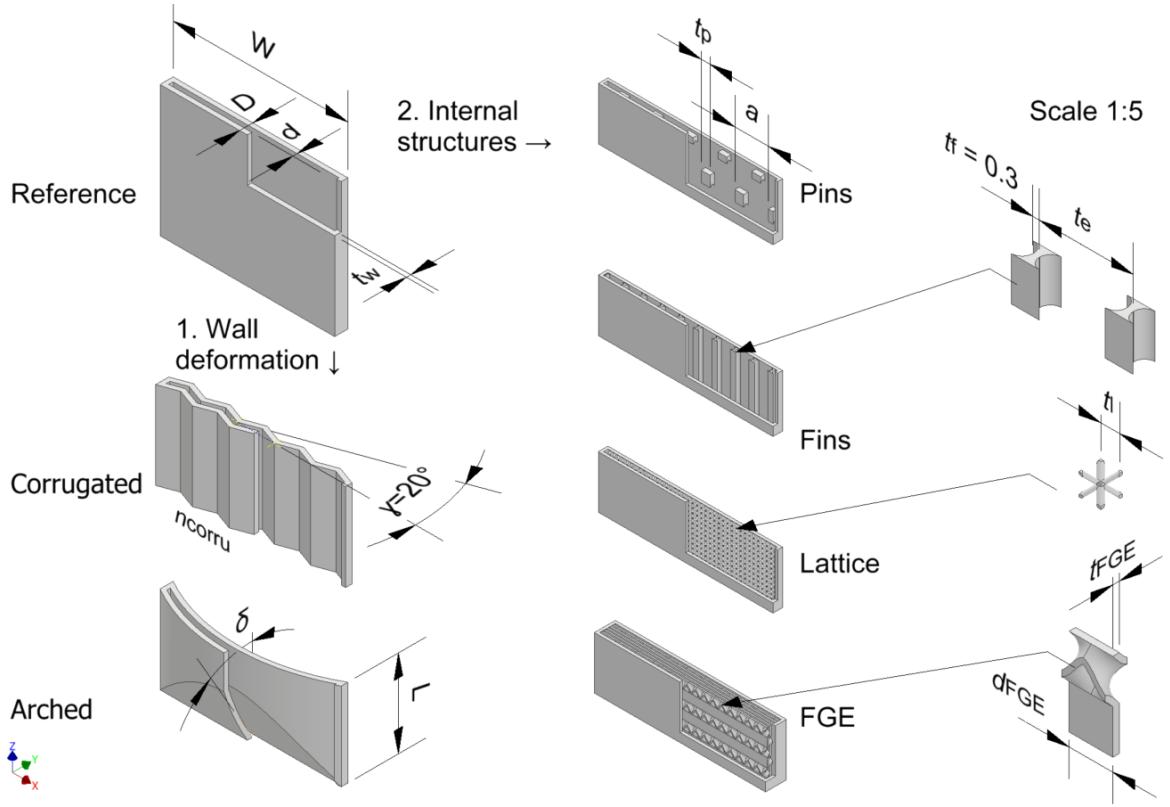
Internal structures have been identified by other persons as well as means to increase the stability of pressure vessels by adding minimum mass [232–234]. The internal structures proposed in this article are unlikely to change the flow-pattern significantly as flow is usually strongly laminar [102] in micro-structured devices. Possible tubular portions are only minor and might occur close to fluid connections. They can be designed against rupture according to well-established formulas (e.g. from Ref. [235]) and are not in the scope of this article. The empty planar module, designated *Empty*, served as a reference and starting point for the design (fig. 4.3, top left).

#### 4.1.1.1. Empty Modules

The first approach was bending the slit walls in three-dimensional space. The entire volume between the corrugated or arched walls was available for fluid ( $\varphi=0$ ). The deflection was effected in a way still permitting multiple modules to be stacked seamlessly. The wall thickness of these samples was  $t_w=1$  mm.

Three of the modules comprised corrugated walls. *Corrugated-5* and *-10* had five and ten corrugations parallel to the  $z$ -axis, respectively. *Corrugated-7'* had seven corrugations parallel to the  $x$ -axis. The angle between corrugation and the  $xz$ -plane was always  $\gamma=20^\circ$ .

*Arched-5*, *-15*, *-30* and *-45* were four modules with walls warped over  $xz$ -plane. The digits denote the cutting angle between wall and the  $xz$ -plane  $\delta$ .



**Figure 4.3.:** Designs for mechanical stability testing.

#### 4.1.1.2. Modules with Internal Structures

Four categories of internal structures were used inside narrow planar slits in this work: pins, fins, lattice, and FGE [210].

Connecting both sides of the slit directly, pins were characterized by their shape and arrangement. The cross-section of pins was a square with side length  $t_p$ , which was the characteristic parameter. To prevent horizontal overhangs, small angles were added at both slit walls when  $d_{\text{slit}} = 1$  mm. When  $d_{\text{slit}} > 1$  mm pins as a whole were inclined. Pins were arranged in a hexagonal manner with spacing  $a$ . Pin-equipped modules were designated with  $\text{Pins-}d_{\text{slit}}\text{-}t_p\text{-}a$ . For these designations, dimensions were expressed in mm and if the arrangement of pins is regular instead of hexagonal the syllable 'reg' was added. If the slit length was lower than the width (slit appeared to be turned  $90^\circ$ ) an apostrophe ' was added to the designation. For studying mechanical stability, the size and spacing of internal pins was varied over a wide range. The side length of quadratic pins was  $t_p = 0.26\text{--}5$  mm, while the spacing was  $a = 1\text{--}20$  mm. The wall thickness was  $t = 0.6$  mm. Width and length were  $w = 40$  mm and  $l = 60$  mm, respectively. The volume fraction was calculated from geometrical considerations and took values of  $\varphi_p = 0.01\text{--}0.19$ .

Fins connected both sides of the slit directly and separated the slit into parallel channels. The thickness of fins was  $t_f = 0.28$  mm = const. The characteristic parameter was the distance between two fins  $t_e = 1\text{--}4$  mm. Fillets were added where the fins transitioned into the walls. Again, the volume fraction was calculated from geometrical considerations and took values of  $\varphi_f = 0.1\text{--}0.33$ . The designation of fin-equipped modules was  $\text{Fins-}t_e$ . If the channels had zig-zag instead of straight shape the syllable 'zig-zag' was be added to the designation.



Lattice was of body-centered cubic type with a side length of  $t_1=1$  mm. Unlike the other internal structures, this one was not derived from CAD, but from the printer's software. Under the used scan strategy, the strut diameter was  $d_{\text{strut}}=0.2$  mm as measured with a caliper. From this, a volume fraction of  $\varphi_1=0.186$  was calculated. The lattice-equipped module was denoted as *Lattice-1*.

The geometry of a planar FGE, consisting of one fluid guiding unit (FGU) repeated with certain distances in three dimensions, can be varied in multiple ways. However, the following simplifications were made: the ratio of depth, width, and length of a FGU was fixed to 1:2:4 (fig. 2.5, top), and distances between repeating units were minimal, e.g. spacing  $a_{\text{FGE}}=l_{\text{FGE}}$  (fig. 2.5, bottom). FGE-equipped modules were denoted as *FGE- $d_{\text{slit}}$ - $d_{\text{FGE}}$* . In the case of FGE, assessing the volume fraction  $\varphi$  was not straightforward. An explicit formula for  $\varphi_{\text{FGE}}$ , based on  $d_{\text{FGE}}$  and the wall thickness  $t_{\text{FGE}}$ , was established and checked with fabricated samples (eq. (4.2)).

$$\varphi_{\text{FGE}} = \frac{5.03 \cdot d_{\text{FGE}}^2 \cdot t}{8 \cdot d_{\text{FGE}}^3} = 0.629 \frac{t}{d_{\text{FGE}}} \quad (4.2)$$

The numerator of eq. (4.2) was obtained with the help of CAD. Knowing it is an ideal, the thickness in CAD was set to  $t_{\text{FGE}}=0.25$  mm. The mass of fabricated FGE samples was assessed, and the wall thickness was measured as 0.3–0.4 mm. Based on this,  $\varphi$  could be calculated. Results from the explicit formula as well as the experiments are shown in table 4.1. Especially at low values of  $d_{\text{FGE}}$ ,  $\varphi$  is much higher than expected, suggesting this wall thickness is much higher than in CAD. This is probably due to the strong curvature of small FGE. For eq. (4.2) to be valid it is also a requirement that the shape of a single FGU and the distances between FGU are as assumed here.

**Table 4.1.:** Calculated and measured values of  $\varphi_{\text{FGE}}$ .

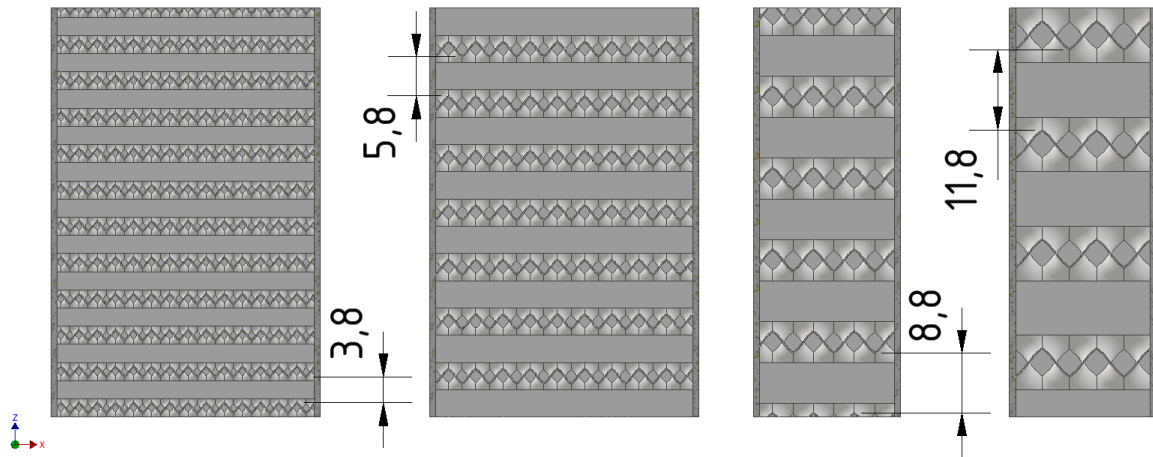
$d_{\text{FGE}}$ / mm	n. of FGU / -	$\varphi_{\text{FGE}}$ meas. / -	$\varphi_{\text{FGE}}$ calc. / -	
			$t_{\text{FGE}} = 0.3$ mm	$t_{\text{FGE}} = 0.4$ mm
1.3	32	0.299	0.145	0.194
2	18	0.149	0.094	0.126
3	8	0.101	0.063	0.084

FGE-equipped modules for stability testing were *FGE-8-1.33*, *FGE-12-2*, *FGE-12-3*, and *FGE-12-4*. They were manufactured with  $t_w=0.8$  mm. At the interface of FGE and wall, the spacing equaled  $\approx 0.75 \cdot l_{\text{FGE}} \approx 3 \cdot d_{\text{FGE}}$  ranging from 3.8–11.8 mm. This is visible in the images in fig. 4.4 which were obtained by slicing the modules in CAD with a plane parallel to the wall which was 0.1 mm inside the wall.

#### 4.1.1.3. Connections and Fabrication

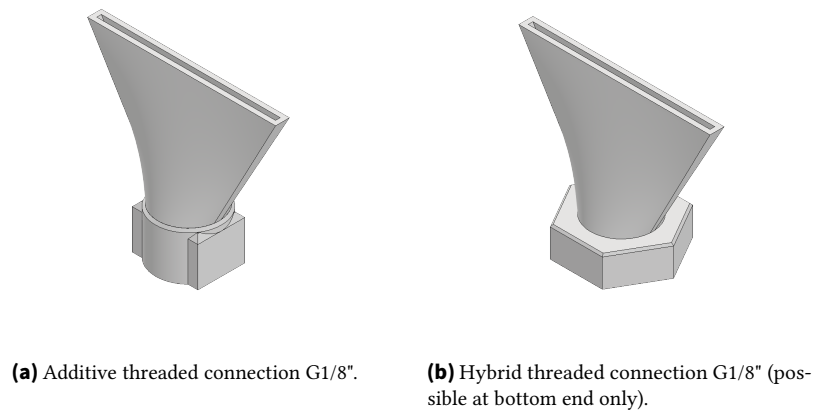
Internal threads enabled the slits to be attached to standard externally threaded connectors. The internal G1/8"-thread was designed individually according to [163] with 4 % higher diameter values to compensate tolerances. It had clamping surfaces on the outside, and cones transitioned the rectangular cross-section of the slit into the circular cross-section of the thread section, resulting in high wall thickness for these sections;  $t_w=1$ –2 mm (fig. 4.5a). The cones, which were not in the scope of the study, allowed for little overhangs, flow-through with smooth cross-section transition, and good depowdering [149].

The internal thread section at the lower end could be omitted when the part was manufactured on a nut which had been positioned inside the printer beforehand (fig. 4.5b). This approach combining



**Figure 4.4.:** CAD images of FGE-equipped modules. Modules were cut with a plane parallel to  $xz$ -plane 0.1 mm behind wall to reveal the distances (in mm) between FGE-wall connections.

conventional nuts and PBF-LB/M additive manufacturing is called hybrid manufacturing and greatly facilitated the production of modules for pressure testing [213].



**Figure 4.5.:** CAD representation of module connectors.

The conventional substrate were 19 mm stainless steel nuts with G1/8" thread from Schrauben-Jäger AG (Karlsruhe, Germany, art.-n. 103806). Nuts were positioned with the help of parallel rests and fixed to the build plate with Loctite superglue by Henkel AG (Düsseldorf, Germany). Figure 4.6 depicts the manufacturing approach with an exemplary module. All modules tested are depicted in appendix B tables B.4 to B.10.

The standard tessellation language (STL) files obtained from the CAD-software Autodesk Inventor (San Rafael, CA, USA) were repaired in Autodesk Netfabb. This was necessary as, under the unrevised version, the locally very complex designs (FGE) resulted in slicing errors in the pre-process software.

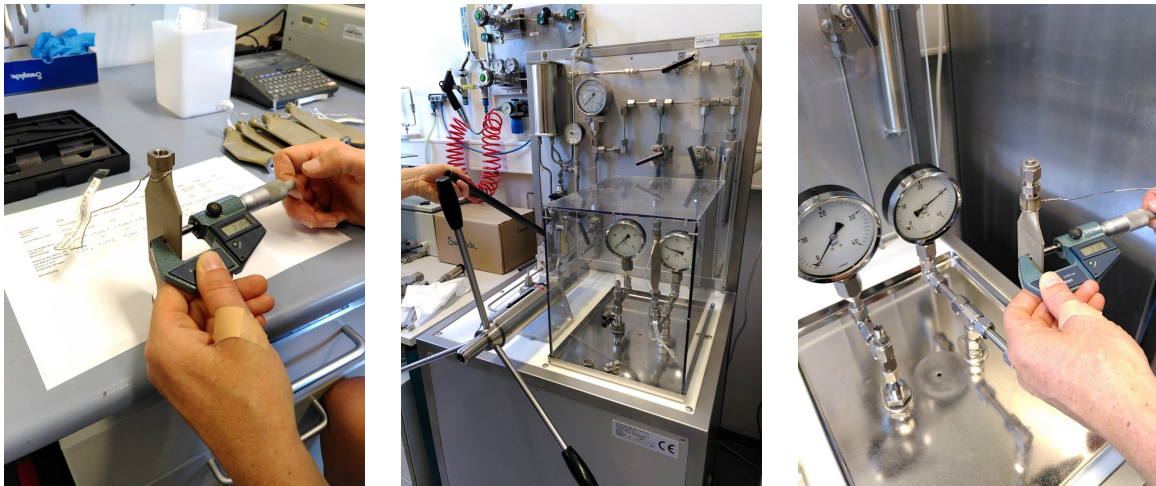
Modules were printed on a Realizer SLM125 (now LASERTEC SLM12) by DMG MORI (Bielefeld, Germany). Powders used, stainless steel 316L, were supplied by Carpenter Additive (Philadelphia, USA) and SLM Solutions (Lübeck, Germany). After printing, the threads at the ends were tapped and countersunk. The end surfaces were milled with a plain cutter on a Deckel (today DMG MORI) FP5 numerically-controlled mill.



**Figure 4.6.:** Hybrid manufacturing of modules on nuts with exemplary empty module (three-quarter cut).

#### 4.1.2. Experimental Method

The procedure described and shown in fig. 4.7 was applied to a clean and leak-tight part in order to determine mechanical stability. The metallic modules were connected to a pressure test rig using threaded connectors and metal-bonded polymer gaskets. The test rig was made by Konstandin und Partner engineering GmbH (Pfinztal, Germany) and employed a hand pump by SITEC Engineering (Maur, Switzerland). The test pressure calculated with  $1.43 \cdot PS$  (Ref. [236]) was rounded to  $p_{\text{test}} = 30$  bar. The external micrometer used had a measuring tip with  $d = 5$  mm. For modules with non-planar walls, parallel rests were employed.



(a) Place marking in the middle of module wall, measure outside depth  $D_0$ , and attach to test port of pressure test rig.

(b) Fill with water by manual pump, close opposite connector, and increase pressure to  $p_{\text{test}} = 30$  bar.

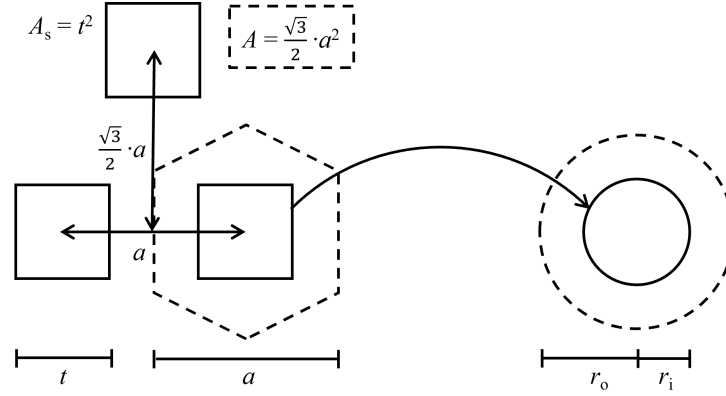
(c) After a minimum  $t = 15$  min measure outside depth  $D_1$  before decreasing to ambient pressure.

**Figure 4.7.:** Experimental procedure for testing mechanical stability.

#### 4.1.3. Calculation Method

For modules equipped with pins, case 2j from Ref. [228] Tab. 11.2 (p. 457) was used for theoretical calculations. This case is for an annular disc, fixed in the middle with guided outer edges, subject to a uniform load. The hexagonally arranged pins were abstracted to the annular disk in said reference as follows: the radius of the circle area equivalent to one quadratic pin was the inner radius in the reference. The radius of the circle area equivalent to one hexagonal repetition unit was the outer radius in the reference, fig. 4.8. The pressure was equal to the load per unit area  $q$ . The vertical deflection of

the plate  $\Delta y$  at the outer radius was the most important: it was assumed as the deflection between pins with spacing  $a$ .



**Figure 4.8.:** Schematic of the dimensions in an hexagonal arrangement of pins and how it was abstracted to an annular disc.

For empty modules and those equipped with fins, case 6a from Ref. [228] Tab 11.4 (p. 506) was used for theoretical calculations. The formulas were evaluated with the help of Microsoft Excel (Redmond, USA) and Matlab R2022b by Mathworks Inc. (Nattick, USA).

Material properties can be found in table 4.2. These properties being standard values for wrought 316L from Ref. [237] are used and confirmed by several authors for additive 316L [231, 238].

**Table 4.2.:** Material properties of 316L at room temperature used in calculation and simulation. [237]

Young's modulus $E$ / MPa	Poisson's ratio $\nu$ / -	Density $\rho$ / kg m <sup>-3</sup>
200,000	0.3	8000

#### 4.1.4. Simulation Method

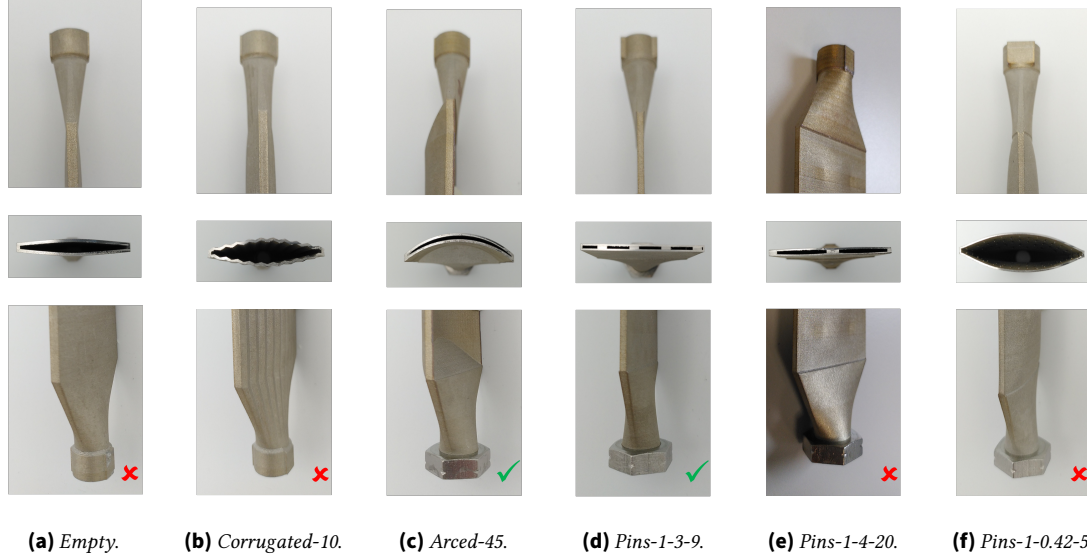
For FEA, software ANSYS 2020 R2 Workbench and Mechanical by ANSYS Inc. (Canonsburg, USA) were used. A custom material with the properties found in table 4.2 was used. Only repetition units of the modules were subjected to FEA also utilizing symmetries. Element size was 0.5 mm if not otherwise mentioned.

Mechanical strength was considered sufficient when the displacement was below  $\Delta y \leq 0.01$  mm or  $\Delta D = D_1 - D_0 \leq 0.02$  mm when referring to a module with external depth  $D$ . This quantity is accessible with all three investigation methods while stress is not accessible for the experimental method chosen. The maximum value was chosen to limit deflection of a slit with  $d=1$  mm to 2 % which is especially important for not crushing catalyst particles present.

#### 4.1.5. Results

In this section, first the experiment's and second the calculation's results are explained. Almost all modules without internal structures ( $\varphi=0$ ) showed poor mechanical stability in experiments, displacement being between  $\Delta y=0.2$ –10 mm. Examples for this are the empty planar module in fig. 4.9a and the empty modules with ten corrugations in fig. 4.9b. The exception was the empty slit with highly

arched walls *Arched-45*, which showed  $\Delta D$  below measuring accuracy (fig. 4.9c). The module *Pins-1-3-9* passed the pressure test (fig. 4.9d), while *Pins-1-4-20* didn't as the wall bent between pins (fig. 4.9e). In module *Pins-1-0.42-5* rupture of all pins occurred (fig. 4.9f).



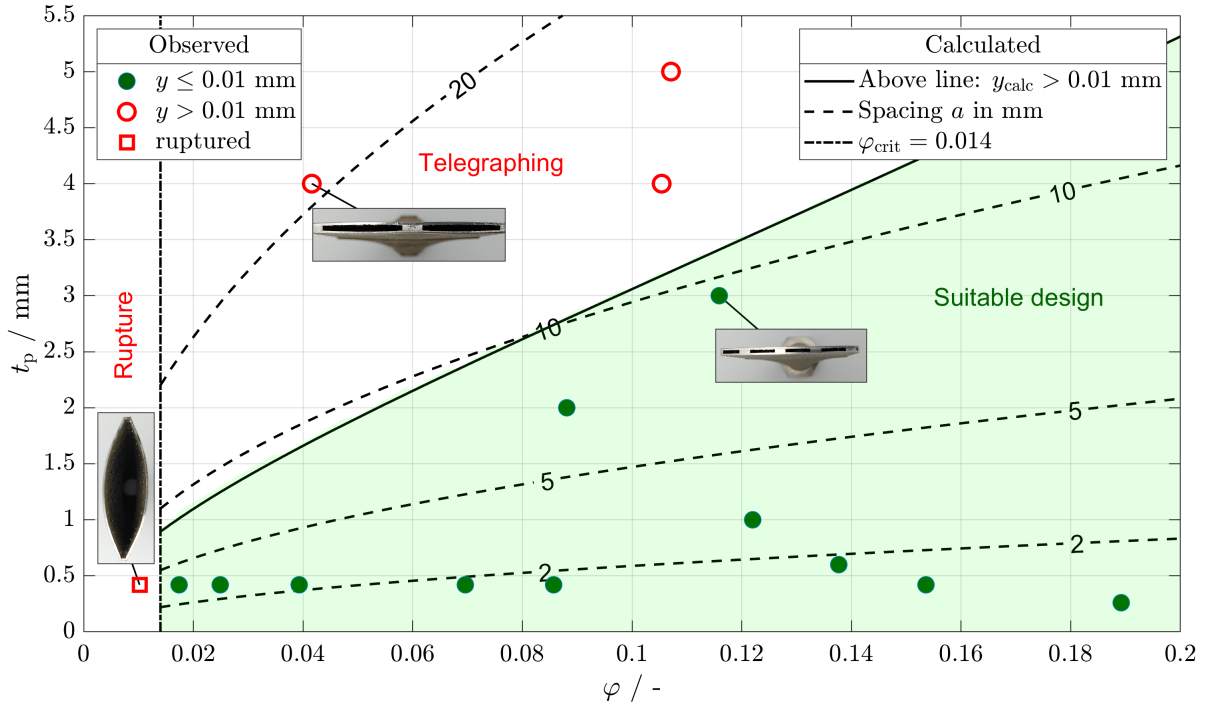
**Figure 4.9.:** Modules after pressure test. (a-c)  $t_w=1$  mm. (d-f)  $t_w=0.6$  mm. Green check marks indicate passing, red x marks failing.

Three pin-equipped modules showed a mode of failure referred to as "Telegraphing" in experiments. This is known from fiber-reinforced composite materials [239]. When the distance between pins was too high  $a \gtrsim 10$  mm, the walls curved outside between pins (red open circles in fig. 4.10). Below a certain volume fraction  $\varphi \leq \varphi_{\text{crit}} \approx 0.014$ , rupture of pins occurred and the structure bent outside as a whole (red open square in fig. 4.10). Apart from that, most modules with pins showed excellent mechanical stability in the investigated region of  $\varphi=0.02-0.19$  and  $t_p=0.26-5$  mm (green full circles in fig. 4.10). The calculation method predicted stable designs to be in the green area below the solid line in fig. 4.10 which concurred with experimental observations. Modules with internal fins, lattice, and FGE all passed the pressure test. The hybrid manufacturing connection was never a source of failure in our experience, which is consistent with the findings of [213].

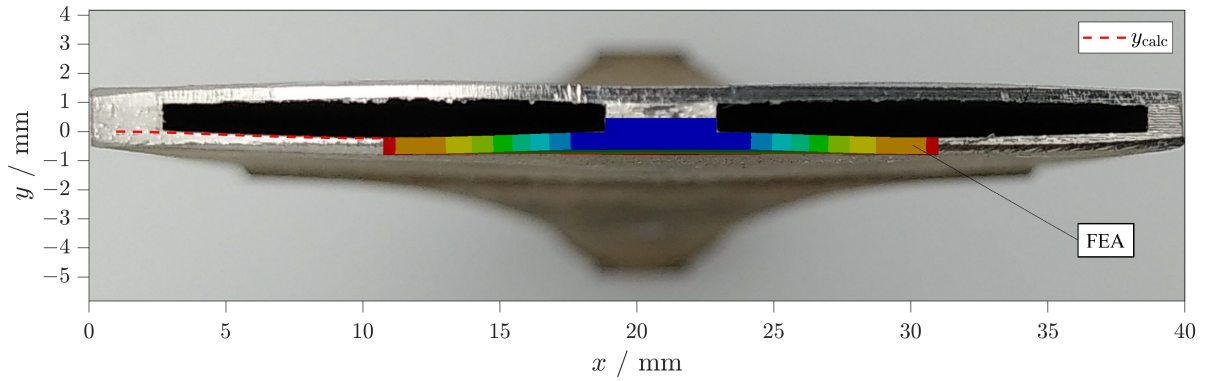
In fig. 4.11, for one module experiment, calculation, and simulation are compared. The module *Pins-1-4-20* deformed notably. The measured displacement of one side was  $\Delta y=0.20$  mm, while the calculated and simulated displacement had been  $\Delta y=0.235$  and  $0.215$  mm, respectively. Both, calculation and simulation overestimated experimental displacement a little and reflected the characteristic shape well.

Results from simulation, experiment, and calculation concurred. Table 4.3 shows results of FEA of rectangular units. Full-size images can be found in Ref. [225]. Mesh size independence was confirmed for each simulation. Mesh size was reduced until maximum deflection did not change anymore (0.5 mm for most cases). An example is provided in Ref. [225] as well. For low width up to 4 mm, displacement was not significant. This confirmed the experimental results of fin-equipped modules but also the fact that modules did not fail at their narrow sides. Rectangular walls with  $w=40$  mm and  $t_w=1$  mm displaced severely in experiment, calculation, and simulation. Displacement was only limited below the accepted value at  $t_w=5$  mm.





**Figure 4.10.:** Results of mechanical stability calculation and experiment for pin-equipped modules. Symbols correspond to modules that passed the pressure test (full green circles) and modules that failed the pressure test by telegraphing (red open circles) or by rupturing (red open square). Location of symbol reveals volume fraction via x-axis, pin size via y-axis, and spacing via the dotted lines in the figure. Modules in the area shaded in green were calculated as to deform less than  $\Delta y \leq 0.01$  mm (pass) which concurs with experimental findings.


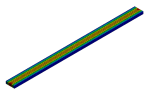
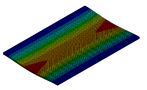
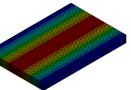


**Figure 4.11.:** Failed module *Pins-1-4-20*: cross-cut after test, calculated, and simulated deflection.

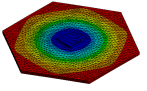
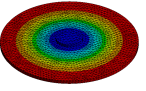
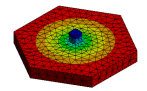
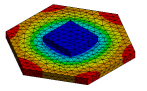
In table 4.4, pin-equipped modules are shown. Abstracting the hexagonally arranged quadratic pins led to an insignificant change in FEA displacement. Calculation and experiment yielded slightly higher values of displacement (first two columns). While the calculated and simulated deflection correctly predicted that there was no telegraphing in the module in column three, the volume fraction was close to its critical value. Simulation predicted that stress inside the pin reached almost yield-strength. Both volume fraction and simulation result explain the rupture of the pin-equipped module with  $\varphi=0.01$  (third column). All three methods agreed that a module as shown in column four did not deform significantly.

Table 4.5 features modules where no calculation method was available. FEA and experiments were in agreement that no significant deflection occurred for the investigated modules with FGE and lattice.

**Table 4.3.:** Results for stability of empty and fin-equipped modules  $l=60$  mm.

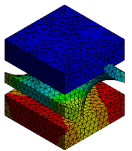
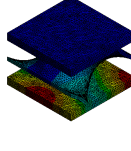
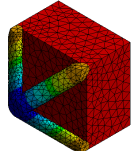
Module	Abstraction of <i>Fins-1</i>	Abstraction of <i>Fins-4</i>	<i>Empty</i>	Variation of <i>Empty</i>
				
$t_w$ / mm	1	1	1	5
$w$ / mm	1	4	40	40
$\Delta y_{\max, \text{FEA}}$ / mm	$-1.007 \times 10^{-5}$	$-2.201 \times 10^{-4}$	-1.2373	-0.0105
$\Delta y_{\max, \text{calc}}$ / mm	$-4.275 \times 10^{-7}$	$-1.094 \times 10^{-4}$	-1.0074	-0.0081
$\Delta y_{\max, \text{exp}}$ / mm	0	0	$\approx -5$	-

**Table 4.4.:** Results for stability of pin-equipped modules.  $t_w=0.6$  mm.

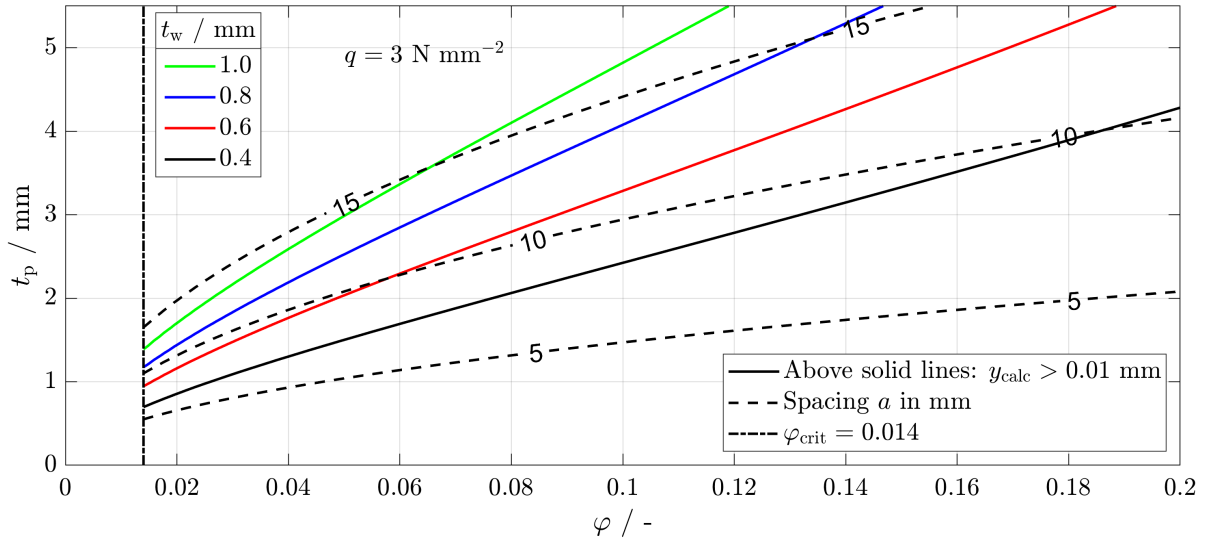
Module	<i>Pins-1-4-20</i>	Abstraction of <i>Pins-1-4-20</i>	<i>Pins-1-0.42-5</i>	<i>Pins-1-3-9</i>
				
$t_p$ / mm	4	-	0.42	3
$d_i$ / mm	-	4.514	-	-
$a$ / mm	20	-	5	9
$d_a$ / mm	-	21.0	-	-
$\varphi$ / -		0.0382	0.0081	0.1283
$\Delta y_{\max, \text{FEA}}$ / mm	-0.219	-0.215	$-2.994 \times 10^{-3}$ <sup>a</sup>	$-5.451 \times 10^{-3}$
$\Delta y_{\max, \text{calc}}$ / mm		-0.235	$-1.286 \times 10^{-3}$	$-3.236 \times 10^{-3}$
$\Delta y_{\max, \text{exp}}$ / mm		-0.20	$\approx -10$	0

<sup>a</sup> Stress reached  $\sigma=436$  MPa inside pin equaling 75 %  $R_{p0.2}$ .

**Table 4.5.:** Results for stability of FGE-equipped ( $t_w=0.8$  mm,  $t_{\text{FGE}}=0.4$  mm) and lattice-equipped ( $t_w=0.6$  mm) modules.

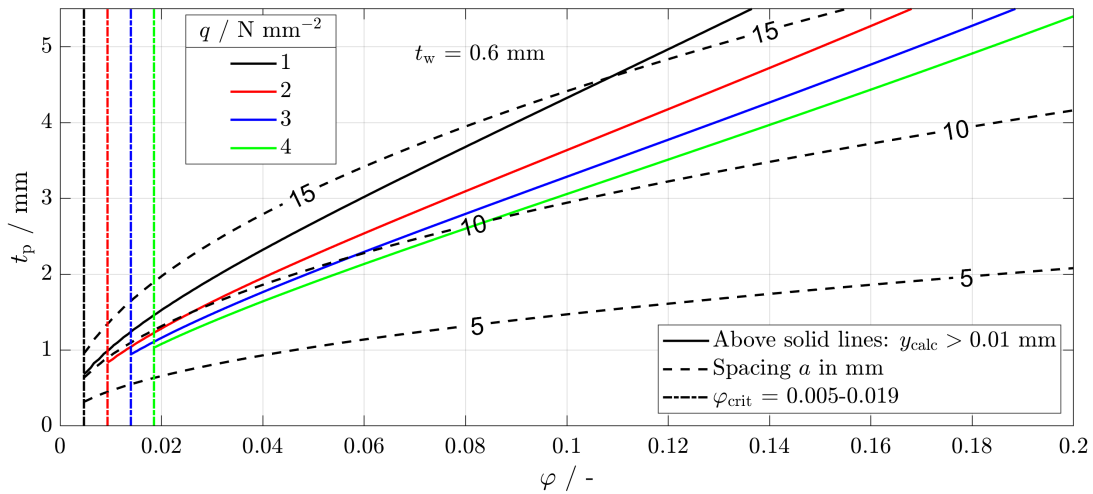
Module	<i>FGE-8-1.33</i>	<i>FGE-12-4</i>	<i>Lattice-1</i>
			
Dimensions / mm	$d_{\text{FGE}}=1.333$	$d_{\text{FGE}}=4$	$d_{\text{strut}}=0.2$
$d$ / mm	2.667	8	0.5
$w$ / mm	2.667	8	1
$l$ / mm	5.333	16	1
$\varphi$ / -	0.1887	0.0629	0.2177
Element size / mm	0.2	0.2	0.1
$\Delta y_{\max, \text{FEA}}$ / mm	$-1.887 \times 10^{-4}/2$	$-3.985 \times 10^{-3}/2$	$-4.820 \times 10^{-4}$
$\Delta y_{\max, \text{exp}}$ / mm	0	0	0

A combination of calculation and checking the volume fraction against its critical value was effective for stability assessment. Having implemented the formula in a programmable script, it was possible to extract information on failure criteria based on all design parameters. In fig. 4.12, the design parameter wall thickness was varied, while the load was constant  $q=3 \text{ MPa}$  referring to an operation pressure of  $p=20 \text{ bar}$  and a safety factor of  $S=1.5$ . Assuming a design with  $\varphi=0.1$  is desired, the pin size can be determined by starting on the abscissa and moving upward until the solid line referring to the aimed-for wall thickness is reached. The pin size must not exceed the respective value on the ordinate. The selected pin size defines the spacing. At  $t_w=0.6 \text{ mm}$  a pins size of  $t_p=2 \text{ mm}$  is selected leading to a spacing of  $a=6.8 \text{ mm}$ .



**Figure 4.12.:** Calculated stability criterion for various thicknesses at constant load.

To prove the power of this approach, fig. 4.13 shows another design figure. Assuming pins with a size of  $t_p=2 \text{ mm}$  are required, the reading is to be started from the ordinate at this value. Moving in positive horizontal direction, one has to go as far (to a volume fraction as high) as to reach below the solid line referring to the design load (pressure difference). Assuming a design load of  $\Delta p=40 \text{ bar}$  (bright green line) the required volume fraction would be  $\varphi \geq 0.08$  and the spacing  $a \leq 7.5 \text{ mm}$ . This specific figure is valid for a wall thickness of  $0.6 \text{ mm}$ .



**Figure 4.13.:** Calculated stability criterion for various loads at constant wall thickness.



The error of the external micrometer was  $\varepsilon_y=0.001$  mm. The error of the analogue pressure gauge was approximately  $\varepsilon_p=1$  bar. This is acceptable considering the critical values of deformation was 0.02 mm and the pressure was  $p=30$  bar. When it comes to design and manufacturing of pressure vessels uncertainties in the range of a couple % are insignificant when a typical safety factor of  $S=1.5$  is used (Ref. [235]).

#### **4.1.6. Interim Summary Mechanical Stability**

Wall thicknesses of several millimeters necessary for slit modules at reasonable size without internal structures to withstand  $p=30$  bar at room temperature are unacceptable.

The first approach (deflection of the walls) was not successful in increasing the mechanical stability of planar slits. Neither corrugated nor arched walls could, except for one instance at a comparatively high thickness, withstand the pressure difference occurring at  $p=30$  bar at room temperature.

Significant insights into stability of micro-structured devices were gained. The second approach of introducing regular internal structures of minimal mass and volume led to stable modules. Evenly spaced internal structures with sufficiently high volume fraction and sufficiently low spacing were stable, the exact values depending on material properties, wall thickness, and load.

For external pressure, no failure is expected, since the internal structures are unlikely to buckle with the highest slenderness ratio being  $\lambda_{\text{buckling}} = 3.33$  for  $t_p = 0.26$  mm. This ensures both process safety and smooth operation without compression of particles on the inside of devices, e.g. catalyst..

To be on the safe side regarding rupture, the volume fraction aimed for should be above the critical value. This is reasonable as there is a chance of cracking formation starting from the points where internal structures meet the walls in steep angles, as well as from surface roughness [240].

Experiment, simulation, and calculation were in good agreement. The calculation is easy to use, especially when being implemented into tables as a graph as shown in this section.

## **4.2. Local Fluid Permeability**

As established in chapter 2, in micro-structured reactor (MSR) for Fischer-Tropsch synthesis (FTS), the alumina-supported cobalt catalyst usually has spherical shape and a diameter of 50–200  $\mu\text{m}$  [33, 49, 51, 54, 55, 60]. It must be and remain stationary to prevent wear, while at the same time fluid must pass through it. In this work, the intermediate approach from the list in section 2.4 is pursued: at one end of the catalyst channel the fluid-permeable region is done with additive manufacturing (AM) and at the other end it is done by mounting of a commercially available sinter metal plate.

Fluid-permeable structures made by AM were investigated, among others, by Klahn et al. [161] and Xie [241]. In the packed-slit reactor concept, the direction of flow and build are identically vertical. Hence, the local fluid permeability is required in the direction of build, and the approach from Ref. [161] was pursued. Design guideline for engineering such structures with respect to fluid permeability and particle impermeability do not exist to date. At the end of this section should stand a design recommendation for the case of micro-structured FTS reactors that can be transferred to other catalyst powders and laser-based powder bed fusion of metals (PBF-LB/M) machines other than Realizer SLM125.

#### 4.2.1. Catalyst Powders

Inert alumina catalyst support was used as dummy for catalyst in the subsections dealing with local fluid permeability, particle loading, and heat transfer as well. A commonly used product is Sasol Puralox. Sasol Deutschland GmbH (Hamburg, Germany) were so kind as to support this work with Puralox SCCa-5/150 and SCCa-150/230. These materials were sieved for 30 min on an Analysette Pro 3 by Fritsch GmbH (Idar-Oberstein, Germany) with sieve mesh grades of 50  $\mu\text{m}$  and 100  $\mu\text{m}$  respectively to remove the smallest approx. 10 % of the original sample masses. The remaining powders were measured with static light scattering (SLS) on an LS-230 by Beckman Coulter GmbH (Krefeld, Germany) and showed Gaussian size distribution with the characteristic values given in table 4.6. Scanning electron microscope images confirmed the spherical shape of the particles. The complete set of data on size distribution and microscopy images can be found in appendix C.1. It is important to note the particle diameters, separating the smallest 5 wt-% of the powder which are  $d_{p,5} = 56$  and 129  $\mu\text{m}$  respectively.

**Table 4.6.:** Characteristic values of particle size distribution of alumina powders.

Powder	$d_{p,5} / \mu\text{m}$	$d_{p,50} \text{ or } d_p / \mu\text{m}$	$d_{p,95} / \mu\text{m}$
Puralox SCCa-5/150 sieved	56	83	126
Puralox SCCa-150/230 sieved	129	194	299

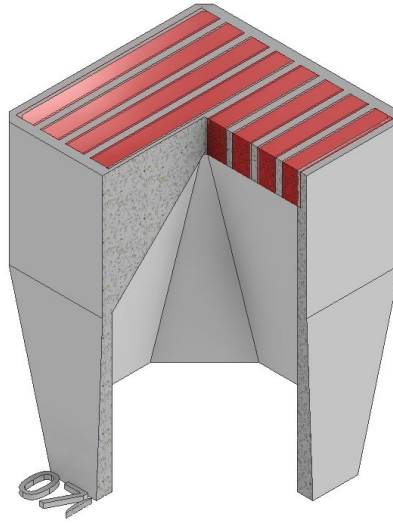
#### 4.2.2. Design and Fabrication

The fluid-permeable regions were characterized via their length, which is the part of the build height over which they are fabricated, the depth of the slit they are covering, and the hatch distance ( $HD$ ), which is the distance between the middle lines of neighboring melting tracks.  $HD$  and melting trace width ( $MTW$ ) result in the distance between melting tracks  $d_{\text{perm}} = HD - MTW$ , which is significant for the permeation of particles with this approximate size.

In this application, the fluid-permeable regions were always within solid walls; hence, they required no contours or fill lines. An overlap of fluid-permeable and solid regions of  $\approx 0.1$  mm seemed reasonable. It is noteworthy that both solid and fluid-permeable region were made within the same PBF-LB/M fabrication step via two different scanning strategies.

It is known from basic PBF-LB/M design guidelines that vertical overhangs with  $\beta = 0^\circ$  are not possible without support. Small vertical overhangs up to  $t = 1.6$  mm are feasible [149, 242]. In order to cover areas with an arbitrary depth with a permeable region without support, it is necessary to subdivide it into compartments with solid walls in-between. Consequently, the area of  $12 \times 12 \text{ mm}^2$  was divided into eight slits with  $1 \times 12 \text{ mm}^2$ . The subdividing walls had  $45^\circ$  overhangs and minimal thickness of  $t_w = 0.6$  mm since there was no mechanical load (fig. 4.14). The scan vectors of the fluid-permeable region were perpendicular to the slit depth, and the unsupported overhang of 1 mm was acceptable. The solid wall was made up by dense hatching in a chess board, while the fluid-permeable regions were made up by loose unaltered hatching (figs. 3.4a to 3.4b).

It was deemed suitable to print modules with fluid-permeable regions with  $HD = 170\text{--}400 \mu\text{m}$ . The  $MTW$  is assumed as  $160 \mu\text{m}$ . Modules were printed in hybrid fashion on stainless steel nuts as described in section 4.1.1 and thoroughly cleaned. Figure 4.15a shows the top view of these modules where the color transition on the top surface indicates an increasing permeability from left (light gray) to right (dark gray).



**Figure 4.14.:** Computer aided design (CAD) image of local fluid permeability module. Red=local fluid-permeable region, gray=solid region.

Planar stainless steel sinter metal SIKA-R 100 AX from GKN Sinter Metals GmbH (Radevormwald, Germany) with  $t=2$  mm are usually used at Institute for Micro Process Engineering (IMVT). They have a porosity of  $\epsilon_s=0.52$  and a mean pore diameter of  $47\text{ }\mu\text{m}$ . The material was milled into circular shape with  $d=50$  mm.

#### 4.2.3. Method

Characterization of flow through fluid-permeable solids can be done according to Ref. [243]. The main matter of interest was, however, whether the solid was locally permeable for fluids but impermeable for a certain powder. A two-step experimental procedure was established; the two steps pressure filtration and vacuum filtration are explained in the following two sections. After this two-step procedure was completed with the smaller-sized powder, the modules were rinsed with de-ionized water, purged with pressurized air, and rinsed again. The procedure was then repeated with the larger-sized powder and followed by another cleaning. This was later confirmed to be an effective method of removal of particles from the fluid-permeable regions.

After the filtration test, the modules with  $HD=170$  and  $300\text{ }\mu\text{m}$  were polished and analyzed with an optical profilometer S neox by Sensofar (Terrassa, Spain). The obtained images were processed in two ways: The dimensions of a subset of struts were measured with the help of graphical software, and the porosity of selected slits was calculated with a self-written Mathworks (Nattick, MA, USA) Matlab code based on pixel brightness [244].

##### 4.2.3.1. Pressure Filtration

A suspension of a known mass  $m_0$  of alumina powder  $m \approx 0.15$  g in  $V \approx 20$  mL of de-ionized water was prepared individually for each module, resulting in a volume fraction of approx. 1 vol-%. The suspension was stirred and guided through the module with the help of a pressurized nutsche-type

filtration device, for which a maximum of  $p=3$  bar was applied. Device and module were connected with NPT threaded connectors, teflon band, tube, threaded connector Swagelok SS-6M0-1-2RS, and self-made flat rubber gaskets. The sinter metal disc was mounted to the device with the help of a special silicone gasket. The device is shown in fig. 4.15b.

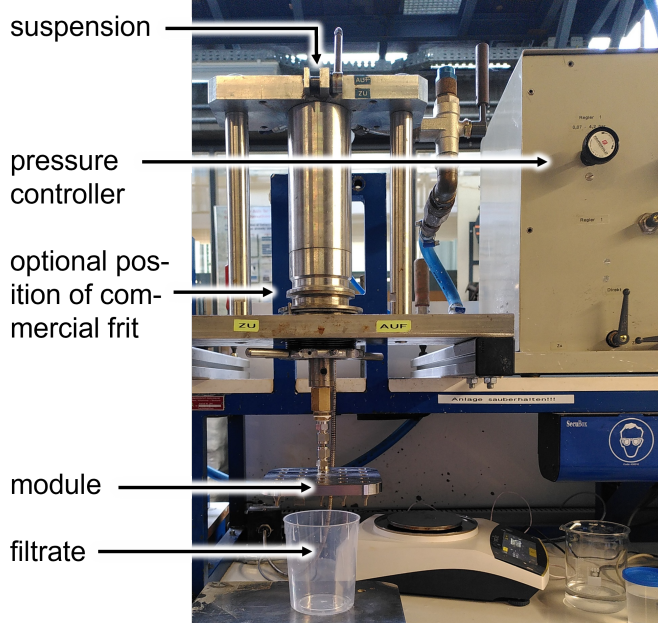
#### 4.2.3.2. Vacuum Filtration

In a prior preparatory process, cellulose acetate filter papers  $d=47$  mm (material description in appendix C) had been dried in an oven at  $T=60$  °C and weighed on a laboratory scale Sartorius (Göttingen, Germany) LE225D-0CE to determine  $m_1$ . The filtrate collected from the first filtration was submitted to a second filtering process through the filter papers in a polymer Büchner-type filtration device by Nalgene (Rochester, NY, USA) depicted in fig. 4.15c. Vacuum was applied and it was ensured that particles present in the suspension were collected on the filter paper and not sticking to the device's walls by rinsing with de-ionized water. The filter material was dried again and subsequently weighed to obtain  $m_2$ . The difference in masses was the permeated particles mass; divided by the original powder mass, the result is defined as the particle permeation  $P_p$  (eq. (4.3)).

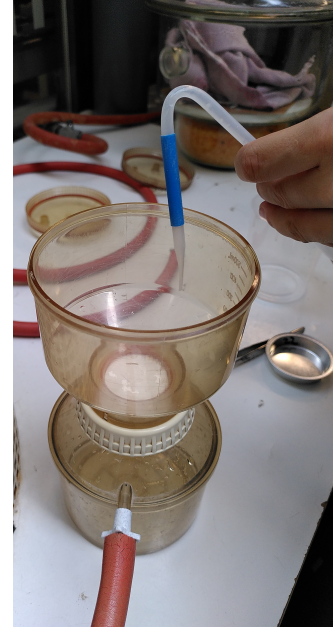
$$P_p = \frac{\Delta m_{1,2}}{m_0} \quad (4.3)$$



(a) Frit modules with  $HD$  increasing from left to right.



(b) Pressure filtration device.



(c) Vacuum filtration device.

**Figure 4.15.:** Modules and materials for local-permeability testing.

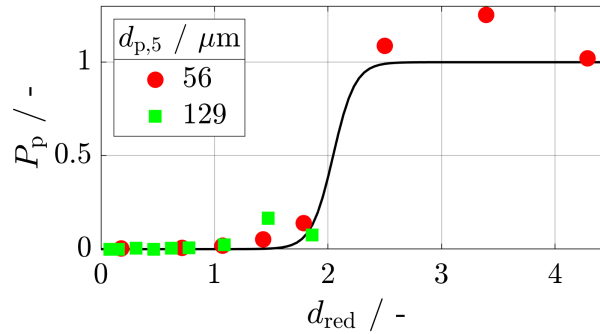
To gather an understanding of the relation of particle permeation  $P_p$  with particle size and fabrication parameters  $HD$  and  $MTW$ , the data was reduced with the help of eq. (4.4).

$$d_{\text{red}} = \frac{d_{\text{perm}}}{d_{5,3}} = \frac{HD - MTW}{d_{p,5}} \quad (4.4)$$

#### 4.2.4. Results

In pressure filtration, liquid passed through modules faster with increasing hatch distance ( $HD$ ) as the associated pressure drop decreased. Ultimately, white particles could be seen in the filtrate, while no particles were seen in the filtrate from vacuum filtration.

Figure 4.16 shows the permeation of additive modules for both sizes of particles. The black line is a logarithmic function adapted to the experiments with  $d_{p,5} = 56 \mu\text{m}$  only. For this batch of powder, the whole range of permeation  $P_p$  from 0 to 1 was covered by the experiments. For the other batch, the maximum value is  $P_p \approx 0.2$ . Experimental results for both powders followed the logarithmic function fairly well. Most important, the permeation only showed values above 0 for  $d_{\text{red}} > 1$ . This was the expected result, and it is a design guideline for local fluid permeability achieved with laser-based powder bed fusion of metals (PBF-LB/M) with this specific strategy.



**Figure 4.16.:** Particle permeation of local-permeability modules plotted over  $d_{\text{red}}$ .

The permeation of the sinter metal frit with both powders is shown in table 4.7. This solution, too, was effective in retaining catalyst in its place and letting fluid pass.

**Table 4.7.:** Particle permeation through commercial sinter metal frits.

Particles $d_{p,5} / \mu\text{m}$	56	129
$P_p / -$	0.000584	0.00102

No classical error calculation was executed at this point. Errors arose more from the operation and solid deposits in the equipment than from weighing. At this point, determining the permeation of particles without using a permeable modules or sinter metal frit and determining the blind permeation of a sample of water not containing any powder was satisfactory.

The desirability of the investigated modules being locally permeable for fluids but impermeable for particles accounts for the most important values of permeation being near  $P_p=0$ . Blind permeation value table 4.8 near zero provides confirmation that the method does not deliver excessive permeation; the method is not over-sensitive. Permeation of particles when no filter was used was  $P_p=0.84$ , even



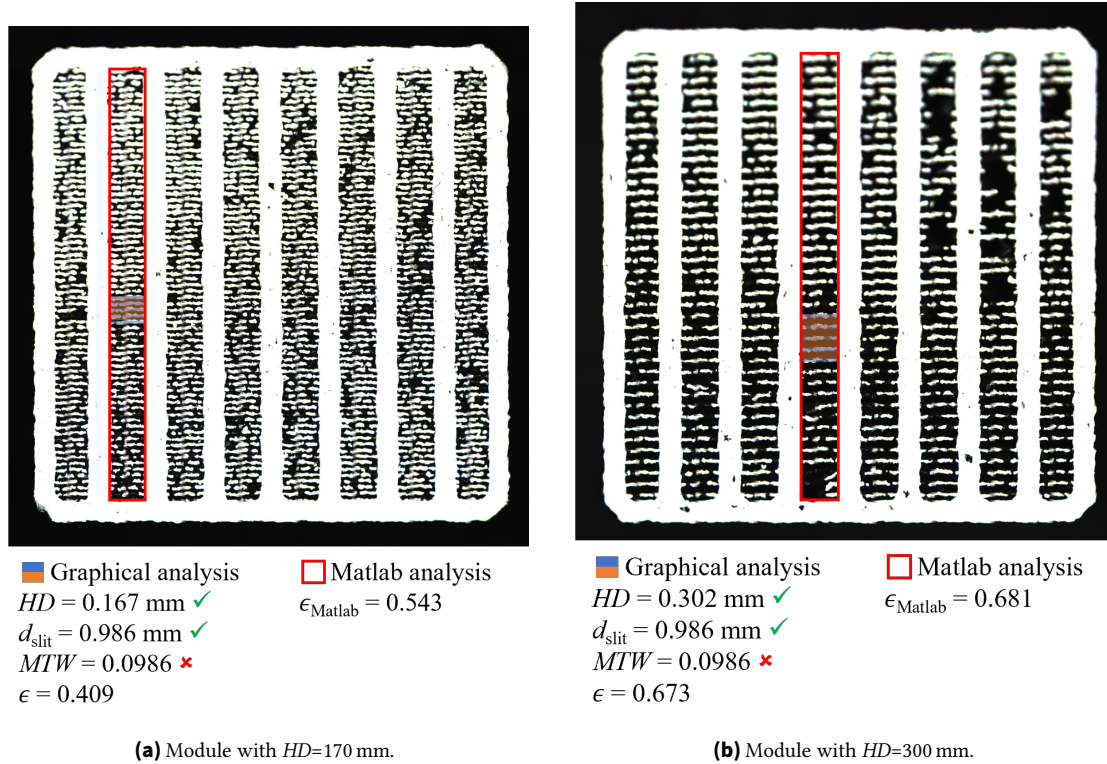
though unity was expected. This is, however, acceptable since it is well above zero and confirms the sensitivity of the method.

**Table 4.8.:** Experimental results for validation of the experiment.

$P_p$ of particles with $d_{p,5} = 56 \mu\text{m}$ in absence of module of frit / -	Blind permeation in absence of particles with reference to $m_p=0.15 \text{ g} / -$
0.840	0.00373

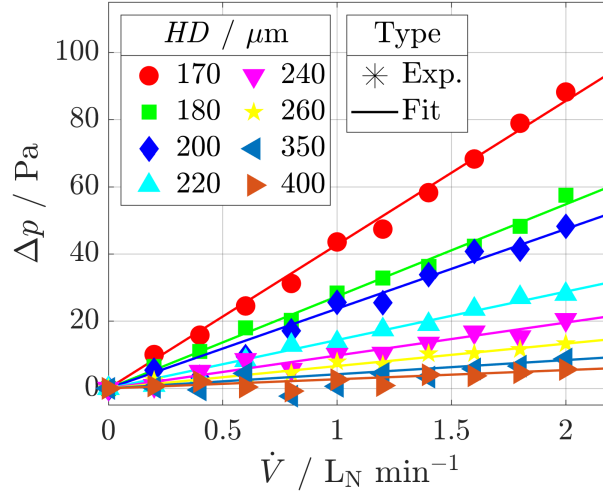
The images obtained with the profilometer are shown in fig. 4.17. The sample with the larger  $HD$  was polished too much, leading to gaps in the top right corner. No alumina particles were seen, indicating that the cleaning procedure in between powder batches seemed to have worked well. The images were measured with a graphical software using the real external size of the units as reference. The distance of subdividing walls was fabricated as intended. The melting trace width ( $MTW$ ) was smaller than expected. The porosities calculated via Matlab were higher than those from the graphical analysis, probably Fischer-Tropsch synthesis (FTS) to the fact that Matlab considered the whole slit, also including some holes. Overlap of fluid-permeable with solid region of  $0.1 \text{ mm}$  led to an acceptable connection between the struts and the solid walls.

The permeation was selective, although the  $MTW$  appeared to be smaller than expected and although there were holes. This had probably two reasons: the image only showed one surface and a hint of what was below. This particular surface and a little below were polished, meaning the visible contours were comparatively "clean" and without spatters. The lower  $MTW$  can, however, also be explained by the low laser power.



**Figure 4.17.:** Pictures of polished modules with  $HD=170$  and  $300 \mu\text{m}$ . Both were analyzed graphically and with Matlab. Green check marks indicate expected, red x marks unexpected measurement results.

Particle retention comes at the prize of additional pressure loss. Figure 4.18 shows the pressure loss obtained with nitrogen at  $p=1$  atm and  $T=20$  °C. The friction at the solid walls and pressure loss of the experimental setup were compensated. Pressure drop of the module with  $HD=170$   $\mu\text{m}$  might have been even higher, considering the module was polished, reducing the length of the fluid-permeable region. Generally speaking, pressure loss increases with decreasing hatch distance and linearly with volumetric flow rate, indicating laminar flow behavior.



**Figure 4.18.:** Pressure loss over locally fluid-permeable regions as a function of volumetric flow rate. Lines signify linear fits.

The data was fitted to the equation for laminar flow in Ref. [245] to obtain the viscous coefficient of permeability  $\Psi_V$  (eq. (4.5)). Results of linear regression are shown in table 4.9. According to Ref. [246], pressure drop of flow through an array of rectangular slits was calculated. The porosity occurring in this formula was calculated based on the real  $MTW$  and  $HD$  (eq. (4.6)). Values of  $\Psi_V$  pertaining to this theoretical calculation, too, are shown in table 4.9.

The calculated values being approximately 2.5 times higher than the measured values needs to be investigated further. Possible reasons are abrupt changes in cross-sectional area FTS due to surface roughness and dimensional tolerances in PBF-LB/M samples.

$$\Delta p = \frac{\dot{V} \cdot \eta \cdot l}{A_{\text{cross}} \cdot \Psi_V} \quad (4.5)$$

$$\epsilon_s = 1 - \frac{MTW}{HD} \quad (4.6)$$

#### 4.2.5. Interim Summary Local Fluid Permeability

The presented strategy and the experimentally validated design guideline are powerful tools for process engineering devices. fluid-permeable regions can be generated, not only at any location in the part, but also at the same time as dense regions. With the help of the experimentally validated criterion, fluid-permeable regions can be tailored to be as permeable as possible for fluid, but selectively impermeable for the particles involved.

The obtained results were only based on modules with pristine fluid-permeable region and solid exterior wall. In preliminary experiments, single samples showed a hole in the wall or warping in the

**Table 4.9.:** Laminar flow pressure loss through locally permeable modules. Values for  $\Psi_V$  as fitted to measurements and as calculated according to Ref. [246].

$HD / \mu\text{m}$	$\epsilon_s \text{ calc.} / -$	$\Psi_V \text{ meas.} / \text{m}^2$	$\Psi_V \text{ calc.} / \text{m}^2$
170	0.41	1.59E-10	4.07E-10
180	0.44	2.48E-10	5.30E-10
200	0.50	2.86E-10	8.23E-10
220	0.55	4.71E-10	1.18E-09
240	0.58	6.92E-10	1.59E-09
260	0.62	1.02E-09	2.06E-09
350	0.71	1.61E-09	4.82E-09
400	0.75	2.49E-09	6.76E-09

topmost surface of the fluid-permeable region. These samples showed a high permeation near unity even at  $d_{\text{red}} \leq 1$ . Flow through the fluid-permeable regions up to  $u_0 = 0.38 \text{ m s}^{-1}$  has to be considered laminar. Calculations of pressure loss through arrays of rectangular slits according to Ref. [246] overestimated pressure loss 2.5 times, possible reasons being surface roughness and manufacturing tolerances. Versatile applications of fluid-permeable media in process engineering with multiple phase flows can be found in fig. B.1.

### 4.3. Particle Loading

Bed porosity is an important factor for micro-structured reactor (MSR) design (section 2.4) for both reactor productivity and pressure drop. Bed porosity can not yet be reliably predicted from literature, for channels with the shape and dimensions of the reactor concept presented here [7]. The most practical approach was to conduct experiments where narrow slits of varying geometries were filled with different-sized alumina powders. In addition, reference experiments with a measuring cylinder were conducted. Bed porosity was calculated from weighing the respective containers empty and with compacted particles. Compaction was achieved by tapping the samples multiple times, compare [181] Fig. 7. For estimation of the bed porosity the infinite mono-disperse bed porosity was initially assumed as  $\epsilon_{\text{bed,pd},\infty} = 0.36$ , obtained from Ref. [7]. The distribution parameter (assessed with static light scattering (SLS), appendix C.1) is listed in table 4.10.

**Table 4.10.:** Distribution parameter of the poly-disperse alumina powders derived from SLS measurements.

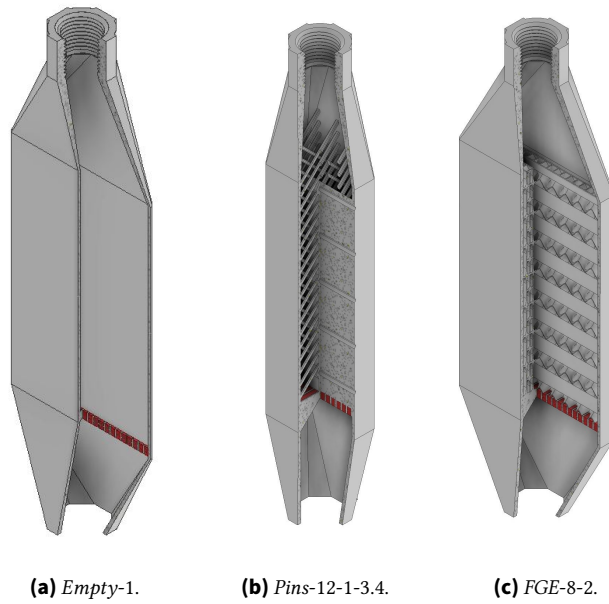
Powder $d_{p,50}$ or $d_p / \mu\text{m}$	$\zeta / -$
83	0.2404
194	0.2593

#### 4.3.1. Materials

For the particle loading experiments, modules from mechanical stability testing (section 4.1) were selected. These modules were empty or featured pins and fluid guiding element (FGE). For modules with pins,  $d_{\text{slit}}$  was the most important parameter for particle loading and took values from  $d_{\text{slit}} = 1\text{--}12 \text{ mm}$ . For modules with FGE, this value ranged from  $d_{\text{slit}} = 8\text{--}16 \text{ mm}$ , although  $d_{\text{PF}} = d_{\text{FGE}}/2$  was considered

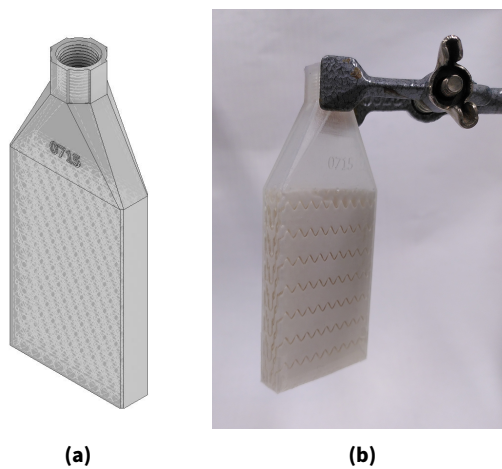


the relevant depth, having ranged from 0.67–2 mm. At the lower end, these modules featured a fluid-permeable region, selectively permeable for fluids, but impermeable for powder (fig. 4.19).



**Figure 4.19.:** Three quarter-cut computer aided design (CAD) representation of metal modules with no internal structures, pins, and FGE. Red are the fluid-permeable regions.

Selected metal module designs were printed with a partially transparent resin in vat photo polymerization. No changes were made to the internal structures. Printing was carried out on a Form 3L by Formlabs GmbH (Berlin, Germany) with Clear Resin. Supports were removed with manual tools and washing took place in a WC1 washing and curing station by Prusa Research a.s. (Prague, Czech Republic). After this external cleansing, the part was attached to the pump skid described in section 3.1.2. Special care was taken to transfer the outflow to a separate container. Curing was effected in the aforementioned station. Remaining isopropanol was removed with pressurized air. The procedure was repeated when the part was still sticky on the outside or showed residues on the inside. This was particularly the case with the FGE-equipped module in fig. 4.20. Clean resin modules were closed with tape at the bottom.



**Figure 4.20.:** CAD representation of resin module *FGE-8-2* (hidden edges visible) and the module being tested.

A polymer measuring cylinder  $10 \pm 0.5$  mL with an inner diameter of 13 mm by Brand GmbH (Wertheim, Germany) was used to assess the infinite bed porosity of the poly-disperse powders in a sufficiently wide container. While modules had aspect ratios as low as  $N_d = d_p/d_{\text{slit}} = 3.5$  the packed bed in the cylinder had  $N_d = d_p/d_t = 67$  for the larger particles and was considered infinite or with negligible influence of the confining walls. In terms of packed-bed height (length) modules and cylinder were considered infinitely extended with  $N_l = d_p/l \geq 309$ .

#### 4.3.2. Method

The finished modules were weighed with an ABS-N ABJ-NM lab scale by Kern und Sohn (Balingen, Germany). They were fixed to a lab stand and filled with powder with the help of a glass funnel. The powder level was checked visually with the help of an endoscopic camera and a smartphone camera. When required, the level was checked with the help of self-made polymer pieces and a micrometer. For resin samples, the powder level could be easily assessed visually. Modules were weighed at the proper fill level and again after emptying. For filling and emptying, they were repeatedly tapped onto a rigid surface from a height of approx. 5 cm.

Presumably during fabrication, the metallic walls of the empty module were deformed slightly and the volume had to be evaluated by filling the unit with liquid with known density and little surface tension. In all other cases,  $V_e$  was taken from CAD. Bed porosity was calculated with the formula presented in eq. (4.7) figuring in the apparent particle density  $\rho_{\text{app}}$  obtained from mercury intrusion porosimetry, appendix C.1.

$$\epsilon_{\text{bed}} = 1 - \frac{m_p / \rho_{\text{app}}}{V_e} \quad (4.7)$$

#### 4.3.3. Results

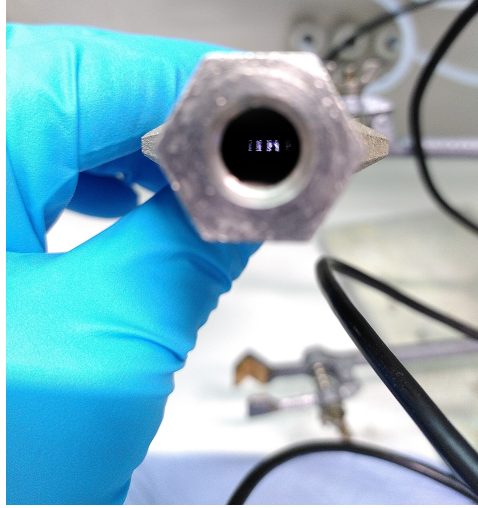
Fabrication of the designed modules with dense walls and a fluid-permeable region was successful; fig. 4.21 shows how light shone through the fluid-permeable region; however, no powder passed through it in these experiments. With the vat photo polymerization part with FGE structure, slight swelling with isopropanol was encountered for the first time due to the many thin walls [247].

Considering eqs. (C.1) to (C.3) in appendix C.1, apparent particle densities in table 4.11 were calculated from the results of mercury intrusion porosimetry. Factoring in a loose packed-bed porosity of  $\epsilon_{\text{bed}} = 0.4$  these particle densities could be transformed into loose bed densities (eq. (C.4)) which were in accordance with claims from the manufacturer of  $\rho_{\text{bed}} = 0.6$  to  $0.85 \text{ g mL}^{-1}$  [248]. With the values for  $\rho_{\text{app}}$ , bed porosities  $\rho_{\text{bed}}$  were calculated in the following.

**Table 4.11.:** Particle density and apparent particle density calculated from mercury intrusion porosimetry results.

$d_p / \mu\text{m}$	$\rho_{\text{app}} / \text{g mL}^{-1}$	$\rho_{\text{bed}} / \text{g mL}^{-1}$
83	1.388	0.833
194	1.231	0.739

Porosities obtained with the measuring cylinder could be considered as infinite porosities of the poly-disperse packing (column 2 in table 4.12) but differed from calculations (column 3 in table 4.12). The value used most often for this in literature was not correct for the fine particles used here apparently.



**Figure 4.21.:** Light shining through locally fluid-permeable bottom of a module.

Corrected values for  $\epsilon_{\text{bed,inf,md}}$  were calculated based on the observations in the measuring cylinder (column 4 in table 4.12).

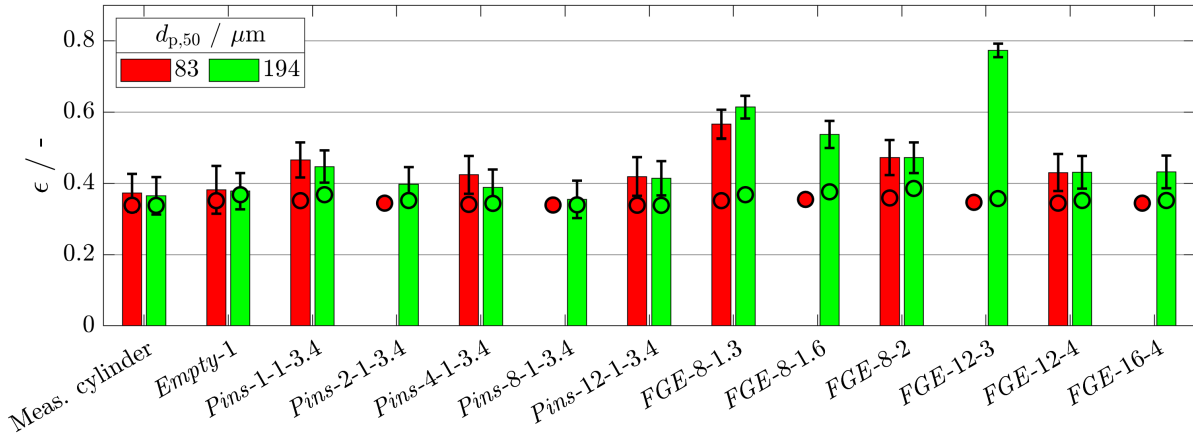
**Table 4.12.:** Calculated and measured infinite bed porosity of the poly-disperse alumina powders. Corrected infinite bed porosity of the mono-disperse packing was obtained by back calculating from the infinite bed porosity of the poly-disperse packing found in the measuring cylinder experiments.

$d_p / \mu\text{m}$	$\epsilon_{\text{bed,inf,pd}}$ calc. with $\epsilon_{\text{bed,inf,md}}=0.36 / -$	$\epsilon_{\text{bed,inf,pd}}$ meas. / -	$\epsilon_{\text{bed,inf,md}}$ corr. / -
83	0.337	0.373	0.399
194	0.336	0.365	0.393

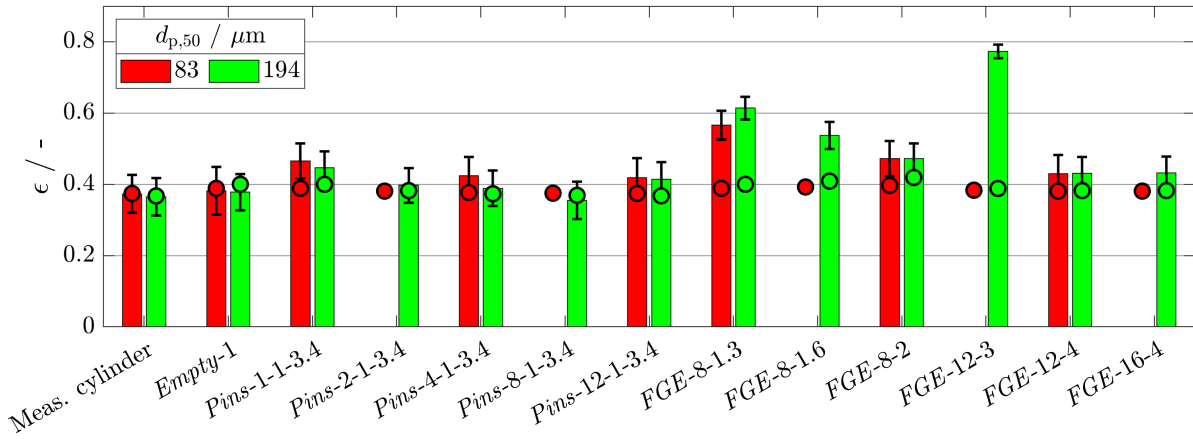
It was possible to load metal and polymer modules with particles. Visual inspection confirmed that the powder did not pass through the locally permeable region. The metal parts of which porosities were reported could be emptied of more than 99.9 % of the inserted powder. The obtained results for the bed porosity  $\epsilon_{\text{bed}}$  in metal modules, together with the calculated values based on  $\epsilon_{\text{bed,inf,md}}=0.36$ , are shown in fig. 4.22. The measured values were higher than expected suggesting that the corrected infinite bed porosity should be used. For pin-equipped modules the numbers in the designation signified  $\text{Pins}-d_{\text{slit}}-t_p-a$ , while they signified  $\text{FGE}-d_{\text{slit}}-d_{\text{FGE}}$  in FGE-equipped modules.

Figure 4.23 shows the measured and calculated bed porosities with the corrected values of  $\epsilon_{\text{bed,inf,md}}$  subjected to the formulas. Now, the experimental values were more conform with the calculations for most modules. The module *FGE-12-3* seemed to be an outlier. It seemed unlikely that this unit could be filled with powder so very less densely than the modules *FGE-12-4* and *FGE-8-2*, which were the modules with the next larger and smaller distance between confining walls, respectively. It could probably not be filled with particles all the way. Possible reasons include remaining metal powder or internal obstruction of some volume due to inexact fabrication. Apparently, the modules with FGE with smaller internal structures cannot be filled as densely as those with larger internal structures and those with pins, see for instance module *FGE-8-1.3*.

Figure 4.24 shows the samples that were printed in both metal and transparent resin. Packed-bed porosities seemed to be independent of the module material. For modules printed in resin uniform



**Figure 4.22.:** Bed porosity in laser-based powder bed fusion of metals (PBF-LB/M) samples assuming  $\epsilon_{\text{bed,inf,md}}=0.36$ . All module dimensions in mm. Circles refer to calculated values.



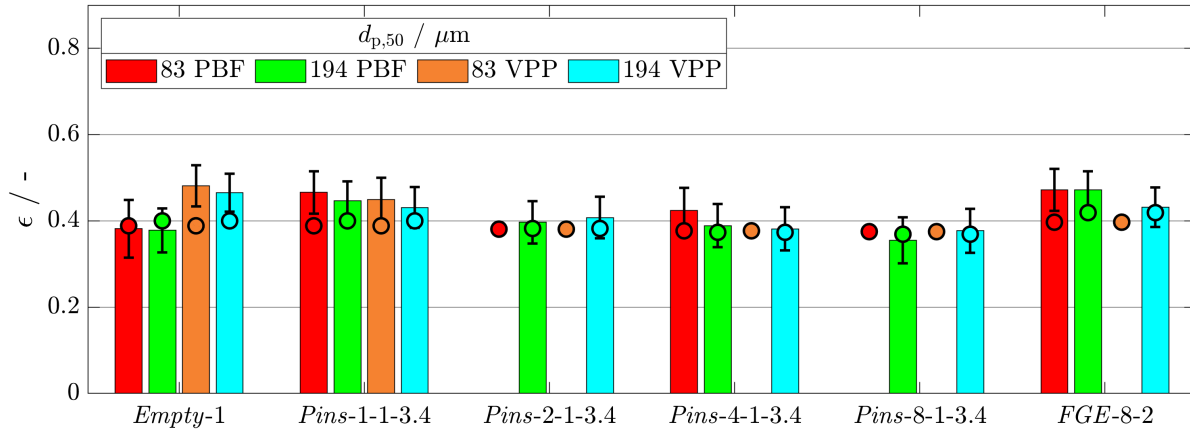
**Figure 4.23.:** Bed porosity in PBF-LB/M samples assuming  $\epsilon_{\text{bed,inf,md}}|_{83\mu\text{m}}=0.399$  and  $\epsilon_{\text{bed,inf,md}}|_{194\mu\text{m}}=0.393$  as obtained experimentally. All module dimensions in mm. Circles refer to calculated values.

filling with particles could be confirmed visually. This went nicely with measured and calculated bed porosities (with corrected assumptions) being close to each other.

Experimental error was taken into account and estimated with linear error propagation based on the following systematic errors: for particle mass  $\epsilon_{m_p}=0.2$  mg, for empty volume  $\epsilon_{V_e}=2$  % of value, and for apparent particle density  $\epsilon_{\rho_{\text{app}}}=0.1$  g mL<sup>-1</sup>. Estimated errors for the applied method were up to 13 % of the measured value of bed porosity. Typical bed porosities were 0.4 and errors 0.05. For This is an acceptable accuracy for an experiment with relatively low requirements in material and labor on the one hand and the the ability to test on realistic modules with complex shapes on the other hand. There were, however, significant deviation of measured from calculated bed porosities of up to 50 % (disregarding outliers).

#### 4.3.4. Interim Summary Particle Loading

Conducted experiments are highly relevant for micro process engineering having studied spherical  $\gamma$ -alumina with particle diameters as low as  $d_{50,3} = 83$   $\mu\text{m}$ . The most important observations are the following:



**Figure 4.24.:** Bed porosity in PBF-LB/M and vat photo polymerization samples assuming corrected infinite porosities. All module dimensions in mm. Circles refer to calculated values.

1. Measured bed porosities conformed well to calculations when the infinite bed porosity was selected for the exact size of the fine powder and internal structures were not too intricate, i.e.  $d_{FGE} \geq 2$  mm.
2. When experimental and calculated bed porosity concurred, visual inspection of resin units showed uniform particles distribution.
3. The bed porosity was independent of module material. This meant results could be transferred from either one of these materials to the other.

The extent to which these findings change when actual catalyst powder is used is not known. It can be assumed, though that loading of actual catalyst powder works similarly or even better Fischer-Tropsch synthesis (FTS) to higher apparent particle density. A possible method for loading particles is to suspend them in a solvent (water, alcohol) and inject the suspension into the container. Loading of FTS catalyst particles would also be possible with molten wax as matrix.

For the module *Pins-1-1-3.4* a bed porosity of  $\epsilon_{bed}=0.413$  was measured for Sasol Puralox SCCa-5/150. With the measured value of apparent particle density  $\rho_p=1.388 \text{ g mL}^{-1}$  and an assumed cobalt (Co) loading of 20 wt-% this results in a bed density of  $\rho_{bed}=0.978 \text{ g mL}^{-1}$ .

#### 4.4. Uniform Gas Distribution

In the following section, pertaining questions will be investigated: Is flow maldistribution an issue in the conceptualized device, and how is it influenced by the packed-bed pressure drop as well as the fluid-permeable region pressure drop? Computational Fluid Dynamics (CFD) simulations are a means to answer these question. But if chemical species and reactions are included, the number of independent variables increases significantly and with it the calculation effort [249]. In the presence of packed beds it has to be decided whether to handle particles discretely which is challenging in its own way (Ref. [250, 251]) or together with fluid as pseudo-homogeneous phase (Ref. [119]). Independent of the chemistry and physics considered in the simulation, for each new design a new mesh has to be generated in CFD. In this work a more convenient method is sought after. An algebraic model incorporating flow rates and CO conversion will be introduced in the following section.

#### 4.4.1. Model and Simulation

In this model pressure loss  $\Delta p$  and CO conversion  $X_{\text{CO}}$  are calculated for each channel. Pressure loss of a channel is proportional to the pertaining flow rate. If pressure loss in one channel increases the pertaining flow rate decreases, however. Mass continuity dictates that an equilibrium over all channels will be reached. Pressure loss across the frit is described by  $\Delta p = \dot{V} \cdot \eta \cdot l / (A_{\text{cross}} \cdot \Psi_V)$  (eq. (4.5)). It was added to the laminar portion of Ergun's equation (eq. (4.8)), resulting in  $\Delta p_{\text{total}}$  (eq. (4.9)). The equations demonstrate dependency of pressure loss on flow rate.

$$\Delta p = 150 \cdot u_0 \cdot \eta \cdot \frac{1}{d_p^2} \cdot \frac{(1 - \epsilon_{\text{bed}})^2}{\epsilon_{\text{bed}}^3} \cdot l_{\text{cat}} \quad (4.8)$$

$$\Delta p_{\text{total}} = \Delta p_{\text{bed}} + \Delta p_{\text{frit}} \quad (4.9)$$

The following assumptions were taken for all slits: constant fluid properties, identical particle size, identical frits, and identical cross-sectional area.  $\Delta p_{\text{total}}$  of slit  $i$  depended on the bed porosity and flow rate (eq. (4.10)). The conditions in eqs. (4.11) to (4.12) had to be fulfilled. A similar approach was pursued by Martin [252] to assess flow maldistribution in heat exchangers.

$$\Delta p_{\text{total},i} = f(\dot{V}_i, \epsilon_{\text{bed},i}) \quad (4.10)$$

$$\Delta p_{\text{total},i} = \Delta p_{\text{total},i+1} \forall i \in [1, n_{\text{slit}} - 1] \quad (4.11)$$

$$\dot{V}_{\text{total}} = \sum_1^{n_{\text{slit}}} \dot{V}_i \quad (4.12)$$

The above-mentioned equations form a system of algebraic equations that can be solved according to [253]. With the obtained equilibrium flow rate per each channel the pertaining CO conversion hence the overall  $X_{\text{CO}}$  of the multi-channel device is determined. The dependence of CO conversion per channel is given via  $X_{\text{CO}} = -340 - 2.5 \cdot SV_{\text{mod}} + 2 \cdot T$  (eq. (2.15)).

Gas distribution was modeled for theoretical lab-scale reactor design, one of which was fabricated and tested as described in chapter 5. The dimensions of these models were roughly the following:  $n_{\text{slit}}=2-8$ ,  $d_{\text{slit}}=1$  mm,  $w=40$  mm,  $l=55$  mm, and  $l_{\text{frit}}=2$  mm. With  $T=200-210$  °C,  $p=20$  bar,  $\text{H}_2/\text{CO}=2$ ,  $\text{N}_2/\text{CO}=0.1$ , and space velocity  $(SV)_{\text{mod}}=1.5-20 \text{ L}_\text{N} \text{ g}_{\text{cat}}^{-1} \text{ h}^{-1}$ , realistic operating conditions were chosen. The particles had the following properties in the model:  $d_p=100$  µm and  $\epsilon_{\text{bed}} \approx 0.5$ . The model describing CO conversion was the one from eq. (2.15).

The performance obtained under uniform flow distribution was calculated as reference. Non-uniform flow was created by variation of  $\epsilon_{\text{bed}}$  in the slits, which is an issue to be expected in micro-structured reactors (micro-structured reactor (MSR)). Different approaches for improving uniformity of flow and performance of the multi-channel device were simulated and their effects analyzed.

An object-oriented approach was taken to implement the necessary calculations in Matlab 2022b from Mathworks Inc. (Nattick, United States of America (USA)). A *class* is a definition of an *object* comprising *properties* and *methods* [254]. There was an object for each unique multichannel device and unique operating conditions. The object's properties stored information on device and conditions, such as

channel geometry and total flow rate, among others. Calculation of flow distribution and visualization of results were implemented as methods of the object for instance. The calculation method solved the equations from section 4.4.1 with help of the non-linear solver *fsolve* by Matlab. Said equation were stored as Matlab *functions* externally and called by the method.

#### 4.4.2. Results

The results of these calculations are shown in fig. 4.25. There the right-most bars of each group and the above number signify the ratio of the actual space time yield (*STY*) resulting from maldistribution to the maximum *STY* possible at uniform distribution. The other bars in each group signify the relative flow rate per each slit. The number above these bars is the standard deviation of the mean of said relative flow rates.

Comparing the simulation cases with optimal bed porosity  $\epsilon_{\text{bed}} \in [0.49, 0.51]$  (fig. 4.25a) and uneven bed porosity  $\epsilon_{\text{bed}} \in [0.45, 0.55]$  (fig. 4.25b), it was clear that the flow was less uniform, independent of the flow rate. The right-most bars of each group decreased steeply with increasing flow rate, meaning that the performance was impacted negatively by flow maldistributions, especially at high flow rates. The remaining simulations all showed possible strategies for improving flow uniformity and device performance above this.

Figure 4.25c was obtained from simulating a case unwanted in a real reactor. While the bed porosity was non-uniform, the catalyst mass was uniform across the slits. Translated to the real world this would mean regions inside the reaction slits without catalyst, meaning particles could potentially move and the flow pattern would be altered. However, under this assumption, the model showed a lower decrease in relative productivity compared to the case before.

In fig. 4.25d, the number of slits and the capacity were doubled. Under otherwise constant conditions the simulation with  $n_{\text{slit}}=4$  showed a way more uniform flow and higher relative productivity compared to case (b).

The same can be said for fig. 4.25e with  $n_{\text{slit}}=8$ . Up to  $SV_{\text{mod}}=6 \text{ L}_N \text{ g}_{\text{cat}}^{-1} \text{ h}^{-1}$  the relative *STY* is only 5 % lower compared to the optimal case.

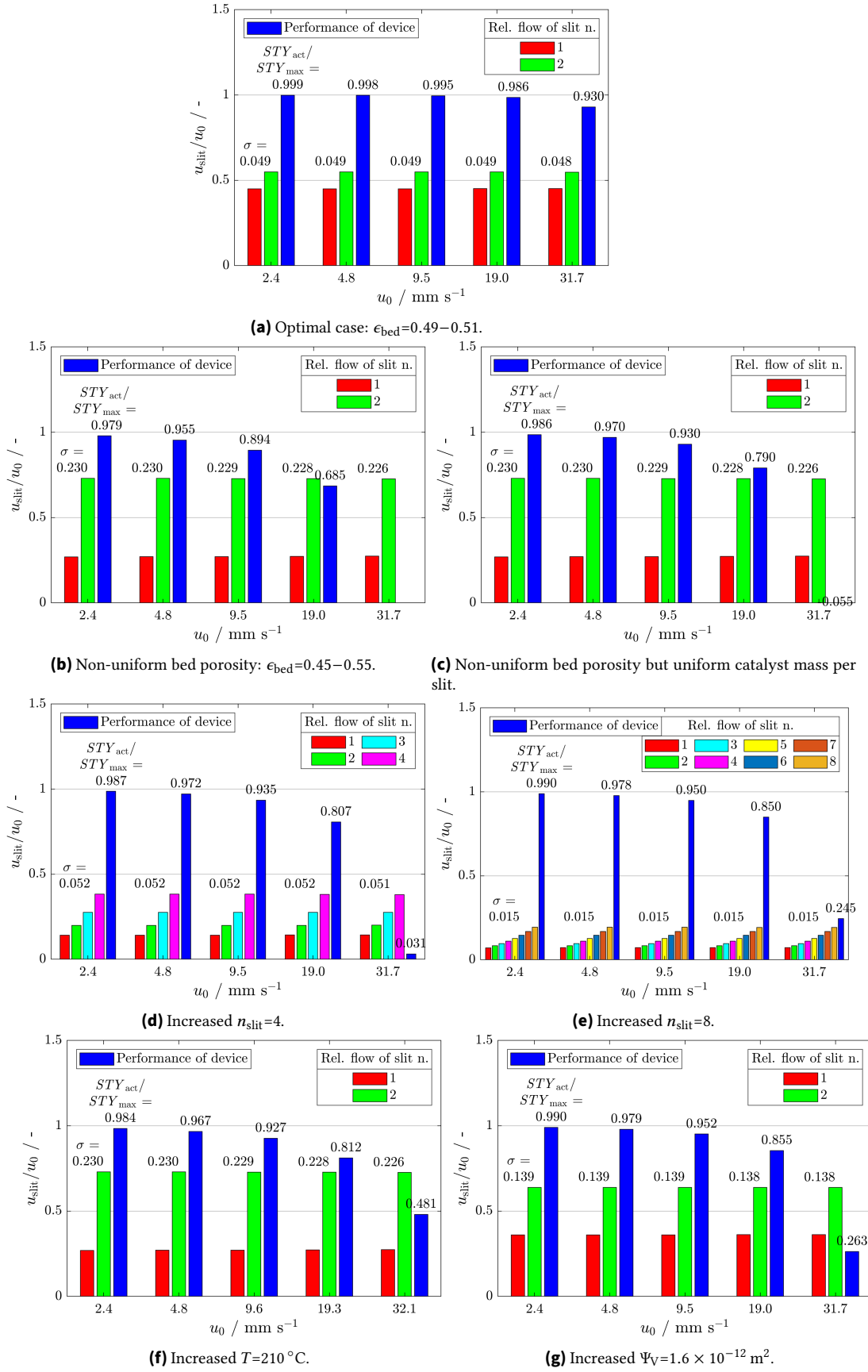
Figure 4.25f highlights that the performance loss was less pronounced at higher temperatures, even when the flow was not distributed better. The risk of a reactor under-performing Fischer-Tropsch synthesis (FTS) to maldistributions was more pronounced at lower values of  $T$  and  $n_{\text{slit}}$ .

In fig. 4.25g the artificial pressure drop was employed. In this case the viscous permeability coefficient of the simulation was set two orders of magnitude below the default value. Among all measures this gave the best results with regard to *STY* up to a space velocity of  $SV_{\text{mod}}=12 \text{ L}_N \text{ g}_{\text{cat}}^{-1} \text{ h}^{-1}$ .

When the permeability of the frit was low enough and imposing a significant pressure drop on all channels, the flow was distributed evenly. 'Significant' in this case meant above the pressure drop of the uneven packed bed creating the non-uniformity. This required the viscous permeability to be  $\Psi_V \leq 1.6 \times 10^{-12} \text{ m}^2$ . However, the lowest permeability that could be achieved experimentally with frits in section 4.2 was  $\Psi_V=1.6 \times 10^{-10} \text{ m}^2$ .

Design could be adapted to feature frits with lower hatch distance ( $HD$ ) and, in turn,  $\epsilon_s$ , or to have layers where frits are oriented differently, or simply with a higher length  $l_{\text{frit}}$ .

With justifiable simplifications the simulations made in this section show the influencing factors on gas distribution as well as the effects of it being non-uniform. To expand the model the non-linear



**Figure 4.25.:** Results of gas distribution simulations. Conditions if not indicated otherwise:  $T=200^\circ\text{C}$ ,  $p=20 \text{ bar}$ ,  $\text{H}_2/\text{CO}=2$ ,  $\epsilon_{\text{bed}}=0.45-0.55$ ,  $\Psi_V=1.6 \times 10^{-10} \text{ m}^2$ , and  $n_{\text{slit}}=2$ .



terms for the pressure-loss equations for frit (eq. (4.5), [255]) and packed bed (eq. (4.8), [256]) could be included. Another possible expansion would be fluid properties that vary with temperature and composition according to Poling et al. [257]. Furthermore, a model of  $n$  slits as applied here could be combined with a simulation of the reactor inlet flow. The inlet flow either passing a distributor ([129, 258]) or an inlet plenum ([258]), of course, would have to be simulated with CFD. Via an appropriate interface the flow rate and pressure of the incoming flow could be combined with the algebraic model proposed here. This would allow to assess gas distribution on a reactor level even more thoroughly.

#### 4.4.3. Interim Summary Gas Distribution

The model is suitable for describing flow distribution in multi-channel devices and the implications on overall CO conversion. A simulation can be solved with a solver for non-linear algebraic equations. The simulations showed that flow maldistribution has a negative impact on reactor productivity. This was pronounced in devices with fewer slits, at lower operating temperatures, and at highest flow rates. An efficient measure in alleviating maldistribution and related underperformance is introducing an artificial pressure drop in the simulation. This had to be constant for all slits and higher than the pressure drop causing the maldistribution. In reality, this could be achieved with adequately designed fluid-permeable regions as per section 4.2 or with long reaction channels with small and uniformly densely-packed particles. The simulations demonstrated that uniform fluid distribution is likely, when bed porosity is uniform over all slits.

Obviously, this increased the total pressure drop over the device from 80–1092 Pa to 155–2091 Pa at  $SV_{\text{mod}} = 1.5\text{--}20 \text{ L}_N \text{ g}_{\text{cat}}^{-1} \text{ h}^{-1}$ . However, the maximum  $STY_{\text{mod}}$ , which was in both cases achieved at  $12 \text{ L}_N \text{ g}_{\text{cat}}^{-1} \text{ h}^{-1}$ , increased from 0.399 to  $0.498 \text{ g}_{\text{C5+}} \text{ g}_{\text{cat}}^{-1} \text{ h}^{-1}$ .

The approach with a artificial pressure drop made with locally permeable regions could be applied to multi-channel systems with evaporation cooling as well. It is a well known problem that non uniform evaporation in this case is a self-enforcing phenomenon [258]. This could be ameliorated with the structures from section 4.2 without further modification as water has a higher viscosity and therefore pressure drop as gas.

### 4.5. Heat Transfer

The theory of heat transfer in micro-structured reactors (MSRs) is vast and has been introduced in section 2.4. Two concepts which are related to heat transfer calculation and experimental evaluation will be presented here: calculation of thermo-physical quantities and calculation of the influence of internal structures on the heat transfer coefficient. Consequently, the test rig is described (section 4.5.1). In section 4.5.2, the experimental procedure, modules used, and the evaluation are provided. The results shed light on heat transfer enhancement with fluid guiding elements (FGEs) as well as heat transfer in micro-packed beds and in micro-structured devices with evaporation cooling (section 4.5.3).

**Thermo-Physical Quantities** Thermo-physical quantities like specific heat capacity, thermal conductivity, and dynamic viscosity are dependent on  $p$ ,  $T$ , and medium composition. They were calculated according to VDI Heat Atlas chap. D3 [7] with the help of an object-oriented Matlab code [259]. An *object* is defined by/is an instance of a *class* and comprises *properties* and *methods* [254]. An object of the class *xMATERIAL* contained methods for calculation of pure substances' thermo-physical quantities, e.g. the molar heat capacity in eq. (4.13). An object of the class *xMATERIAL* contained properties encoding

parameters for these calculations, e.g. the parameters  $A$  to  $G$  for the calculation of  $\tilde{c}_p$  of  $N_2$  as depicted in table 4.13.

$$\frac{\tilde{c}_p}{\tilde{R}} = B + (C - B) \left( \frac{T}{A + T} \right)^2 \left[ 1 - \frac{A}{A + T} \left( D + E \frac{A}{A + T} + F \left( \frac{T}{A + T} \right)^2 + G \left( \frac{T}{A + T} \right)^3 \right) \right] \quad (4.13)$$

**Table 4.13.:** Parameters for the calculation of  $c_p$  of  $N_2$ .

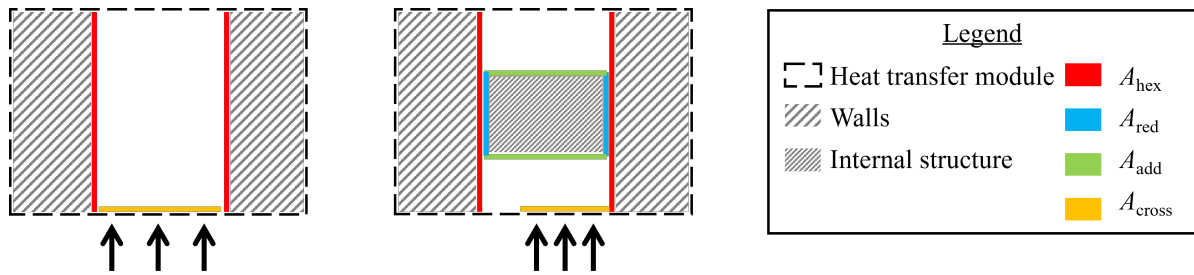
Parameter	$A$	$B$	$C$	$D$	$E$	$F$	$G$
Value	432.2027	3.516	2.8021	-4.1924	42.0153	-114.25	111.1019

An object of class *MIXTURE* contained methods calculating mixture rules, e.g. the molar heat capacity of a mixture in eq. (4.14). An object of class *MIXTURE* contained properties which were instances of class *xMATERIAL* for calculating the pure-component quantity and the medium composition for calculating the mixture quantity.

$$\tilde{c}_{p,\text{mix}} = \sum_i y_i \cdot \tilde{c}_{p,i} \quad (4.14)$$

Thermo-physical quantities of boiling liquid and condensing vapor are denoted by one (') or two apostrophes (''). For calculation of the evaporation heat-transfer coefficient, they were looked up in VDI Heat Atlas chap. D2 [7]. The compressibility factor of gaseous  $N_2$  under the conditions investigated was negligible; the Mach number was well below 0.3. Hence, there was no friction-induced heating considered. Some details on the following calculations are provided in appendix D.

**One-Phase Heat Transfer with Internal Structures** Formulas for convective heat transfer in planar slits with and without packed bed were presented in section 2.4. However, these formulas do not consider internal structures as intended for this modular concept. Internal structures reduced the heat exchange area of the wall  $A_{\text{hex}}$  by  $A_{\text{red}}$  (fig. 4.26). The surface of the structures added  $A_{\text{add}}$  to the heat exchange area. For all structures considered in these experiments,  $A_{\text{add}} > A_{\text{red}}$ . Internal structures also reduced the cross-sectional area of the flow, thereby increasing its velocity.



**Figure 4.26.:** Schematic representation of heat transfer modules without and with internal structures. Note internal structure also reduced cross-sectional area.

For a single unit of the internal structures pins, fins, and lattice, these surrogates were chosen respectively: overflow pin, plane, and inclined pin. Their heat transfer coefficients were calculated as per chapters G4 and G6 in Ref. [7]. In the following four equations,  $l$  is the length of one overflow unit.

This is either a fin's length or a pin's or lattice strut's half circumference. Reynolds number is calculated according to eq. (4.15). In any case  $\alpha$  of the single unit is obtained via eq. (4.16).

$$\text{Re}_l = \frac{u_0 \cdot l}{(1 - \varphi) \cdot \nu} \quad (4.15)$$

$$\alpha_{\text{single}} = \frac{\text{Nu} \cdot \lambda}{l} \quad (4.16)$$

According to VDI G4, a parallel flow along a plate is laminar up to a critical value of the Reynolds number of  $10^5$ , which was always the case in this work. Nusselt number is given in eq. (4.17).

$$\text{Nu}_{\text{lam}} = 0.664 \sqrt{\text{Re}_l} \sqrt[3]{\text{Pr}} \quad (4.17)$$

VDI G6 states that above equation is almost identical for cross-flow around single tubes, wires, and profiled cylinders (eq. (4.18)).

$$\text{Nu}_{\text{lam}} = 0.3 + 0.664 \sqrt{\text{Re}_l} \sqrt[3]{\text{Pr}} \quad (4.18)$$

For an inclination of wire/tube/profiled cylinder of  $45^\circ$ , Nu has to be reduced according to eq. (4.19).

$$\text{Nu}_{\text{lam},45} = 0.8 \cdot \left( 0.3 + 0.664 \sqrt{\text{Re}_l} \sqrt[3]{\text{Pr}} \right) \quad (4.19)$$

According to Ref. [7], the heat transfer coefficient with the influence of internal structures (also referred to as 'ribs') can be calculated according to eq. (4.20).

$$\alpha = \alpha_{\text{slit}} \cdot \left( 1 - \frac{A_{\text{red}}}{A_{\text{hex}}} \right) + \alpha_{\text{single}} \cdot \frac{A_{\text{add}}}{A_{\text{hex}}} \cdot \eta \quad (4.20)$$

Values of  $\alpha_{\text{single}}$  for single units of the respective internal structures pins, fins, and lattice were in the range of  $0.3 \cdot \alpha_{\text{slit}}$  to  $4 \cdot \alpha_{\text{slit}}$ . The internal structure's effect on the overall heat transfer coefficient is dependent on the type and size, the relationship of added to reduced area, the flow velocity, and the overall heat transfer situation. A positive contribution on the heat transfer coefficient was expected for the following situations:

- low size of internal structures,
- high mass flux  $G$ ,
- the whole internal structure being at heating temperature which is only valid as long as the conductive heat transfer rate inside the structure is higher than the heat transfer rate to the fluid (so-called rib efficiency factor  $\eta=1$ ), and
- the added surface area of the internal structures being large enough compared to the reduced surface area of the channel walls.

The rib efficiency factor of the internal structures under investigation was not documented in literature [7]. Therefore,  $\eta$  was fitted to experimental results.

**Calculation of Heat Transfer Coefficient** Values for the heat-transfer coefficient  $\alpha$  for different conditions were calculated, table 4.14. These conditions include realistic operating conditions for an MSR Fischer-Tropsch synthesis (FTS) reactor as well as conditions prevalent in the heat-transfer experiments in this section. Values in this table do not consider the effect of internal structures; this will be discussed exclusively for the heat transfer results obtained with water. Among convective cooling with water and thermal oil, the maximum value was  $\alpha_c=2682 \text{ W m}^{-2} \text{ K}^{-1}$  for the former. The heat transfer coefficient within the reaction zone was  $\alpha_r=2916\text{--}5641 \text{ W m}^{-2} \text{ K}^{-1}$ , depending on the particle size. Thermal conductivity of 316L steel is comparatively low [178], but with the low wall thickness, heat transfer was still high (eq. (4.21)) [7, 104]. Except for that, the heat-transfer coefficient of evaporation cooling was well above the others. Even when only the convective component was considered, it took a value of  $\alpha_{\text{evap}}=16,346 \text{ W m}^{-2} \text{ K}^{-1}$  averaged over a vapor fraction of  $\dot{x}=0$  to 0.5.

$$\frac{\lambda_s}{t_w} = \frac{16.3 \text{ W m}^{-1} \text{ K}^{-1}}{1 \text{ mm}} = 1.63 \times 10^4 \text{ W m}^{-2} \text{ K}^{-1} \quad (4.21)$$

The lengths up to which hydrodynamic and thermal development is reached were calculated, too. It was adopted from literature that flow through packed beds and flow of evaporating water were developed immediately. By calculation, flows of  $\text{N}_2$ , non-evaporating water, and thermal oil (chapter 5) were strongly developing. While the hydrodynamic development sometimes happened within the module length, the thermal development never did, according to calculations. Developing flows are supposed to have higher heat transfer coefficients than similar developed flows. Longitudinal conduction parameter (*LCP*) is only significant for the reaction side operated under reaction conditions. Under testing conditions with  $\text{N}_2$  it was not significant for the reaction side, neither was it for the cooling side under realistic or testing conditions.

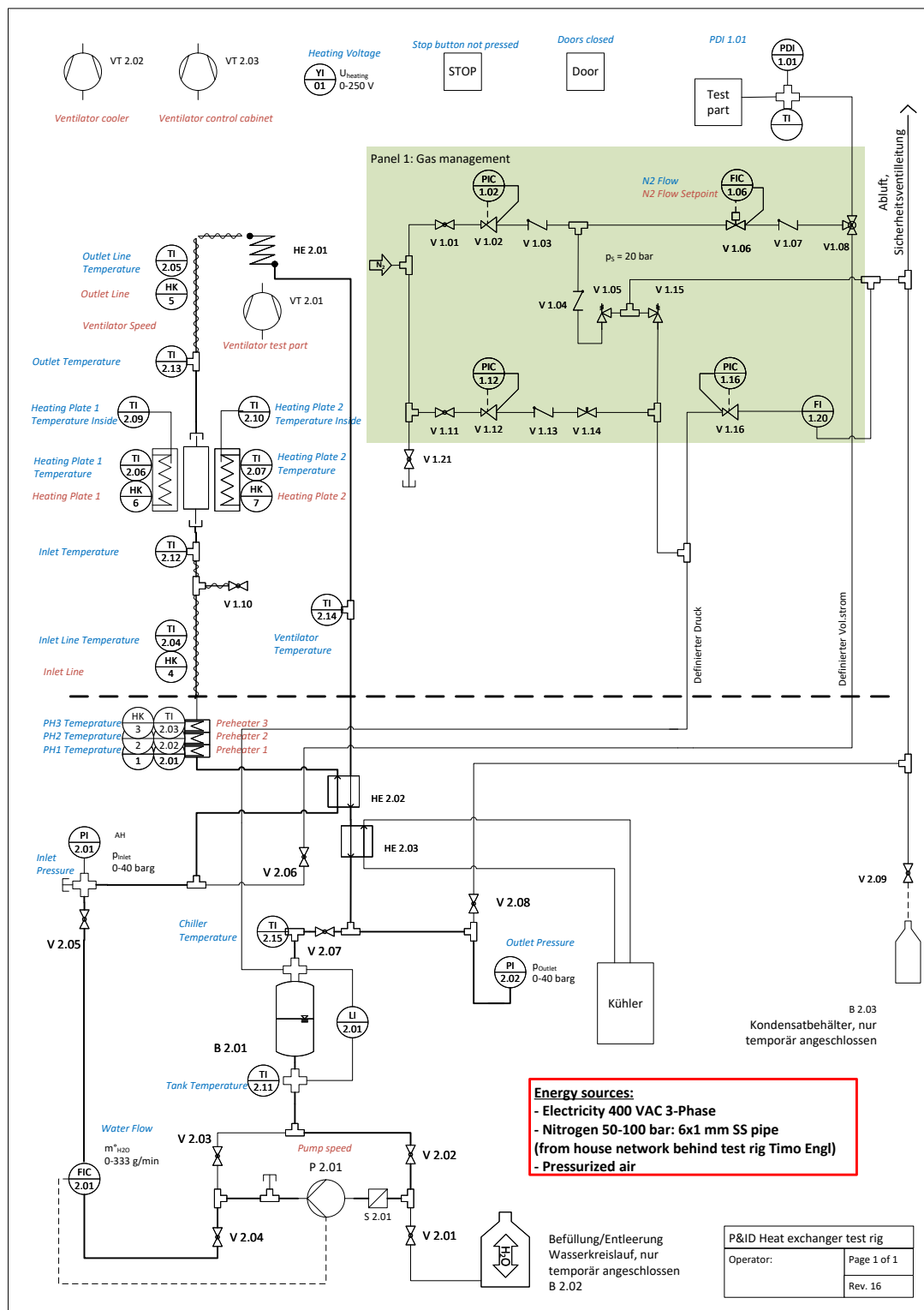
As mentioned in section 2.4, cooling consists of three main steps, in consecutive order [134]: convection in reaction zone, conduction in the separating wall, and convection in cooling zone. Based on the calculation results in table 4.14, the slowest cooling step is either the reaction zone or the cooling zone, depending on the exact operating conditions assumed for calculation, but never wall thermal conductivity. Theoretical calculations for macroscopic devices are not necessarily valid for the dimensions of packed micro-structured reactors [7]. Biffar et al. [136] suggested for the first time a calculation method for  $\alpha$  in FGE. This had been validated by simulations and should also be verified in practice. For these two reasons, heat transfer was determined experimentally for both the reaction and cooling side. Therefore, a new test rig, especially suited for partial evaporation cooling, was designed and constructed.

**Table 4.14.:** Values of heat transfer coefficients for rate determining step estimation and underlying assumptions. It was assumed that the slit was without internal structures ( $\varphi=0$ ),  $d_{\text{slit}}, t_w=1$  mm, and  $l=55$  to  $60$  mm, if not otherwise mentioned. With eq. (2.15),  $T=213$  °C and  $SV_{\text{mod}}=6 \text{ L}_N \text{ g}_{\text{cat}}^{-1} \text{ h}^{-1}$  result in  $X_{\text{CO}}=70$  %.  $\lambda_p=1 \text{ W m}^{-1} \text{ K}^{-1}$  [260].

Chapter in [7], according to which calculation was done and additional assumptions	$p$ / barg	$T$ / °C	$u_0$ / $\text{m s}^{-1}$	$\alpha$ / $\text{W m}^{-2} \text{ K}^{-1}$	$LCP$ / -	$l_{\text{dev,h}}$ / mm	$l_{\text{dev,t}}$ / mm
Syngas with alumina particles							
M7; $d_p=194 \mu\text{m}$ ; $\epsilon_{\text{bed}}=0.577$	20	213	0.007	$\alpha_r = 2916$	6.16	0	0
M7; $d_p=83 \mu\text{m}$ ; $\epsilon_{\text{bed}}=0.492$	20	213	0.007	$\alpha_r = 5641$	6.16	0	0
Syngas							
G2 if $\text{Re}<2300$ ; else G1 equation for turbulent pipe flow with adjusted characteristic length, when the resulting value was higher than G2	20	213	0.007	$\alpha_r = 367$	6.16	0	1
$\text{N}_2$ with alumina particles $d_{\text{slit}}=4$ mm							
M7; $d_p=83 \mu\text{m}$ ; $\epsilon_{\text{bed}}=0.492$	20	200	0.367	$\alpha_r = 3364$	0.02	0	0
M7; $d_p=194 \mu\text{m}$ ; $\epsilon_{\text{bed}}=0.577$	20	200	0.367	$\alpha_r = 1809$	0.02	0	0
M7; $d_p=194 \mu\text{m}$ ; $\epsilon_{\text{bed}}=0.577$	20	300	0.444	$\alpha_r = 1973$	0.02	0	0
$\text{N}_2$ $d_{\text{slit}}=4$ mm							
G2 if $\text{Re}<2300$ ; ...	20	200	0.367	$\alpha_r = 61$	0.02	156	3115
316L							
D6.1	-	200	-	$\frac{\lambda_s}{t_w} = 16,361$	-	-	-
Water							
G1/G2	30	200	0.051	$\alpha_c = 2682$	0	17	393
G1/G2	20	200	0.083	$\alpha_c = 2820$	0	27	641
H3.4; partial evaporation	15	200	0.003	$\alpha_{\text{evap}} = 16,346$	-	-	-
Thermal oil							
G1/G2	0	200	0.099	$\alpha_c = 578$	0	6	2423
G1/G2	0	200	0.986	$\alpha_c = 1731$	0	61	24,228

#### 4.5.1. Test Rig

A test rig for determining heat transfer coefficients was designed and built as shown in fig. 4.27. The test rig hardware was divided into two groups: 1. process engineering hardware, and 2. electrical, measuring, steering, and regulating hardware. The first included pressure controllers, pressure gauges, vessels, pump, filters, piping, and instrumentation. The second included sensors, heaters, cables, and the complete measuring and control system. For some items, a clear distinction between group one or two could not be made. The hardware was installed in a self-contained structure made of aluminum profiles and acrylic glass (fig. 4.28). The test rig was continuously supplied with internet, power, nitrogen ( $\text{N}_2$ ), and pressurized air, and with de-ionized water when necessary.



**Figure 4.27.:** Piping and instrumentation diagram (P&ID) of test rig. Meaning of symbols can be found in Ref. [261].



(a) Left side containing water circuit and (b) Right side containing N<sub>2</sub> supply, system pressure control, and mass-flow controller for pressure difference testing in section 4.2.

**Figure 4.28.:** Photos of test rig.

Heating plates (HPs), manufactured by Institute for Micro Process Engineering (IMVT) workshop, were used to heat modules from the outside. Consisting of copper (Cu), each HP exhibited excellent heat conduction and was considered isothermal. Its temperature was measured with an inserted thermocouple and controlled via inserted heating cartridges. The measuring and control system's purpose was data acquisition and control of the test rig. The software LabView 2022 by National Instruments (NI) (Austin, TX, USA) was running subroutines on a Microsoft Windows 10 PC and on a NI cRIO, the latter being equipped with digital and analogue input and output modules. The heating power was controlled via opto-coupler-type solid state relays. The LabView programming and the measuring and control system concept were based on the work of Kant [262]. The control cabinet was assembled by Bilfinger Life Science Automation GmbH (Flensburg, Germany). Prior to testing, modules passed the leakage test. For insertion of thermocouples and heating cartridges, thermal paste was applied. An array of insulation plates, HP, and module was sandwiched between the brackets of a vise. The array and pipes were subsequently insulated with alu-faced pipe sections and slabs. Details on all materials used can be found in appendix C.

#### 4.5.2. Method

It can be confirmed that the heat transfer rate is independent of the direction of heat flow, except for the temperature dependency of material properties [134]. In the experiments, heat was going into the flow within the (particle-loaded) module. The walls of the slit module were kept at constant wall temperature  $T_w$  above the fluid temperature. Error was estimated, based on the systematic error of the directly measured values and the dimensions of the modules. This was facilitated by automating the experiment procedure and the data logging via comma-separated value files edited/read with Excel. The hold-time of a specific set-point was typically 10 min.

Experiments with water and nitrogen were conducted separately, the former relating more to cooling zone and the latter more to reaction zone. Hence, methods and results have been split up. Experiments with water were conducted first. They provided interesting learnings, leading to slightly adapted

experimental design for experiments with nitrogen. After the general procedure is presented, however, it is logical to first explain method and evaluation of experiments with nitrogen, then water.

#### 4.5.2.1. Nitrogen

The geometry of modules for these experiments was chosen based on standard dimensions of laboratory MSR:  $d=1-16$  mm,  $w=20-38$  mm, and  $l=38-60$  mm. Modules with pins and FGE on the inside were used, so the modules were partially the same pieces as used for section 4.1 and section 4.3. They incorporated fluid-permeable regions as in section 4.2. Internal pins were placed in hexagonal arrangement. Wall thickness was  $t_w=0.8$  mm. The gas flowing through the packed slit from bottom to top was  $N_2$  with  $T_{in} \approx 30$  °C. HPs were set to  $T_{HP}=400$  °C. The mass flow was adjusted to result in a mass flux of  $G \approx 0.5-4$  kg m<sup>-2</sup> s<sup>-1</sup> without particles (eq. (4.22)). The experiments were carried out at a pressure of  $p_{out} \approx 20$  bar. The conditions were chosen in order to obtain a meaningful measurement.

$$G = \frac{\dot{m}}{A_{cross}} \quad (4.22)$$

The directly measured values were  $\dot{m}$ ,  $T_{in}$ ,  $T_{out}$ ,  $p_{in}$ , and  $p_{out}$ . From these, the logarithmic mean temperature difference  $\Delta T_{LM}$  was calculated according to eq. (4.23), and the heat flow  $\dot{Q}$  was calculated according to eq. (4.24). Heat flux  $\dot{q}$  and heat transmission coefficient  $k$  are given in eqs. (4.25) to (4.26). The sought-after heat transfer coefficient  $\alpha$  is calculated according to eq. (4.27).

$$\Delta T_{LM} = \frac{T_{HP} - T_{in} - (T_{HP} - T_{out})}{\ln \left( \frac{T_{HP} - T_{in}}{T_{HP} - T_{out}} \right)} \quad (4.23)$$

$$\dot{Q} = \Delta \dot{H} = \dot{m} \cdot c_p \cdot (T_{out} - T_{in}) \quad (4.24)$$

$$\dot{q} = \frac{\dot{Q}}{A_{hex}} \quad (4.25)$$

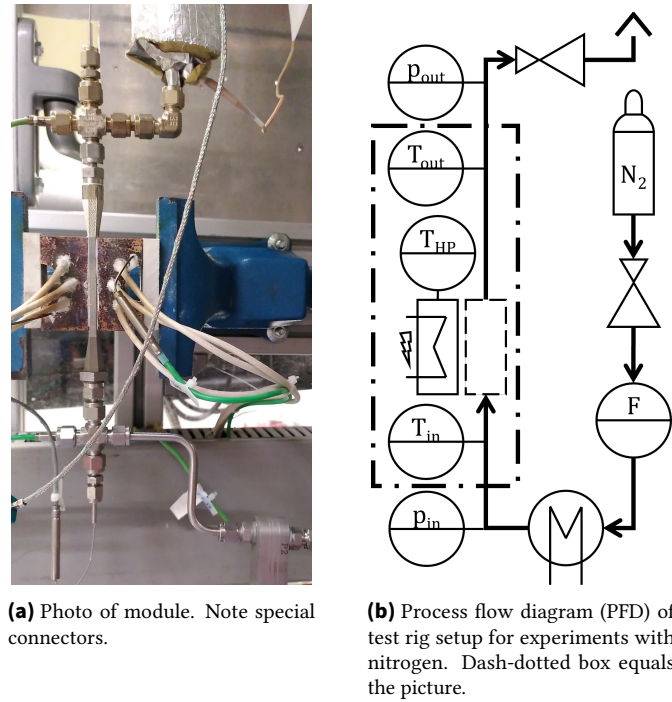
$$k = \frac{\dot{q}}{\Delta T_{LM}} \quad (4.26)$$

$$\alpha = \left( \frac{1}{k} - \frac{t_w}{\lambda_s} \right)^{-1} \quad (4.27)$$

When applicable, modules were filled with powder in the planar section. The remaining conical section was filled with quartz wool 9 µm art.-n. 24950.152 by VWR International GmbH (Darmstadt, Germany). The bottom end was sealed with a metal-bonded rubber gasket DR 18 HD ES by Landefeld GmbH (Kassel, Germany), while the top end was sealed with a flat copper gasket CU-2-RP-2 by Swagelok (Solon, OH, USA). All Swagelok parts were ordered from Swagelok Stuttgart B.E.S.T. Fluidsysteme GmbH (Reutlingen, Germany).

It is worth mentioning that the inlet and outlet temperatures were measured very close to the heat transfer area, right at the narrow end of the conical sections; hence, no heat loss was expected. This had been learned from experiments with water and was applied to experiments with nitrogen. The special connectors used were SS-6-MTA-1-2RS by Swagelok and can be seen in fig. 4.29a. The most relevant section of the test-rig for these experiments is depicted in fig. 4.29b.





**Figure 4.29.:** Picture of module and process flow diagram (PFD) of heat transfer testing with nitrogen.

#### 4.5.2.2. Water

Modules for these experiments incorporated pins, fins, and lattice, and had the following dimensions:  $d=1$  mm,  $w=38$  mm, and  $l=60$  mm. The modules were partially the same pieces as used for mechanical stability experimentation (section 4.1). Wall thickness was  $t_w=0.6-1$  mm. Pins were in hexagonal arrangement in all but one module, where they were in quadratic arrangement (called 'regular'). Width and length were exchanged for the pin-containing module (called 'transposed').

Both ends of a module were sealed with metal-bonded rubber gaskets (DR 18 HD ES by Landefeld) and connectors Swagelok SS-6M0-1-2RS. For these experiments, inlet and outlet temperatures were measured with sheathed thermocouples, sealed via the shell, which were immersed into the fluid via a T-piece, (fig. 4.39 middle). Even with optimal design, a considerable distance remained between thermocouple tip and module inlet/outlet (fig. 4.30a).

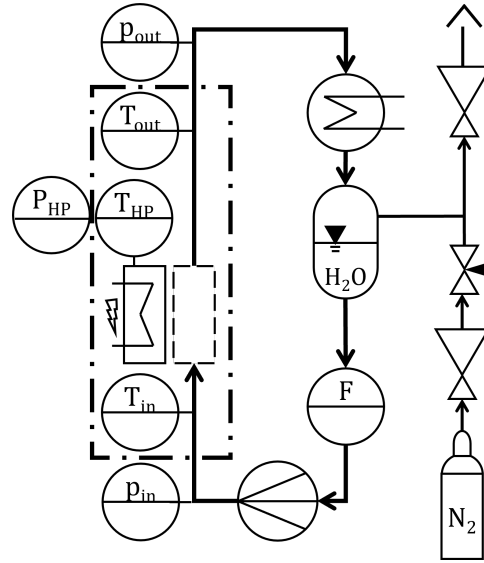
Experiments were conducted with multiple variations: for one-phase heat transfer, the inlet temperature was varied between  $T_{in}=150-195$  °C and the mass flux between  $G=10-100$  kg m<sup>-2</sup> s<sup>-1</sup>. For one-phase heat transfer, the system pressure, expressed as the outlet pressure, was kept at  $p_{out} \geq 20$  bar. This was above the vapor pressure  $p_{boil}=15.6$  bar at  $T_{HP}=200$  °C.

For evaporation-cooling experiments, the boiling temperature was controlled via the system pressure. The system pressure was controlled by a cushion of gaseous nitrogen above the water in the vessel of the water circuit, as can be seen in the relevant section of the test rig in fig. 4.30b. Flow of N<sub>2</sub> from the line to the vessel was limited with the help of a needle valve. The pressure was controlled with a manual backpressure valve KBP1J0G4A5A20000 by Swagelok connecting the vessel to the vent.

A system pressure of  $p_{out}=14.0$  bar=13 barg corresponded to  $T_{boil}=195$  °C and  $T_{in}=185$  °C. The water was entering with a subcooling of  $T_{in}=T_{boil}-10$  K to avoid boiling before the actual heat transfer area. For the calculation of  $\alpha_{evap}$  only the heat of evaporation was considered.



(a) Photo of module. Note distance between thermocouples (in T-pieces) and inlet/outlet.



(b) PFD of test rig setup for experiments with water. Dash-dotted box equals the picture. Thick lines are water, thin lines nitrogen.

**Figure 4.30.:** Picture of module and PFD of heat transfer testing with water.

Inlet temperature ranged from  $T_{in}=170-185\text{ }^{\circ}\text{C}$ . Mass flux was kept constant at  $G\approx 13\text{ kg m}^{-2}\text{ s}^{-1}$ . Heat flow was calculated according to eq. (4.29), where  $\dot{Q}_{loss}$  was derived from a one-phase heat transfer experiment without changing the test rig according to eq. (4.28). The resistance was corrected for the actual temperature of the heating element. The relevant temperature difference was considered to be  $\Delta T_{(LM)}=T_{HP}-T_{boil}$ . In two-phase heat transfer calculation, the latent enthalpy change was considered as the relevant heat flow. Latent enthalpy change  $\dot{H}_{latent}$  and vapor fraction  $\dot{x}$  were calculated according to eqs. (4.29) to (4.30).

$$\dot{Q}_{loss} = P_{HP} - \Delta\dot{H} \quad (4.28)$$

$$\dot{Q} = \Delta\dot{H}_{latent} = P_{HP} - \dot{Q}_{loss} - \Delta\dot{H} \quad (4.29)$$

$$\dot{x} = \frac{\dot{m}_{vapor}}{\dot{m}} = \frac{\dot{Q}/h_{evap}}{\dot{m}} \quad (4.30)$$

### 4.5.3. Results

The results are reported below, again in chronological order, starting with those for water and ending with those for nitrogen.

#### 4.5.3.1. Heat Transfer Results Water

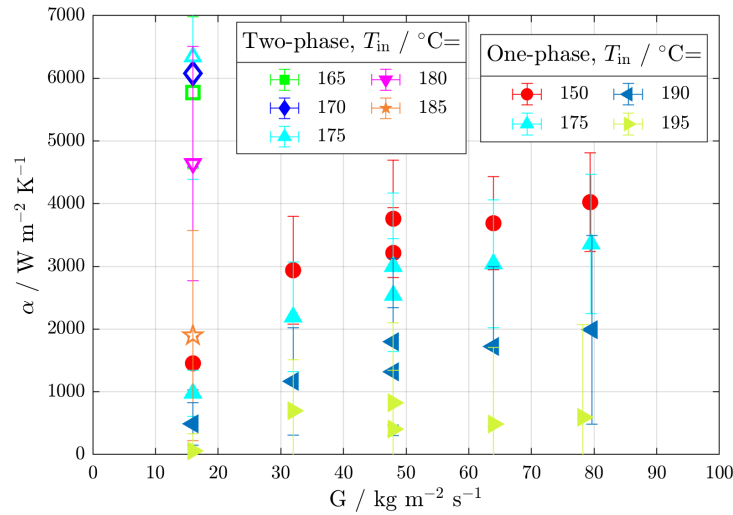
One-phase heat transfer with water presented the challenge that the outlet temperature took the value of  $T_{out}\approx 195\text{ }^{\circ}\text{C}$  at most set points, except those with lowest inlet temperature and highest mass flow. It was concluded that the fluid temperature reached the heating plate temperature  $T_{HP}=200\text{ }^{\circ}\text{C}$  somewhere inside the module and subsequently cooled down  $\approx 5\text{ K}$  due to heat loss before the temperature was

measured at the outlet thermocouple. The fluid temperature may possibly have reached the heating temperature. Should this have been the case, the calculated heat-transfer coefficient  $\alpha$  would only have represented the minimum value, the reason being that the area needed for the fluid to reach heating temperature was not known, but  $\leq A_{\text{hex}}$ . This issue was addressed with two measures during heat-transfer testing with nitrogen:

1. set points were chosen for  $T_{\text{out}}$  to be minimum preferably  $T_{\text{out}} < T_{\text{HP}} - 15 \text{ K}$ , and
2. thermocouples were moved closer to the heat-transfer area with the help of special connectors.

The challenge was visible in the results for the module with pins with  $t_p=0.42 \text{ mm}$  (fig. 4.31). Experimental results were always reported as symbols, closed symbols marking one-phase heat transfer and open symbols marking two-phase heat transfer. Different types of lines indicated different ways of calculating heat transfer. The coefficient for one-phase heat transfer reached values of up to  $\alpha=4000 \text{ W m}^{-2} \text{ K}^{-1}$  and depended on the inlet temperature, much differently from what had been expected.  $\alpha$  also depended on  $G$ , strongly so for lower, and slightly for higher values of  $T_{\text{in}}$ . This had not been expected to be so profound, considering that the flow was always laminar according to the Re number being  $<1500$ . This confirmed that the values for  $\alpha$ , obtained for lower values of  $G$  and higher values of  $T_{\text{in}}$ , mark only minimum values. The linear conduction parameter  $LCP$  was not significant with values  $<0.01$  in all cases.

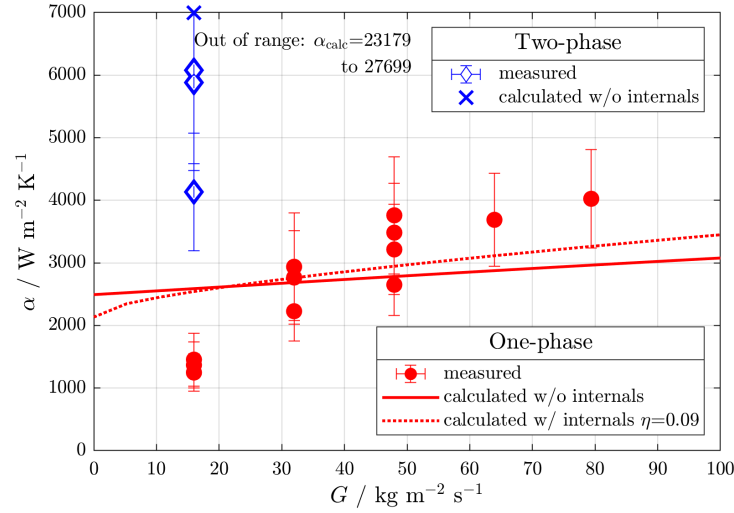
In two-phase heat transfer, as expected, outlet temperature was very close to  $T_{\text{boil}}$ . The heat transfer coefficient reached values of up to  $\alpha=6000 \text{ W m}^{-2} \text{ K}^{-1}$ , even at low values of  $G$ . Experimental data in fig. 4.31 had acceptable errors of approx. 20 % when the inlet temperature was low and thereby heat transfer high. The opposite held true otherwise, with errors having been unacceptably large with 50 % to well above 100 % for the highest inlet temperatures for one-phase and two-phase heat transfer. Errors were mainly due to uncertainty in temperature measurement and were higher for two-phase heat transfer due to the more complex calculation required (eqs. (4.28) to (4.29)).



**Figure 4.31.:** Module Pins-1-0.42-1.4 with  $t_w=0.6 \text{ mm}$ . Experimental results for heat-transfer coefficient of one-phase (closed symbols) and two-phase (open symbols) heat-transfer with  $\text{H}_2\text{O}$  with  $T_{\text{in}}=150\text{--}195 \text{ }^\circ\text{C}$  indicated by symbol shape and color. All set-points are shown without repetitions.

Therefore, heat transfer performance of different modules will be discussed for results of selected set-points. For one-phase heat transfer,  $T_{\text{in}}=150 \text{ }^\circ\text{C}$  was chosen, which marked the lowest value. This resulted in a logarithmic mean temperature difference of  $\Delta T_{\text{LM}} \approx 20 \text{ K}$  in most cases. Hence, for two-phase heat transfer,  $T_{\text{in}}=170 \text{ }^\circ\text{C}$  was chosen. This meant that the system pressure was set in a way that

$T_{\text{boil}}=180\text{ }^{\circ}\text{C}$ . Due to the characteristics of evaporation cooling, this signified a relevant temperature difference of  $\Delta T_{(\text{LM})}\approx 20\text{ K}$  as well. This meant a maximum Re number of 1500 for all cases and a maximum vapor fraction of  $\dot{x}=0.292$  in case of two-phase heat transfer. Figure 4.32 shows the results of the module with pins described directly above in a reduced way. The heat transfer coefficient  $\alpha$  is depicted as a function of the mass flux  $G$ . The figure includes experimental and calculated results for one- and two-phase heat transfer.

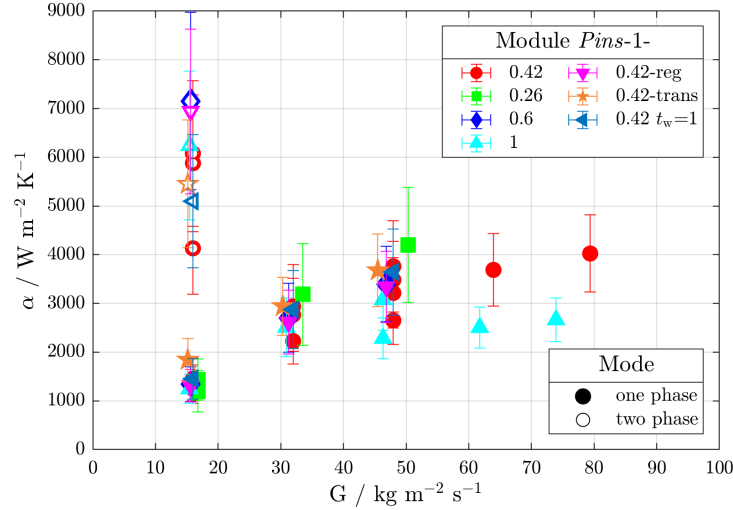


**Figure 4.32.:** Module *Pins-1-0.42-1.4* with  $t_w=0.6\text{ mm}$ . Experimental and calculated results for heat-transfer coefficient of one-phase (closed symbols) and two-phase (open symbols) heat-transfer with  $\text{H}_2\text{O}$  with  $T_{\text{in}}=150$  and  $170\text{ }^{\circ}\text{C}$ , respectively. This resulted in  $\Delta T_{\text{LM}}\approx 20\text{ K}$  in most cases. Only selected set-points are shown with repetitions.

For one-phase heat transfer,  $\alpha$  was proportional to  $G$ , but more severely so than expected from calculations neglecting the rib effect of internal structures (red closed circles vs. red solid line in fig. 4.32). The measured value also surpassed the calculated value for higher values of  $G$  reaching  $\alpha=4025\text{ W m}^{-2}\text{ K}^{-1}$  at  $G=79\text{ kg m}^{-2}\text{ s}^{-1}$ . Figuring in the influence of the internal structures, a rib efficiency of  $\eta=0.09$  resulted in the best agreement between calculated values (red dotted line) and experimental values of  $\alpha$ : absolute calculated values were similar to experimental ones and the relation of  $\alpha$  to  $G$  seen in experiments was reproduced well by the calculation. The experimental values of  $\alpha$  being higher than the calculated ones could also be explained by the flow not being fully developed. According to calculations (eqs. (2.22) to (2.23)), the flow was not developed hydrodynamically up to a significant length of  $l_{\text{dev,h}} = 11\text{ mm}$  into the heat transfer area ( $l=60\text{ mm}$ ) and was never thermally developed inside the heat transfer area ( $l_{\text{dev,t}} = 65\text{ mm}$ ). Experiments at identical set points were repeated for this module. The considerable variation of  $\alpha$  was attributed to variations in clamping module and heating plates, which was done manually by the operator. For two-phase heat transfer,  $\alpha=6078\text{ W m}^{-2}\text{ K}^{-1}$  was higher compared to one-phase, even though  $G=16\text{ kg m}^{-2}\text{ s}^{-1}$  was minimal (blue oped diamonds). For two-phase heat transfer,  $\alpha$  was, however, measured much lower than calculated, even though the measured value of  $\dot{q}$  and  $\dot{x}$  was fed into the calculation (blue x-marks).

Results of heat transfer for the subset of modules comprising pins as internal structures are shown in fig. 4.33. The highest one-phase heat transfer coefficient (closed symbols)  $\alpha=4203\text{ W m}^{-2}\text{ K}^{-1}$  was obtained by module *Pins-1-0.26-0.88* with  $t_w=0.6\text{ mm}$  at  $G=50\text{ kg m}^{-2}\text{ s}^{-1}$ . It was concluded that one-phase heat transfer was slightly dependent on the inverse of the pin size. The thermal resistance of the wall with  $t_w=1\text{ mm}$  compared to  $0.6\text{ mm}$  was not visible in the results, being much smaller than the one of convective cooling. Regular arrangement as opposed to hexagonal arrangement of pins did not influence  $\alpha$  significantly, although Brandner [263] implied that staggered (hexagonal)

arrangement exhibited higher heat transfer above linear (regular) arrangement. The transposed module showed higher  $\alpha$  compared to other modules at low  $G$ . Moving over to two-phase heat transfer (open symbols), this benefit of the transposed module was not visible. Other observations from one-phase heat transfer could not be confirmed either. Modules with larger pins and regular arrangement seemed to be advantageous. The highest heat transfer coefficient  $\alpha=7154 \text{ W m}^{-2} \text{ K}^{-1}$  was obtained by module *Pins-1-0.6-2* with  $t_w=0.6 \text{ mm}$ .

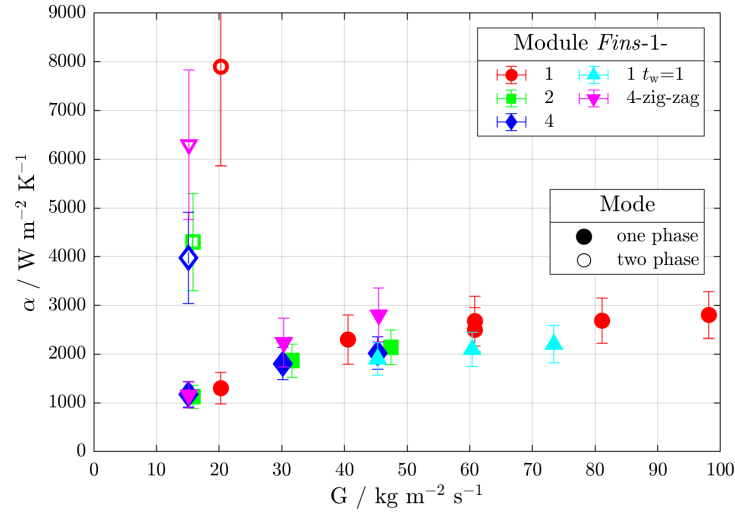


**Figure 4.33.:** Pin-equipped modules. Experimental results for one-phase (closed symbols) and two-phase (open symbols) heat transfer with  $\text{H}_2\text{O}$  with  $T_{\text{in}}=150$  and  $170^\circ\text{C}$ , respectively. This resulted in  $\Delta T_{\text{LM}} \approx 20 \text{ K}$  in most cases. If not otherwise mentioned  $t_w=0.6 \text{ mm}$ . Spacing between pins  $a$  is not indicated but was chosen for constant volume fraction  $\varphi$ . All dimensions in mm.

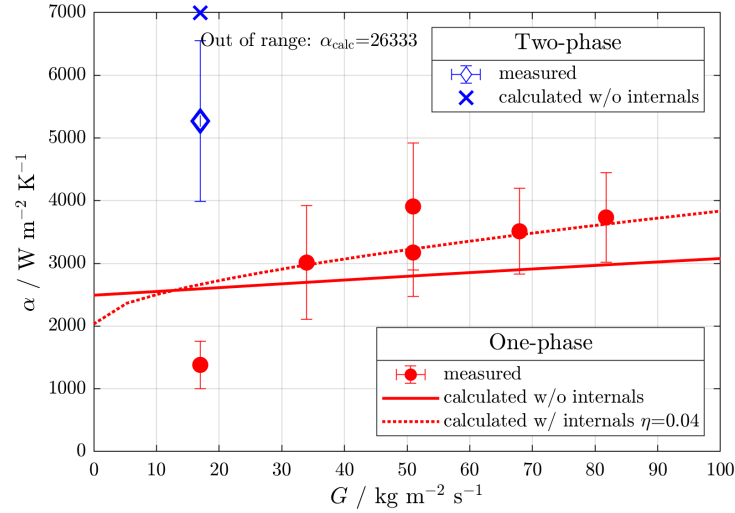
Several modules containing fins as internal structures were tested as well, results being depicted in fig. 4.34. Different from modules with pins, these parts contained individual channels for the flow. This could be a reason for  $\alpha$  being generally smaller compared to  $\alpha$  in pin-equipped modules in one-phase cooling (closed symbols). Among the structures investigated, those with smaller channels (smaller  $t_e$ ) showed a higher value of  $\alpha$ . In the module with zig-zag channels,  $\alpha$  was higher compared to similar modules with straight channels. The maximum values of the one-phase heat transfer coefficient were  $\alpha=2804 \text{ W m}^{-2} \text{ K}^{-1}$  at  $G=45 \text{ kg m}^{-2} \text{ s}^{-1}$  for the zig-zag modules and  $\alpha=2804 \text{ W m}^{-2} \text{ K}^{-1}$  at  $G=98 \text{ kg m}^{-2} \text{ s}^{-1}$  for the modules with the narrowest straight channels. The former module also showed the maximum value for two-phase heat transfer (open symbols)  $\alpha=7900 \text{ W m}^{-2} \text{ K}^{-1}$  at  $G=20 \text{ kg m}^{-2} \text{ s}^{-1}$ .

Figure 4.35 depicts the experimental results for one- and two-phase heat transfer for the module *Lattice-1* with  $t_w=0.6 \text{ mm}$ . Results for  $\alpha$  of this module were similar to those of *Pins-1-0.42-1.4* in fig. 4.32. For one-phase flow, experimental heat-transfer coefficients (red closed circles) were in best agreement with calculated values (red dotted line) when the effect of internal structures was considered assuming  $\eta=0.04$ . The calculations reflected the absolute values and progress of  $\alpha$  with  $G$  observed in experiments well. In accordance with all other modules, the two-phase heat transfer coefficient was lower in experiments (blue open diamonds) than calculated with the formulas from Ref. [7] with  $\alpha=5271 \text{ W m}^{-2} \text{ K}^{-1}$  at  $G=17 \text{ kg m}^{-2} \text{ s}^{-1}$  (blue x-mark) but higher than the one-phase  $\alpha$ .

Internal structures obstructing the flow, such as pins and lattice, generated secondary flow [264]. This could be an explanation for the increased heat transfer in one-phase flow of modules containing pins and lattice compared to those containing fins. For evaporation cooling, the opposite seemed to be true. The error through axial heat conduction in the module wall according to Ref. [265] was not significant in these experiments, with  $LCP < 0.01$  in all cases. Measured and calculated results for all



**Figure 4.34.:** Fin-equipped modules. Experimental results for one-phase (closed symbols) and two-phase (open symbols) heat transfer with H<sub>2</sub>O with  $T_{in}=150$  and  $170$  °C, respectively. This resulted in  $\Delta T_{LM} \approx 20$  K in most cases. If not otherwise mentioned  $t_w=0.6$  mm. All dimensions in mm.



**Figure 4.35.:** Module *Lattice-1* with  $d_{strut}=0.2$  mm and  $t_w=0.6$  mm. Experimental and calculated results for heat-transfer coefficient of one-phase (closed symbols) and two-phase (open symbols) heat-transfer with H<sub>2</sub>O with  $T_{in}=150$  and  $170$  °C, respectively. This resulted in  $\Delta T_{LM} \approx 20$  K in most cases.

modules individually are depicted in fig. D.1. The maximum heat flux achieved was  $\dot{q} \approx 80,000$  W m<sup>-2</sup> and 160,000 W m<sup>-2</sup> for one- and two-phase heat transfer respectively, which is at the lower end of the range that conventionally micro-structured heat exchangers with smaller internal dimensions achieve in Refs. [266, 267]. Experimental one-phase heat transfer coefficients being higher than calculated ones at high  $G$  can be explained with flow being clearly developing in the experiments. The flow being developing arose from choosing dimensions common to (micro-structured) laboratory devices. It means that the velocity and temperature field are more uniform over the channel cross section compared to developed flow. Therefore, the effective temperature gradient at the wall, and in turn heat transfer, are higher. The consideration of this in the equations from VDI HA [7] was possibly not drastic enough. Experimental two-phase heat transfer coefficients being lower than calculated ones is likely due to the fact that calculations were developed for conventional heat exchangers with much larger dimensions.

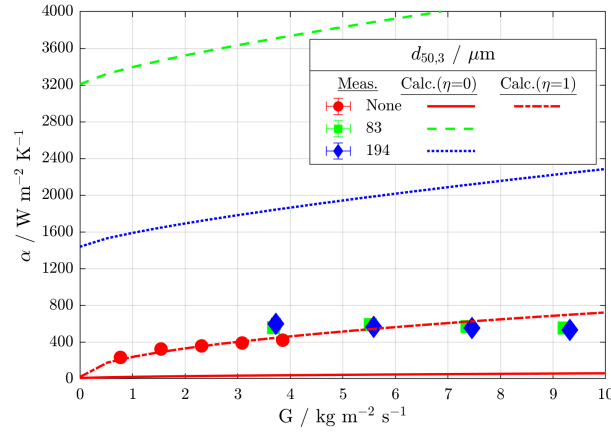
#### 4.5.3.2. Heat Transfer Results Nitrogen

Modules with internal pins were fabricated with  $d=1-12$  mm. Heat transfer coefficients were determined for those with  $d \geq 4$  mm. Modules with internal FGE were fabricated with  $d=4-16$  mm. The heat transfer coefficient was determined for those with  $d=8$  mm and 12 mm. The *LCP* revealed that longitudinal heat conduction was relevant in the theoretical calculation for the reaction zone under realistic conditions (table 4.14). However, it was negligible in the  $N_2$  experiments with  $LCP < 0.05$ , as experimental conditions were chosen in a way to gain significant results in all cases. This was mainly achieved by having a higher temperature difference between heating plates and fluid, which also resulted in the relative error of  $\alpha$  being much lower compared to the experiments with water. For the experiments without particle loading, the length before the nitrogen flow was hydro-dynamically and thermally developed was above the module length in all cases.

In fig. 4.36, the heat transfer coefficient of the module *Pins-12-1-3.4* is shown on the ordinate. The abscissa shows the mass flux  $G$ . Red circles mark the experimental results for the module without powder. Green squares and blue diamonds mark those for modules with particles with  $d_{50,3} = 83$  and  $194 \mu\text{m}$ , respectively. Solid, dashed, and dotted lines denote the results of theoretical calculation not considering the effect of internal pins, while the dash-dotted line was calculated assuming the rib effect with  $\eta=1$  for the case without particle loading. It is interesting to observe that the experimental particle-free heat transfer coefficient was approximately ten times higher than calculated neglecting internal structures, but was in accordance with calculations acknowledging the rib effect of internal pins. The maximum value was  $\alpha=423 \text{ W m}^{-2} \text{ K}^{-1}$  at  $G \approx 3.9 \text{ kg m}^{-2} \text{ s}^{-1}$ . A slight increase of  $\alpha$  with  $G$  was characteristic to both theory and observation. It is worth noting that the critical Re number of  $Re=3600$  is first reached at  $G \approx 3.8 \text{ kg m}^{-2} \text{ s}^{-1}$ . For the particle-filled modules, the experimental  $\alpha$  were two to six times lower than the corresponding theoretical values. Other than expected from theory, there was no proportional dependency but rather a very slight decrease of  $\alpha$  with  $G$ . The influence of  $d_{50,3}$  was the most striking. Theory suggested an inverse proportionality, but in practice both particle sizes delivered almost the exact same result of  $\alpha \approx 600 \text{ W m}^{-2} \text{ K}^{-1}$ . This could be explained through a strong effect of the confining walls. At confining walls the porosity of packed beds, especially of small particles, increases as does the fluid velocity. Most of the fluid having flown at the walls explained why the presence and particle size of the packed did not increase  $\alpha$  significantly. The equations used to calculate the experimental  $\alpha$  assumed analogy between fluid dynamics and heat transfer, which could have been an oversimplification but one unavoidable from a metrological point of view. More results of heat transfer with  $N_2$  in pin-equipped modules can be seen in fig. D.2. Figure D.2a and fig. D.2b confirm that experimental and theoretical  $\alpha$  concurred, when a rib efficiency of  $\eta=1$  was assumed. Figure D.2b confirms  $\alpha \approx 600 \text{ W m}^{-2} \text{ K}^{-1}$  for  $G \approx 15.5 \text{ kg m}^{-2} \text{ s}^{-1}$  and  $d_p=194 \mu\text{m}$ .

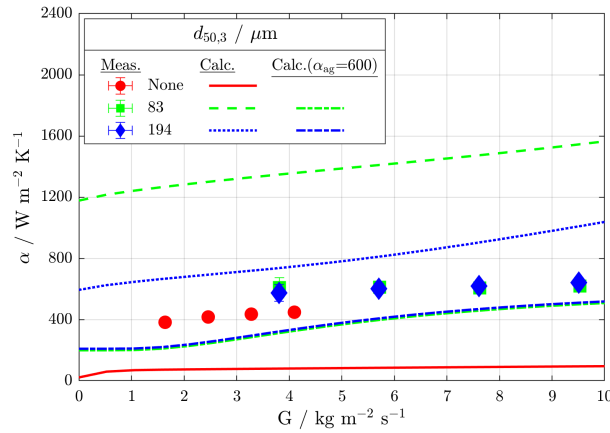
Below, fig. 4.37 depicts the heat transfer coefficient of the module *FGE-12-4*. The heat transfer coefficient  $\alpha$  is depicted as a function of the mass flux  $G$ . Symbols have the same meaning as in fig. 4.36. Solid, dashed, and dotted lines denote the results of theoretical calculation where  $\alpha_{os}$  was calculated according to [7], while the dash-dotted lines were calculated with  $\alpha_{os}=600 \text{ W m}^{-2} \text{ K}^{-1}$  adopted from the experimental results in fig. 4.36. For FGE, too, the experimental particle-free heat transfer coefficient was approximately five times higher than calculated. Calculating the rib effect of internal FGE was not reasonable due to their complex shape and different working principle. The increase of  $\alpha$  with  $G$  was marginal as theoretically expected reaching a value of  $\alpha \approx 450 \text{ W m}^{-2} \text{ K}^{-1}$  at  $G \approx 4.1 \text{ kg m}^{-2} \text{ s}^{-1}$ . Due to the FGE-induced subdivision of the channel into partial flows, the characteristic length was lower and the (particle-free) flow clearly laminar. For the modules being filled with particles with  $d_{50,3} = 194 \mu\text{m}$ , theory and experiment resulted in similar values of  $\alpha$  for  $G \approx 3.9 \text{ kg m}^{-2} \text{ s}^{-1}$ . For the smaller particles, the experimental  $\alpha$  were almost identical, while the theoretical  $\alpha$  were almost double.





**Figure 4.36.:** Module *Pins*-12-1-3.4 with  $t_w=0.8$  mm. Experimental and calculated results for heat-transfer coefficient with  $N_2$  without particles (red, circles and solid line) and with particles with  $d_p=83$   $\mu\text{m}$  (green, squares and dashed line) and  $d_p=194$   $\mu\text{m}$  (blue, triangles and dotted line).

For both particle sizes experimental  $\alpha \approx 600 \text{ W m}^{-2} \text{ K}^{-1}$  were almost independent of  $G$ . As theoretical values of  $\alpha$  supposedly increased with  $G$ , they differed significantly from experimental values at high mass flux. The calculation method of Ref. [136] (section 2.4) was used for FGE. The value of  $\alpha_{ag}$  had so far been calculated according to VDI HA [7]. The dash-dotted lines were calculated with the value of  $\alpha_{ag}=600 \text{ W m}^{-2} \text{ K}^{-1}$  submitted to the novel calculation by Biffar et al. [136]. This value was obtained from experiments with pin-equipped modules discussed before. In doing so, calculations did not predict a dependency of  $\alpha$  on  $d_p$  as observed experimentally but underestimated  $\alpha$  by approx. one third.

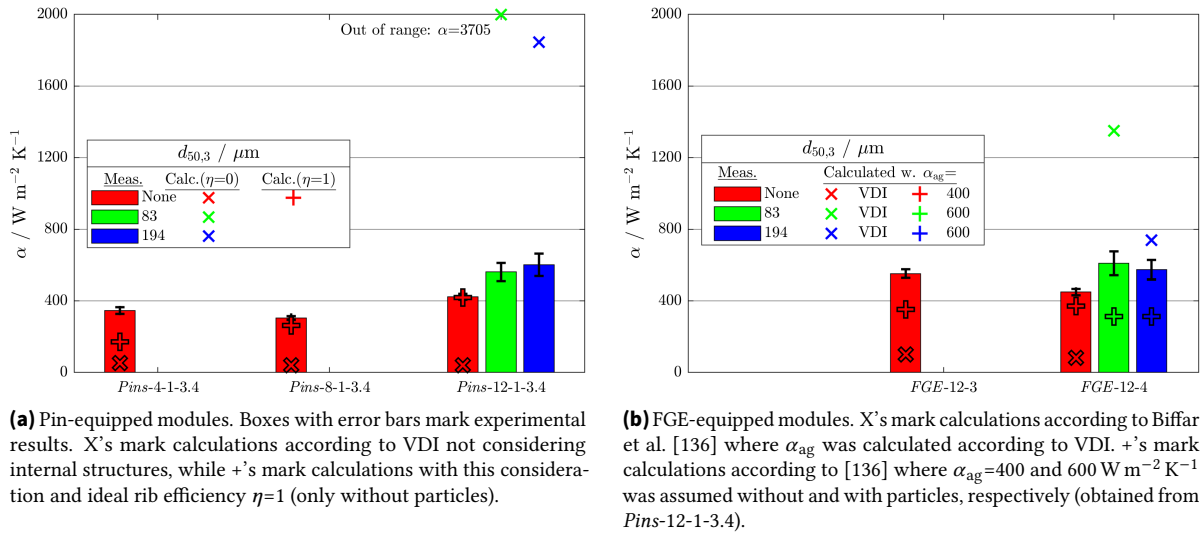


**Figure 4.37.:** Module *FGE*-12-4 with  $t_w=0.8$  mm. Experimental and calculated results for heat-transfer coefficient with  $N_2$  without particles (red, circles and solid line) and with particles with  $d_p=83$   $\mu\text{m}$  (green, squares and dashed line) and  $d_p=194$   $\mu\text{m}$  (blue, triangles and dotted line).

Figure 4.38 shows the results for  $\alpha$  for all modules tested at values of  $G \approx 3.8 \text{ kg m}^{-2} \text{ s}^{-1}$ . First, the cases of pin-equipped modules without powders were considered. The experimentally determined values of  $\alpha$  were almost independent of the slit depth and ten times higher than expected, which is beneficial for the packed-slit reactor concept. Theoretically, an inverse proportionality of  $\alpha$  and slit depth was expected neglecting the rib effect of internal structures. Heat transfer coefficients were more in accordance with calculations when the rib effect was considered to the full extent ( $\eta=1$ ). This was a reasonable explanation for the experimental observations: with slit depth the added area of internal pins increased proportionally and contributed with  $\eta=1$  to the overall heat transfer. Next, theoretical calculation and experiments of heat transfer coefficients in FGE-equipped planar modules



were considered. These were conducted for the first time in this thesis. When the annular gap heat transfer coefficient was inserted into the FGE calculation, the calculated value was only one fifth of the experimentally obtained value. When  $\alpha_{ag}=400 \text{ W m}^{-2} \text{ K}^{-1}$ , obtained from experiments with *Pins-12*, was submitted to the calculation instead, agreement with experiments was better. Further, heat transfer with particle loading is discussed. As indicated before, experimental  $\alpha$  were much lower than calculated ones and independent of  $d_p$  for both pin- and FGE-equipped modules. For the latter, accordance was better when a more realistic value of  $\alpha_{ag}=600 \text{ W m}^{-2} \text{ K}^{-1}$  was submitted to the FGE-specific calculation. This emphasizes the following: 1. experimental validation of innovative designs is compulsory, and 2. the novel calculation method for FGE is strongly influenced by the  $\alpha_{ag}$  used. Whether the novel calculation method for FGE from Ref. [136] obtained for tubular systems can be applied to planar systems unaltered remains a question. More experiments acknowledging the many influencing factors are required to answer this question. FGE internal structures can increase the heat transfer coefficient compared to pin internal structures, provided conditions remain similar. Further experiments should provide a better understanding of the heat transfer. Among the internal structures investigated, FGE had a relatively high  $\phi$ , leaving less space for catalyst particles.



**Figure 4.38.:** Experimental (boxes) and calculated (symbols) results for heat-transfer coefficient with  $\text{N}_2$  at  $G \approx 3.8 \text{ kg m}^{-2} \text{ s}^{-1}$  without particles (red) and with particles with  $d_p=83 \mu\text{m}$  (green) and  $d_p=194 \mu\text{m}$  (blue). Modules with  $t_w=0.8 \text{ mm}$ . All dimensions in mm if not specified otherwise.

#### 4.5.4. Interim Summary Heat Transfer

The newly built test rig served its purpose. It is worth mentioning that evaporation heat transfer at elevated pressure could be measured with sufficient accuracy. Experiment automation and data logging facilitated quick experimental campaigns and evaluation. The modular approach where modules could be connected fluid-wise and then clamped between heating plates and insulators by a vise was advantageous. Geometries other than the planar one used are possible. Heating could potentially come from heating lines or thermal fluids as well. Unger [268] inserted heating cartridges into his copper-powder filled laser-based powder bed fusion of metals (PBF-LB/M) specimens. This saved post-processing effort on his parts.

A challenge lay in the design of experiments. Having aimed for realistic conditions, the micro-structured modules with low slit depths, low flow-rates, and small temperature differences were chosen. Each one

of these aspects makes sense in an FTS reactor, but led to unsatisfactory experimental results and large relative errors in  $\alpha$ . This was lessened by the appropriate choice of experimental conditions in heat transfer experiments with  $N_2$ . Errors in mass flux  $G$  were approx. 0.1 % of the measured values and thus insignificant. Results presented here were mainly obtained at set-points not really resembling micro-reactor operation: high flow rates, high temperature differences, and sometimes with modules with dimensions on the high end for "micro".

Experimental results were differing from theoretical calculations in both directions, depending on the situation. These results served as a good orientation for further reactor-development on this work. Surprising was the fact that micro packed-bed heat transfer was not dependent on particle size which should be re-evaluated with the more sophisticated  $\Lambda_r(r)$  heat transfer model. Partially evaporating water had an immense cooling potential compared to purely convective cooling with water, as was expected. It can be summarized that experimental heat transfer analysis is necessary to identify the limiting steps of heat-transfer in the envisioned micro-structured concept. Theoretical calculation and experiments of heat transfer coefficients in FGE-equipped planar modules were conducted for the first time, yielding satisfactory results. This signifies a significant step forward and suggests that additional research is promising.

## 4.6. Control Systems Integration

Control systems, common in process engineering, are the subject of this section. A popular implementation is a feedback loop: it consists of a process with a process variable that should equal the set point, but is disturbed by a load. The controller influences a control variable in order to minimize the difference between process variable and set point [269]. Some important process variables and related control variables are given in table 4.15, with the subsections addressing the respective variables shown in frames. Composition and pressure measurement both require a physical connection to the medium. The former requires a connection to transfer some of the medium to analysis devices while the latter needs medium contact to assess static pressure.

**Table 4.15.:** Important process variables, examples of sensors, actors, and respective requirements.

Process variable	Sensor	Requirement	Control variable	Actor	Requirement
Temperature 4.6.1 4.6.2	Sheathed thermocouple	Thermal connection	Heating power 4.6.3 4.6.4	Heating cartridge, heating tape	Thermal connection
Pressure 4.6.5	Pressure transmitter	Fluidic connection			
Composition 4.6.5	Spectrometer, Gas chromatograph	Fluidic connection			

In each subsection, first conventional solutions for industrial-scale and laboratory-scale process devices will be demonstrated. Second, additive solutions possible with the packed-slit reactor concept will be discussed. The goal of this section is to share findings on these very important aspects of reactor design.

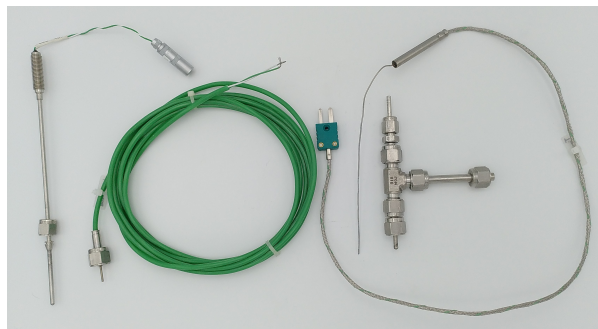
### 4.6.1. Measuring Temperature of Fluid

Both the exact measurement and the exact control of temperature are critical in Fischer-Tropsch synthesis (FTS), as the reaction temperature greatly influences safety and selectivity [43]. As indicated in section 2.4, the adiabatic temperature rise of FTS is approx. 1800 K. If the reaction got out of control, damage to the catalyst and equipment and in turn danger to the environment would be likely. As little as a couple of kelvins decide on the selectivity to an extent that influences the profitability of an FTS plant [31, 62].

Contact temperature measurement in process engineering is often executed with resistance thermometers, e.g. made of Pt100, or thermocouples [269]. A thermocouple is a pair of metallic wires forming a closed circuit. One junction of the circuit is for measuring while the other is for reference [269]. When the wires run through a narrow tube with the measuring junction at the closed end, this is called a sheathed thermocouple. The sheath protects the wires against temperature and corrosion and can be used to form a pressure resistant and leak-tight interface between process and environment [270]. Sheathed thermocouples are extensively used in research. The conflicting goals are precise measurement on one hand, and, on the other hand, leak-tightness, accessibility, and removability.

#### Conventional Manufacturing

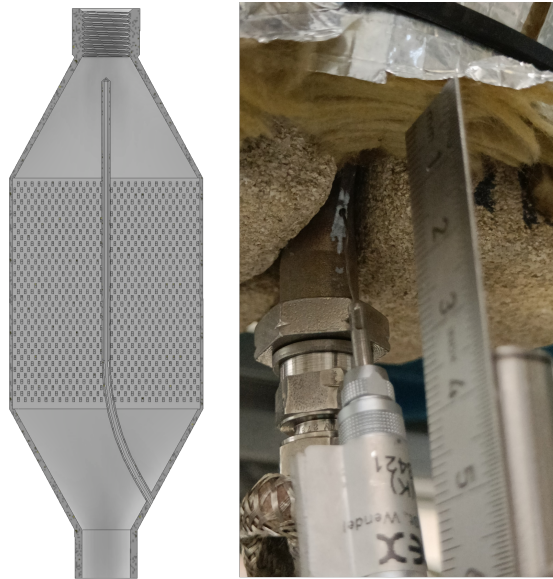
In conventional designs for laboratories, the sheathed thermocouple is placed in the fluid, either inside a protective tube or directly into the fluid (fig. 4.39). In the former case, a tube sealed on one side and a connector are required. In the latter case, requiring only a connector, the thermocouple can usually not be replaced without replacing the connector as well, due to risk of leakage, and never without exposing the fluid to the environment. To avoid any hazards to the measuring point's surrounding, this potentially necessitates depressurizing, cooling down, and inertizing of the process. In industrial applications, however, process interruptions are not tolerated, so welded, threaded, or flanged protective tubes (so-called thermowells) are used.



**Figure 4.39.:** Sheathed thermocouples used in laboratory applications. Sealing is done from left to right via: sheath, shell, and protective tube, respectively.

#### Additive Manufacturing

In the additive case, generating a protective tube along with the device causes no effort other than the additional material. Figure 4.40 shows that channel shape can be free-form. The sheathed thermocouple can be inserted into the additive protective tube without additional parts or fabrication steps. It can be replaced without exposing fluid to the environment.



**Figure 4.40.:** Additive manufacturing (AM) channel for thermocouples to measure fluid temperature.

#### 4.6.2. Measuring Temperature of Casing

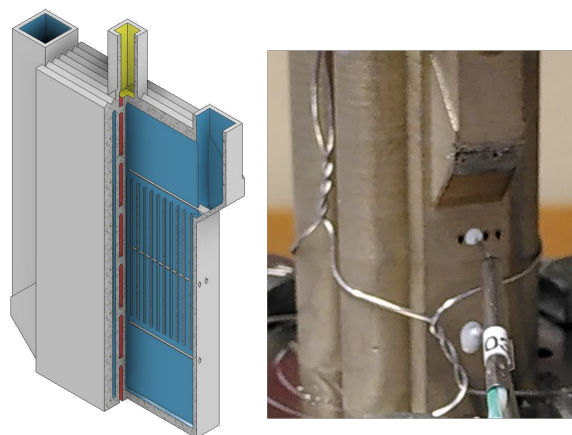
Measuring the temperature of the solid casing (also called wall temperature or skin temperature in Ref. [55]) is common practice in micro-structured reactors (MSRs). Considering the small wall thicknesses, casing temperature might even be a good approximation for the fluid temperature.

##### Conventional Manufacturing

On first glance, no more than a thin and deep hole is needed to insert a thermocouple, but it is increasingly difficult to fabricate a hole with increasing length-to-diameter ratio [272]. The ratio necessary for thermocouples may require sinker electric discharge machining. Alternatively, in diffusion bonding designs, a plate with slots can be used. Even when deformed in the process, this approach usually leads to thermocouple channels without a need for post-processing. For macro-scale reactors, measuring fluid temperatures is preferred over measuring wall temperatures. Due to the larger dimensions and wall thicknesses, wall temperature is not necessarily relevant. If desired, a temperature sensor can be added with the help of drilling (optional) and welding, soldering, or bolting. These are comparatively easy fabrication steps but they require labor and additional parts.

##### Additive Manufacturing

With laser-based powder bed fusion of metals (PBF-LB/M), a cavity can be included in the device walls where the thermocouple is designed to go. With AM, this does not increase fabrication effort, fig. 4.41. AM design guidelines have to be acknowledged [273]: to maintain minimum wall thickness or overhang angles, potentially material has to be added locally.



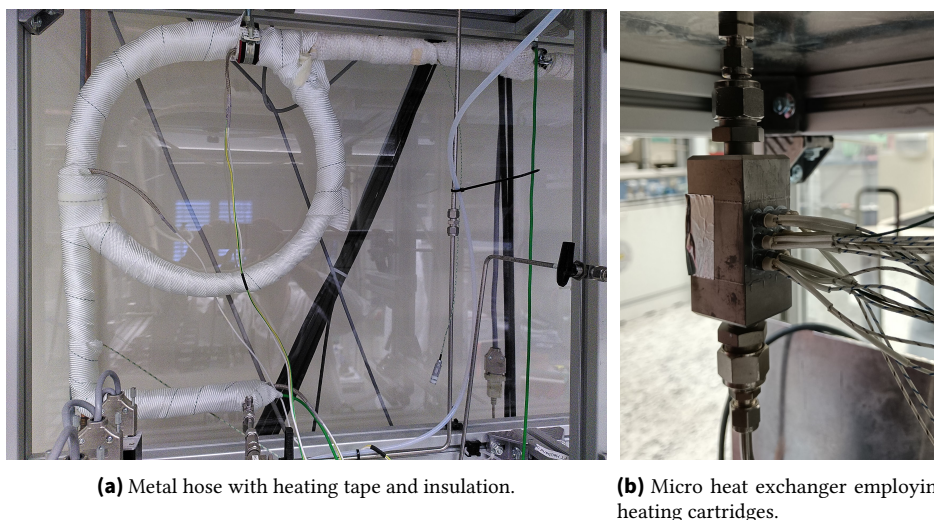
**Figure 4.41.:** AM channels for thermocouples to measure solid temperature.

### 4.6.3. Electrical Heating of Fluid

For carrying out the FTS reaction in a safe and highly selective manner, the precise control of temperature is crucial. Therefore, electrical heating of the fluid should be efficient and dynamic. To achieve this, the heating element should be positioned close to the fluid, avoiding unnecessary material to be heated up in the process. In micro-structured devices, electrical heating of the fluid is often carried out via heating the casing of the fluidic device. Therefore, this and the next subsection have no clear separation.

#### Conventional Manufacturing

Flange heaters are commonly used in industry. In laboratories, metal pipes/hoses wrapped with heating tapes are frequently used (fig. 4.42a). Heat transfer testing in this work was performed with an IMVT standard electrically-heated micro heat exchanger (section 4.5.2), its advantages being high installed power, robust design, and small space requirement (fig. 4.42b).



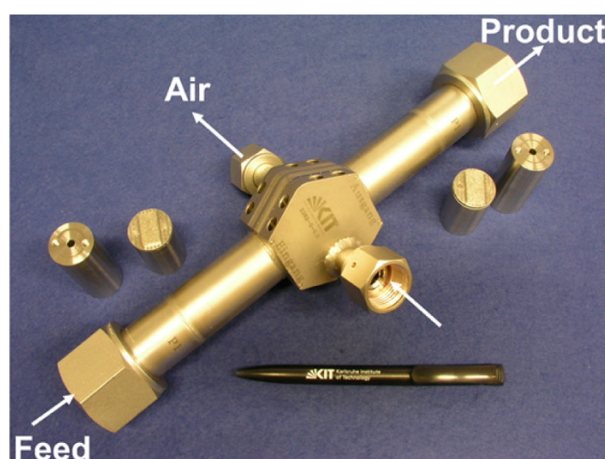
**Figure 4.42.:** Heating of a flow in laboratory settings with heating line and micro-structured heat-exchanger.



#### 4.6.4. Electrical Heating of Casing

##### Conventional Manufacturing

Heating jackets are independent of the heated device's fabrication method and are commonly used. Some FTS micro-reactors employ heating plates bolted to the reactor casing, the plates being equipped with heating cartridges (fig. 2.4). Some Institute for Micro Process Engineering (IMVT) reactors contain channels for heating cartridges (fig. 4.43), which requires an additional foil incorporated in the diffusion bonding process. Even if distortion is limited to an acceptable value, the channels still have to be post-processed due to the strict tolerance requirements of heating cartridges.



**Figure 4.43.:** Conventionally manufactured diffusion-bonded MSR with holes for heating cartridges [274]. Reprinted with permission from American Chemical Society (©2017).

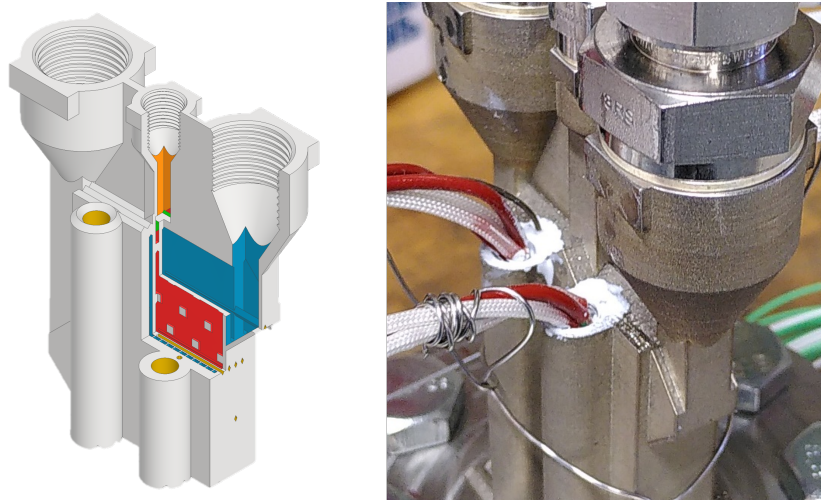
##### Additive Manufacturing

The additive solution approaches were vertical channels for heating cartridges, with a slight under-size in diameter, post-processed to the design value and surface quality (fig. 4.44). On the outside wall of an AM device, grooves can be fabricated without additional effort to accommodate a heating line wrapped around the device [275]. With the packed-slit reactor concept, its subfunctions established, and the design freedom of AM, it is also possible to include a fluidic heat exchanger in the design. Feed-effluent heat exchangers and intermediate cooling stages are common in process engineering [32].

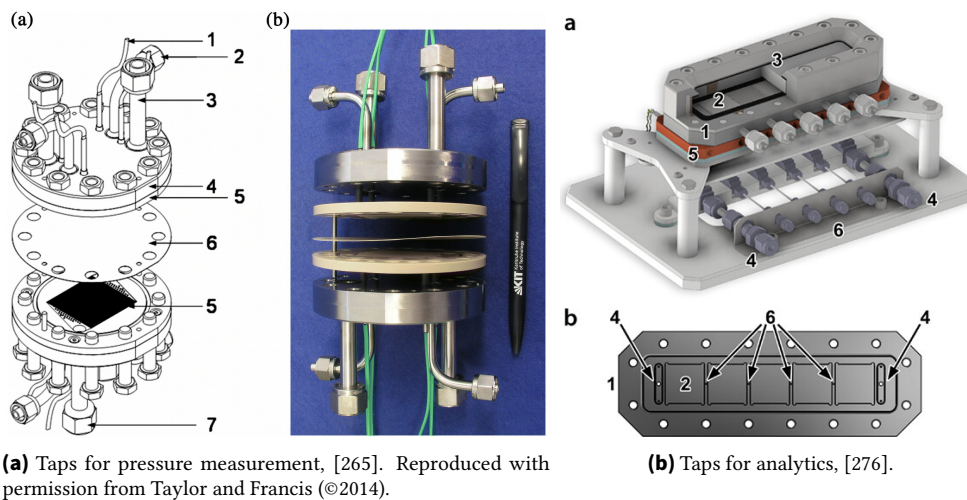
#### 4.6.5. Measuring Pressure and Composition

##### Conventional Manufacturing

An actual connection to the fluid - a tap - is required for measuring pressure and composition. In large-scale reactors, a nozzle is welded to a tank; standardized fittings exist for pipes. In MSR, connection of the fluid channel to the device shell is ensured and a suitable adaptation is welded to the respective position after diffusion bonding. Figure 4.45 shows examples.



**Figure 4.44.:** AM reactor with pre-fabricated holes for heating cartridges. Left: Computer aided design (CAD) representation with holes in gold. Right: Actual reactor with heating cartridges inserted into holes with thermal conductivity paste (white fluid).



**Figure 4.45.:** Micro process engineering devices with taps.

## Additive Manufacturing

As shown in the previous subsection, in additive manufacturing (AM), free-form channels can be guided through solid walls of the device. Additive connections for G1/8" threads were demonstrated as examples in section 4.1.1. Combining those two, taps for pressure and composition analysis can be implemented in the packed-slit reactor concept comparatively easily.

### 4.6.6. Results

Control system components are highly important for process engineering devices. Sensors for temperature, taps for pressure and composition measurement, and electrical heating are integrated into industrial-scale reactors or the adjacent piping. While thermowells are off-the-shelf parts, flanged heaters are an engineering discipline of their own. The connections used extend from bolting to

soldering or welding. In conventionally manufactured laboratory applications, thermocouples and taps for pressure and composition measurement are connected via fittings or are included in the specially-designed reactor. Heating lines are used as well as heating cartridges requiring narrow-tolerance bores.

These control system components can be well implemented into AM parts. AM is not necessarily the way to implement these in a design that is otherwise conventional, but in the case of a comprehensive new design or redesign regarding the fabrication method, implementing these AM features can be highly advantageous. This was proven for measurement of temperature, pressure, and composition as well as for electrical heating: i.e, with the exception of the controller, all parts of a temperature control loop could be implemented in an AM device. In doing so, fabrication steps and additional parts can be omitted in all demonstrated cases.

## 4.7. Removable Connection

A removable connection is required to service the fabricated device. Catalyst has to be inserted and extracted, potentially multiple times over the reactor's life time, requiring the complete cross-section of the part to be accessible. A huge thread around the whole device being as impractical as a clamping mechanism of some sort, the only removable connection fulfilling these criteria is a flange pair.

Flat graphite sealants are common for this application. Requiring considerable compression, [277], and high contact pressure, this much force can only be exerted with a flange plate of high thickness.

Two approaches are presented and evaluated: first, a fully additive design was created, second, a hybrid approach was pursued.

### 4.7.1. Fully Additive Flanged Reactor

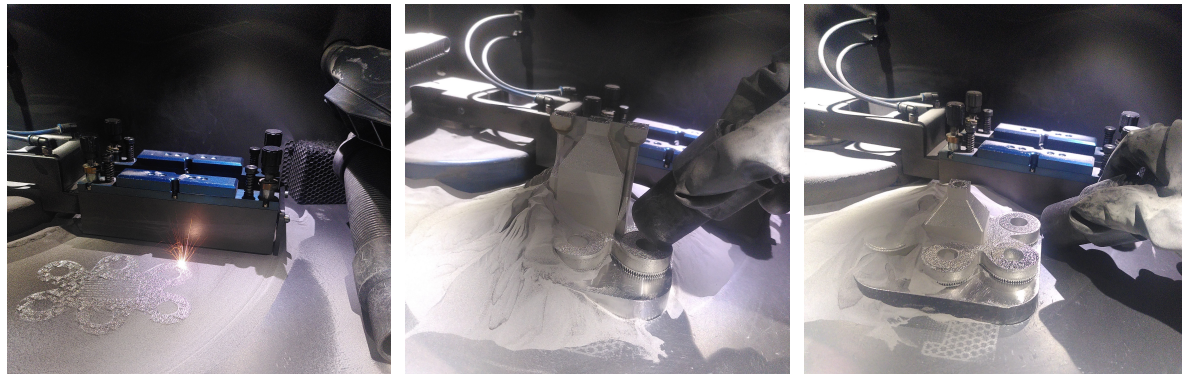
The volume available for reaction was  $V_r=12.8$  mL divided onto eight empty slits having a depth of  $d_{\text{slit}}=1$  mm and width and height of 40 mm. Depth of cooling slits and wall thickness were 1 mm while front and back wall were thicker for stability reasons. External width, depth, and length of the device were  $W=42$  mm (54 mm with manifolds),  $D=31$  mm, and  $L=81.8$  mm respectively.

The flange was  $t=10$  mm thick, measured 120 mm×101 mm, and was designed for six M12 bolts. It had a volume of  $V=65.4$  mL out of the 113.1 mL of the whole device.

Pictures of fabricating this fully additive design are given in fig. 4.46. The cross-sectional area of the reactor flange was immense. In fig. 4.46a soot particles on top of the powder layer are visible. In fact so much soot was produced, that the purge-gas systems' filter was clogged early into the print job. The purge-gas flow reduced and soot accumulated in the build chamber. This, of course, led to non-ideal laser absorption and to porosity via intrusion of particles. After depowdering inside the machine (fig. 4.46b), the reactor was subjected to further cleaning and post-processing.

A counterflange was designed and manufactured as well (fig. 4.46c). Although it had the same flange geometry, this time, fabrication was cleaner. This was explained with the paper filter being replaced right before the print job.





(a) A layer of the reactor flange being scanned. Visible on powder surface is dark soot.

(b) Depowdering of reactor body.

(c) Depowdering of counterpart.

**Figure 4.46.:** Fabrication of fully additive reactor.

#### 4.7.2. Hybrid Flanged Reactor

This design consisted of two parts: flange and reactor body. They were in principal fabricated separately but formed a monolithic part during additive manufacturing (AM) of the reactor body on top of the flange.

From a round blank flange (type 5) according to DIN EN 1092-1 the flange was manufactured as depicted in fig. 4.47a. Fabrication steps were milling on a numerically controlled mill and wire electric discharge machining. A three-jaw chuck was used for fixation. The final flange featured eight slits to be able to carry a reactor body with up to eight reaction slits. While the upper side of the flange was flat the lower side was highly functionalized (fig. B.8):

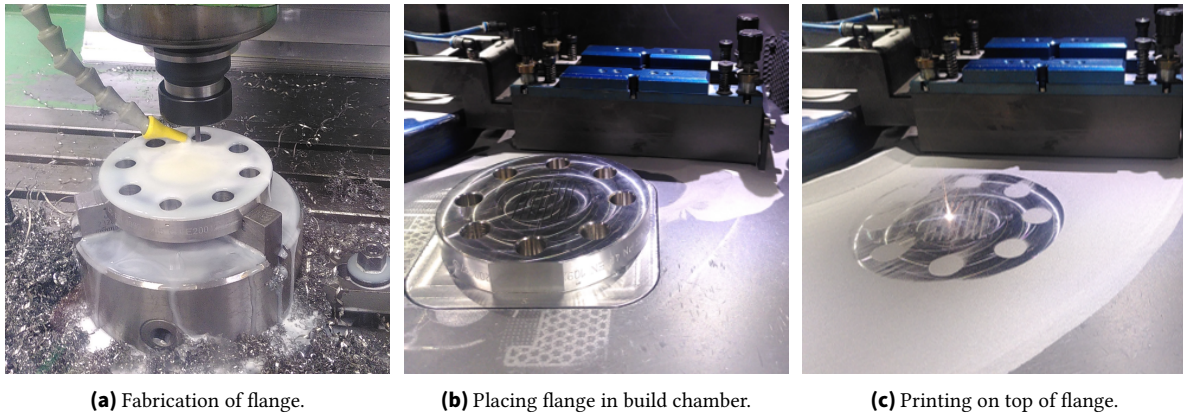
- a pocket was milled to accommodate a commercial sinter-metal frit,
- taps were made inside the pocket for fixating said frit,
- a groove was milled to hold a gasket, and
- holes for dowel pins were drilled to align flange on build plate.

Optional L-shaped holes from the flange's sides to the upper side were fabricated in order to transfer syngas/coolant to the reactor body. The original fitting being intended for PN40 DN25, the flange had thickness of 18 mm and a diameter of 115 mm.

The flange was placed on a build plate with dowel pins (fig. 4.47b) and both were placed inside the SLM125. After the considerable voids in and around this assembly were filled with powder, the build platform was leveled to its final height. At the final height, the flange top was still visible but coated with a thin layer of powder which meant, that it was in focus of the laser beam (fig. 4.47c).

Subsequently the print of reactor body was started. Notably, the reactor body was prepared without support with the first layer starting immediately. This way it was firmly bonded to the flange.

Realizing that  $V_r=4.4$  mL were enough for subsequent tests, the reactor body featured two slits with  $d_{\text{slit}}=1$  mm,  $w=40$  mm, and  $l=55$  mm. Each reaction slit contained pins ( $t_p=2$  mm,  $a=5$  mm) occupying  $\varphi=0.1$ . They design had three cooling slits equipped with fins. The reactor body had a volume of  $V=54$  mL.

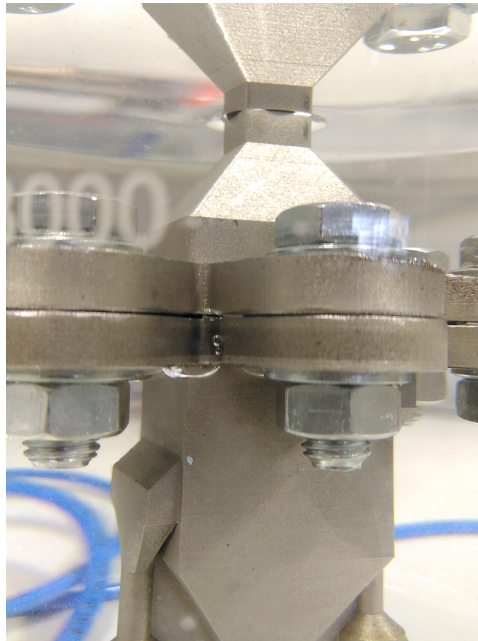


**Figure 4.47.:** Hybrid manufacturing of reactor concept.

#### 4.7.3. Results

Weight, volume, and external dimensions of part as well as fabrication time are parameters easily accessible via computer aided design (CAD), printer operation software. They are highly relevant for techno-economic assessment of the reactor concept. The fully additive design took two days to manufacture. The flange being only one eighth of the total height, it took half of the fabrication time, which corresponds with its share of the material volume. The powder surface turned dark and the paper filter got clogged during the fabrication of the flange. This was explained by the formation of too much welding dust, which the internal system could not deal with. This has never been reported in literature, though.

The fully additive reactor was full of pores and clearly not leak-tight. A severe leak could be seen in the massive flange (fig. 4.48).

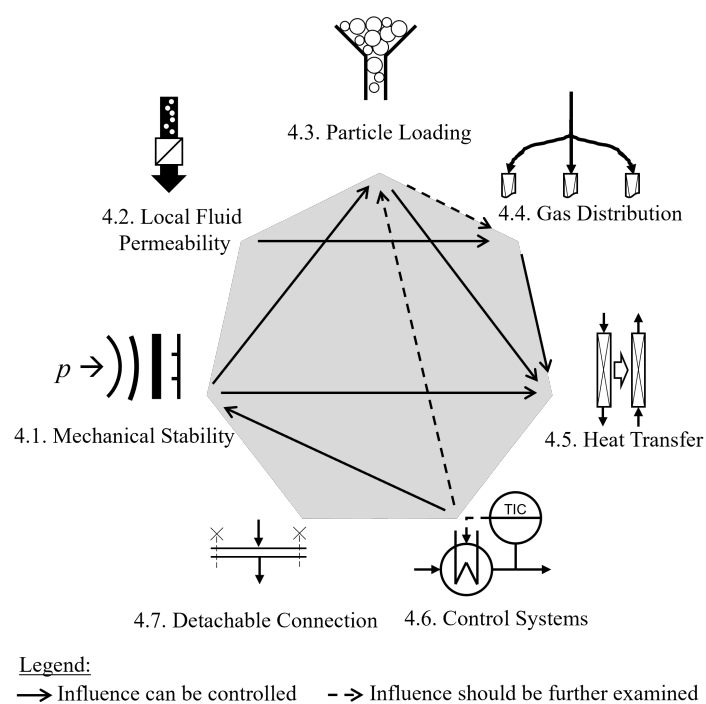


**Figure 4.48.:** Fully additive reactor during bubble-test. Note bubbles coming out of the side of the reactor-flange.

The hybrid approach was much cleaner and faster. After some fine-tuning, it led to a leak-tight and pressure-resistant reactor. During all experiments, the hybrid-additive connection was never a source of leaks or instability.

### **4.8. Interim Summary of Design for Reactor Subfunctions**

After reactor subfunctions have been investigated, a statement on the interactions can be made. These interactions of the AM packed-slit reactor concept are shown as schematic in fig. 4.49. First, there are subfunctions that do not interact at all (no arrow). Second, there are interactions that are known and can be controlled (solid arrow). Third, there are influences that should be further investigated (dashed arrow). Mechanical stability influences particle loading and heat-transfer under known mechanisms. A slit is stable under constant boundary conditions (load, wall thickness, material) with varying internal structures as long as the distances between internal structures are small enough and the density is high enough. But if distances get too low, particle loading will be hindered. The influence of internal structures on heat transfer depends on whether convective or evaporation cooling is considered. Both cooling strategies reacted differently to pins arrangement and size. Local fluid permeability influences gas distribution with the pressure drop it induces. Particle loading influences gas distribution if it is not uniform over multiple channels, which has to be further investigated. Particle loading influences heat transfer by increasing the transfer rate by about 50 % under otherwise constant conditions. Other than expected from literature, heat transfer coefficients were independent of particle diameter. Gas distribution, or more generally: fluid distribution, influences heat transfer via the mass flux or, in other words fluid velocity or Re number. Control systems integration can influence particle loading, just like internal structures for mechanical stability did when being too narrowly spaced. A thermocouple or heating cartridge channel being guided through a slit poses an obstruction of the particle bed which has to be further investigated. This should not be significant if the remaining space does not become too small relative to particle size. Control systems integration has an influence on mechanical stability, which will be considered in the design of a device. The detachable connection, which is only bordering the region where the other subfunctions act, has no interactions with any of them. It is, however, indispensable for the heterogeneous catalytic reactor concept and a big lever for printing economics.



**Figure 4.49.:** Packed-bed reactor subfunctions. Interactions within the AM packed-slit reactor concept.



## 5. Integrated Test of Packed-Slit Reactor Concept

The author's findings described in this section have been partially published in Ref. [278]. Some details have been slightly altered and wording has been partially revised to facilitate reading. The goal of this research being development and demonstration of a reactor concept that can be scaled-up to production size, the reactor experiments were intended as laboratory-scale proof of the concept and as a baseline for further optimization. Measurement of data relevant for kinetic parameter estimation was not in the work scope. The test rig used for this investigation featured an oil thermostat for controlling the reactor temperature.

The objective for the reactor was to produce as much Fischer-Tropsch synthesis (FTS) raw product per time and catalyst amount as possible while maintaining excellent control over temperature and in turn product quality, good product quality being defined as low methane selectivity  $S_{CH_4}$ , high C5+ selectivity  $S_{C5+}$ , and high chain-growth probability  $\alpha_{ASF}$ . This was challenging, as high productivity happens at a high flow rate, temperature, and conversion, being coupled to the highest heat release from the catalyst. Productivity was related to C5+, which is the raw FTS product or hydrocarbons liquid (oil) and solid (wax) at ambient conditions. Given proper upgrading in a real plant, this could be transformed into norm-conforming gasoline, kerosene, diesel, and/or wax. The volume available for the catalyst was defined as the volume of the reaction zone within the AM part minus the volume of internal structures. It was estimated as  $V_{cat}=4.0$  mL. The initial design values (refer to section 2.4) for the lab-scale reactor were:

- loading of catalyst with a particle size of  $d_p=100-150$   $\mu m$ ,
- performing FTS with undiluted catalyst and synthesis gas at  $H_2/CO = 2.0$  and modified space velocity  $SV_{mod}=\dot{n}_{total}/V_{cat}=2$  to  $10$   $L_N g_{cat}^{-1} h^{-1}$  ( $\tau_{mod}=0.1$  to  $0.5$   $h g_{cat} L_N^{-1}$ ) at the highest possible temperature,
- scalability achieved with modular slit design,
- spatially resolved  $T$  measurement to confirm efficient cooling [58],
- possibility of connection to standard laboratory equipment,
- streamlined workflow from fabrication to operation,
- operating pressure of 20 barg and temperature of 250 °C [67],
- reduction temperature of 400 °C at 0 barg [49, 279], and
- Helium standard leakage rate at  $q_{He}<1 \times 10^{-8}$  mbar  $L s^{-1}$ , [160].

The following subsections describe the design and manufacturing (section 5.1), the comprehensive testing phase (section 5.2), and the obtained results (section 5.3).

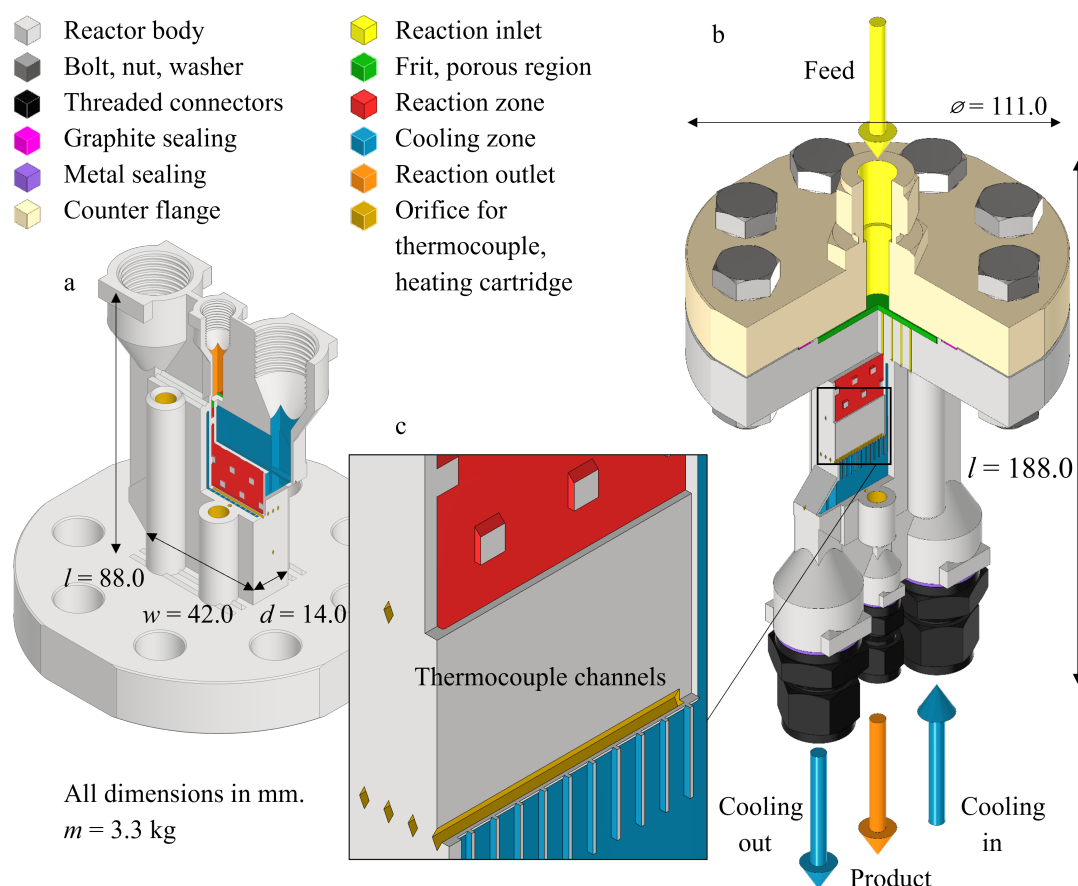
### 5.1. Design and Manufacturing

Several design revisions were made (fig. B.9) and fabricated in order to arrive at a fully functional laboratory reactor.

### 5.1.1. Design

The final reactor was designed as a slit reactor (fig. 5.1), based on modules which were thoroughly investigated in the previous chapter 4. The slits belonged alternately to the reaction zone (slits 2 and 4) and the cooling zone (slits 1, 3 and 5). The slits had a depth  $d_{\text{slit}}=1$  mm, width  $w=40$  mm and length  $l_{\text{cat}}=55$  mm (cooled length = 53 mm) and contained internal structures. The wall thickness was  $t_w=1$  mm. The reaction zone contained square pins with a side length  $t_p=2$  mm in a hexagonal arrangement with a spacing  $a=6.6$  mm, resulting in a volume fraction  $\varphi \approx 0.1$ . The ratio of the catalyst volume  $V_{\text{cat}}$  to the heat transfer surface  $A_{\text{hex}}$  was approx.  $2000 \text{ m}^{-1}$ .

This paragraph is written with the operation situation in mind. In the chemical experiments the gas flowed through from top to bottom. The cooling zone contained fins with a thickness of  $t_f=0.3$  mm and a distance of  $t_e=2$  mm. The thermal oil flowed through from top to bottom, while the inlet and outlet were located lateral on the sides of the reactor body. There were no fins in these areas.

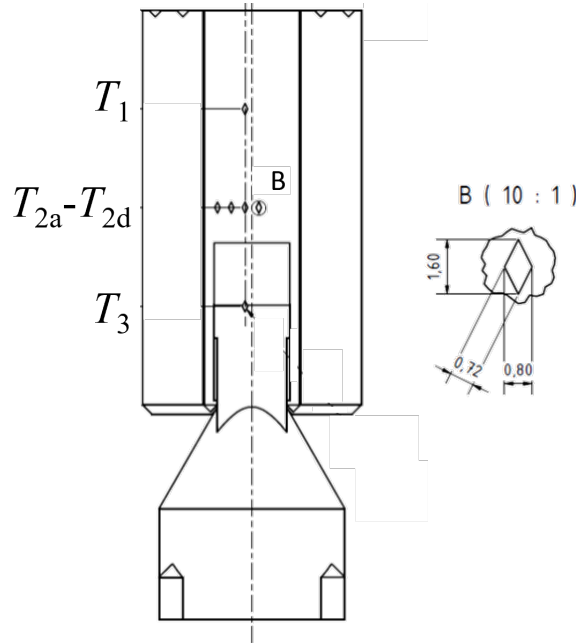


**Figure 5.1.:** Computer aided design (CAD) representation of reactor with parts cut out to show internal structure. (a) Manufacturing situation. (b) Filling and operating situation. Feed flow from the reaction inlet (yellow) through the reaction zone (red) to the reaction outlet (orange), passing through fluid-permeable regions (green). (c) Detailed view.

For spatially resolved temperature measurement, six horizontal thermocouple channels were placed inside the reactor, extending from the side to half the width of the device. Three channels were evenly distributed along the length of the reaction zone ( $l_1=13.7$ ,  $l_2=27.5$ , and  $l_3=41.3$  mm from the flange) in a wall between the reaction and cooling slits. At length  $l_2$ , three channels were positioned in further walls between the slits. The cross section of these channels was a rhombus at the tip. The readings of



these thermocouples were referred to as  $T_1$ ,  $T_{2a}$  to  $T_{2d}$ , and  $T_3$  (fig. 5.2). Two cylindrical channels for heating cartridges and one for a thermocouple were positioned both at the front and at the back of the reactor.



**Figure 5.2.:** Drawing of reactor with thermocouple holes.

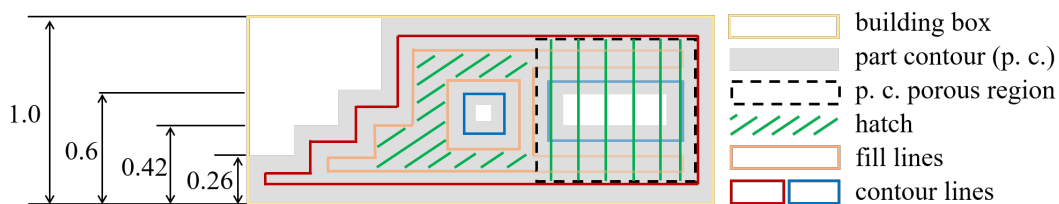
The following paragraph is described with the fabrication situation in mind. At the top end of the reaction slits, a fluid-permeable region was manufactured simultaneously with the dense walls of the reactor. The fluid-permeable region held the catalyst in place but allowed fluids from the reaction zone to pass through to the G1/8" taps. The inlet and outlet of the cooling zone were both routed upward to G1/2" taps that terminated at the same level as the reaction port. This unit complied with most design guidelines for PBF-LB/M [149], e.g. it contained no overhanging surfaces with an angle to the building plane below the threshold of  $\beta < 45^\circ$ . In smaller sections, wall thicknesses below the recommendations  $t_w = 0.26 \text{ mm} \leq 0.6 \text{ mm}$  occurred. Preliminary tests showed that printed horizontal top surfaces ( $\beta = 0^\circ$ ) should be avoided, as they could potentially lead to leakage. Therefore, zigzag volumes were added to such surfaces.

### 5.1.2. Manufacturing

The reactor was built with a hybrid approach. A conventionally fabricated flange plate was placed in the laser-based powder bed fusion of metals (PBF-LB/M) machine as a base for the AM part. Both parts were fused together during the fabrication process to form the monolithic reactor body as shown in fig. 5.1. The scanning strategy for the solid walls included hatching with a rectangular pattern and rotation between layers as well as double scanning of both the fill line and the contour line. The scanning strategy for the fluid-permeable region comprised only non-rotating hatching [211]. Here, melting tracks were one upon the other, and the distance between two adjacent melt tracks was as small as possible, but large enough to avoid inter-track fusing,  $d_{\text{perm}} \approx 30 \mu\text{m}$  (fig. 5.3).

Fabrication was performed on a DMG MORI Realizer SLM125, using 316L stainless steel powder, and took 20 h, with no subsequent heat treatment required. The design of the reactor body did not require





**Figure 5.3.:** Reactor scan strategy. Depending on their size, features were made with contour lines, fill lines, and hatching. A porous area can be seen on the right. It overlapped with the solid region and consisted entirely of hatching.

support structures, so almost no post-processing was required (fig. 5.4). The following machining operations were performed on the connections using an numerically controlled mill and manual tools: finishing and chamfering of the threads and milling of the upper level, holes for the heating cartridge were drilled and reamed, male threaded connections with metal gaskets (Swagelok) were connected to the reactor.

The reactor was thoroughly vacuum cleaned and depowdered before being rinsed with isopropanol. It was then subjected to an ultrasonic bath with water and detergent for 30 min before being dried in an oven.

## 5.2. Experimental Procedure

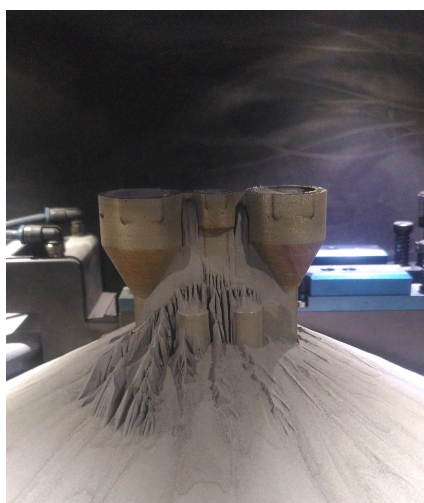
This section describes catalyst, reactor preparation, test rig and analytics, and the steps of continuous Fischer-Tropsch synthesis experiments. All materials used are listed in appendix C.

### 5.2.1. Catalyst

A Co-Pt-Si/ $\gamma$ -alumina catalyst was prepared by incipient wetness co-impregnation of cobalt nitrate ( $\text{Co}(\text{NO}_3)_2 \cdot 6 \text{H}_2\text{O}$ ) and platinum nitrate ( $\text{Pt}(\text{NO}_3)_2$ ). Tetraethoxysilane ( $\text{C}_8\text{H}_{20}\text{SiO}_4$ ) was impregnated in a subsequent separate step on  $\gamma\text{-Al}_2\text{O}_3$  support (Puralox SCCa 5–150,  $A_{\text{BET}}=140 \text{ m}^2 \text{ g}^{-1}$ ,  $V_{\text{pore}}=0.46 \text{ mL g}^{-1}$ , and  $d_{\text{pore}}=13.2 \text{ nm}$ ). The catalyst was dried in a rotary evaporator ( $T=80^\circ\text{C}$ , 60 min) and calcination was carried out under continuous air flow at  $T=250^\circ\text{C}$  (ramp  $2 \text{ K min}^{-1}$ ,  $1 \text{ L}_\text{N} \text{ g}_{\text{cat}}^{-1} \text{ h}^{-1}$ ) for 4 h. After the calcination, the catalyst was sieved, and a 50–150  $\mu\text{m}$  particle size fraction was collected. The resulting catalyst had 21.4 wt-% cobalt, 0.2 wt-% platinum, and 1.6 wt-% silicon. A platinum promoter assisted hydrogen reduction, and silicon was added to prevent support leaching. The catalyst was supplied by Technical Research Center of Finland and sieved to  $d_p=100\text{--}150 \mu\text{m}$ . [33]

### 5.2.2. Reactor Preparation

With the counter-flange and a preliminary polymer gasket the standard He leak rate of the reactor was determined using a PhoenixXL leak detector by Leybold GmbH (Cologne, Germany). A pressure test with water was performed. The reactor was then dried and reopened. Both reaction slits were filled with half of  $m_{\text{cat}}=3.3357 \text{ g}$  each. With the catalyst bed density  $\rho_{\text{cat}}=0.978 \text{ mL}$  calculated in section 4.3.4 it can be said that with  $V_{\text{cat}}=3.41 \text{ mL}$  not the entire space available for catalyst was filled with it. Clearly the catalyst bed was fully within the zone that was cooled by thermal oil. The total volumetric flow rate was  $\dot{V}_{\text{total}}=6.2\text{--}30 \text{ L}_\text{N} \text{ g}_{\text{cat}}^{-1} \text{ h}^{-1}$ . This resulted in space velocity ( $SV$ )= $\dot{V}_{\text{total}}/V_{\text{cat}}=1760$  to  $8800 \text{ h}^{-1}$  or



**(a)** Hybrid-additive manufacturing reactor during depowdering. The upper end of the reactor is visible above the powder that has flow characteristics almost like a liquid due to its fine grain size.



**(b)** Hybrid reactor after post-processing. Note different surface of conventionally and additively manufactured sections.



**(c)** Hybrid reactor with counterflange and accessories.

**Figure 5.4.:** Hybrid manufacturing of reactor.

$\tau=1.14 \times 10^{-4}$ – $5.68 \times 10^{-4}$  h=0.41 to 2.1 s. Remaining space on top of the catalyst bed was filled with SiC with  $d_p=200$ – $300 \mu\text{m}$  not diluting the catalyst. A porous metal frit was added to the reactor and the counter flange was secured with a graphite gasket using eight M12 bolts. The bolts were tightened until the gasket was sufficiently compressed to  $t=0.6 \text{ mm}$ , which was checked with a feeler gauge between the flanges. The reactor was also equipped with thermocouples and heating cartridges, which were coated with thermal paste prior to insertion.

### 5.2.3. Test Rig and Analytics

The reactor was installed in a test rig that included: gas supply, reactor, insulation, oil thermostat, hot trap ( $T=170\text{ }^{\circ}\text{C}$ ), cold trap ( $T=5\text{ }^{\circ}\text{C}$ ), backpressure regulator, and online gas chromatograph (GC) (fig. 5.5). The feed gas was preheated in the feed line which was wrapped with heating tape. The thermal oil had a flow rate of up to  $\dot{m}=35\text{ L min}^{-1}$ .

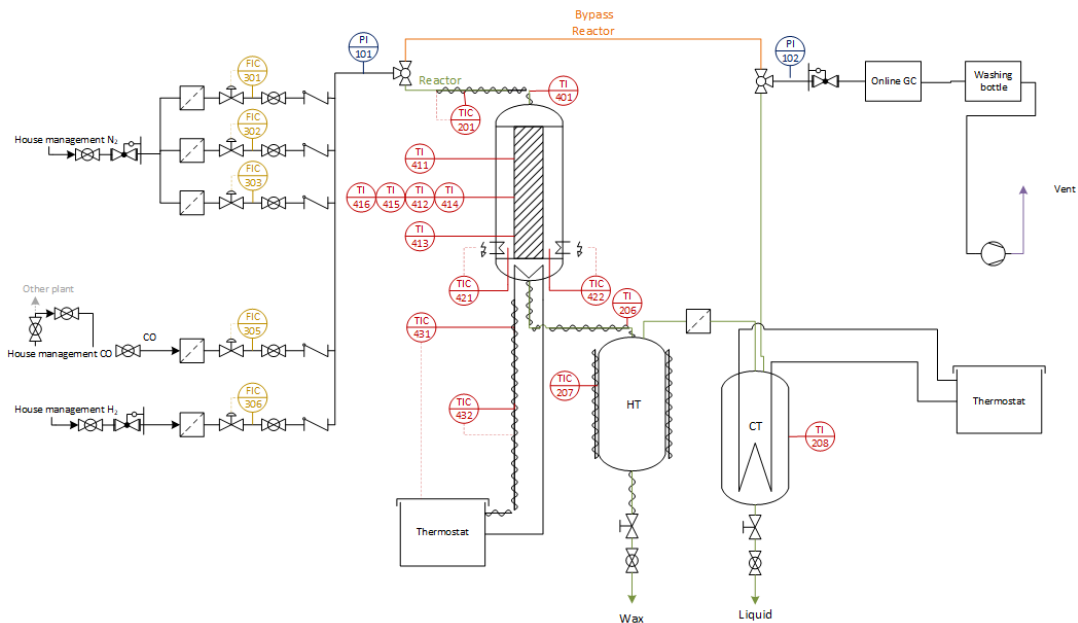
Hot and cold trap were insulated pressure vessels with a heating jacket and a cooling coil respectively. They possessed one inlet and two outlets for gaseous as well as liquid products, the latter being located at the bottom of each vessel. Oil and water were sampled from the cold trap and separated with a syringe. All samples were weighed to determine the productivity of wax, oil, and water after each setpoint.

The Agilent 6890N online GC by Agilent Technologies (Santa Clara, CA, USA) was equipped with two columns: Agilent 19095P-QO4 and Agilent 19095P-MS0.  $\text{H}_2$ ,  $\text{CO}$ ,  $\text{N}_2$  and  $\text{CO}_2$  were quantified using a thermal conductivity detector, while C1 to C7 was quantified using a flame ionization detector. Wax was sampled from the hot trap and analyzed using an Agilent 7890B offline GC equipped with a MXT-1 column by Restek GmbH (Bad Homburg, Germany) and a flame ionization detector. Oil and water were analyzed on an Agilent 7820A offline GC equipped with a Restek Rtx-1 and a flame ionization detector. The online GC was calibrated before experiments. Calibration gas mixtures with relevant composition of all measured gases were used.

Molar flows from online GC were calculated according to eq. (5.1). Mass fraction of components with  $n$  C atoms were calculated according to eq. (5.2).

$$\dot{n}_{\text{Cn,out}} = y_{\text{Cn,out}} \cdot \frac{\dot{n}_{\text{N}_2}}{y_{\text{N}_2,\text{out}}} \quad (5.1)$$

$$\omega_{\text{Cn}} = \frac{A_{\text{Cn}}}{\sum A_{\text{Cn}}} \quad (5.2)$$



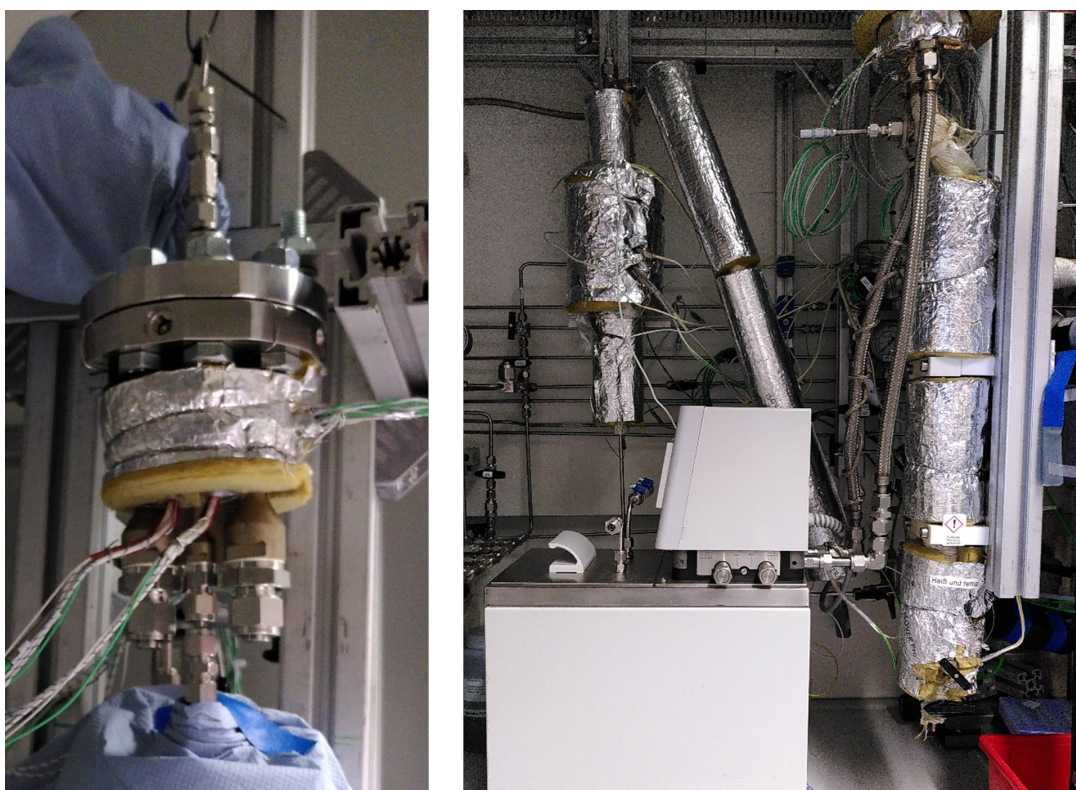
**Figure 5.5.:** Process flow diagram (PFD) of test rig used for FTS [278].



#### 5.2.4. Reduction, Activation, and Operation

The reactor was flushed with  $\dot{V}_{\text{N}_2}=200 \text{ mL}_\text{N} \text{ min}^{-1}$  to remove atmospheric oxygen. Subsequently, 10 % of the  $\text{N}_2$  flow was replaced with  $\text{H}_2$  to ensure reducing conditions during high-temperature operation. The reactor was heated at a ramp of  $1.5 \text{ K min}^{-1}$  using the heating cartridges. At  $T=400^\circ\text{C}$ , the catalyst in the reactor was reduced. This step lasted  $t = 20 \text{ h}$  at  $p = 1 \text{ bara}$  with  $\dot{V}_{\text{H}_2}=200 \text{ mL}_\text{N} \text{ min}^{-1}$  [54, 62]. Finally, the reactor was cooled and pressurized to  $p = 20 \text{ barg}$ .

The reactor was connected to an oil thermostat circulating thermal oil Fragoltherm 660 by Fragol AG (Solingen, Germany). The oil inlet line was equipped with a heat tracing system. The reactor and oil lines were fully insulated (fig. 5.6). From this point on, the temperature was controlled with the oil thermostat Proline P12 by Lauda GmbH (Lauda-Königshofen, Germany), and the heating cartridges were set to a temperature  $\Delta T=15 \text{ K}$  below the oil temperature  $T_{\text{oil}}$ . An activation period of  $t = 123 \text{ h}$  was implemented at  $T=200^\circ\text{C}$ ,  $p = 20 \text{ barg}$  with  $\dot{V}_{\text{total}}=200 \text{ mL}_\text{N} \text{ min}^{-1}$  at  $\text{H}_2/\text{CO} = 2.5$ .



**Figure 5.6.:** Pictures of reactor and oil thermostat.

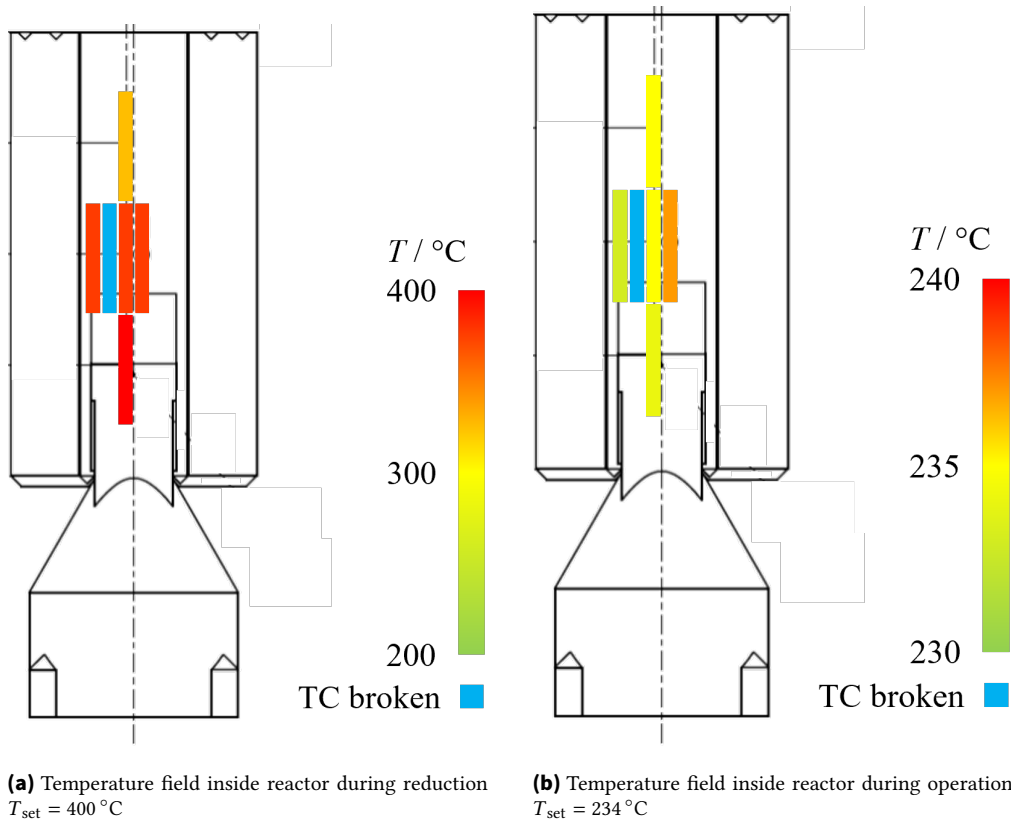
After this period, time on stream (TOS) was considered to have started. The reactor was operated at constant pressure  $p = 20 \text{ barg}$  and a ratio of  $\text{H}_2/\text{CO} = 2$  and  $\text{N}_2/\text{CO} = 0.1$  which was considered more challenging than industrial FTS and realistic for e-fuels production. Suitability of the lab-scale reactor for flexible operation in a decentralized Power-to-Liquid (PtL) plant was checked by varying the total flow rate between  $\dot{V}_{\text{total}}=6.2\text{--}30 \text{ L}_\text{N} \text{ h}^{-1}$  and the temperature between  $T=190$  and  $T=234^\circ\text{C}$ . During time on stream (TOS) = 479 h, the reactor environment was periodically checked for  $\text{H}_2$  and  $\text{CO}$ .

### 5.3. Results

This section is divided into preliminary tests, FTS experiments, and the dynamic behavior and overall performance of the reactor.

#### 5.3.1. Safety Tests and Reduction

The observed leakage rate was below the threshold of  $q_{\text{He}} < 1 \times 10^{-8} \text{ mbar L s}^{-1}$ . The pressure test with  $p_{\text{test, rct}} = 51 \text{ bar}$  and  $p_{\text{test, c}} = 20 \text{ bar}$  at room temperature was performed successfully. The reactor was found to be safe for operation. During the reduction phase, the thermocouples next to the heating cartridges reached their setpoint  $T = 400^\circ\text{C}$ , but not all thermocouples inside the reactor reached this temperature. Thermocouple  $T_{2b}$  broke apparently after the installation, showing always  $T = 20^\circ\text{C}$ . Due to the insufficient design of the heating of the feed line, the maximum temperature at which feed entered the reactor was  $T_{\text{in}} = 179^\circ\text{C}$ . Therefore, the temperature increased along the reaction axis from  $T_1 = 325^\circ\text{C}$  to  $T_{2a}$  to  $T_{2d} = 381$  to  $383^\circ\text{C}$  to  $T_3 = 398^\circ\text{C}$  (fig. 5.7a).



**Figure 5.7.:** Temperature field inside reactor during reduction (electrical heating) and operation (thermal oil heating/cooling). Mind the different temperature scales.

#### 5.3.2. Stationary Fischer-Tropsch Synthesis

A maximum CO conversion  $X_{\text{CO}} = 80\%$  was allowed. The reactor was operated for  $TOS = 479 \text{ h}$  and 15 set points were successfully tested as shown in table 5.1. Set point 1 was run at the beginning  $TOS_1 =$

0-21 h and repeated at the end  $TOS_{1R} = 446-479$  h. From the respective mean values of CO conversion of  $X_{CO,1} = 39.3$  % and  $X_{CO,1R} = 41.2$  %, it was concluded that no catalyst deactivation had occurred.

When the reactor was operated with the oil thermostat, the temperature values in the reactor were in the range of  $T_1$  to  $T_3 \in [T_{oil} - 1 \text{ K to } T_{oil} + 2 \text{ K}]$  most of the time, independent of the feed inlet temperature (fig. 5.7b). This proved that the reactor concept and cooling with oil was effective at controlling temperature even under challenging reaction conditions to be faced in a decentralized PtL plant.

Methane selectivity was low at all set points  $S_{CH_4} < 10$  %, which is an indication for the efficient cooling observed. The O/P ratio increased with decreasing conversion and increasing space velocity as indicated by van der Laan and Beenackers [37]. The highest C5+ productivity was  $\dot{m}_{C5+} = 3.43 \text{ g}_{C5+} \text{ h}^{-1}$  and occurred at set point 14. It was determined via gravimetric analysis of oil and wax phase figuring in the results from online GC for C5 to C7. This corresponded to a (modified) space time yield ( $STY$ ) =  $1006 \text{ kg}_{C5+} \text{ m}_{cat}^{-3} \text{ h}^{-1}$  and  $STY_{mod} = 1.03 \text{ g}_{C5+} \text{ g}_{cat}^{-1} \text{ h}^{-1}$ . At this set point, high conversion  $X_{CO,14} = 71.0$  %, a chain growth probability  $\alpha_{ASF} = 0.862$ , and a C5+ selectivity  $S_{C5+} = 85.7$  % were observed. The heat released by the enthalpy of reaction was approximately  $\dot{Q} = 12.6 \text{ W}$ .

For large-scale multi-tubular and slurry bubble-column reactors  $STY \approx 100$  and  $200 \text{ kg}_{C5+} \text{ m}_{cat}^{-3} \text{ h}^{-1}$  respectively are reported in literature [23]. These reactors and operating sites are huge, designed for steady-state operation, and take years to construct. Productivities  $STY \approx 1600, 1785$ , and  $1950 \text{ kg}_{C5+} \text{ m}_{cat}^{-3} \text{ h}^{-1}$  are reported for micro-structured reactors operated with much more active catalysts [46, 54, 109]. These reactors are fabricated using a variety of steps, including micromachining, diffusion bonding, further machining, and welding [54, 56].

Over the course of all experiments, the determined total output mass from the test rig (online GC measurements, wax, oil, and water sample weights) was -10.2 % compared to the mass supplied to the test rig (gas supply). For each of the set points, the deviation ranged from +7.8 to -19.4 %. This was attributed to deviations in the online GC measurement as well as incorrect sampling from the traps and spill losses. It was possible that portions of a sample were not removed from the trap and attributed to a later time period. Keeping pressure constant and avoiding hazardous material leakage required at best no gas from above the liquid sample. This was, however, less severe at setpoints with high productivity. The pressure drop was not significant. No  $H_2$  or CO was detected in the reactor environment during testing.

### 5.3.3. Dynamic Operation

The CO conversion was fitted to a model equation in the form of eq. (2.14). The fit seen in eq. (5.3) had a coefficient of determination exceeding 0.95. In fig. 5.8 it is clearly visible that the fit was in good accordance with experimental data points.

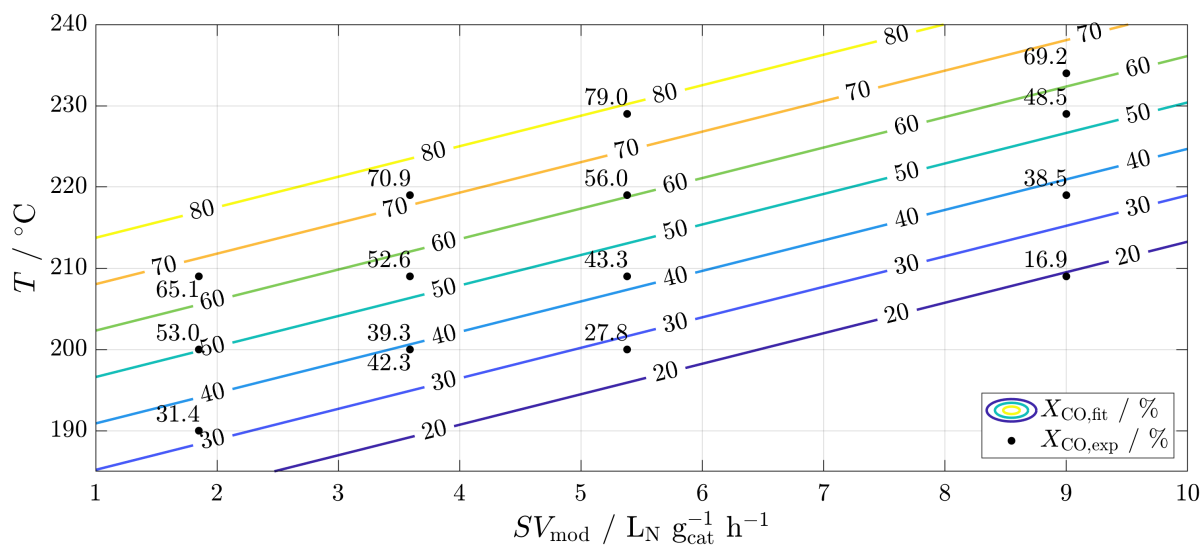
$$X_{CO,fit} = -287.5 - 6.572 \cdot SV_{mod} + 1.750 \cdot T \quad (5.3)$$

From the fit, it was deduced that the reactor design is capable of maintaining constant high conversion at different loads by adjusting temperature. The load would be the incoming feed which, in a decentralized plant, is dictated by the supply of renewable energy. With this reactor,  $X_{CO} = 70$  % could be maintained from  $\dot{V}_{total} = 30 \text{ L}_N \text{ h}^{-1}$  (100 % load) to  $\dot{V}_{total} = 6 \text{ L}_N \text{ h}^{-1}$  (20 % load) by adjusting the temperature from about  $T = 238$  to  $210$  °C. Regarding the dynamics of the reactor and its periphery, the following was observed: 1. the MFCs adjusted each new flow rate within seconds, 2. the thermostat had a heating rate

**Table 5.1.:** Overview of experimental set points and results. Constant for all set points were  $p = 20$  barg;  $H_2/CO = 2$ ;  $N_2/CO = 0.1$ .

N.	$T / ^\circ C$	$SV_{mod} / L_N$ $g_{cat}^{-1} h^{-1}$	$\dot{V}_{total} /$ $L_N h^{-1}$	$\dot{m}_{C5+} /$ $g_{C5+} h^{-1}$	$X_{CO} / \%$	$X_{H_2} / \%$	$S_{C1} / \%$	$S_{C2} / \%$	$S_{C3} / \%$	$S_{C4} / \%$	$S_{C5+} / \%$	$O/P / -$	$\alpha_{ASF}^{-1} / -$
1	200	3.59	12.0	0.43	39.3	36.7	4.3	0.6	2.1	2.2	90.8	1.81	
2	209	3.59	12.0	0.55	52.6	51.5	5.2	0.6	2.3	1.0	90.8	0.94	
3	219	3.59	12.0	2.82	70.9	72.4	6.4	0.8	2.5	1.1	89.2	0.63	
4	219	5.38	17.9	1.38	56.0	55.8	6.8	0.8	2.8	1.4	88.1	0.79	
5	229	5.38	17.9	2.77	79.0	80.6	7.5	0.9	2.6	1.3	87.7	0.47	
6	209	5.38	17.9	0.81	43.3	41.2	6.1	0.7	2.5	1.2	89.6	0.92	
7	200	5.38	17.9	0.46	27.8	26.5	5.2	0.6	2.0	2.1	90.0	2.06	
8	209	1.85	6.2	1.41	65.1	67.7	6.9	0.9	2.9	1.3	88.1	0.62	
9	200	1.85	6.2	0.49	53.0	53.5	6.4	0.8	3.2	1.6	88.1	0.83	
10	190	1.85	6.2	0.28	31.4	31.2	6.5	0.8	3.3	2.8	86.5	1.50	
11	209	9.00	30.0	0.58	16.9	16.6	9.2	1.2	3.4	3.7	82.5	2.15	
12	229	9.00	30.0	2.07	48.5	50.5	8.8	1.1	3.4	1.7	85.0	0.81	
13	219	9.00	30.0	1.15	38.5	38.4	6.2	0.8	2.4	1.0	89.6	1.14	
14	234	9.00	30.0	3.43	69.2	71.0	8.6	1.1	3.0	1.6	85.7	0.54	0.862
1R	200	3.59	12.0	0.54	42.3	41.2	4.8	0.6	2.2	1.6	90.9	1.30	

<sup>1</sup> Related to C28 to C32.



**Figure 5.8.:** Experimental and fitted results for CO conversion in the plane generated by modified space velocity and temperature.

of about  $0.5 \text{ K min}^{-1}$ , and 3. the thermostat had a cooling rate (passive cooling) of about  $-1 \text{ K min}^{-1}$ . This meant that such an adjustment happened within one online GC measurement (about 1 h) in this experimental set-up, as can be seen in the annex after set point 14.

#### 5.3.4. Interim Summary Integrated Test

Clearly, a reactor concept suitable for decentralized production of sustainable aviation fuels (SAF) was demonstrated. The laboratory-scale reactor was successfully operated under fluctuating input conditions for FTS. The catalyst and syngas not being diluted and modified space velocities of up to  $SV_{\text{mod}} = 10 \text{ L}_N \text{ g}_{\text{cat}}^{-1} \text{ h}^{-1}$  are characteristic to decentralized SAF production. A high productivity of FTS raw product above the productivity of conventional industrial reactors was achieved at  $STY = 1006 \text{ kg}_{\text{C5+}} \text{ m}_{\text{cat}}^{-3} \text{ h}^{-1}$ . The reactor is ready for operation with an even more active catalyst. Catalyst particles with low diameter  $d_p = 50 \mu\text{m}$  for low intra-particle mass transfer limitation can be held in place by the locally porous region (see also section 4.2).

Readings of six thermocouples in the reactor wall close to the catalyst zone being close to the thermal oil temperature confirmed that temperature management was excellent even at high flow rate and temperature. High C5+ productivity, high chain-growth probability  $\alpha_{\text{ASF}} = 0.862$ , and low methane selectivity  $S_{\text{CH}_4} < 10 \%$  were observed. No catalyst deactivation was observed. The reactor was operated with up to  $X_{\text{CO}} = 70 \%$  and  $T = 234^\circ\text{C}$ .

Utilizing function integration and design freedom, the additive manufacturing (AM) reactor required less sealing surfaces and assembly steps compared to a conventional micro-reactor for FTS [56, 280]. The planar packed-slit reactor concept is inherently scalable and can be manufactured efficiently with a combination of a conventional flange plate and PBF-LB/M. The concept is especially suitable for laboratory-scale reactors and can be directly connected to standard lab equipment via male threaded connectors and nut-ferrule pipe connections. The reactor achieved leakage-free operation up to  $p = 20$  barg and up to  $T = 400^\circ\text{C}$  with wall thicknesses of 1 mm or less.

Mass-spectrometry would be beneficial for a more in-depth investigation of reactor behavior under dynamic input conditions, as the analysis happens much faster than gas chromatography [137].



For scaled-up reactors, thermal oil cooling should be replaced by convective or, ideally, partially evaporating water cooling. This would mean significantly lower flow rates for the same cooling performance and in turn less pump power required (see also section 4.5). Furthermore, thermal oil is combustible and harmful to the environment [281]. Gruber [204] points out that saturated steam at up to  $p=33.5$  bar or  $T=240$  °C becomes super-heated steam when expanded to a lower pressure. In an integrated PtL plant, this super-heated steam could be used as heat source for direct air capture (DAC) or on a material level as feed for high-temperature electrolysis [35].

## 6. Scalability of Reactor Concept

This chapter comprises an investigation whether the proposed reactor concept can be scaled up to such capacities as required for industrial decentralized production of sustainable aviation fuels (SAF). As stated before, there are commercially available micro-structured reactors (MSRs) for Fischer-Tropsch synthesis (FTS) with capacities in the range of 20-30 barrel d<sup>-1</sup> (section 2.3.3). This capacity should also be ultimately aimed for with the additively-manufactured (AM) packed-slit reactor concept for decentralized SAF production.

Subfunctions of the packed-slit reactor concept have been investigated and a lab-scale reactor has been tested successfully. Based on these findings it will be discussed how the concept can be scaled up and what limitations exist. It will be discussed whether the comparatively expensive additive manufacturing is economical on a large scale.

As a starting point, the concept will be explained. Theory on scale-up of MSR will be discussed in section 6.1. Design improvements are the subject of section 6.2. In section 6.3, material and energy consumption of fabrication are highlighted before cost estimation and results of a Round Robin comparison are shown in section 6.4. The chapter will be concluded with a summary of the findings and a statement whether the additive manufacturing (AM) reactor concept is possible and economic on the large scale (section 6.5).

The packed-slit reactor concept comprises the following parts:

- reaction zone consisting of slits with a depth of one to several mm and common inlet and outlet,
- catalyst particles with  $d_p=50-200\text{ }\mu\text{m}$  fixed in the reaction zone slits,
- cooling zone consisting of slits with a depth of around one mm and common inlet and outlet,
- separating walls between slits,
- external walls to the environment, and
- a flange plate that is used as base plate for the AM process and that incorporates at least the reaction zone inlet to load/unload the catalyst.

The following is a direct consequence of the design or can be integrated into the design and fabricated simultaneously in the AM step:

- pressure-resistant and leak-tight casing,
- complex-shaped heat transfer-enhancing internal structures,
- inlets and outlets are moved to the conventional flange plate,
- few remaining sealing surfaces have standard connections like taps and flange pair,
- channels for sensors and raw channels for heating elements, and
- locally fluid-permeable regions holding catalyst particles in place.

With exceptions, a part with similar features can be manufactured from sheet metal without AM but with a process called diffusion bonding (DB), chapter 3. Both manufacturing routes are shown in fig. 3.1. The AM packed-slit reactor concept will be compared to DB reactors. This objective of project Kopernikus P2X was executed in cooperation with Ineratec GmbH. The comparison was done based on

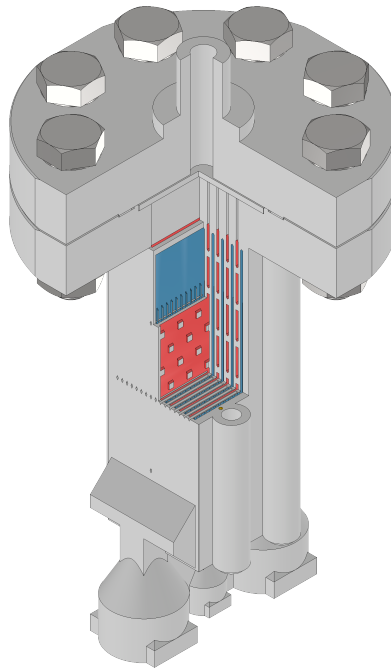
results from AM reactors that were manufactured and tested, that were designed in CAD, or based on thorough estimations.

## 6.1. Scale-Up Aspects

According to Brandner [108], there are three possible approaches to increase the throughput of micro-structured devices:

### 6.1.1. Internal Numbering Up

Alternatively also called "equaling", internal numbering-up is an approach by which the non-characteristic dimensions and/or the number of channels are increased. Non-characteristic dimensions are those not influencing the limiting heat and mass transfer steps. In this case, the length was a non-characteristic while the slit depth was a characteristic dimension. The chapter 5 reactor had a catalyst volume of  $V_{\text{cat}}=4 \text{ mL}$  and a total mass of  $m=3.25 \text{ kg}$ , of which  $m_{\text{AM}}=0.43 \text{ kg}$  was additively manufactured. The reaction volume was scaled up by factor 8 to  $V_{\text{cat}}'=30.2 \text{ mL}$  by increasing the length to  $l_{\text{cat}}=107 \text{ mm}$  and the number of channels to eight (fig. 6.1).

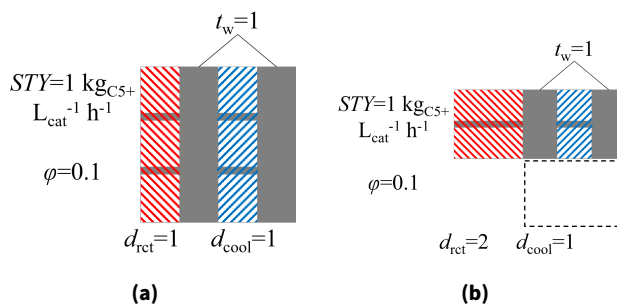


**Figure 6.1.:** Computer aided design (CAD) representation of internal numbering-up of the reactor from chapter 5. Parts cut out to show internal structure.

While reactor length was regarded as a non-characteristic dimension, by far the most important characteristic dimension, the slit depth, was kept constant at  $d_{\text{slit}}=1 \text{ mm}$ . With this approach, the temperature control should be equally good. The weight of the AM part increased to  $m_{\text{AM}}=1.2 \text{ kg}$  and that of the entire part to  $m=4.02 \text{ kg}$ . The production time with an optimized scanning strategy would be about two days on the same printer. Neither fabrication nor testing could be carried out due to time constraints, though.

### 6.1.2. Scaling

An example of scaling was created in section 4.5 by increasing the characteristic dimension slit depth. The experiments revealed that heat transfer was independent of the slit depth in the investigated range of  $d_{\text{slit}}=4\text{--}12\text{ mm}$ . Piermartini et al. [55] also confirmed that FTS performance was almost independent of the channel depth being 0.8 or 1.5 mm. This means that more catalyst volume up to a certain limit is possible with the same reactor mass, fig. 6.2. This is a big lever for decreasing cost of reactor fabrication, as will be shown in table 6.1.



**Figure 6.2.:** Schematic representation: slit depth was increased from (a) to (b). While the catalyst volume stayed constant, the required volume of walls and cooling zone relatively decreased. All dimensions in mm.

### 6.1.3. External Numbering Up

Alternatively named simply "numbering-up", this approach employs the connection of several identical devices. This can be done if and when internally numbered-up and scaled-up devices reach their size limits but are still not sufficient. While the multitude of required control loops and connections between devices are a disadvantage, the possibility of performing maintenance on some units while others keep operating is a clear advantage. As this option is independent of the design and fabrication method of the single device, it will not be discussed hereafter.

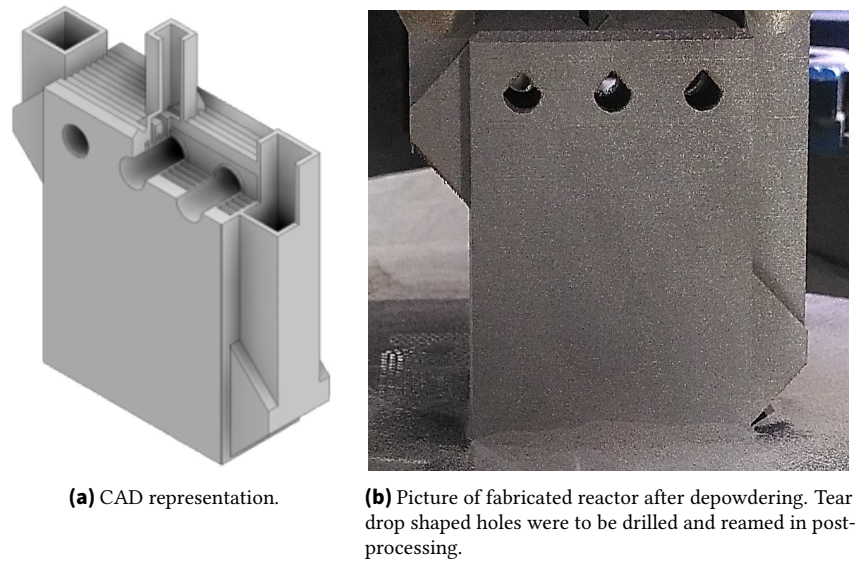
## 6.2. Design Improvement

With growing experience from the work on packed-slit reactors and modules, the following improvements were identified and partially demonstrated:

### 6.2.1. Optimized Design for Operation

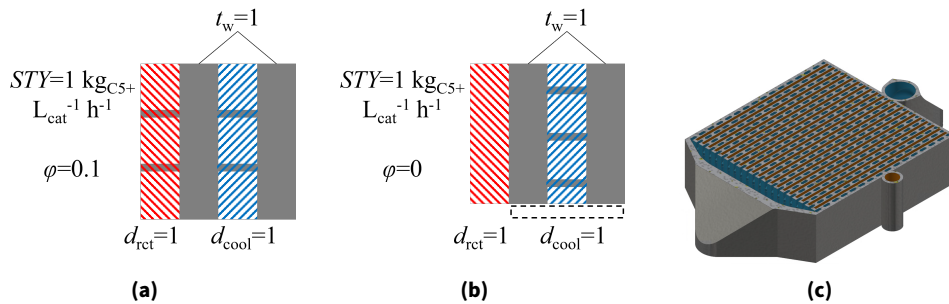
As documented in chapter 5, the high temperatures required for catalyst reduction were not uniformly reached in the reactor with vertical heating cartridges. It was assumed that heat transfer was insufficient from the front and back walls to the reactor center. This would be even more critical in reactors of larger size. Successful scale-up requires optimization. In consequence, holes for heating cartridges, penetrating the entire reactor body, were then designed horizontally instead of vertically (fig. 6.3).

The removal of spent catalyst remained a challenge. One approach was the design of reaction slits without internal structures (fig. 6.4c), which required the stability of the design to come from other features, though. With this design change, catalyst could be removed with the help of tools like a



**Figure 6.3.:** Reactor with horizontal holes for heating cartridges.

scraper. Furthermore, the volume having been occupied by internal structures (volume fraction  $\varphi=0.1$ ) would then be available for catalyst.

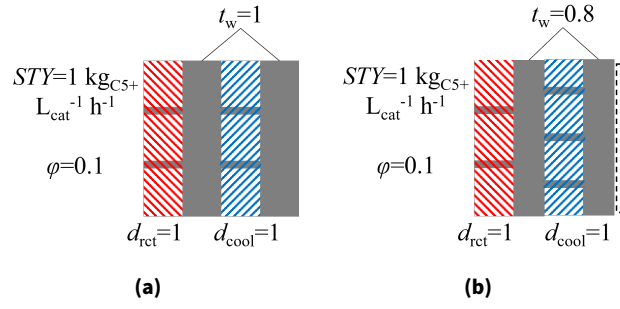


**Figure 6.4.:** Schematic representation: internal structure was removed from (a) to (b). While the catalyst volume stayed constant, the required volume of walls and cooling zone relatively decreased. All dimensions in mm. In (c) a possible execution of this is shown as CAD representation with the reaction zone colored in orange being without internal structures and the cooling zone colored in blue containing internal structures.

### 6.2.2. Optimized Design for Fabrication

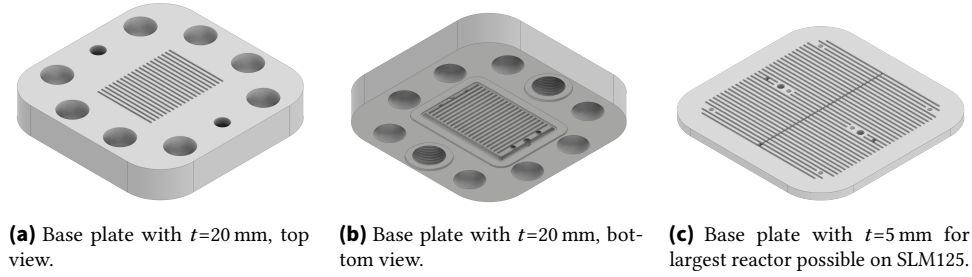
During the course of this thesis, the wall thickness was reduced, temporarily even below the standard design guidelines. However, as this led to an increased rate of unsuccessful print jobs, it was not pursued any further. A wall thickness of  $t_w=0.8 \text{ mm}$  is state of the art and should be sought after in future designs since it contributed to a higher relation of catalyst volume to required construction material, fig. 6.5

Up to this point, the hybrid manufacturing base plate had been fabricated from a standard pipe fitting. Eight slits had been manufactured into the circular blind flange. A novel base plate had a rectangular shape, to better utilize the printing space of the SLM125, and 20 slits, figs. 6.6a to 6.6b. The reactor depicted in fig. 6.7 was designed for this novel base plate by Georg Rabsch (IMVT). It had a volume available for catalyst of  $V_{cat}=130 \text{ mL}$ . The features of the reactor concept repeated at the beginning of

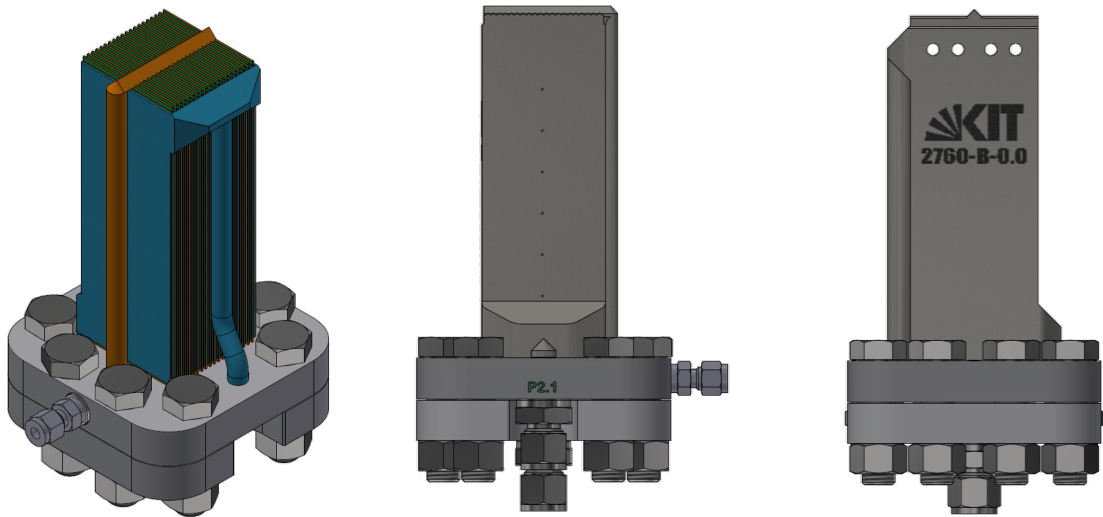


**Figure 6.5.:** Schematic representation: wall thickness was decreased from (a) to (b). While the catalyst volume stayed constant, the required volume of walls relatively decreased. All dimensions in mm.

this section were complemented by optimizations: the catalyst zone was free of internal structures and the holes for heating cartridges went through the whole reactor body horizontally (figs. 6.7a to 6.7c).



**Figure 6.6.:** CAD representation of rectangular flange plates with external dimensions of  $(124 \text{ mm})^2$  for Realizer SLM125.

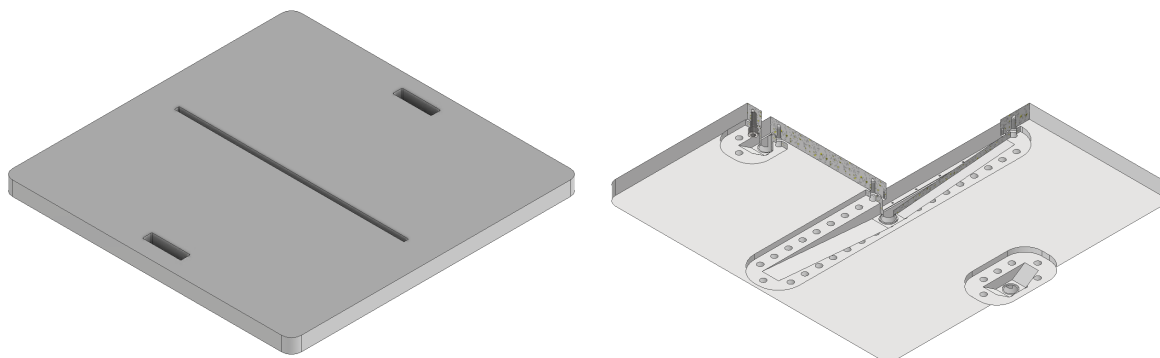


**(a)** CAD isometric view of the internal vol- **(b)** CAD front view showing holes for thermo- **(c)** CAD side view showing holes for heating  
umes of reaction zone (orange) and cooling zones (blue).  
zones (blue).  
couples.  
cartridges.

**Figure 6.7.:** Reactor design with  $V_{cat} = 130 \text{ mL}$  for rectangular base plate for SLM125.

The base plate in fig. 6.6c was designed for the printer SLM125 at Institute for Micro Process Engineering (IMVT) as well. It utilized the total available printing space and could accommodate a reactor body with a cross-sectional area of  $33 \text{ cm}^2$  and a volume of  $561 \text{ mL}$  in the reaction zone. It would, however,

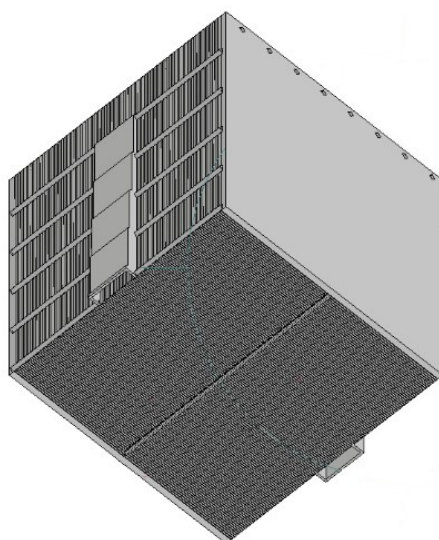
print very long and would require two flanges as depicted in fig. 2.4. Since the whole cross-section of the printing space would be occupied by reactor body, connections for coolant would have to be connected to the sides by welding in a subsequent step. Printers with much larger build space and higher build rates are available (section 3.2). Hence, even larger build plates were designed. To avoid wire electric discharge machining, a slot which distributed catalyst and flow to all slits was designed, fig. 6.8. This design was intended for a printer with a build space of  $(60\text{ cm})^3$ .



**(a)** Top view with a slot instead of slits as reaction inlet and slots as **(b)** Bottom view with adapters bolted to the slots in a three-quarter cut.

**Figure 6.8.:** CAD representation of rectangular flange plate with external dimensions of  $(60\text{ cm})^2 \times 3\text{ cm}$ .

The biggest design so far was intended for a plate with slots. In the bottom view of the reactor fig. 6.9 it can be seen that the lower end had a notch and two openings matching the slots of the base plate. The reactor was designed for production in a printer with a build volume of at least  $(60\text{ cm})^3$ , fig. 6.9, and represented a challenge in the pre-processing. The author ran out of 64 GB memory at the final design steps and also the manufacturer struggled to open the file and calculate build time. This problem needs to be solved for future work, possibly by the division of a reactor into several units, of which the file for repeating units only has to be opened once.

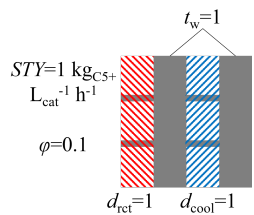
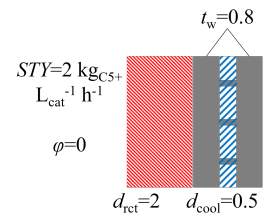


**Figure 6.9.:** Reactor design for production in a printer with a build volume of  $(60\text{ cm})^3$ .



Findings for the subfunctions in chapter 4 are not affected in a negative way by the scale-up and optimization considerations in this chapter. Other than expected, heat transfer was not decreased by increasing slit depth from  $d_{\text{slit}}=4$  to 12 mm under the conditions investigated. For the results in table 6.1, the following scale-up/optimization steps were considered: use of a more productive catalyst ( $STY=2000 \text{ kg}_{\text{C5+}} \text{ m}_{\text{cat}}^{-3} \text{ h}^{-1}$ ), removal of reaction zone internal structures ( $\varphi=0$ ), increasing reaction slit depth ( $d_r=2 \text{ mm}$ ), decreasing wall thickness ( $t_w=0.8 \text{ mm}$ ), and decreasing cooling slit depth ( $d_c=0.5 \text{ mm}$ ). In said table, only the main reactor body without base plate or connections is considered. This is justified since, for a scaled-up reactor, the main body dominates the size and material requirement. Table 6.1 estimated the build space and material requirement for a reactor with a capacity of 20 barrel  $\text{d}^{-1}$ . The scale-up and optimization are necessary to design a reactor with this capacity at a reasonable size and with reasonable material demand. Said reactor could look like the one in fig. 6.9 and would require at least around  $V_{\text{metal}}=42 \text{ L}$  of material and weigh  $m_{\text{metal}}=336 \text{ kg}$ . It could be built on printers with a build volume of at least  $V>110 \text{ L}$  like DMP Factory 500 (3D Systems), NXG XII600 (SLM Solutions), or FS721M (Farsoon Technologies). With the assumptions made at the end of section 2.3, around 860 of these reactors would be needed to produce the amount of SAF required in Germany in 2030.

**Table 6.1.:** Calculations for scale-up of packed-slit reactor concept to a capacity of 20 barrel  $\text{d}^{-1}$ .

Category	Chapter 5	Scaled-up and optimized
Schematic representation		
$V_{\text{cat}} / \text{L}$	106	53
$V_{\text{cat}}' / \text{L}$	118	53
$V_{\text{metal}} / \text{L}$	236	42
$V_{\text{bounding box}} / \text{L}$	472	109
Possible AM machines from table 3.2	EP-M1550, FS1521M, BLT-S1500	Additionally DMP Factory 500, FS721M, XLine 2000R, NXG XII 600, SLM800

### 6.3. Energy Intensity of Fabrication

In order for laser-based powder bed fusion of metals (PBF-LB/M) and the proposed concept to be scalable as well as reasonable, it has to be ecological, making a thorough examination of energy consumption indispensable: Specific energy consumption (SEC) of materials and fabrication steps is listed in tables 6.2 to 6.3. The SEC of 316L stainless steel emphasizes that material efficiency means energy efficiency. Energy consumption for the raw material production is equaled by that for the fabrication process (table 6.3). Azevedo et al. [282] reported that after gas atomization only half of the powder has the correct particle size while the other half has to be recycled. This should be optimized in the future. However, Fischmann et al. [283] found promising results on using a wider range of particle size to gain good part quality in PBF-LB/M than is currently state of the art. An energy consumption of  $\text{SEC}=250 \text{ MJ kg}^{-1}=69 \text{ kW h kg}^{-1}$  for the production of one mass unit of AM reactor is assumed. The start-up powder before a print job should always contain a sufficient amount of fresh powder. During



one year of operation of the SLM125 at IMVT around 16 kg out of 100 kg of stainless steel powder used were discarded due to increased particle size [284]. This could possibly be attributed to the sintering of metal particles or to the scattering of weld droplets. It was estimated that around 30 % of material was removed from sheet metal by milling to produce an MSR by IMVT used for instance in Ref. [54]. When sheet metal is processed with wet chemical etching, problematic liquid waste with heavy metal ions is created [285].

**Table 6.2.:** Energy consumption of fabrication materials.

Component	Fraction in 316L / wt-%	SEC / MJ kg <sup>-1</sup>	Source
Fe	0.71	10	[178, 286]
Cr	0.17	604	[286]
Ni	0.12	194	[286]
316L	-	133	
SEC of steel: 20 MJ kg <sup>-1</sup> [287]			

**Table 6.3.:** Energy consumption of powder production and PBF-LB/M manufacturing.

Step	SEC / MJ kg <sup>-1</sup>	Source
Powder gas atomization	7.6	[288]
Powder gas atomization	27	[282]
PBF-LB/M	112-140	[184]
PBF-LB/M	125-218	[289]
PBF-LB/M	97	[290]

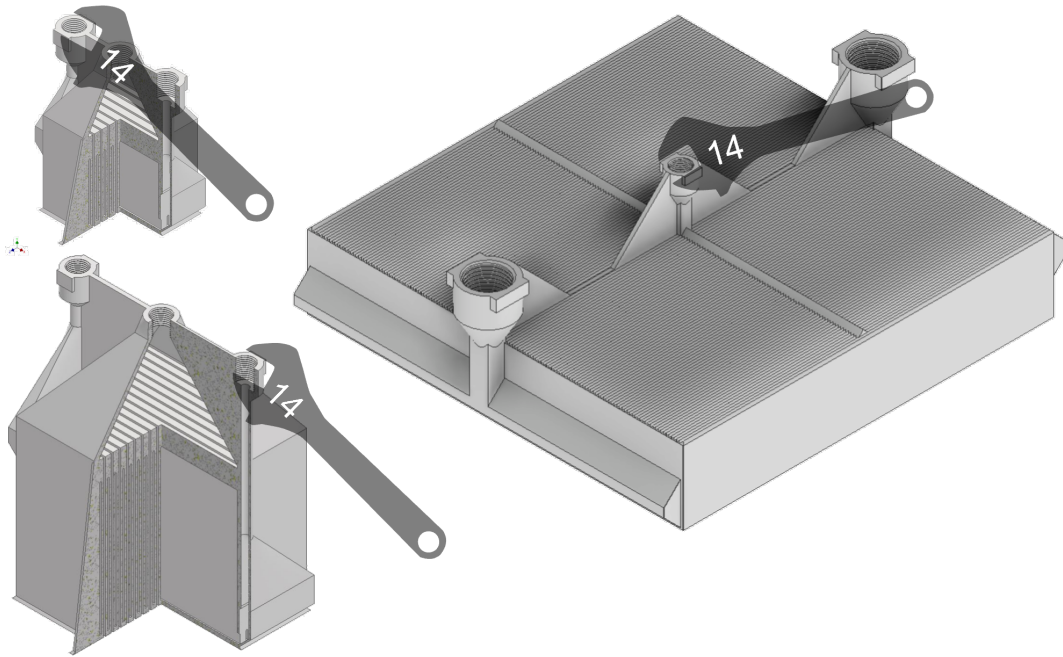
## 6.4. Fabrication Cost

Fabrication cost estimation by several authors is summarized in table 6.4.

**Table 6.4.:** Cost estimation for PBF

Cost / € g <sup>-1</sup>	Cost / € cm <sup>-3</sup>	Cost / € h <sup>-1</sup>	Comment	Build rate / cm <sup>3</sup> h <sup>-1</sup>	Year	Source
Buy						
1.36-9.38	10.84-75.05				2014	[291]
Make						
0.13	1				2023	[292]
0.48	3.83	19.14	EOSINT M270; 17-4 PH	5	2010	[293]
0.91	7.27			5	2010	[294]
0.28	2.24	11.22		5	2015	[295]
0.88	7.03				2013	[296]
1.3					2020	Own est.

Fabrication cost depends on both part shape and packing mode [172, 297]. Therefore, quotations from service providers in Germany and neighboring countries were requested. The designs for which quotes were requested are shown in fig. 6.10. These were not fully functional reactors, but realistic mock-ups. The service providers were not asked to quote on hybrid manufacturing. None of the service providers listed hybrid manufacturing in their quotations; consequently, they quoted removal of part from build plate as well. Some service providers provided advice on design details such as wall thickness.



**Figure 6.10.:** CAD representation of realistic reactor models for round-robin test.

The cost per mass compiled in the quotations table 6.5 are above the values of "make" scenario and within the values of "buy" scenario in the literature shown in table 6.4. Obviously, service providers need to make profits. Also, post-processing being a big cost factor [149], it is likely another important reason for the higher prices. It is to be noted that post-processing was reduced to a minimum in the presented concept.

**Table 6.5.:** Results of a Round Robin done with realistic reactor models of different sizes. Results for the largest arrived in December 2022 and January 2023, the rest in February and March 2022. Cost excluding value-added tax.

$V_{\text{cat}} / \text{L}$	$m_{\text{metal}} / \text{kg}$	Companies	Average cost / €	Standard deviation / €	Cost per mass / € g <sup>-1</sup>
0.013	0.47	1-7	821.31	316.22	1.76
0.102	2.5	1-3	3748.83	1230.96	1.5
0.507	5.2	1-3,5,8 <sup>a</sup>	8119.75	2402.95	1.57

<sup>a</sup> Offers included machines EOS M280 and 3DS DMP500

### 6.5. Interim Summary of Scalability of Reactor Concept

Scale-up and optimization steps for the AM packed-slit reactor concept have been identified. These steps have been carried out in designs and used for estimations of large FTS reactors. The immediate result was to reduce the amount of metal required relatively to the catalyst volume. This is advantageous considering the specific energy consumption of the AM fabrication route. Costs of fabrication have been analyzed from literature and with the help of service providers. The lower and upper bound of relative costs are applied to the scaled-up reactors to estimate fabrication cost and compare them to costs from literature and from the project partner Ineratec, table 6.6.

**Table 6.6.:** Cost and material demand of reactors up to a capacity of 20 barrel d<sup>-1</sup> that were constructed, designed, or estimated during this work.

Property	Reactors						
	constructed		designed			estimated	
$\dot{m}_{C5+}$ / barrel d <sup>-1</sup>	$7.55 \times 10^{-4}$	$2.45 \times 10^{-3}$	0.019	0.096	2.77	20	20
$\dot{m}_{C5+}$ / kg <sub>C5+</sub> h <sup>-1</sup>	0.004	0.013	0.102	0.507	14.7	106	106
$STY_{mod}$ / kg <sub>C5+</sub> kg <sub>cat</sub> <sup>-1</sup> h <sup>-1</sup>	1	1	1	1	1	1	2
$m_{cat}$ / kg	0.004 <sup>a</sup>	0.013	0.102	0.507	14.7	106	53
$m_{AM}$ / kg	0.43	0.47	2.5	5.2			
$m_{AM}/m_{cat}$ / -	128	76.7	56.0	19.5	16.0	16.0	6.4
$m_{AM,est.}$ / kg					235.2	1696	339.2
$C_{AM}$ / € (cheapest make scenario) <sup>b</sup>	55.9	61.1	325	676	30,576	220,480	44,096
$C_{AM}$ / € (costliest make scenario) <sup>b</sup>	559	611	3250	6760	305,760	2,204,800	440,960
$\dot{Q}_{C5+}$ / kW <sup>c</sup>	0.048	0.156	1.22	6.08	176	1272	1272
Energy demand / kWh <sup>d</sup>	30	33	174	361	16,323	117,702	23,540
Comparison of AM to DB reactor		x		x	x		
Was included in Round Robin		x	x	x			

<sup>a</sup> only 0.003 mL was used in experiments

<sup>b</sup> cost of metal powder already included

<sup>c</sup> based on  $LHV=12 \text{ kW h kg}^{-1}$  of diesel

<sup>d</sup> based on  $SEC=250 \text{ MJ kg}^{-1}$  for material, atomization, and AM

For the reactors listed in table 6.6 that were fabricated or designed in CAD, the following can be said: With increasing catalyst volume (productivity), the volume of metal required relatively decreased. The most material-efficient reactor (last column of table 6.6: 20 barrel d<sup>-1</sup>) would have a mass of 339 kg. Its fabrication at the lowest reported cost (0.13 € g<sup>-1</sup>) would cause expenses of 44,000 €. However, the estimations go up to ten times higher for 'make'-scenarios. This specific cost (1.3-1.8 € g<sup>-1</sup>) is where reports for 'buy'-scenarios start and where quotations from service providers lay. When following the calculation of Adelung and Dietrich [298], a conventional FTS reactor of the same capacity would have cost around 288,000 € in 2019. According to Marchese et al. [299], a conventional reactor at this capacity would even have cost around 674,000 € in 2021. The plant with the lowest construction cost

per capacity in table 2.3 is Oryx Gas-to-Liquid (GtL) with 1 B\$ for 33,000 barrel d<sup>-1</sup>. Relating this cost of the complete plant to a reactor capacity of 20 barrel d<sup>-1</sup> results in costs of 588,000 €. Ineratec GmbH disclosed that with increasing reactor capacity, the AM reactor concept had an advantage in mass and a disadvantage in cost compared to their DB reactors.

If low specific fabrication costs are assumed, AM reactors can be produced at comparable or lower prices than with conventional micro-fabrication. The sizes of reactors where this holds true have to be identified by further research. Low fabrication cost and time are both achieved with multi-laser machines [300]. Installing multiple lasers in these machines enhances their productivity more than it increases their cost [168].



## 7. Summary

A concept for the laser-based powder bed fusion of metals (PBF-LB/M)-based design of a micro-structured Fischer-Tropsch synthesis (FTS) reactor has been developed and thoroughly analyzed. It was optimized to leverage the benefits of this powder-based additive manufacturing technique (AM) and its advantages over commonly used conventional micro-fabrication methods. The reactor concept is based on planar narrow slits separated by thin walls. The slits may include one of the internal structures such as pins, fins, lattice, and/or fluid guiding element (FGE). Interfaces between additively and conventionally fabricated parts as well as cost, safety, possibility of scale-up, and performance were considered. Being ideally suited for heterogeneously catalyzed exothermic reactions, the modular design can be used for other metallic process engineering devices.

Seven important reactor subfunctions for FTS in decentralized plants were identified. The design concept for the modules performing these subfunctions was investigated one by one. The important findings for each were:

**Mechanical stability** A single slit could withstand significant internal pressure at a low wall thickness, the condition being that structures connecting its walls were adequately designed. The important design parameters were the volumetric fraction of internal structures to slit and the structures' spacing. These findings are the result of formulas validated by experiments. Figures for the design of slit modules with hexagonally arranged pins on the inside were derived. These are powerful tools for the mechanical design of the concept subject to various boundary conditions.

**Local fluid permeability** Fluid-permeable regions (permeable in the direction of build) were generated in the course of the same fabrication step as the solid reactor walls at an arbitrary location in the part. These regions can be tuned to hold back particles of a required size with a formula combining fabrication parameters and parameters for powder size distribution.

**Particle loading** Catalyst powder was loaded into slit modules with and without internal structures. Loading was considered good when the measured porosity came close to the theoretical value. This was the case for modules whose internal structures were not too fine, given that the infinite porosity fed into calculations was adjusted for the fine particles used. Otherwise, porosity was higher than expected. Porosity was not dependent on module material being metal or transparent resin.

**Gas distribution** Gas distribution is a critical feature of multi-channel devices like those featuring in the proposed concept. Uniform gas distribution could be ensured in model calculations when flow resistance in all channels was constant and larger than the flow resistance causing the non-uniformity. This flow resistance could be generated by both the packed bed and a locally fluid-permeable region.

**Heat transfer** On a theoretical level, heat transfer in micro-structured devices is still not perfectly understood. Dealing with dimensions on the larger end of the spectrum typical for micro-structured devices, experimental determination of heat transfer in both reaction and cooling were necessary, but difficult. However, it can be said that flow in the investigated devices without particles had a much higher heat transfer coefficient than expected. Heat transfer with nitrogen

in the same devices filled with particles was only slightly higher and, most importantly, not dependent on particle size. For heat transfer with water it was confirmed that partial evaporation cooling was much higher compared to purely convective cooling, notably with an effective temperature difference maintained over the complete heat transfer area.

**Control systems integration** The integration of sensors for  $p$ ,  $T$ , as well as access for measurement of composition and heaters in both conventional and additive devices were investigated, and it can be concluded that additive manufacturing (AM) allows for convenient solutions, often reducing space, labor, and the number of parts required.

**Removable connection** A detachable connection is an indispensable feature of a reactor for the application under investigation. AM can likely not play out its advantages to compensate for the extremely expensive fabrication of an AM flange plate. With hybrid manufacturing on a conventionally manufactured flange, however, the best of both techniques was used and the usually required post-processing for AM was reduced to a minimum.

From the individual experiments it was concluded that most subfunctions do not affect each other or, if they do, the influence can be controlled. An integrative test of all these subfunctions was the test of a laboratory-scale reactor with  $m_{\text{cat}}=3.3$  g of catalyst. This test further confirmed, that the combination of subfunctions did not impair the individual subfunction.

The laboratory experiments demonstrated that the proposed packed-slit reactor concept is well-designed along the complete process from fabrication to operation. Its streamlined fabrication facilitates realization of a complex reactor geometry with fewer parts and seamless integration of sensors. The production time for the described laboratory-scale reactor was about one day. Compared to other manufacturing methods, the AM reactor offers both a shorter lead time and considerably lower cost. At higher reactor capacities and lot sizes, other fabrication methods are likely to be advantageous due to economies of scale. For medium-sized reactors, as required for decentralized production concepts like those presented in Ref. [83, 301], AM is an economically viable option in serial production.

The investigation was focused on the raw FTS product C5+ or the hydrocarbons being liquid (oil) and solid (wax) at ambient conditions. This is justified since the reactor could be operated stable with varying input conditions similar to those necessary for influencing the raw product composition. The finer upgrading steps to kerosene or other products generally take place in separate, usually conventionally-manufactured, reactors anyway, having lower requirements.

## 8. Outlook

This thesis is one of many establishing the novel additive manufacturing (AM) technique, adding to its increasing popularity in chemical and process engineering. There are several interesting application opportunities to pursue, not limited to the packed-slit reactor concept, which will be presented below. The packed-slit reactor concept is, however, a validated device. Any future work in this area can employ the findings in this work and have a starting point of a working versatile reactor.

An advantage of this work is hybrid additive manufacturing: large numbers of parts (for instance geometry variations) can be manufactured efficiently and possibly used directly after the print job is finished. Another advantage is the heat transfer test rig that is ready to conduct experiments on gaseous and liquid heat transfer at elevated pressures. The test rig is mobile and could also be attached to an existing Fischer-Tropsch synthesis (FTS) test rig complementing it with a evaporation cooling circle.

### Performance

The reactor design described in chapter 5 can be revised regarding temperature control during catalyst reduction. Horizontal heating cartridges are accessible from both ends and can be pushed out from the side opposite their cables. A feed-effluent heat exchanger is promising as well. A commercial customized heating jacket can be employed to balance heat loss.

Spent catalyst (including product wax solid at standard conditions) can be removed from the reactor independent of its design by removing the frit on one end to flush out the catalyst with oil. This would be facilitated by the design of a reaction slit without internal structures. For this purpose, the mechanical load has to be taken up by the surrounding walls, see "Mechanical Stability" below. Furthermore it would allow scraping out the catalyst from the reaction slit.

More thermocouples could be included. Taps could be integrated for product sampling and subsequent composition analysis. A staged reactor with different temperature set points within one device is possible. Along the reaction axis, conditions could be adapted to result in the best possible product composition. This could be extended to executing several reactions with different catalysts within one reactor, FTS and hydro-cracking being obvious choices. While the former requires cooling, the latter would be carried out in portion of the reactor without cooling. Furthermore, the integration of a distillation step performed inside additive structures is viable [275].

Subsequent work must implement the scale-up and optimization steps into fabrication and seek certification of a larger AM reactor by a notified body.



## Fabrication

The hybrid manufacturing approach proposed in section 4.7 and chapter 5 requires wire electric discharge machined flange plates. A simpler flange plate design, not requiring wire electric discharge machining, is preferable, as it would lower cost and improve availability. Raw material for flange plates with the cross section of the Realizer printer and thicknesses between 10–20 mm were delivered to Institute for Micro Process Engineering (IMVT) and could be milled with the present machines.

An entirely monolithic design is viable and would require neither a flange pair, nor commercial frits or gaskets. In this case, however, the print job would have to be interrupted, metal powder be suctioned away, and catalyst powder be inserted before the print job could be completed. A similar approach for multi-material laser-based powder bed fusion of metals (PBF-LB/M) is described in Ref. [302].

## Heat and Mass Transfer

AM design flexibility could be employed to further improve heat and mass transfer. The fact that heat transfer was fairly independent of slit size in the modules with powder shows that more reaction volume is possible at the same good heat transfer rate. It would be interesting to find out more about heat transfer in packed beds with particles in the size of  $d_p=50\text{--}200\text{ }\mu\text{m}$ . In this work the heat transfer coefficient was lower than expected and independent of  $d_p$ . Experimental campaigns, Computational Fluid Dynamics (CFD), and the more sophisticated  $\Lambda_r(r)$  heat transfer model are promising options.

Fluid guiding element (FGE) are a fascinating invention. With suitable cages for catalyst particles, they could be used to retrofit conventional multi-tubular reactors.

## Mechanical Stability

It should be examined whether two slits with internal structures are stiff enough to stabilize a third slit without internal structures between them. Outer reactor walls could be stabilized with grid-stiffened structures. Such structures, which are common in rocket engines, are also shown in Ref. [302].

In conclusion, it can be said that the described examinations, calculations, and experiments within this thesis not only clearly prove the viability of the proposed concept for AM slit reactors, but also convincingly demonstrate its future potential. It is possible to create trust in the novel technology by thorough investigation and documentation.

## Bibliography

- [1] Valérie Masson-Delmotte, Panmao Zhai, Anna Pirani, Sarah L. Connors, Clotilde Péan, Yang Chen, Leah Goldfarb, Melissa I. Gomis, J.B. Robin Matthews, Sophie Berger, Mengtian Huang, Ozge Yelekci, Rong Yu, Baiquan Zhou, Elisabeth Lonnoy, Thomas K. Maycock, Tim Waterfield, Leitzell, and Nada Caud. *Climate Change 2021: The Physical Science Basis: Summary for Policymakers*. Jan. 1, 2021. 40 pp.
- [2] M Klöwer, M R Allen, D S Lee, S R Proud, L Gallagher, and A Skowron. “Quantifying Aviation’s Contribution to Global Warming”. In: *Environmental Research Letters* 16.10 (Oct. 1, 2021), p. 104027. ISSN: 1748-9326. DOI: 10.1088/1748-9326/ac286e. URL: <https://iopscience.iop.org/article/10.1088/1748-9326/ac286e> (visited on 10/09/2023).
- [3] D. S. Lee, D. W. Fahey, A. Skowron, M. R. Allen, U. Burkhardt, Q. Chen, S. J. Doherty, S. Freeman, P. M. Forster, J. Fuglestvedt, A. Gettelman, R. R. León, L. L. Lim, M. T. Lund, R. J. Millar, B. Owen, J. E. Penner, G. Pitari, M. J. Prather, R. Sausen, and L. J. Wilcox. “The Contribution of Global Aviation to Anthropogenic Climate Forcing for 2000 to 2018”. In: *Atmospheric environment (Oxford, England : 1994)* 244 (Jan. 1, 2021), p. 117834. ISSN: 1352-2310. DOI: 10.1016/j.atmosenv.2020.117834. pmid: 32895604.
- [4] Fuel Cells and Hydrogen 2 Joint Undertaking. *Hydrogen-Powered Aviation: A Fact-Based Study of Hydrogen Technology, Economics, and Climate Impact by 2050*. Luxembourg: Publications Office of the European Union, May 2020. 196 pp. DOI: 10.2843/471510. URL: <https://data.europa.eu/doi/10.2843/471510>.
- [5] Alexander Tremel. *Electricity-Based Fuels*. Cham: Springer International Publishing, Jan. 1, 2018. ISBN: 978-3-319-72458-4. DOI: 10.1007/978-3-319-72459-1.
- [6] Michael Sterner and Ingo Stadler, eds. *Energiespeicher - Bedarf, Technologien, Integration*. Berlin, Heidelberg: Springer Berlin Heidelberg, 2017. ISBN: 978-3-662-48892-8. DOI: 10.1007/978-3-662-48893-5. URL: <http://link.springer.com/10.1007/978-3-662-48893-5> (visited on 10/09/2023).
- [7] VDI e. V., ed. *VDI Heat Atlas*. 2nd ed. Berlin Heidelberg: Springer, Jan. 1, 2010. ISBN: 978-3-540-77876-9. DOI: 10.1007/978-3-540-77877-6.
- [8] Sophie Jürgens, Patrick Oßwald, Manuel Selinsek, Paolo Piermartini, Johannes Schwab, Peter Pfeifer, Uwe Bauder, Stephan Ruoff, Bastian Rauch, and Markus Köhler. “Assessment of Combustion Properties of Non-Hydroprocessed Fischer-Tropsch Fuels for Aviation”. In: *Fuel Processing Technology* 193 (Jan. 1, 2019), pp. 232–243. ISSN: 03783820. DOI: 10.1016/j.fuproc.2019.05.015.
- [9] Nils Bullerdiek, Ulf Neuling, and Martin Kaltschmitt. “A GHG Reduction Obligation for Sustainable Aviation Fuels (SAF) in the EU and in Germany”. In: *Journal of Air Transport Management* 92 (Jan. 1, 2021), p. 102020. ISSN: 09696997. DOI: 10.1016/j.jairtraman.2021.102020.
- [10] Jürgen Kern. “Decarbonisation or Defossilisation? Innovative Alternative Fuels for the Aviation in Brazil.: An International Reference Model.” (Bonn). June 20, 2019. URL: <https://unfccc.int/sites/default/files/resource/1.5DLR-TT-SYS-Refuels.pdf>.
- [11] Directorate General for Communication. *Make Transport Greener*. European Commission, 2021. URL: [doi.org/10.2775/421628](https://doi.org/10.2775/421628) (visited on 06/17/2024).

- [12] Naturschutz und nukleare Sicherheit Bundesministerium für Umwelt. *PtL-Roadmap: Nachhaltige Strombasierte Kraftstoffe Für Den Luftverkehr in Deutschland*. Apr. 1, 2021. URL: [https://bmdv.bund.de/SharedDocs/DE/Anlage/LF/ptl-roadmap.pdf?\\_\\_blob=publicationFile](https://bmdv.bund.de/SharedDocs/DE/Anlage/LF/ptl-roadmap.pdf?__blob=publicationFile) (visited on 05/10/2024).
- [13] Bundesministerium für Verkehr. *ICAO State Action Plan for CO2 Emissions Reduction - Germany*. Sept. 2018.
- [14] Eelco T. C. Vogt and Bert M. Weckhuysen. “The Refinery of the Future”. In: *Nature* 629.8011 (May 9, 2024), pp. 295–306. ISSN: 0028-0836, 1476-4687. DOI: 10.1038/s41586-024-07322-2. URL: <https://www.nature.com/articles/s41586-024-07322-2> (visited on 05/10/2024).
- [15] X. Lu and D. Hildebrandt. “Fischer–Tropsch Synthesis Reactors”. In: *Chemicals and Fuels from Biomass via Fischer–Tropsch Synthesis*. Ed. by Joshua Gorimbo, Xinying Liu, Yali Yao, and Diane Hildebrandt. The Royal Society of Chemistry, Nov. 18, 2022, pp. 214–260. ISBN: 978-1-83916-393-7. DOI: 10.1039/9781839167829-00214. URL: <https://books.rsc.org/books/book/2009/chapter/4590927/Fischer-Tropsch-Synthesis-Reactors> (visited on 10/06/2023).
- [16] Roland Dittmeyer, Tim Böltken, Paolo Piermartini, Manuel Selinsek, Marcel Loewert, Felix Dallmann, H. Kreuder, M. Cholewa, Alexander Wunsch, Michael Belimov, Sarvenaz Farsi, and Peter Pfeifer. “Micro and Micro Membrane Reactors for Advanced Applications in Chemical Energy Conversion”. In: *Current Opinion in Chemical Engineering* 17 (Jan. 1, 2017), pp. 108–125. ISSN: 22113398. DOI: 10.1016/j.coche.2017.08.001.
- [17] Juergen J. Brandner, Lothar Bohn, Torsten Henning, Ulrich Schygulla, and Klaus Schubert. “Microstructure Heat Exchanger Applications in Laboratory and Industry”. In: *Heat Transfer Engineering* 28.8-9 (Jan. 1, 2007), pp. 761–771. ISSN: 0145-7632. DOI: 10.1080/01457630701328528.
- [18] Ian Gibson, David Rosen, Brent Stucker, and Mahyar Khorasani. *Additive Manufacturing Technologies*. Cham: Springer International Publishing, Jan. 1, 2021. 685 pp. DOI: 10.1007/978-3-030-56127-7.
- [19] Evelyn Naudorf. *Layer upon Layer – and Safe!: First 3D-printed Pressure Equipment Manufactured and Certified; Autoclave Manufactured by Selective Laser Melting; Adapted Geometry Allows for Faster Temperature Cycles*. Nov. 6, 2019.
- [20] Rapid News Group. *Pressure’s On*. 30-1. Jan. 1, 2022.
- [21] 3DPrint.com. *Shell Certifies 3D Printed Valve from Bonney Forge*. Jan. 1, 2023. URL: <https://3dprint.com/303181/shell-certifies-3d-printed-valve-from-bonney-forge/>.
- [22] Daniel Omidvarkarjan, Daniele Cipriano, Ralph Rosenbauer, Manuel Biedermann, and Mirko Meboldt. “Implementation of a Design Support Tool for Additive Manufacturing Using a Feature Database: An Industrial Case Study”. In: *Progress in Additive Manufacturing* 5.1 (Jan. 1, 2020), pp. 67–73. ISSN: 2363-9512. DOI: 10.1007/s40964-020-00119-5.
- [23] Steve LeViness, Anna Lee Y. Tonkovich, Kai Jarosch, Sean Fitzgerald, Bin Yang, and Jeff McDaniel. *Improved Fischer-Tropsch Economics Enabled by Microchannel Technology*. Jan. 1, 2011. URL: [https://www.researchgate.net/publication/267236523\\_Improved\\_Fischer-Tropsch\\_Economics\\_Enabled\\_by\\_Microchannel\\_Technology](https://www.researchgate.net/publication/267236523_Improved_Fischer-Tropsch_Economics_Enabled_by_Microchannel_Technology).
- [24] Karlsruher Institut für Technologie. *Carbon-Neutral Fuels from Air and Green Power*. Aug. 19, 2019. URL: [https://www.kit.edu/kat/english/pi\\_2019\\_107\\_carbon-neutral-fuels-from-air-and-green-power.php](https://www.kit.edu/kat/english/pi_2019_107_carbon-neutral-fuels-from-air-and-green-power.php) (visited on 05/06/2024).
- [25] Institut für Mikroverfahrenstechnik. *IMVT Patente*. May 11, 2023. URL: <https://www.imvt.kit.edu/448.php> (visited on 01/12/2024).

- [26] Franz Fischer and Hans Tropsch. "Über Die Direkte Syntehse von Erdölkohlenwasserstoffen Bei Gewöhnlichem Druck. (Erste Mitteilung)". In: *Berichte der deutschen chemischen Gesellschaft* 59 (Jan. 1, 1923), pp. 830–831.
- [27] Franz Fischer and Hans Tropsch. "Über Die Direkte Syntehse von Erdölkohlenwasserstoffen Bei Gewöhnlichem Druck. (Zweite Mitteilung)". In: *Berichte der deutschen chemischen Gesellschaft* 59 (Jan. 1, 1923), pp. 832–836.
- [28] Peter M. Maitlis and Arno Klerk. *Greener Fischer-Tropsch Processes for Fuels and Feedstocks*. 1. Aufl. Weinheim: Wiley-VCH, Jan. 1, 2013. 390 pp. ISBN: 978-3-527-32945-8. DOI: 10.1002/9783527656837. URL: <https://onlinelibrary.wiley.com/doi/book/10.1002/9783527656837>.
- [29] Robert Güttel, U. Kunz, and Thomas Turek. "Reactors for Fischer-Tropsch Synthesis". In: *Chemical Engineering & Technology* 31.5 (Jan. 1, 2008), pp. 746–754. ISSN: 09307516. DOI: 10.1002/ceat.200800023.
- [30] Mark Dry. "The Fischer-Tropsch Process: 1950-2000". In: *Catalysis Today* 71 (Jan. 1, 2002), pp. 227–241. ISSN: 09205861.
- [31] J. van de Loosdrecht, F. G. Botes, I. M. Ciobica, A. Ferreira, P. Gibson, D. J. Moodley, A. M. Saib, J. L. Visagie, C. J. Weststrate, and J. W. Niemantsverdriet. "Fischer-Tropsch Synthesis: Catalysts and Chemistry". In: *Comprehensive Inorganic Chemistry II*. Ed. by Jan Reedijk and Kenneth Poepelmeier. Elsevier, Jan. 1, 2013, pp. 525–557. ISBN: 978-0-08-096529-1. DOI: 10.1016/B978-0-08-097774-4.00729-4.
- [32] Andreas Jess and Peter Wasserscheid. *Chemical Technology: An Integral Textbook*. CourseSmart. Weinheim, Germany: Wiley-VCH, Jan. 1, 2013. 890 pp. ISBN: 978-3-527-30446-2.
- [33] Niko Heikkinen, Laura Keskiäli, Jasmiina Palo, Matti Reinikainen, and Matti Putkonen. "Effect of Co-fed Water on a Co-Pt-Si/ $\gamma$ -Al<sub>2</sub>O<sub>3</sub> Fischer-Tropsch Catalyst Modified with an Atomic Layer Deposited or Molecular Layer Deposition Overcoating". In: *ACS omega* 7.9 (Jan. 1, 2022), pp. 7725–7736. DOI: 10.1021/acsomega.1c06512. pmid: 35284741.
- [34] Andreas Jess and C. Kern. "Modeling of Multi-Tubular Reactors for Fischer-Tropsch Synthesis". In: *Chemical Engineering & Technology* 32.8 (Jan. 1, 2009), pp. 1164–1175. ISSN: 09307516. DOI: 10.1002/ceat.200900131.
- [35] Florian Ausfelder and Hanna Dura. 3. *Roadmap Des Kopernikus-Projektes P2X Phase II: Optionen Für Ein Nachhaltiges Energiesystem Mit Power-to-X Technologien*. Aug. 1, 2021.
- [36] Deutsche Gesetzliche Unfallversicherung e.V. *GESTIS-Stoffdatenbank*. 2023. URL: <https://gestis.dguv.de/> (visited on 11/11/2023).
- [37] Gerard P. van der Laan and A. A. C. M. Beenackers. "Kinetics and Selectivity of the Fischer-Tropsch Synthesis: A Literature Review". In: *Catalysis Reviews* 41.3-4 (Jan. 1, 1999), pp. 255–318. ISSN: 0161-4940. DOI: 10.1081/CR-100101170.
- [38] F. Bertoncini, M. C. Marion, N. Brodusch, and S. Esnault. "Unravelling Molecular Composition of Products from Cobalt Catalysed Fischer-Tropsch Reaction by Comprehensive Gas Chromatography: Methodology and Application". In: *Oil & Gas Science and Technology - Revue de l'IFP* 64.1 (Jan. 1, 2009), pp. 79–90. ISSN: 1294-4475. DOI: 10.2516/ogst/2008054.
- [39] Tabea J. Stadler, Jan-Hendrik Knoop, Simon Decker, and Peter Pfeifer. "Numerical Simulation Approach for a Dynamically Operated Sorption-Enhanced Water-Gas Shift Reactor". In: *Processes* 10.6 (Jan. 1, 2022), p. 1160. DOI: 10.3390/pr10061160. URL: <https://www.mdpi.com/2227-9717/10/6/1160>.
- [40] Deutsche Rohstoffagentur and Bundesanstalt für Geowissenschaften. "Preismonitor September 2023". In: (2023).

- [41] Johnson Matthey. *PGM Management*. 2023. URL: <https://matthey.com/products-and-markets/pgms-and-circularity/pgm-management> (visited on 11/10/2023).
- [42] European Central Bank. *Euro-Referenzkurse*. Nov. 10, 2023. URL: [https://www.ecb.europa.eu/stats/policy\\_and\\_exchange\\_rates/euro\\_reference\\_exchange\\_rates/html/eurofxref-graph-usd.de.html](https://www.ecb.europa.eu/stats/policy_and_exchange_rates/euro_reference_exchange_rates/html/eurofxref-graph-usd.de.html) (visited on 11/10/2023).
- [43] Mark E. Dry. "High Quality Diesel via the Fischer-Tropsch Process - a Review". In: *Journal of Chemical Technology & Biotechnology* 77.1 (Jan. 1, 2002), pp. 43–50. ISSN: 0268-2575. DOI: 10.1002/jctb.527.
- [44] Moritz Wolf, Hendrik Kotzé, Nico Fischer, and Michael Claeys. "Size Dependent Stability of Cobalt Nanoparticles on Silica under High Conversion Fischer-Tropsch Environment". In: *Faraday Discussions* 197 (2017), pp. 243–268. ISSN: 1359-6640, 1364-5498. DOI: 10.1039/C6FD00200E. URL: <http://xlink.rsc.org/?DOI=C6FD00200E> (visited on 11/11/2023).
- [45] Luis Alvarado Rupflin, Hendrik van Rensburg, Marco Zanella, Elliot J. Carrington, Rebecca Vismara, Alexios Grigoropoulos, Troy D. Manning, John B. Claridge, Alexandros P. Katsoulidis, Robert P. Tooze, and Matthew J. Rosseinsky. "High-Throughput Discovery of Hf Promotion on the Stabilisation of Hcp Co and Fischer-Tropsch Activity". In: *Journal of Catalysis* 396 (Jan. 1, 2021), pp. 315–323. ISSN: 00219517. DOI: 10.1016/j.jcat.2021.02.022.
- [46] Soumitra R. Deshmukh, Anna Lee Y. Tonkovich, Kai T. Jarosch, Luke Schrader, Sean P. Fitzgerald, David R. Kilanowski, Jan J. Lerou, and Terry J. Mazanec. "Scale-Up of Microchannel Reactors For Fischer-Tropsch Synthesis". In: *Industrial & Engineering Chemistry Research* 49.21 (Jan. 1, 2010), pp. 10883–10888. ISSN: 0888-5885. DOI: 10.1021/ie100518u.
- [47] Shell. *Pearl GTL Overview*. Jan. 1, 2023. URL: <https://www.shell.com/about-us/major-projects/pearl-gtl/pearl-gtl-an-overview.html> (visited on 07/03/2023).
- [48] INERATEC GmbH and Sasol Deutschland GmbH. *INERATEC and SASOL Join Forces - Broadening the Range of Applicable Areas for the Fischer-Tropsch Process and Extend the Sustainable Power-to-X and Gas-to-X Market*. Mar. 23, 2020.
- [49] Hannah Kirsch. "Dezentrale Synthese Strombasierter Flüssiger Kraftstoffe Über Die Fischer-Tropsch Route". PhD thesis. Karlsruhe, Germany: Karlsruher Institut für Technologie, Oct. 5, 2020. 297 pp.
- [50] Chenghao Sun, Tiantian Zhan, Peter Pfeifer, and Roland Dittmeyer. "Influence of Fischer-Tropsch Synthesis (FTS) and Hydrocracking (HC) Conditions on the Product Distribution of an Integrated FTS-HC Process". In: *Chemical Engineering Journal* 310 (Jan. 1, 2017), pp. 272–281. ISSN: 13858947. DOI: 10.1016/j.cej.2016.10.118.
- [51] Marco Marchese, Niko Heikkinen, Emanuele Giglio, Andrea Lanzini, Juha Lehtonen, and Matti Reinikainen. "Kinetic Study Based on the Carbide Mechanism of a Co-Pt/ $\gamma$ -Al<sub>2</sub>O<sub>3</sub> Fischer-Tropsch Catalyst Tested in a Laboratory-Scale Tubular Reactor". In: *Catalysts* 9.9 (Jan. 1, 2019), p. 717. DOI: 10.3390/catal9090717.
- [52] Christian Schulz, Peter Kolb, Dennis Krupp, Lars Ritter, Alfred Haas, Mario Soorholtz, Thomas Emmerich Maldonado, Tobias Benjamin Thiede, and Carsten Knobloch. "Preparation and High-Throughput Testing of TiO<sub>2</sub>-Supported Co Catalysts for Fischer-Tropsch Synthesis". In: *Catalysts* 11.3 (Jan. 1, 2021), p. 352. DOI: 10.3390/catal11030352.

- [53] Laura Fratalocchi, Gianpiero Groppi, Carlo Giorgio Visconti, Luca Lietti, and Enrico Tronconi. "Adoption of 3D Printed Highly Conductive Periodic Open Cellular Structures as an Effective Solution to Enhance the Heat Transfer Performances of Compact Fischer-Tropsch Fixed-Bed Reactors". In: *Chemical Engineering Journal* 386 (Jan. 1, 2020), p. 123988. ISSN: 13858947. DOI: 10.1016/j.cej.2019.123988.
- [54] Rune Myrstad, Sigrid Eri, Peter Pfeifer, Erling Rytter, and Anders Holmen. "Fischer-Tropsch Synthesis in a Microstructured Reactor". In: *Catalysis Today* 147 (Jan. 1, 2009), pp. 301–304. ISSN: 09205861. DOI: 10.1016/j.cattod.2009.07.011.
- [55] Paolo Piermartini, Tim Böltken, Manuel Selinsek, and Peter Pfeifer. "Influence of Channel Geometry on Fischer-Tropsch Synthesis in Microstructured Reactors". In: *Chemical Engineering Journal* 313 (Jan. 1, 2017), pp. 328–335. ISSN: 13858947. DOI: 10.1016/j.cej.2016.12.076.
- [56] Luciano C. Almeida, Oihane Sanz, Jorge D'olhaberriague, Simon Yunes, and Mario Montes. "Microchannel Reactor for Fischer-Tropsch Synthesis: Adaptation of a Commercial Unit for Testing Microchannel Blocks". In: *Fuel* 110 (Jan. 1, 2013), pp. 171–177. ISSN: 00162361. DOI: 10.1016/j.fuel.2012.09.063.
- [57] Qinhong Wei, Hangjie Li, Guoguo Liu, Yingluo He, Yang Wang, Yen Ee Tan, Ding Wang, Xiaobo Peng, Guohui Yang, and Noritatsu Tsubaki. "Metal 3D Printing Technology for Functional Integration of Catalytic System". In: *Nature communications* 11.1 (Jan. 1, 2020), p. 4098. DOI: 10.1038/s41467-020-17941-8. PMID: 32796863.
- [58] Marcel Loewert, Julian Hoffmann, Paolo Piermartini, Manuel Selinsek, Roland Dittmeyer, and Peter Pfeifer. "Microstructured Fischer-Tropsch Reactor: Scale-up and Opportunities for Decentralized Application". In: *Chemical Engineering & Technology* 42.10 (Jan. 1, 2019), pp. 2202–2214. ISSN: 09307516. DOI: 10.1002/ceat.201900136.
- [59] Marcel Loewert, Michael Riedinger, and Peter Pfeifer. "Dynamically Operated Fischer-Tropsch Synthesis in PtL-Part 2: Coping with Real PV Profiles". In: *ChemEngineering* 4.2 (Jan. 1, 2020), p. 27. DOI: 10.3390/chemengineering4020027.
- [60] Peter Pfeifer, Sebastian Schmidt, Florian Betzner, Max Kollmann, Marcel Loewert, Tim Böltken, and Paolo Piermartini. "Scale-up of Microstructured Fischer-Tropsch Reactors – Status and Perspectives". In: *Current Opinion in Chemical Engineering* 36 (Jan. 1, 2022), p. 100776. ISSN: 22113398. DOI: 10.1016/j.coche.2021.100776.
- [61] Steve LeViness, Soumitra R. Deshmukh, Laura A. Richard, and Heinz J. Robota. "Velocys Fischer-Tropsch Synthesis Technology—New Advances on State-of-the-Art". In: *Topics in Catalysis* 57.6-9 (Jan. 1, 2014), pp. 518–525. ISSN: 1022-5528. DOI: 10.1007/s11244-013-0208-x.
- [62] Hannah Kirsch, Natalie Lochmahr, Christiane Staudt, Peter Pfeifer, and Roland Dittmeyer. "Production of CO<sub>2</sub>-neutral Liquid Fuels by Integrating Fischer-Tropsch Synthesis and Hydrocracking in a Single Micro-Structured Reactor: Performance Evaluation of Different Configurations by Factorial Design Experiments". In: *Chemical Engineering Journal* 393 (Jan. 1, 2020), p. 124553. ISSN: 13858947. DOI: 10.1016/j.cej.2020.124553.
- [63] Andreas Jess, R. Popp, and K. Hedden. "Fischer-Tropsch-synthesis with Nitrogen-Rich Syngas Fundamentals and Reactor Design Aspects". In: *Applied Catalysis A: General* 186 (Jan. 1, 1999), pp. 321–342. ISSN: 0926860X.
- [64] Ian C. Yates and Charles N. Satterfield. "Intrinsic Kinetics of the Fischer-Tropsch Synthesis on a Cobalt Catalyst". In: *Energy & Fuels* 5.1 (Jan. 1, 1991), pp. 168–173.

- [65] Seung-Ho Kwack, Myung-June Park, Jong Wook Bae, Kyoung-Su Ha, and Ki-Won Jun. "Development of a Kinetic Model of the Fischer–Tropsch Synthesis Reaction with a Cobalt-Based Catalyst". In: *Reaction Kinetics, Mechanisms and Catalysis* 104.2 (Jan. 1, 2011), pp. 483–502. ISSN: 1878-5190. DOI: 10.1007/s11144-011-0369-1.
- [66] Carlo Giorgio Visconti, Enrico Tronconi, Luca Lietti, Roberto Zennaro, and Pio Forzatti. "Development of a Complete Kinetic Model for the Fischer–Tropsch Synthesis over Co/Al<sub>2</sub>O<sub>3</sub> Catalysts". In: *Chemical Engineering Science* 62.18-20 (Sept. 2007), pp. 5338–5343. ISSN: 00092509. DOI: 10.1016/j.ces.2006.12.064. URL: <https://linkinghub.elsevier.com/retrieve/pii/S0009250907000334> (visited on 10/09/2023).
- [67] L. C. Almeida, F. J. Echave, O. Sanz, M. A. Centeno, G. Arzamendi, L. M. Gandía, E. F. Sousa-Aguiar, J. A. Odriozola, and M. Montes. "Fischer–Tropsch Synthesis in Microchannels". In: *Chemical Engineering Journal* 167.2-3 (Jan. 1, 2011), pp. 536–544. ISSN: 13858947. DOI: 10.1016/j.cej.2010.09.091.
- [68] Wikipedia. *Liste Der Größten Deutschen Onshore-Windparks*. Jan. 2, 2024. URL: [https://de.wikipedia.org/wiki/Liste\\_der\\_gr%C3%B6%C3%9Ften\\_deutschen\\_Onshore-Windparks](https://de.wikipedia.org/wiki/Liste_der_gr%C3%B6%C3%9Ften_deutschen_Onshore-Windparks) (visited on 05/10/2024).
- [69] Wikipedia. *Liste von Solarkraftwerken in Deutschland*. Apr. 10, 2024. URL: [https://de.wikipedia.org/wiki/Liste\\_von\\_Solarkraftwerken\\_in\\_Deutschland](https://de.wikipedia.org/wiki/Liste_von_Solarkraftwerken_in_Deutschland) (visited on 05/10/2024).
- [70] Wikipedia. *Liste Der Deutschen Offshore-Windparks*. Mar. 24, 2024. URL: [https://de.wikipedia.org/wiki/Liste\\_der\\_deutschen\\_Offshore-Windparks](https://de.wikipedia.org/wiki/Liste_der_deutschen_Offshore-Windparks) (visited on 05/10/2024).
- [71] Philipp Rentschler, Christoph Klahn, and Roland Dittmeyer. "The Need for Dynamic Process Simulation: A Review of Offshore Power-to-x Systems". In: *Chem.-Ing.-Tech.* 96.1-2 (2024), pp. 1–13.
- [72] Florian Ausfelder and Dinh Du Tran. *4. Roadmap Des Kopernikus-Projektes P2X Phase II: OPTIONEN FÜR EIN NACHHALTIGES ENERGIE-SYSTEM MIT POWER-TO-X-TECHNOLOGIEN*. Jan. 1, 2023.
- [73] Michael Klumpp, Tim Böltken, Alexander Gräfenhahn, Michael Riedinger, Peter Pfeifer, and Roland Dittmeyer. "CO<sub>2</sub>-neutrale Kraftstoffe Aus Dezentralen Syntheseanlagen – Ansatz, Status Quo Und Der Blick Nach Vorne". In: *Journal für Mobilität und Verkehr* 3 (Jan. 1, 2019), pp. 20–29.
- [74] Steffen Schemme. "Techno-Ökonomische Bewertung von Verfahren Zur Herstellung von Kraftstoffen Aus H<sub>2</sub> Und CO<sub>2</sub>". Aachen, Jan. 1, 2020. 378 pp.
- [75] Daniel König. "Techno Ökonomische Prozessbewertung Der Herstellung Synthetischen Flugturbinentreibstoffes Aus CO<sub>2</sub> Und H<sub>2</sub>". Stuttgart, Jan. 1, 2016.
- [76] Maria Fernanda Rojas-Michaga, Stavros Michailos, Evelyn Cardozo, Muhammad Akram, Kevin J. Hughes, Derek Ingham, and Mohamed Pourkashanian. "Sustainable Aviation Fuel (SAF) Production through Power-to-Liquid (PtL): A Combined Techno-Economic and Life Cycle Assessment". In: *Energy Conversion and Management* 292 (Sept. 2023), p. 117427. ISSN: 01968904. DOI: 10.1016/j.enconman.2023.117427. URL: <https://linkinghub.elsevier.com/retrieve/pii/S0196890423007732> (visited on 10/14/2023).
- [77] Joshua Heyne, Bastian Rauch, Patrick Le Clercq, and Meredith Colket. "Sustainable Aviation Fuel Prescreening Tools and Procedures". In: *Fuel* 290 (Jan. 1, 2021), p. 120004. ISSN: 00162361. DOI: 10.1016/j.fuel.2020.120004.
- [78] Arno de Klerk. *Fischer-Tropsch Refining*. 1. ed. Hoboken, NJ; Weinheim: Wiley; Wiley-VCH, Jan. 1, 2011. 620 pp. ISBN: 978-3-527-32605-1. DOI: 10.1002/9783527635603. URL: <http://gbv.eblib.com/patron/FullRecord.aspx?p=1184147>.

- [79] K. Zech, K. Naumann, Franziska Müller-Langer, P. Schmidt, W. Weindorf, Z. Matra, W. Grimme, M. Hepting, C. Heidt, and Bundesministerium für Verkehr. *Drop-In-Kraftstoffe Für Die Luftfahrt: Studie Im Rahmen Des Auftrags Wissenschaftliche Begleitung, Unterstützung Und Beratung Des BMVI In Den Bereichen Verkehr Und Mobilität Mit Besonderem Fokus Auf Kraftstoffe Und Antriebstechnologien Sowie Energie Und Klima Für Das Bundesministerium Für Verkehr Und Digitale Infrastruktur (BMVI) AZ Z14 / SeV / 288.3 / 1179 / UI40, Ausschreibung Vom 19. 12. 2011*. Jan. 1, 2014.
- [80] Christopher Zschiesche, Dieter Himsl, Rainer Rakoczy, Andreas Reitzmann, Jens Freiding, Nicole Wilde, and Roger Gläser. "Hydroisomerization of Long-Chain n -Alkanes over Bifunctional Zeolites with 10-Membered- and 12-Membered-Ring Pores". In: *Chemical Engineering & Technology* 41.1 (Jan. 1, 2018), pp. 199–204. ISSN: 09307516. DOI: 10.1002/ceat.201700236.
- [81] Christoph Kost, Shivenes Shammugam, Verena Fluri, Dominik Peper, Aschkan Davoodi Memar, and Thomas Schlegl. "Levelized Cost of Electricity Renewable Energy Technologies". In: (June 2021).
- [82] Peter Pfeifer, Linus Biffar, Friedemann Timm, and Tim Böltken. "Influence of Power-to-Fuel Plant Flexibility Towards Power and Plant Utilization and Intermediate Hydrogen Buffer Size". In: *Chemie Ingenieur Technik* 92.12 (Jan. 1, 2020), pp. 1976–1982. ISSN: 0009286X. DOI: 10.1002/cite.202000084.
- [83] Roland Dittmeyer, Michael Klumpp, Paul Kant, and Geoffrey Ozin. "Crowd Oil Not Crude Oil". In: *Nature communications* 10.1 (Jan. 1, 2019), p. 1818. DOI: 10.1038/s41467-019-09685-x. pmid: 31040282.
- [84] Martin Luther, Juergen J. Brandner, Lioubov Kiwi-Minsker, Albert Renken, and Klaus Schubert. "Forced Periodic Temperature Cycling of Chemical Reactions in Microstructure Devices". In: *Chemical Engineering Science* 63.20 (Jan. 1, 2008), pp. 4955–4961. ISSN: 00092509. DOI: 10.1016/j.ces.2007.08.008.
- [85] David W. Agar, Martin Bertau, Marion Börnhorst, and Markus Busch. *Roadmap Chemical Reaction Engineering an Initiative of the Dechema/VDI Subject Division Chemical Reaction Engineering 3rd Edition September 2023*. Dechema e.V.; VDI e.V., Sept. 2023. URL: [https://dechema.de/dechema\\_media/Downloads/Positionspapiere/2023+Roadmap+%E2%80%9EChemical+Reaction+Engineering\\_+engl\\_-p-20009528.pdf](https://dechema.de/dechema_media/Downloads/Positionspapiere/2023+Roadmap+%E2%80%9EChemical+Reaction+Engineering_+engl_-p-20009528.pdf).
- [86] Thomas Bieringer, Christian Bramsiepe, Stefan Brand, Andreas Brodhagen, Christian Dreiser, Christoph Fleischer-Trebes, Norbert Kockmann, Stefan Lier, Dirk Schmalz, Christian Schwede, Schweiger, and Frank Stenger. *Modular Plants*. White Paper. Dechema e.V., Jan. 1, 2016. 36 pp. URL: <https://dechema.de/en/About+DECHEMA/Press/Reports+and+position+papers/ProcessNet+Positionspapiere/2016+7+White+Paper+Modular+Plants.html>.
- [87] Michael Kleiber. *Process Engineering: Addressing the Gap between Studies and Chemical Industry*. De Gruyter Textbook. Berlin/Boston: De Gruyter, Jan. 1, 2016. 424 pp. ISBN: 978-3-11-031209-6. URL: <https://ebookcentral.proquest.com/lib/gbv/detail.action?docID=4749738>.
- [88] Michael F. Ashby. *Materials Selection in Mechanical Design*. 4th ed. Amsterdam: Butterworth-Heinemann, Jan. 1, 2011. ISBN: 978-1-85617-663-7. URL: <https://www.sciencedirect.com/book/9781856176637/materials-selection-in-mechanical-design>.
- [89] D. J. Moodley. "On the Deactivation of Cobalt Based Fischer-Tropsch Synthesis Catalysts". PhD thesis. Eindhoven, The Netherlands: Technical University Eindhoven, 2008.
- [90] Technip. *Oryx GTL*. Sept. 1, 2011. URL: <https://docplayer.net/45263490-Our-projects-oryx-gtl.html>.



- [91] International Gas Union. *ORYX GTL and the GTL Sector*. Mar. 2007. URL: <http://members.igu.org/old/gas-knowhow/publications/igu-publications/publications/mag/apr07/p126-150.pdf> (visited on 01/26/2024).
- [92] Wikipedia and Energy Intelligence. *Escravos GTL*. June 8, 2023. URL: [https://en.wikipedia.org/wiki/Escravos\\_GTL](https://en.wikipedia.org/wiki/Escravos_GTL).
- [93] S. T. Sie, M.M.G. Senden, and H.M.H. van Wechem. "Conversion of Natural Gas to Transportation Fuels via Shell Middle Distillate Synthesis Process (SMDS)". In: *Catalysis Today* 8 (1991), pp. 371–394.
- [94] Robert Rapier, Petroleum Energy, and Energy Central. *Inside Shell's Bintulu GTL Plant*. Nov. 16, 2010. URL: <https://energycentral.com/c/ec/inside-shell%E2%80%99s-bintulu-gtl-plant> (visited on 01/26/2024).
- [95] Hydrocarbons Processing. *Pearl Gas-to-Liquids Project, Ras Laffan*. Sept. 27, 2017. URL: <https://www.hydrocarbons-technology.com/projects/pearl/> (visited on 01/26/2024).
- [96] Uzbekneft Gas. *History of the Project*. 2021. URL: [https://www.uzgtl.com/history?lang\\_is=set&lang\\_data=English](https://www.uzgtl.com/history?lang_is=set&lang_data=English) (visited on 05/04/2024).
- [97] Kun.uz. *Construction of Uzbekistan GTL Plant Nears Final Stage*. May 31, 2021. URL: <https://kun.uz/en/news/2021/05/31/constriction-of-uzbekistan-gtl-plant-nears-final-stage> (visited on 05/04/2024).
- [98] S. Chambrey, P. Fongarland, H. Karaca, S. Piché, A. Griboval-Constant, D. Schweich, F. Luck, S. Savin, and A. Y. Khodakov. "Fischer-Tropsch Synthesis in Milli-Fixed Bed Reactor: Comparison with Centimetric Fixed Bed and Slurry Stirred Tank Reactors". In: *Catalysis Today* 171.1 (Jan. 1, 2011), pp. 201–206. ISSN: 09205861. DOI: 10.1016/j.cattod.2011.04.046.
- [99] Laura Fratalocchi, Carlo Giorgio Visconti, Gianpiero Groppi, Luca Lietti, and Enrico Tronconi. "Intensifying Heat Transfer in Fischer-Tropsch Tubular Reactors through the Adoption of Conductive Packed Foams". In: *Chemical Engineering Journal* 349 (Jan. 1, 2018), pp. 829–837. ISSN: 13858947. DOI: 10.1016/j.cej.2018.05.108.
- [100] DIN e.V. *DIN EN ISO 10991:2010-3 Mikroverfahrenstechnik - Begriffe (ISO 10991:2009); Dreisprachige Fassung EN ISO 10991:2009*. Berlin, Germany, Mar. 1, 2010. URL: <https://nautos.de/OJG/search> (visited on 09/22/2023).
- [101] Matthias Schöffler. *Herstellung von Mikroreaktor Mittels Diffusionsschweißen*. E-mail. July 27, 2023.
- [102] Norbert Kockmann. *Transport Phenomena in Micro Process Engineering*. SpringerLink Bücher. Berlin, Heidelberg: Springer Berlin Heidelberg, Jan. 1, 2008. 365 pp. ISBN: 978-3-540-74616-4. DOI: 10.1007/978-3-540-74618-8.
- [103] Michael T. Janicke, Harry Kestenbaum, Ulrike Hagendorf, Ferdi Schüth, Maximilian Fichtner, and Klaus Schubert. "The Controlled Oxidation of Hydrogen from an Explosive Mixture of Gases Using a Microstructured Reactor/Heat Exchanger and Pt/Al<sub>2</sub>O<sub>3</sub> Catalyst". In: *Journal of Catalysis* 191.2 (Jan. 1, 2000), pp. 282–293. ISSN: 00219517. DOI: 10.1006/jcat.2000.2819.
- [104] Peter Pfeifer. "Application of Catalysts to Metal Microreactor Systems". In: *Chemical Kinetics*. Ed. by Vivek Patel. Chemical Kinetics. Rijeka, Croatia: InTech Europe, Jan. 1, 2012, pp. 325–345. ISBN: 978-953-51-0132-1.
- [105] CHEManager. *Millireaktor Im Produktionsbetrieb*. Nov. 21, 2016. URL: <https://www.chemanager-online.com/news/millireaktor-im-produktionsbetrieb> (visited on 01/14/2023).

- [106] David W. Agar, Martin Bertau, Markus Busch, Maria Casapu, Peter Claus, Karla Herrera Delgado, Dana Demtröder, Olaf Deutschmann, Roland Dittmeyer, Christian Dreiser, David Eckes, Bastian Etzold, Georg Fleg, Hannsjörg Freund, Jan-Dierk Grunwaldt, Robert Güttel, Erik Harbou, Thomas Herrmann, Kai-Olaf Hinrichsen, Johannes Khinast, Elias Klemm, Norbert Kockmann, Ulrike Krewer, Michael Nilles, Holger Marschall, Martin Muhler, Stefan Palkovits, Michael Paul, Kristina Pflug, Stefan Radl, Jörg Sauer, Stephan Andreas Schunk, Andreas Seidel-Morgenstern, Michael Schlüter, Markus Schubert, Kai Sundmacher, Thomas Turek, Iakovos Vittorias, Herbert Vogel, Olaf Wachsen, Horst-Werner Zanthoff, Dirk Ziegenbalg, and Dechema e.V. *Roadmap Chemical Reaction Engineering: An Initiative of the ProcessNet Subject Division Chemical Reaction Engineering*. Jan. 1, 2017.
- [107] Institut für Mikroverfahrenstechnik. *Industrial Production of Fine Chemicals Using Microstructured Reactors*. Mar. 6, 2018. URL: [https://www.imvt.kit.edu/english/1540\\_1554.php](https://www.imvt.kit.edu/english/1540_1554.php) (visited on 01/14/2024).
- [108] Juergen J. Brandner. “Microfabrication in Metals and Polymers”. In: *Micro Process Engineering: Fundamentals, Devices, Fabrication, and Applications*. Ed. by Norbert Kockmann. [Elektronische Ressource]. Vol. 5. Advanced Micro & Nanosystems. Weinheim: Wiley-VCH, Jan. 1, 2008. ISBN: 3-527-31246-3.
- [109] Manuel Selinsek. “Compact Fischer-Tropsch Synthesis in Gas-to-Liquid Applications” (Litvinov, Czech Republic; Prague, Czech Republic). May 23, 2019. URL: [https://www.comsynproject.eu/app/uploads/2019/06/SELINSEK\\_INERATEC-.pdf](https://www.comsynproject.eu/app/uploads/2019/06/SELINSEK_INERATEC-.pdf).
- [110] Gregor Herz, Michael Gallwitz, Ralf Näke, Stefan Megel, Matthias Jahn, and Erik Reichelt. “Lab-Scale Demonstration of By-Product Utilization in an Integrated Power-to-Liquid Process Applying Co-Electrolysis”. In: *Energy Technology* 11.4 (Apr. 2023), p. 2201057. ISSN: 2194-4288, 2194-4296. DOI: 10.1002/ente.202201057. URL: <https://onlinelibrary.wiley.com/doi/10.1002/ente.202201057> (visited on 10/20/2023).
- [111] Michael Riedinger. “Gekoppelte Umsatz-Temperatursteuerung Eines Mikrostrukturierten Fischer-Tropsch Reaktors Bei Instationären Feed-Bedingungen”. Karlsruhe, Sept. 1, 2018.
- [112] Marcel Loewert, M.-A. Serrer, T. Carambia, M. Stehle, A. Zimina, K. F. Kalz, H. Lichtenberg, E. Saraçi, Peter Pfeifer, and Jan-Dierk Grunwaldt. “Bridging the Gap between Industry and Synchrotron: An Operando Study at 30 Bar over 300 h during Fischer-Tropsch Synthesis”. In: *Reaction Chemistry & Engineering* 5.6 (Jan. 1, 2020), pp. 1071–1082. DOI: 10.1039/c9re00493a.
- [113] René Lebl, Yutong Zhu, Derrick Ng, Christian H. Hornung, David Cantillo, and C. Oliver Kappe. “Scalable Continuous Flow Hydrogenations Using Pd/Al<sub>2</sub>O<sub>3</sub>-coated Rectangular Cross-Section 3D-printed Static Mixers”. In: *Catalysis Today* 383 (Jan. 2022), pp. 55–63. ISSN: 09205861. DOI: 10.1016/j.cattod.2020.07.046. URL: <https://linkinghub.elsevier.com/retrieve/pii/S0920586120305174> (visited on 01/10/2024).
- [114] Ehrfeld Mikrotechnik GmbH. *Rechteckig Strömt Besser*. 2022. URL: [https://www.ehrfeld.com/\\_files/ugd/4e49c4\\_dda0531961a840a0b7e225c3419d05ee.pdf](https://www.ehrfeld.com/_files/ugd/4e49c4_dda0531961a840a0b7e225c3419d05ee.pdf) (visited on 10/10/2023).
- [115] Amin Delparish and Ahmet K. Avci. “Intensified Catalytic Reactors for Fischer-Tropsch Synthesis and for Reforming of Renewable Fuels to Hydrogen and Synthesis Gas”. In: *Fuel Processing Technology* 151 (Jan. 1, 2016), pp. 72–100. ISSN: 03783820. DOI: 10.1016/j.fuproc.2016.05.021.
- [116] Gunther Kolb. “Review: Microstructured Reactors for Distributed and Renewable Production of Fuels and Electrical Energy”. In: *Chemical Engineering and Processing - Process Intensification* 65 (Jan. 1, 2013), pp. 1–44. ISSN: 02552701. DOI: 10.1016/j.cep.2012.10.015.

- [117] Ignacio Melián-Cabrera. “Catalytic Materials: Concepts to Understand the Pathway to Implementation”. In: *Industrial & Engineering Chemistry Research* 60.51 (Dec. 29, 2021), pp. 18545–18559. ISSN: 0888-5885, 1520-5045. DOI: 10.1021/acs.iecr.1c02681. URL: <https://pubs.acs.org/doi/10.1021/acs.iecr.1c02681> (visited on 05/10/2024).
- [118] Elmeri Lahtinen, Lotta Turunen, Mikko M. Hänninen, Kalle Kolari, Heikki M. Tuononen, and Matti Haukka. “Fabrication of Porous Hydrogenation Catalysts by a Selective Laser Sintering 3D Printing Technique”. In: *ACS omega* 4.7 (Jan. 1, 2019), pp. 12012–12017. DOI: 10.1021/acsomega.9b00711. pmid: 31460313.
- [119] Yesol Woo, Da Bin Oh, Jae Eun Park, Seung Ju Han, Yun-Jo Lee, and Myung-June Park. “CFD Modeling of a Multichannel Fischer–Tropsch Reactor Module with Microscale Cooling Channels: Effects of Mirrored Structure Cooling Layers”. In: *Korean Journal of Chemical Engineering* 40.10 (Jan. 1, 2023), pp. 2572–2580. DOI: 10.1007/s11814-023-1497-9.
- [120] Marcel Loewert. “Dynamische Untersuchungen Bei Intensivierter Fischer-Tropsch Synthese”. Karlsruhe, Jan. 1, 2021.
- [121] GKN Sinter Metals. *Filter-Elements - High Porosity Sintered Parts SIKA-R...AX*. July 18, 2005.
- [122] Philipp Stoll. “Functionality Integration in Powder Bed Based Additive Manufacturing Processes”. Jan. 1, 2020. 203 pp. DOI: 10.3929/ETHZ-B-000449021.
- [123] Oliver Bey. “Strömungsverteilung Und Wärmetransport in Schüttungen”. PhD thesis. Stuttgart, Germany: Universität Stuttgart, July 1998.
- [124] Markus Winterberg and Evangelos Tsotsas. “Modelling of Heat Transport in Beds Packed with Spherical Particles for Various Bed Geometries and/or Thermal Boundary Conditions”. In: *International Journal of Thermal Sciences* 39.5 (May 2000), pp. 556–570. ISSN: 12900729. DOI: 10.1016/S1290-0729(00)00251-9. URL: <https://linkinghub.elsevier.com/retrieve/pii/S1290072900002519> (visited on 11/06/2023).
- [125] R. F. Benenati and C. B. Brosilow. “Void Fraction Distribution in Beds of Spheres”. In: *AIChE Journal* 8.3 (Jan. 1, 1962), pp. 359–361. ISSN: 00011541. DOI: 10.1002/aic.690080319.
- [126] Jennie Von Seckendorff and Olaf Hinrichsen. “Review on the Structure of Random Packed-beds”. In: *The Canadian Journal of Chemical Engineering* 99.S1 (Oct. 2021). ISSN: 0008-4034, 1939-019X. DOI: 10.1002/cjce.23959. URL: <https://onlinelibrary.wiley.com/doi/10.1002/cjce.23959> (visited on 11/13/2023).
- [127] Stefan Maikowske, Juergen J. Brandner, and R. Lange. “A Novel Device for the Optical Investigation of Phase Transition in Micro Channel Array Evaporators”. In: *Applied Thermal Engineering* 30.13 (Jan. 1, 2010), pp. 1872–1876. ISSN: 13594311. DOI: 10.1016/j.applthermaleng.2010.02.015.
- [128] Young-June Park, Taejong Yu, Se-Jun Yim, Donghyun You, and Dong-Pyo Kim. “A 3D-printed Flow Distributor with Uniform Flow Rate Control for Multi-Stacked Microfluidic Systems”. In: *Lab on a chip* 18.8 (Jan. 1, 2018), pp. 1250–1258. DOI: 10.1039/c8lc00004b. pmid: 29569667.
- [129] Daniel Tondeur and Lingai Luo. “Design and Scaling Laws of Ramified Fluid Distributors by the Constructal Approach”. In: *Chemical Engineering Science* 59.8-9 (Jan. 1, 2004), pp. 1799–1813. ISSN: 00092509. DOI: 10.1016/j.ces.2004.01.034.
- [130] Peter Pfeifer, Achim Wenka, Klaus Schubert, M. A. Liauw, and G. Emig. “Characterization of Flow Distribution in Microchannel Reactors”. In: *AIChE Journal* 50.2 (Jan. 1, 2004), pp. 418–425.
- [131] Peter Pfeifer and Klaus Schubert. “Hot Wire Anemometry for Experimental Determination of Flow Distribution in Multilayer Microreactors”. In: *Chemical Engineering Journal* 135 (Jan. 1, 2008), pp. 173–178. ISSN: 13858947. DOI: 10.1016/j.cej.2007.07.034.

- [132] Wolf Wibel, Achim Wenka, Jürgen J. Brandner, and Roland Dittmeyer. “Measuring and Modeling the Residence Time Distribution of Gas Flows in Multichannel Microreactors”. In: *Chemical Engineering Journal* 215–216 (Jan. 1, 2013), pp. 449–460. ISSN: 13858947. DOI: 10.1016/j.cej.2012.10.011.
- [133] U. Imke and Juergen J. Brandner. *3D-Simulation Des Mikrowärmeübertragers 792-K-5.2 Mit TwoPorFlow*.
- [134] Hans Dieter Baehr and Karl Stephan. *Heat and Mass Transfer*. 3. 3rd ed. 2011. Berlin, Heidelberg: Springer Berlin Heidelberg, Jan. 1, 2011. 737 pp. ISBN: 978-3-642-20020-5. URL: <https://link.springer.com/book/10.1007/978-3-662-03659-4>.
- [135] Karl Stephan. “Wärmeübergang Und Druckabfall Bei Nicht Ausgebildeter Laminarströmung in Rohren Und in Ebenen Spalten”. In: *Chemie Ingenieur Technik* 31.12 (Jan. 1, 1959), pp. 773–778. ISSN: 0009286X.
- [136] Linus Biffar, Walther Benzinger, and Peter Pfeifer. “A Simplified Approach for Calculating Heat Transfer Coefficients for Fluid Guiding Elements with Alternating Redirections of Flow”. In: *Chemie Ingenieur Technik* (May 2024), cite.202300104. ISSN: 0009-286X, 1522-2640. DOI: 10.1002/cite.202300104. URL: <https://onlinelibrary.wiley.com/doi/10.1002/cite.202300104> (visited on 05/03/2024).
- [137] Marcel Loewert and Peter Pfeifer. “Dynamically Operated Fischer-Tropsch Synthesis in PtL-Part 1: System Response on Intermittent Feed”. In: *ChemEngineering* 4.2 (Jan. 1, 2020), p. 21. DOI: 10.3390/chemengineering4020021.
- [138] Satish G. Kandlikar. “Two-Phase Flow Patterns, Pressure Drop, and Heat Transfer during Boiling in Minichannel Flow Passages of Compact Evaporators”. In: *Heat Transfer Engineering* 23.1 (Jan. 1, 2002), pp. 5–23. ISSN: 0145-7632. DOI: 10.1080/014576302753249570.
- [139] SLM Solutions. *Material Data Sheet 316L*. Apr. 2023. URL: [https://www.slm-solutions.com/fileadmin/Content/Powder/MDS/MDS\\_316L\\_2023-04\\_EN.pdf](https://www.slm-solutions.com/fileadmin/Content/Powder/MDS/MDS_316L_2023-04_EN.pdf) (visited on 04/26/2024).
- [140] Yahui Yang, Gian Luca Morini, and Juergen J. Brandner. “Experimental Analysis of the Influence of Wall Axial Conduction on Gas-to-Gas Micro Heat Exchanger Effectiveness”. In: *International Journal of Heat and Mass Transfer* 69 (Jan. 1, 2014), pp. 17–25. ISSN: 00179310. DOI: 10.1016/j.ijheatmasstransfer.2013.10.008.
- [141] Wohlers Associates, ed. *Wohlers Report 2023: 3D Printing and Additive Manufacturing Global State of the Industry*. Washington (D.C.): Wohlers Associates, 2023. ISBN: 978-1-62204-966-0.
- [142] Elsevier. *ScienceDirect Results for 'Additive Manufacturing'*. Jan. 1, 2021. URL: <https://www.sciencedirect.com/search?q=additive%20manufacturing>.
- [143] DIN e.V. *DIN EN ISO/ASTM 52900:2022-1 Additive Fertigung - Grundlagen - Terminologie (ISO/ASTM 52900:2021); Deutsche Fassung EN ISO/ASTM 52900:2021*. Berlin, Germany, Mar. 1, 2022. URL: <https://nautos.de/OJG/search> (visited on 09/22/2023).
- [144] John O. Milewski. *Additive Manufacturing of Metals: From Fundamental Technology to Rocket Nozzles, Medical Implants, and Custom Jewelry*. Vol. v.258. Springer Series in Materials Science. Cham: Springer International Publishing, Jan. 1, 2017. 351 pp. ISBN: 978-3-319-58204-7.
- [145] Prashanth Konda Gokuldoss, Sri Kolla, and Jürgen Eckert. “Additive Manufacturing Processes: Selective Laser Melting, Electron Beam Melting and Binder Jetting-Selection Guidelines”. In: *Materials (Basel, Switzerland)* 10.6 (Jan. 1, 2017). ISSN: 1996-1944. DOI: 10.3390/ma10060672. PMID: 28773031.

- [146] DIN e.V. *DIN SPEC 17071:2019-12 Additive Fertigung – Anforderungen an Qualitätsgesicherte Prozesse Für Additive Fertigungszentren; Text in Deutsch Und Englisch*. Berlin, Germany, Dec. 1, 2019. URL: <https://nautos.de/OJG/search>.
- [147] Marc Saunders. “How Process Parameters Drive Successful Metal AM Part Production”. In: *Metal Additive Manufacturing* 4.2 (Jan. 1, 2018), pp. 127–135.
- [148] N. Ahmed, I. Barsoum, G. Haidemenopoulos, and R. AbuK. Al-Rub. “Process Parameter Selection and Optimization of Laser Powder Bed Fusion for 316L Stainless Steel: A Review”. In: *Journal of Manufacturing Processes* 75 (Jan. 1, 2022), pp. 415–434. ISSN: 15266125. DOI: 10.1016/j.jmapro.2021.12.064.
- [149] Eujin Pei, Alain Bernard, Dongdong Gu, Christoph Klahn, Mario Monzón, Maren Petersen, and Tao Sun, eds. *Springer Handbook of Additive Manufacturing*. Springer Handbooks. Cham: Springer International Publishing, 2023. ISBN: 978-3-031-20751-8. DOI: 10.1007/978-3-031-20752-5. URL: <https://link.springer.com/10.1007/978-3-031-20752-5> (visited on 10/29/2023).
- [150] Maximilian Munsch. “Schriftenreihe Lasertechnik: Band 6: Reduzierung von Eigenspannungen Und Verzug in Der Laseradditiven Fertigung”. PhD thesis. Hamburg, Germany: Technische Universität Hamburg-Harburg, Jan. 1, 2013.
- [151] Thomas G. Spears and Scott A. Gold. “In-Process Sensing in Selective Laser Melting (SLM) Additive Manufacturing”. In: *Integrating Materials and Manufacturing Innovation* 5.1 (Dec. 2016), pp. 16–40. ISSN: 2193-9764, 2193-9772. DOI: 10.1186/s40192-016-0045-4. URL: <http://link.springer.com/10.1186/s40192-016-0045-4> (visited on 10/20/2023).
- [152] Yves Küsters. “Robuster Strahlschmelzprozess Durch Methodische Parameterfindung”. PhD thesis. Universität Duisburg-Essen, Oct. 4, 2011.
- [153] Evren Yasa, Jan Deckers, and Jean-Pierre Kruth. “The Investigation of the Influence of Laser Re-Melting on Density, Surface Quality and Microstructure of Selective Laser Melting Parts”. In: *Rapid Prototyping Journal* 17.5 (Jan. 1, 2011), pp. 312–327.
- [154] Evren Yasa, K. Kempen, Jean-Pierre Kruth, L. Thijs, and J. Humbeeck. *Microstructure and Mechanical Properties of Maraging Steel 300 after Selective Laser Melting*. 2010.
- [155] Peter Mercelis and Jean-Pierre Kruth. “Residual Stresses in Selective Laser Sintering and Selective Laser Melting”. In: *Rapid Prototyping Journal* 12.5 (Jan. 1, 2006), pp. 254–265. ISSN: 1355-2546. DOI: 10.1108/13552540610707013.
- [156] Jean-Pierre Kruth, L. Froyen, J. van Vaerenbergh, P. Mercelis, M. Rombouts, and B. Lauwers. “Selective Laser Melting of Iron-Based Powder”. In: *Journal of Materials Processing Technology* 149.1-3 (Jan. 1, 2004), pp. 616–622. ISSN: 09240136. DOI: 10.1016/j.jmatprotec.2003.11.051.
- [157] K. Kempen, Evren Yasa, L. Thijs, Jean-Pierre Kruth, and J. van Humbeeck. “Microstructure and Mechanical Properties of Selective Laser Melted 18Ni-300 Steel”. In: *Physics Procedia* 12 (Jan. 1, 2011), pp. 255–263. ISSN: 18753892. DOI: 10.1016/j.phpro.2011.03.033.
- [158] Markus Eisen. “Optimierte Parameterfindung Und Prozessorientiertes Qualitätsmanagement Für Das Selective Laser Melting Verfahren”. PhD thesis. Duisburg, Germany: Universität Duisburg-Essen, Jan. 1, 2009.
- [159] Daniel Thomas. “The Development of Design Rules for Selective Laser Melting”. PhD thesis. Cardiff, Wales: University of Wales Institute, Jan. 1, 2009.

- 
- [160] Fabian Grinschek, Amal Charles, Ahmed Elkaseer, Christoph Klahn, Steffen G. Scholz, and Roland Dittmeyer. "Gas-Tight Means Zero Defects - Design Considerations for Thin-Walled Fluidic Devices with Overhangs by Laser Powder Bed Fusion". In: *Materials & Design* (Jan. 1, 2022), p. 111174. ISSN: 02641275. DOI: 10.1016/j.matdes.2022.111174.
  - [161] Christoph Klahn, Bastian Leutenecker-Twelsiek, and Mirko Meboldt. "Design Strategies for the Process of Additive Manufacturing". In: *Design Strategies for the Process of Additive Manufacturing*. Ed. by Moshe Shpitalni, Anath Fischer, and Gila Molcho. Vol. 36. Procedia CIRP. Jan. 1, 2015, pp. 230–235.
  - [162] Hazman Hasib, Ola L.A. Harrysson, and Harvey A. West. "Powder Removal from Ti-6Al-4V Cellular Structures Fabricated via Electron Beam Melting". In: *JOM* 67.3 (Jan. 1, 2015), pp. 639–646. ISSN: 1047-4838. DOI: 10.1007/s11837-015-1307-x.
  - [163] DIN e.V. *DIN EN ISO 228-1:2003-5 Rohrgewinde Für Nicht Im Gewinde Dichtende Verbindungen, Teil 1: Maße, Toleranzen Und Bezeichnung (ISO 228-1:2000); Deutsche Fassung EN ISO 228-1:2003*. Berlin, Germany, May 1, 2003. URL: <https://nautos.de/OJG/search> (visited on 09/22/2023).
  - [164] Olaf Rehme. "Cellular Design for Laser Freeform Fabrication". PhD thesis. Hamburg, Germany: Technische Universität Hamburg-Harburg, Jan. 1, 2009. 296 pp.
  - [165] Andreas Gebhardt and Jan-Steffen Hötter. *Additive Manufacturing: 3D Printing for Prototyping and Manufacturing*. Munich; Hanser Publishers; Cincinnati: Hanser Publications, Jan. 1, 2016. ISBN: 978-1-56990-582-1. URL: <http://www.sciencedirect.com/science/book/9781569905821>.
  - [166] Karlsruher Institut für Technologie. *Metall-3D-Druck in Endlosfertigung*. May 29, 2020.
  - [167] Rapid News Group and Laura Griffiths. *TCT Buyer's Guide 2022*. Jan. 1, 2022.
  - [168] Christoph Klahn. *PBF-LB/M machines mith multiple lasers*. E-mail. Dec. 18, 2023.
  - [169] Karlsruher Institut für Technologie. *Verformungskontrolle Beim Diffusionsschweißen*. May 29, 2020.
  - [170] Institut für Mikroverfahrenstechnik. *Anlagentechnik Diffusionsschweißen*. July 29, 2021. URL: <https://www.imvt.kit.edu/2167.php> (visited on 02/11/2024).
  - [171] PVA TePla Vacuum Processing Service. *Diffusionsschweißanlagen*. 2024. URL: <https://www.pvatepla-lwt.com/anlagen/diffusionsschweissanlagen/> (visited on 01/11/2024).
  - [172] Martin Baumann, C. Tuck, R. Wildman, Ashcroft I., and R. Hague. "Energy Inputs to Additive Manufacturing: Does Capacity Utilization Matter?" Jan. 1, 2011.
  - [173] E-Plus-3D. *E-Plus-3D M1550*. 2023. URL: <https://www.eplus3d.com/products/ep-m1550-metal-3d-printer/> (visited on 01/12/2024).
  - [174] Farsoon. *Farsoon Announces Development of 16-Laser, Next-Generation FS1521M Metal AM System*. Sept. 12, 2023. URL: <https://www.farsoon-gl.com/news/farsoon-announces-development-of-16-laser-next-generation-fs1521m-metal-am-system/> (visited on 01/11/2024).
  - [175] GE Additive. *X Line 2000R Steel 316L*. Jan. 1, 2022.
  - [176] Xi'an Bright Light Technology. *BLT-S1500*. Dec. 20, 2023. URL: <https://www.xa-blte.com/en/product/blt-s1500/> (visited on 01/11/2024).
  - [177] Velo 3D. *Sapphire XC and Sapphire XC 1MZ Printer*. Jan. 1, 2022. URL: <https://velo3d.com/wp-content/uploads/2022/09/Sapphire-XC-and-XC-1MZ-Product-Brief-Sept-7-2022.pdf>.
  - [178] Deutsche Edelstahlwerke GmbH. *Werkstoffdatenblatt X2CrNiMo17-12-2 1.4404*. Witten, Germany, June 8, 2016.

- [179] Elias Jelis, Matthew Clemente, Michael Hespos, Shana Groeschler, Eli Golden, and Ryan Carpenter. "Round Robin Study Evaluating Consistency of 4340 Steel Specimens Manufactured by Different Laser Powder Bed Fusion Machines". In: *Journal of Materials Engineering and Performance* 30.9 (Jan. 1, 2021), pp. 6832–6843. ISSN: 1059-9495. DOI: 10.1007/s11665-021-06020-8.
- [180] Bhrigu Ahuja, Adam Schaub, Daniel Junker, Michael Karg, Felix Tenner, Raoul Plettke, Marion Merklein, and Michael Schmidt. "A Round Robin Study for Laser Beam Melting in a Metal Powder Bed". In: *South African Journal of Industrial Engineering* 27.2 (Jan. 1, 2016). DOI: 10.7166/27-2-1201.
- [181] Toby dTingskog. "An Introduction to Metal Powders for AM: Manufacturing Processes and Properties". In: *Metal Additive Manufacturing* 4.2 (Jan. 1, 2018), pp. 111–119.
- [182] Wilhelm Meiners. "Direktes selektives Laser Sintern einkomponentiger metallischer Werkstoffe". Aachen: RWTH Aachen, 1999. 125 pp.
- [183] VDI e. V. *Additive Fertigungsverfahren - Strahlschmelzen Metallischer Bauteile. Qualifizierung, Qualitätssicherung Und Nachbearbeitung (VDI 3405-2)*. Aug. 1, 2013.
- [184] Martin Baumers, C. Tuck, R. Hague, Ashcroft I., and R. Wildman. *A Comparative Study of Metallic Additive Manufacturing Power Consumption*. Jan. 1, 2010.
- [185] Chandrika Kamath, Bassem El-dasher, Gilbert F. Gallegos, Wayne E. King, and Aaron Sisto. "Density of Additively-Manufactured, 316L SS Parts Using Laser Powder-Bed Fusion at Powers up to 400 W". In: *The International Journal of Advanced Manufacturing Technology* 74.1-4 (Jan. 1, 2014), pp. 65–78. ISSN: 0268-3768. DOI: 10.1007/s00170-014-5954-9.
- [186] Elliott W. Jost, John C. Miers, Aron Robbins, David G. Moore, and Christopher Saldana. "Effects of Spatial Energy Distribution-Induced Porosity on Mechanical Properties of Laser Powder Bed Fusion 316L Stainless Steel". In: *Additive Manufacturing* 39 (Mar. 2021), p. 101875. ISSN: 22148604. DOI: 10.1016/j.addma.2021.101875. URL: <https://linkinghub.elsevier.com/retrieve/pii/S2214860421000403> (visited on 01/12/2024).
- [187] DIN e.V. *DIN EN 10088-2:2014-12, Nichtrostende Stähle - Teil 2: Technische Lieferbedingungen für Blech und Band aus korrosionsbeständigen Stählen für allgemeine Verwendung; Deutsche Fassung EN\_10088-2:2014*. Berlin, Germany, Dec. 2014. DOI: 10.31030/2102107. URL: <https://nautos.de/OJG/search> (visited on 01/12/2024).
- [188] DIN e.V. *DIN EN 10028-7:2016-10 Flacherzeugnisse Aus Druckbehälterstählen - Teil 7: Nichtrostende Stähle; Deutsche Fassung EN 10028-7:2016*. Berlin, Germany, Oct. 2016. URL: <https://nautos.de/OJG/search> (visited on 01/12/2024).
- [189] Tobias Ronneberg, Catrin M. Davies, and Paul A. Hooper. "Revealing Relationships between Porosity, Microstructure and Mechanical Properties of Laser Powder Bed Fusion 316L Stainless Steel through Heat Treatment". In: *Materials & Design* 189 (Jan. 1, 2020), p. 108481. ISSN: 02641275. DOI: 10.1016/j.matdes.2020.108481.
- [190] *Verordnung Über Sicherheit Und Gesundheitsschutz Bei Der Verwendung von Arbeitsmitteln: BetrSichV*. July 13, 2015.
- [191] Itziar Tolosa, Fermín Garcíandía, Fidel Zubiri, Fidel Zapirain, and Aritz Esnaola. "Study of Mechanical Properties of AISI 316 Stainless Steel Processed by "Selective Laser Melting", Following Different Manufacturing Strategies". In: *The International Journal of Advanced Manufacturing Technology* 51.5-8 (Jan. 1, 2010), pp. 639–647. ISSN: 0268-3768. DOI: 10.1007/s00170-010-2631-5.

- [192] Björn Ringel, David Schwarz, Hoang Minh Vu, Steffen Meiniger, Georg Schlick, Christian Seidel, and Matthias Oechsner. “Investigation on a Predetermined Point of Failure for Stainless Steel 316L Pressure Loaded Components Made by Laser Powder Bed Fusion through Stress Analysis and Experimental Testing”. In: *Progress in Additive Manufacturing* 8.1 (Jan. 1, 2023), pp. 27–35. ISSN: 2363-9512. DOI: 10.1007/s40964-022-00388-2.
- [193] *Richtlinie Zur Harmonisierung Der Rechtsvorschriften Der Mitgliedstaaten Über Die Bereitstellung von Druckgeräten Auf Dem Markt*. Jan. 1, 2014.
- [194] Martin Boche. *Zulassung additiv gefertigter Druckgeräte*. Nov. 17, 2022.
- [195] O. H. Laguna, P. F. Lietor, F. IglesiasJ. Godino, and F. A. Corpas-Iglesias. “A Review on Additive Manufacturing and Materials for Catalytic Applications: Milestones, Key Concepts, Advances and Perspectives”. In: *Materials & Design* 208 (Jan. 1, 2021), p. 109927. ISSN: 02641275. DOI: 10.1016/j.matdes.2021.109927.
- [196] Alexander Jastram, Senada Schaack, and Christoph Kiener. “Simulation-Driven Design of an Additively Manufactured Reactor for Exothermic Liquid-Liquid Reactions”. In: *Chemie Ingenieur Technik* 94.7 (Jan. 1, 2022), pp. 948–957. ISSN: 0009286X. DOI: 10.1002/cite.202200049.
- [197] Alexander Hauser, Michael Neubert, Alexander Feldner, Alexander Horn, Fabian Grimm, and Jürgen Karl. “Design and Implementation of an Additively Manufactured Reactor Concept for the Catalytic Methanation”. In: *Applied Sciences* 12.18 (Jan. 1, 2022), p. 9393. DOI: 10.3390/app12189393.
- [198] Lisa Stolz. “AM bei BASF”. Vortrag im Rahmen der Vorlesung. Digital Design for Process Engineering (Karlsruhe, Germany). July 13, 2023.
- [199] Byron Blakey-Milner, Paul Gradl, Glen Snedden, Michael Brooks, Jean Pitot, Elena Lopez, Martin Leary, Filippo Berto, and Anton Du Plessis. “Metal Additive Manufacturing in Aerospace: A Review”. In: *Materials & Design* 209 (Jan. 1, 2021), p. 110008. ISSN: 02641275. DOI: 10.1016/j.matdes.2021.110008.
- [200] Martin Czekalla and Arthur Seibel. “On the Effectiveness of Triply-Periodic Minimal Surface Structures for Heat Sinks Used in Automotive Applications”. In: *Industrializing Additive Manufacturing: Proceedings of AMPA2023*. Ed. by Christoph Klahn, Mirko Meboldt, and Julian Ferchow. Springer Tracts in Additive Manufacturing. Cham: Springer International Publishing, Jan. 1, 2024, pp. 353–364. ISBN: 978-3-031-42982-8. DOI: 10.1007/978-3-031-42983-5\_24.
- [201] Natrah Binti Kamaruzaman, Flavio Brighenti, Juergen J. Brandner, and Aminuddin Saat. “Prediction of Micro Surface Cooler Performance for Different Rectangular Type Microchannels Dimensions”. In: *International Journal of Heat and Fluid Flow* 44 (Jan. 1, 2013), pp. 644–651. ISSN: 0142727X. DOI: 10.1016/j.ijheatfluidflow.2013.09.005.
- [202] Uwe Scheithauer, Richard Kordaß, Kevin Noack, Martin F. Eichenauer, Mathias Hartmann, Johannes Abel, Gregor Ganzer, and Daniel Lordick. “Potentials and Challenges of Additive Manufacturing Technologies for Heat Exchanger”. In: *Advances in Heat Exchangers*. Ed. by Laura Castro Gómez and Víctor Manuel Velázquez Flores. IntechOpen, Jan. 1, 2019. ISBN: 978-1-78985-073-4. DOI: 10.5772/intechopen.80010.
- [203] David Saltzman, Michael Bichnevicius, Stephen Lynch, Timothy W. Simpson, Edward W. Reutzel, Corey Dickman, and Richard Martukanitz. “Design and Evaluation of an Additively Manufactured Aircraft Heat Exchanger”. In: *Applied Thermal Engineering* 138 (Jan. 1, 2018), pp. 254–263. ISSN: 13594311. DOI: 10.1016/j.applthermaleng.2018.04.032.



- [204] Manuel Gruber. “Detaillierte Untersuchung des Wärme- und Stofftransports in einem Festbett-Methanisierungsreaktor für Power-to-Gas Anwendungen”. PhD thesis. Karlsruhe, Germany: Karlsruher Institut für Technologie, Dec. 13, 2019. 293 pp. DOI: 10.5445/IR/1000105268.
- [205] Corinna Busse, Hannsjörg Freund, and Wilhelm Schwieger. “Intensification of Heat Transfer in Catalytic Reactors by Additively Manufactured Periodic Open Cellular Structures (POCS)”. In: *Chemical Engineering and Processing - Process Intensification* 124 (Jan. 1, 2018), pp. 199–214. ISSN: 02552701. DOI: 10.1016/j.cep.2018.01.023.
- [206] Edgar Hansjosten, Walther Benzinger, Andreas Hensel, and Achim Wenka. “Strömungsleitelemente in Einem Kanal; Flow Conducting Elements in a Channel”. Pat. Jan. 1, 2017.
- [207] Miriam González-Castaño, Francisco M. Baena-Moreno, Juan Carlos Navarro de Miguel, Kamal U. M. Miah, Fátima Arroyo-Torralvo, Ralf Ossenbrink, Jose Antonio Odriozola, Walther Benzinger, Andreas Hensel, Achim Wenka, and Harvey Arellano-García. “3D-printed Structured Catalysts for CO<sub>2</sub> Methanation Reaction: Advancing of Gyroid-Based Geometries”. In: *Energy Conversion and Management* 258.115464 (Jan. 1, 2022). URL: <https://doi.org/10.1016/j.enconman.2022.115464>.
- [208] Francisco M. Baena-Moreno, Miriam González-Castaño, Juan Carlos Navarro de Miguel, Kamal U. M. Miah, Ralf Ossenbrink, Jose Antonio Odriozola, and Harvey Arellano-García. “Stepping toward Efficient Microreactors for CO<sub>2</sub> Methanation: 3D-Printed Gyroid Geometry”. In: *ACS Sustainable Chemistry & Engineering* 9.24 (Jan. 1, 2021), pp. 8198–8206. ISSN: 2168-0485. DOI: 10.1021/acssuschemeng.1c01980.
- [209] Benedikt Hirt, Edgar Hansjosten, Andreas Hensel, Volker Gräf, and Mario Stahl. “Improvement of an Annular Thin Film UV-C Reactor by Fluid Guiding Elements”. In: *Innovative Food Science & Emerging Technologies* 77 (Jan. 1, 2022), p. 102988. ISSN: 14668564. DOI: 10.1016/j.ifset.2022.102988.
- [210] Edgar Hansjosten, Achim Wenka, Andreas Hensel, Walther Benzinger, Michael Klumpp, and Roland Dittmeyer. “Custom-Designed 3D-printed Metallic Fluid Guiding Elements for Enhanced Heat Transfer at Low Pressure Drop”. In: *Chemical Engineering and Processing - Process Intensification* 130 (Jan. 1, 2018), pp. 119–126. ISSN: 02552701. DOI: 10.1016/j.cep.2018.05.022.
- [211] Christoph Klahn. “Laseradditiv Gefertigte, Luftdurchlässige Mesostrukturen: Herstellung Und Eigenschaften Für Die Anwendung”. PhD thesis. Hamburg, Germany: TUHH, Jan. 1, 2015. DOI: 10.1007/978-3-662-47761-8. URL: <http://search.ebscohost.com/login.aspx?direct=true&scope=site&db=nlebk&AN=1080791>.
- [212] Christoph Klahn. *Additive Manufacturing Process Principles*. Images. Aug. 20, 2017. URL: <https://www.research-collection.ethz.ch/handle/20.500.11850/181623> (visited on 01/12/2024).
- [213] Julian Ferchow, Marvin Bühler, Marcel Schlüssel, Livia Zumofen, Christoph Klahn, Urs Hofmann, Andreas Kirchheim, and Mirko Meboldt. “Design and Validation of a Sheet Metal Clamping System for Additive Manufacturing and Post-Processing”. In: *The International Journal of Advanced Manufacturing Technology* 119 (Jan. 1, 2022), pp. 7947–7967. ISSN: 0268-3768. DOI: 10.1007/s00170-022-08773-5.
- [214] Philipp Stoll, Adriaan Spierings, and Konrad Wegener. “Impact of a Process Interruption on Tensile Properties of SS 316L Parts and Hybrid Parts Produced with Selective Laser Melting”. In: *The International Journal of Advanced Manufacturing Technology* 103.1-4 (Jan. 1, 2019), pp. 367–376. ISSN: 0268-3768. DOI: 10.1007/s00170-019-03560-1.
- [215] De Dietrich Process Systems and InnoSyn B.V. *CryoFlowSkid*. Nov. 4, 2019. URL: <https://www.dedietrich.com/de/news/produkte/cryoflowskid> (visited on 01/12/2024).

- [216] DIN e.V. *DIN 13-1:1999-11 Metrisches ISO-Gewinde Allgemeiner Anwendung, Teil 1: Nennmaße Für Regelgewinde; Gewinde-Nenndurchmesser von 1 Bis 68 Mm*. Berlin, Germany, Nov. 1999. URL: <https://nautos.de/OJG/search> (visited on 05/10/2024).
- [217] Manuel Biedermann, Patrick Beutler, and Mirko Meboldt. “Automated Design of Additive Manufactured Flow Components with Consideration of Overhang Constraint”. In: *Additive Manufacturing* 46 (Jan. 1, 2021), p. 102119. ISSN: 22148604. DOI: 10.1016/j.addma.2021.102119.
- [218] Manuel Biedermann, T. Kamps, and Christoph Kiener. “Redesign of a Burner Tip with Multiple Integrated Flow Distributors” (Berlin). Mar. 14, 2018.
- [219] VDI e. V. *VDI 2221-1:2019-11 Entwicklung Technischer Produkte Und Systeme; Modell Der Produktentwicklung*. Berlin, Germany, Nov. 2019. URL: <https://nautos.de/OJG/search> (visited on 02/05/2024).
- [220] Susanne Lux. “Application of the TRIZ Contradictory Matrix to Foster Innovation for Sustainable Chemical Engineering”. In: *Chemie Ingenieur Technik* 94.8 (Jan. 1, 2022), pp. 1071–1079. ISSN: 0009286X. DOI: 10.1002/cite.202100205.
- [221] Mertcan Kaya and Christoph Klahn. “Sequential Parameter Optimization for Algorithm-Based Design Generation Using Data from Multiphysics Simulations”. 33rd CIRP Design Conference (Sydney, Australien). May 17, 2023.
- [222] Amer Ćatić. “Knowledge-Based Engineering in Product Development Processes: Process, IT and Knowledge Management Perspectives”. PhD thesis. Göteborg, Sweden: Chalmers Univ. of Technology, 2011. 235 pp.
- [223] Ferdi Schüth. “Heterogene Katalyse. Schlüsseltechnologie Der Chemischen Industrie”. In: *Chemie in unserer Zeit* 40.2 (Jan. 1, 2006), pp. 92–103. ISSN: 00092851. DOI: 10.1002/ciuz.200600374.
- [224] CIRP and Cranfield University. *Welcome to CIRP Design Conference 2024*. 2023. URL: <https://cranfield.shorthandstories.com/cirp-2024/index.html> (visited on 01/13/2024).
- [225] David F Metzger, Christoph Klahn, and Roland Dittmeyer. “A Simplified Design Method for the Mechanical Stability of Slit-Shaped Additively Manufactured Reactor Modules”. In: (2024).
- [226] Ehud Kroll and Eldad Buchris. “Weight Reduction of 3D-printed Cylindrical and Toroidal Pressure Vessels through Shape Modification”. In: *Procedia Manufacturing* 21 (Jan. 1, 2018), pp. 133–140. ISSN: 23519789. DOI: 10.1016/j.promfg.2018.02.103.
- [227] S. Unnikrishnan Nair and S. Somanath, eds. *Introduction to Finite Element Analysis: A Textbook for Engineering Students*. Singapore: Springer Nature Singapore, 2024. ISBN: 978-981-19798-8-0. DOI: 10.1007/978-981-19-7989-7. URL: <https://link.springer.com/10.1007/978-981-19-7989-7> (visited on 01/19/2024).
- [228] Warren Clarence Young and Richard Gordon Budynas. *Roark’s Formulas for Stress and Strain*. 7. ed. New York, NY: McGraw-Hill, Jan. 1, 2007. 852 pp. ISBN: 0-07-072542-X.
- [229] Hoang Minh Vu, Steffen Meiniger, Björn Ringel, Holger Hoche, Matthias Oechsner, Matthias Weigold, and Christian Seidel. “Investigation on Surface Characteristics of Wall Structures out of Stainless Steel 316L Manufactured by Laser Powder Bed Fusion”. In: *Progress in Additive Manufacturing* (Feb. 13, 2024). ISSN: 2363-9512, 2363-9520. DOI: 10.1007/s40964-023-00559-9. URL: <https://link.springer.com/10.1007/s40964-023-00559-9> (visited on 02/20/2024).
- [230] Wenzheng Zhuang, Chao Yang, and Zhigang Wu. “Mechanical Stability of Hybrid Corrugated Sandwich Plates under Fluid-Structure-Thermal Coupling for Novel Thermal Protection Systems”. In: *Applied Sciences* 10.8 (Apr. 17, 2020), p. 2790. ISSN: 2076-3417. DOI: 10.3390/app10082790. URL: <https://www.mdpi.com/2076-3417/10/8/2790> (visited on 10/20/2023).

- [231] A. Charmi, R. Falkenberg, L. Ávila, G. Mohr, K. Sommer, A. Ulbricht, M. Sprengel, R. Saliwan Neumann, B. Skrotzki, and A. Evans. “Mechanical Anisotropy of Additively Manufactured Stainless Steel 316L: An Experimental and Numerical Study”. In: *Materials Science and Engineering: A* 799 (Jan. 2021), p. 140154. ISSN: 09215093. DOI: 10.1016/j.msea.2020.140154. URL: <https://linkinghub.elsevier.com/retrieve/pii/S092150932031220X> (visited on 04/26/2024).
- [232] Jonathan Meyer. “Pressure Vessel”. U.S. pat. 20160238193A1. Airbus Group Ltd. Aug. 18, 2016. URL: <https://patents.google.com/patent/US20160061381A1/en> (visited on 06/14/2024).
- [233] Igor K. Kotilar. “Pressure Vessels, Design and Method of Manufacturing Using Additive Printing”. Pat. Jan. 1, 2016.
- [234] Christoph Kiener, Stefan Boschert, Yves Küsters, Alexander Nicolai, and Robert Otto. “Hochdruckgeeignete AM-Konstruktionselemente Mit Hierarchisch-funktionalen Metallstrukturen”. In: *Chemie Ingenieur Technik* 94.7 (Jan. 1, 2022), pp. 1040–1045. ISSN: 0009286X. DOI: 10.1002/cite.202200050.
- [235] DIN e.V. *DIN EN 13445-1:2018-12 Unbefeuerte Druckbehälter - Teil1: Allgemeines; Deutsche Fassung EN 13445-1:2014*. Berlin, Germany, June 2018. URL: <https://nautos.de/OJG/search> (visited on 10/04/2023).
- [236] BG RCI. *Druckprüfungen von Druckbehältern Und Rohrleitungen: Flüssigkeitsdruckprüfungen, Gasdruckprüfungen*. Apr. 1, 2012.
- [237] IMA Materialforschung und Anwendungstechnik GmbH. *WIAM(R) Metallinfo*. Jan. 1, 2022. URL: <https://www.wiamonline.de/wiamdb/wiamlogin.php> (visited on 02/19/2021).
- [238] Leonhard Hitzler, Johann Hirsch, Burkhard Heine, Markus Merkel, Wayne Hall, and Andreas Öchsner. “On the Anisotropic Mechanical Properties of Selective Laser-Melted Stainless Steel”. In: *Materials* 10.10 (Sept. 26, 2017), p. 1136. ISSN: 1996-1944. DOI: 10.3390/ma10101136. URL: <http://www.mdpi.com/1996-1944/10/10/1136> (visited on 04/26/2024).
- [239] Daniel-Alexander Türk. “Exploration and Validation of Integrated Lightweight Structures with AM and FRP Parts”. Zürich, Switzerland: ETH Zürich, Jan. 1, 2017.
- [240] Brecht van Hooreweder, Yanni Apers, Karel Lietaert, and Jean-Pierre Kruth. “Improving the Fatigue Performance of Porous Metallic Biomaterials Produced by Selective Laser Melting”. In: *Acta biomaterialia* 47 (Jan. 1, 2017), pp. 193–202. DOI: 10.1016/j.actbio.2016.10.005. pmid: 27717912.
- [241] Dongxu Xie. “Additively Manufactured Permeable-Dense Composites and Its Applications in Microstructured Reactors”. Karlsruhe, Oct. 11, 2021.
- [242] Guido A. O. Adam. “Systematische Erarbeitung von Konstruktionsregeln Für Die Additiven Fertigungsverfahren Lasersintern, Laserschmelzen Und Fused Deposition Modeling”. Jan. 1, 2015. 172 pp.
- [243] *Permeable Sintered Metal Materials: Determination of Bubble Test Pore Size*. Berlin, Germany, Jan. 1, 1990. URL: <https://nautos.de/OJG/search>.
- [244] Paul Kant, David Metzger, and Marcel Kreitner. *codeADD - Analyse Porosity*. Aug. 15, 2023. URL: <https://github.com/DavidMetzgerKIT/codeADD> (visited on 05/14/2024).
- [245] DIN e.V. *DIN EN ISO 4022:2018-12 Durchlässige Sintermetallwerkstoffe - Bestimmung Der Flüssigkeitsdurchlässigkeit (ISO 4022:2018); Deutsche Fassung EN ISO 4022:2018*. Berlin, Germany, Dec. 1, 2018. URL: <https://nautos.de/OJG/search> (visited on 09/22/2023).

- 
- [246] R. K. Shah and A. L. London. *Advances in Heat Transfer*. Ed. by THomas F. Irvine and James P. Hartnett. Jan. 1, 1978. 482 pp.
  - [247] Formlabs. *Formlabs Design Guide*. Jan. 1, 2023. URL: <https://archive-media.formlabs.com/upload/formlabs-design-guide.pdf>.
  - [248] Sasol Deutschland GmbH. *PURALOX ATALOX High-Purity Calcined Aluminas 09/18*. Aug. 1, 2019.
  - [249] Matteo Maestri and Alberto Cuoci. “Coupling CFD with Detailed Microkinetic Modeling in Heterogeneous Catalysis”. In: *Chemical Engineering Science* 96 (Jan. 1, 2013), pp. 106–117. ISSN: 00092509. DOI: 10.1016/j.ces.2013.03.048.
  - [250] Steffen Flaischlen, Martin Kutscherauer, and Gregor D. Wehinger. “Local Structure Effects on Pressure Drop in Slender Fixed Beds of Spheres”. In: *Chemie Ingenieur Technik* 93.1-2 (Jan. 1, 2021), pp. 273–281. ISSN: 0009286X. DOI: 10.1002/cite.202000171.
  - [251] S. Schulze, P. Nikrityuk, F. Compant, A. Richter, and B. Meyer. “Particle-Resolved Numerical Study of Char Conversion Processes in Packed Beds”. In: *Fuel* 207 (Jan. 1, 2017), pp. 655–662. ISSN: 00162361. DOI: 10.1016/j.fuel.2017.05.071.
  - [252] Holger Martin. “Low Peclet Number Particle-to-Fluid Heat and Mass Transfer in Packed Beds”. In: *Chemical Engineering Science* 33 (Jan. 1, 1977), pp. 913–919. ISSN: 00092509.
  - [253] Mathworks Inc. *Fsolve-Solve System of Nonlinear Equations*. 2024. URL: <https://de.mathworks.com/help/optim/ug/fsolve.html> (visited on 05/01/2024).
  - [254] Ulrich Stein. *Objektorientierte Programmierung Mit MATLAB: Klassen, Vererbung, Polymorphie; Mit 31 Aufgaben Und Zahlreichen Listings*. München: Hanser Carl, Jan. 1, 2015. 179 pp. ISBN: 978-3-446-44536-9. DOI: 10.3139/9783446445369. URL: <http://www.hanser-elibrary.com/isbn/9783446445369>.
  - [255] R. K. Shah and A. L. London. “Laminar Flow Forced Convection in Ducts”. In: *Advances in Heat Transfer*. Ed. by THomas F. Irvine and James P. Hartnett. Jan. 1, 1978, pp. 1–482.
  - [256] Sabri Ergun. “Fluid Flow through Packed Columns”. In: *Chemical Engineering Progress* 48.2 (Jan. 1, 1952), pp. 89–94.
  - [257] Bruce E. Poling, John M. Prausnitz, and John P. O’Connell. *Properties of Gases and Liquids, Fifth Edition*. Fifth edition. McGraw-Hill’s AccessEngineering. New York, N.Y.: McGraw-Hill Education; McGraw Hill, Jan. 1, 2001. 803 pp. ISBN: 0-07-149999-7. URL: <https://www.accessengineeringlibrary.com/content/book/9780070116825>.
  - [258] Juergen J. Brandner and Stefan Maikowske. “Influence of Fluid Flow Distribution in Micro-Channel Arrays to Phase Transition Processes”. In: *Experimental heat Transfer* 25.3 (Jan. 1, 2012), pp. 172–180. DOI: 10.1080/08916152.2011.609961.
  - [259] David F. Metzger, Anselm Dreher, and Paul Kant. *materialData*. May 28, 2024. URL: <https://github.com/DavidMetzgerKIT/materialData> (visited on 05/17/2024).
  - [260] Jianmin Wu, Haitao Zhang, Weiyong Ying, and Dingye Fang. “Thermal Conductivity of Cobalt-Based Catalyst for Fischer–Tropsch Synthesis”. In: *International Journal of Thermophysics* 31.3 (Mar. 2010), pp. 556–571. ISSN: 0195-928X, 1572-9567. DOI: 10.1007/s10765-010-0740-x. URL: <http://link.springer.com/10.1007/s10765-010-0740-x> (visited on 10/09/2023).
  - [261] DIN e.V. *DIN EN ISO 10628-2:2013-4 Schemata für die chemische und petrochemische Industrie - Teil\_2: Graphische Symbole (ISO\_10628-2:2012); Deutsche Fassung EN ISO 10628-2:2012*. Berlin, Germany, Apr. 2013. DOI: 10.31030/1912391. URL: <https://nautos.de/OJG/search> (visited on 05/03/2024).

- [262] Paul Philipp Kant. “Optimierung von Fotokatalysatoren und Fotoreaktoren für die Synthese solarer Kraftstoffe = Optimizing photocatalysts and photoreactors for solar fuel synthesis”. PhD thesis. Karlsruhe, Germany: Karlsruher Institut für Technologie, July 10, 2023.
- [263] Juergen J. Brandner. “Microstructure Devices for Process Intensification: Influence of Manufacturing Tolerances and Design”. In: *Applied Thermal Engineering* 59.1-2 (Jan. 1, 2013), pp. 745–752. ISSN: 13594311. DOI: 10.1016/j.applthermaleng.2013.01.003.
- [264] Brendan Harding. “A New Benchmark for the Secondary Fluid Flow through Curved Ducts”. In: *Chemical Engineering Science* 248 (Jan. 1, 2022), p. 117196. ISSN: 00092509. DOI: 10.1016/j.ces.2021.117196.
- [265] Y. Yang, Iris Gerken, Juergen J. Brandner, and Gian Luca Morini. “Design and Experimental Investigation of a Gas-to-Gas Counter-Flow Micro Heat Exchanger”. In: *Experimental heat Transfer* 27.4 (Jan. 1, 2014), pp. 340–359.
- [266] Flavio Brighenti, Natrah Binti Kamaruzaman, and Juergen J. Brandner. “Investigation of Self-Similar Heat Sinks for Liquid Cooled Electronics”. In: *Applied Thermal Engineering* 59.1-2 (Jan. 1, 2013), pp. 725–732. ISSN: 13594311. DOI: 10.1016/j.applthermaleng.2013.01.001.
- [267] Santosh Krishnamurthy and Yoav Peles. “Flow Boiling of Water in a Circular Staggered Micro-Pin Fin Heat Sink”. In: *International Journal of Heat and Mass Transfer* 51.5-6 (Jan. 1, 2008), pp. 1349–1364. ISSN: 00179310. DOI: 10.1016/j.ijheatmasstransfer.2007.11.026.
- [268] Sebastian Unger. “Experimentelle Und Numerische Untersuchung Der Wärmeübertragungs- Und Strömungscharakteristik von Berippten Einzelrohren Und Rohrbündeln Mit Neuartigem Rippendesign”. PhD thesis. Dresden: Technische Universität Dresden, Jan. 1, 2021.
- [269] Robert H. Perry and Don W. Green, eds. *Perry’s Chemical Engineers’ Handbook*. 7. ed., [3. Nachdr.] Perry’s Chemical Engineers’ Platinum Edition. New York, NY: McGraw-Hill, Jan. 1, 1999. ISBN: 0-07-049841-5.
- [270] DIN e.V. *DIN EN 61515:2017-3 Mineralisolierte Metallgeschirmte Mantelthermoelementleitung Und Mantelthermoelemente (IEC 61515:2016); Deutsche Fassung EN 61515:2016*. Berlin, Germany, Mar. 2017. URL: <https://nautos.de/OJG/search> (visited on 06/10/2024).
- [271] Prozesstechnik Online. *Temperaturmessstellen Richtig Dimensionieren*. Oct. 10, 2017. URL: <https://prozesstechnik.industrie.de/chemie/temperaturmessstellen-richtig-dimensionieren/> (visited on 01/29/2024).
- [272] Beate Bender, Dietmar Göhlich, and Heinrich Dubbel, eds. *Dubbel Taschenbuch für den Maschinenbau. 2: Anwendungen / Beate Bender, Dietmar Göhlich (Hrsg.)* 26., überarbeitete Auflage. Berlin [Heidelberg]: Springer Vieweg, 2020. 1374 pp. ISBN: 978-3-662-59713-2. URL: <http://nbn-resolving.org/urn:nbn:de:bsz:31-epflicht-1813725>.
- [273] Christoph Klahn, Mirko Meboldt, Filippo Fontana, Bastian Leutenecker-Twelsiek, Daniel Omidvarkarjan, and Jasmin Jansen, eds. *Entwicklung Und Konstruktion Für Die Additive Fertigung: Grundlagen Und Methoden Für Den Einsatz in Industriellen Endkundenprodukten*. 2. Auflage. Ein Fachbuch von Konstruktionspraxis. Würzburg: Vogel Communications Group, Jan. 1, 2021. 224 pp. ISBN: 978-3-8343-6269-8.
- [274] Benjamin Mutz, Michael Belimov, Wu Wang, Paul Sprenger, Marc-André Serrer, Di Wang, Peter Pfeifer, Wolfgang Kleist, and Jan-Dierk Grunwaldt. “Potential of an Alumina-Supported Ni<sub>3</sub>Fe Catalyst in the Methanation of CO<sub>2</sub>: Impact of Alloy Formation on Activity and Stability”. In: *ACS Catalysis* 7.10 (Oct. 6, 2017), pp. 6802–6814. ISSN: 2155-5435, 2155-5435. DOI: 10.1021/acscatal.7b01896. URL: <https://pubs.acs.org/doi/10.1021/acscatal.7b01896> (visited on 01/20/2024).

- [275] Fabian Grinschek. “Entwicklung Additiv Gefertigter, Modularer, Mikrostrukturierter Rektifikationsapparate”. PhD thesis. Karlsruhe, Germany: Karlsruher Institut für Technologie, 2024.
- [276] Timo Engl, Moritz Langer, Hannsjörg Freund, Michael Rubin, and Roland Dittmeyer. “Tap Reactor for Temporally and Spatially Resolved Analysis of the CO<sub>2</sub> Methanation Reaction”. In: *Chemie Ingenieur Technik* 95.5 (Jan. 1, 2023), pp. 658–667. ISSN: 0009286X. DOI: 10.1002/cite.202200204.
- [277] Robin Dürschnabel. *Reaktorflansch Mit Dichtung*. E-mail. July 30, 2021.
- [278] David F. Metzger, Christoph Klahn, and Roland Dittmeyer. “Downsizing Sustainable Aviation Fuel Production with Additive Manufacturing - An Experimental Study on a 3D Printed Reactor for Fischer-Tropsch Synthesis”. In: *Energies* 16.19 (Sept. 25, 2023), p. 6798. ISSN: 1996-1073. DOI: 10.3390/en16196798. URL: <https://www.mdpi.com/1996-1073/16/19/6798> (visited on 10/04/2023).
- [279] Vahid Vosoughi, Ajay K. Dalai, Nicolas Abatzoglou, and Yongfeng Hu. “Performances of Promoted Cobalt Catalysts Supported on Mesoporous Alumina for Fischer-Tropsch Synthesis”. In: *Applied Catalysis A: General* 547 (Jan. 1, 2017), pp. 155–163. ISSN: 0926860X. DOI: 10.1016/j.apcata.2017.08.032.
- [280] Chunshe Cao, Jianli Hu, Shari Li, Wayne Wilcox, and Yong Wang. “Intensified Fischer-Tropsch Synthesis Process with Microchannel Catalytic Reactors”. In: *Catalysis Today* 140.3-4 (Jan. 1, 2009), pp. 149–156. ISSN: 09205861. DOI: 10.1016/j.cattod.2008.10.016.
- [281] FRAGOL AG. *Therminol 660 Produktinformation*. 2019.
- [282] José M.C. Azevedo, André CabreraSerrenho, and Julian M. Allwood. “Energy and Material Efficiency of Steel Powder Metallurgy”. In: *Powder Technology* 328 (Jan. 1, 2018), pp. 329–336. ISSN: 00325910. DOI: 10.1016/j.powtec.2018.01.009.
- [283] Patrick Fischmann, Fionn Schrauth, and Frederik Zanger. “Influence of Particle Size Distribution on Surface Roughness in Powder Bed Fusion - A Contribution to Increase Resource Efficiency”. In: *CIRP Annals* 72.1 (2023), pp. 145–148. ISSN: 00078506. DOI: 10.1016/j.cirp.2023.04.018. URL: <https://linkinghub.elsevier.com/retrieve/pii/S0007850623000598> (visited on 02/28/2024).
- [284] Fabian Grinschek. *Ausschuss Metallpulver Bei Selektivem Laserschmelzen*. E-mail. Dec. 11, 2020.
- [285] T. Gietzelt, V. Toth, T. Wunsch, and Manfred Kraut. “Evaluation of Different Routes for Manufacturing of Micro Process Devices”. In: *1st International Conference on Engineering Manufacture 2022*. Ed. by Lucas F. M. da Silva, Digavalli Ravi Kumar, Maria de Fátima Reis Vaz, and Ricardo J. C. Carbas. Proceedings in Engineering Mechanics. Cham: Springer International Publishing, Jan. 1, 2023, pp. 87–103. ISBN: 978-3-031-13233-9. DOI: 10.1007/978-3-031-13234-6\_7.
- [286] Jürgen Giegrich, Axel Liech, and Horst Fehrenbach. *Ableitung von Kriterien Zur Beurteilung Einer Hochwertigen Verwertung Gefährlicher Abfälle: Forschungsprojekt Im Auftrag Des Umweltbundesamtes FuE-Vorhaben Förderkennzeichen 202 35 310*. Dec. 1, 2007.
- [287] Wirtschaftsvereinigung Stahl. *Fakten Zur Stahlindustrie in Deutschland*. Berlin, Germany, 2022. URL: [https://www.stahl-online.de/wp-content/uploads/WV-Stahl\\_Fakten-2022\\_RZ\\_neu\\_Web.pdf](https://www.stahl-online.de/wp-content/uploads/WV-Stahl_Fakten-2022_RZ_neu_Web.pdf) (visited on 06/14/2024).
- [288] Vladislav Kruzhanov and Volker Arnhold. “Energy Consumption in Powder Metallurgical Manufacturing”. In: *Powder Metallurgy* 55.1 (Jan. 1, 2012), pp. 14–21. ISSN: 0032-5899. DOI: 10.1179/174329012X13318077875722.

- [289] Pascal Mognol, Denis Lepicart, and Nicolas Perry. “Rapid Prototyping: Energy and Environment in the Spotlight”. In: *Rapid Prototyping Journal* 12.1 (Jan. 1, 2006), pp. 26–34. ISSN: 1355-2546. DOI: 10.1108/13552540610637246. URL: <https://www.emerald.com/insight/content/doi/10.1108/13552540610637246/full/html> (visited on 01/21/2024).
- [290] Karel Kellens, Evren Yasa, Wim Dewulf, and Joost R. Dufloy. *Environmental Assessment of Selective Laser Melting and Selective Laser Sintering*. Wien, Österreich, Nov. 8, 2010. 8 pp.
- [291] Matthias Baldinger, Gideon N. Levy, Paul Schönsleben, and Matthias Wandfluh. “Additive Manufacturing Cost Estimation for Buy Scenarios”. In: *Rapid Prototyping Journal* 22.6 (Jan. 1, 2016), pp. 871–877. ISSN: 1355-2546. DOI: 10.1108/RPJ-02-2015-0023.
- [292] Michael Dinkel. *Ökonomie große AM Maschinen*. E-mail. Dec. 1, 2023.
- [293] Martin Baumers, C. Tuck, R. Wildmann, Ashcroft I., E. Rosamond, and R. Hague. *Combined Build-Time, Energy Consumption and Cost Estimation for DMLS*. Jan. 1, 2012.
- [294] Martin Baumers, Chris Tuck, Ricky Wildman, Ian Ashcroft, Emma Rosamond, and Richard Hague. “Transparency Built-in: Energy Consumption and Cost Estimation for Additive Manufacturing”. In: *Journal of Industrial Ecology* 17.3 (June 2013), pp. 418–431. ISSN: 1088-1980, 1530-9290. DOI: 10.1111/j.1530-9290.2012.00512.x. URL: <https://onlinelibrary.wiley.com/doi/10.1111/j.1530-9290.2012.00512.x> (visited on 01/21/2024).
- [295] Martin Baumers and Matthias Holweg. “On the Economics of Additive Manufacturing: Experimental Findings”. In: *Journal of Operations Management* 65.8 (Jan. 1, 2019), pp. 794–809. ISSN: 0272-6963. DOI: 10.1002/joom.1053.
- [296] Tom Vaneker, Alain Bernard, Giovanni Moroni, Ian Gibson, and Yicha Zhang. “Design for Additive Manufacturing: Framework and Methodology”. In: *CIRP Annals* 69.2 (2020), pp. 578–599. ISSN: 00078506. DOI: 10.1016/j.cirp.2020.05.006. URL: <https://linkinghub.elsevier.com/retrieve/pii/S0007850620301396> (visited on 10/09/2023).
- [297] L. Rickenbacher, Adriaan Spierings, and K. Wegener. “An Integrated Cost-model for Selective Laser Melting (SLM)”. In: *Rapid Prototyping Journal* 19.3 (Jan. 1, 2013), pp. 208–214. ISSN: 1355-2546. DOI: 10.1108/13552541311312201.
- [298] Sandra Adelung and Ralph-Uwe Dietrich. “Impact of the Reverse Water-Gas Shift Operating Conditions on the Power-to-Liquid Fuel Production Cost”. In: *Fuel* 317 (June 2022), p. 123440. ISSN: 00162361. DOI: 10.1016/j.fuel.2022.123440. URL: <https://linkinghub.elsevier.com/retrieve/pii/S0016236122003064> (visited on 12/27/2023).
- [299] Marco Marchese, Giulio Buffo, Massimo Santarelli, and Andrea Lanzini. “CO<sub>2</sub> from Direct Air Capture as Carbon Feedstock for Fischer-Tropsch Chemicals and Fuels: Energy and Economic Analysis”. In: *Journal of CO<sub>2</sub> Utilization* 46 (Jan. 1, 2021), p. 101487. ISSN: 22129820. DOI: 10.1016/j.jcou.2021.101487.
- [300] Rapid News Group. “Bigger & Better: SLM Solutions Unveils the New NXG XII 600E with Extended 1.5m Axis.” In: 30.6 (Jan. 1, 2022). URL: <https://www.tctmagazine.com/additive-manufacturing-3d-printing-industry-insights/technology-insights/bigger-better-slm-solutions-launch-nxg-xii-600e/>.
- [301] Francisco Vidal Vidal-Vázquez, Joonas Koponen, Vesa Ruuskanen, Cyril Bajamundi, Antti Kosonen, Pekka Simell, Jero Ahola, Christian Frilund, Jere Elfving, Matti Reinikainen, Niko Heikkinen, Juho Kauppinen, and Paolo Piermartini. “Power-to-X Technology Using Renewable Electricity and Carbon Dioxide from Ambient Air: SOLETAIR Proof-of-Concept and Improved Process Concept”. In: *Journal of CO<sub>2</sub> Utilization* 28 (Jan. 1, 2018), pp. 235–246. ISSN: 22129820. DOI: 10.1016/j.jcou.2018.09.026.

- [302] Christian Seidel. *Multi-Material Metal Parts by Powder Bed Fusion: New Application Opportunities*. 2022.
- [303] Ulf Neuling and Martin Kaltschmitt. “Techno-Economic and Environmental Analysis of Aviation Biofuels”. In: *Fuel Processing Technology* 171 (Mar. 2018), pp. 54–69. ISSN: 03783820. DOI: 10.1016/j.fuproc.2017.09.022. URL: <https://linkinghub.elsevier.com/retrieve/pii/S0378382017307828> (visited on 10/11/2023).
- [304] Jan Torsten Sehart. “Möglichkeiten Und Grenzen Bei Der Generativen Herstellung Metallischer Bauteile Durch Das Strahlschmelzverfahren”. PhD thesis. Duisburg: Universität Duisburg-Essen, Jan. 1, 2010. 162 pp.
- [305] Martin Boche. *Vorlage ITP*. E-mail. Mar. 14, 2023.
- [306] Wikipedia. *Antoine Equation*. Oct. 20, 2023. URL: [https://en.wikipedia.org/wiki/Antoine\\_equation](https://en.wikipedia.org/wiki/Antoine_equation) (visited on 02/25/2024).





# List of Symbols

## Latin Symbols

Symbol	Meaning	Unit
$A$	Area	$\text{mm}^2$
$a$	Spacing	$\text{mm}$
$c$	Concentration	$\text{mol m}^{-3}$
$C$	Cost	€
$\tilde{c}_p$	Molar heat capacity at constant pressure	$\text{J mol}^{-1} \text{K}^{-1}$
$c_p$	Specific heat capacity at constant pressure	$\text{J kg}^{-1} \text{K}^{-1}$
$D$	Diffusion coefficient	$\text{m}^2 \text{s}^{-1}$
$D$	Depth external	$\text{mm}$
$d$	Depth	$\text{mm}$
$d$	Diameter	$\text{mm}$
$E_a$	Activation energy	$\text{J mol}^{-1}$
$E$	Young's modulus	$\text{MPa}$
$f$	Factor FGE heat transfer	-
$G$	Mass flux	$\text{kg m}^{-2} \text{s}^{-1}$
$\dot{H}$	Enthalpy flow	$\text{W}$
$h_{\text{evap}}$	Specific enthalpy of evaporation	$\text{J kg}^{-1}$
$H_R^0$	Molar enthalpy of reaction at standard conditions	$\text{J mol}^{-1}$
$\tilde{h}$	Molar enthalpy	$\text{J mol}^{-1}$
$h$	Specific enthalpy	$\text{J kg}^{-1}$
$H$	Enthalpy	$\text{J}$
$h$	Height	$\text{mm}$
$k_{\text{bed}}$	Reduced thermal conductivity of packed bed	-
$k$	Overall heat transfer coefficient	$\text{W m}^{-2} \text{K}^{-1}$
$L$	Length external	$\text{mm}$
$l$	Length	$\text{mm}$
$\tilde{M}$	Molar weight	$\text{kg mol}^{-1}$
$\dot{m}$	Mass flow rate	$\text{kg s}^{-1}$
$m$	Mass	$\text{kg}$
$N_d$	Ratio of slit depth to particle diameter	-
$N_l$	Ratio of slit length to particle diameter	-
$\dot{n}$	Molar flow rate	$\text{mol s}^{-1}$
$n$	Number	-
$n$	Molar amount	$\text{mol}$

Symbol	Meaning	Unit
$n$	Reaction order	various
$P$	Heating power	W
$P_p$	Particle permeation	-
$p$	Pressure	Pa
$\dot{Q}$	Heat flow	W
$q$	Mechanical load	MPa
$q_{\text{He}}$	Standard He leakage rate	mbar L s <sup>-1</sup>
$\dot{q}$	Heat flux	W m <sup>-2</sup>
$R$	Electrical resistance	$\Omega$
$\tilde{R}$	Universal gas constant	J mol <sup>-1</sup> K <sup>-1</sup>
$r$	Radius	mm
$r^V$	Volumetric reaction rate	mol m <sup>-3</sup> s <sup>-1</sup>
$R_{p0.2}$	Proof strength at 0.2% strain	MPa
$S_a$	Average surface roughness	$\mu\text{m}$
$S$	Selectivity	-
$S$	Safety factor	-
$T$	Temperature	K
$t$	Dimension	mm
$t$	Thickness	mm
$t$	Time	s
$U$	Voltage	V
$u_0$	Superficial velocity	m s <sup>-1</sup>
$\dot{V}$	Volumetric flow rate	m <sup>3</sup> s <sup>-1</sup>
$V$	Volume	mL
$v$	Specific volume	mL g <sup>-1</sup>
$W$	Width external	mm
$w$	Width	mm
$X$	Conversion	-
$\dot{x}$	Vapor fraction	-
$y$	Molar fraction	-

### Greek Symbols

Symbol	Meaning	Unit
$\Delta$	Difference	various
$\Delta y$	Deflection	mm
$\Psi_I$	Inertia permeability coefficient	m
$\Psi_V$	Viscous permeability coefficient	m <sup>2</sup>
$\alpha_{\text{ASF}}$	Chain-growth probability	-
$\alpha$	Convective heat transfer coefficient	W m <sup>-2</sup> K <sup>-1</sup>
$\beta$	Angle between build plate and overhanging face	°
$\chi$	Description parameter FGE	-
$\delta$	Angle of inclination of parabola	°
$\varepsilon$	Error	-

Symbol	Meaning	Unit
$\epsilon_{\text{bed}}$	Packed bed porosity	-
$\epsilon_{\text{p}}$	Catalyst particle porosity	-
$\epsilon_{\text{s}}$	Fluid-permeable region porosity	-
$\epsilon$	Porosity	-
$\eta$	Efficiency	-
$\eta$	Dynamic viscosity	$\text{kg m}^{-1} \text{s}^{-1}$
$\gamma$	Angle of corrugation	$^{\circ}$
$\lambda_{\text{b}}$	Buckling ratio	-
$\lambda$	Thermal conductivity	$\text{W m}^{-1} \text{K}$
$\nu$	Kinematic viscosity	$\text{m}^2 \text{s}^{-1}$
$\nu$	Poisson's ratio	-
$\omega$	Weight fraction	-
$\varphi$	Volume fraction	-
$\rho$	Density	$\text{kg m}^{-3}$
$\rho_{\text{app}}$	Apparent particle density	$\text{kg m}^{-3}$
$\rho_{\text{bed}}$	Packed bed density	$\text{kg m}^{-3}$
$\rho_{\text{p}}$	Particle density	$\text{kg m}^{-3}$
$\tilde{\rho}$	Molar density	$\text{mol m}^{-3}$
$\tilde{\rho}_{\text{N}}$	Molar density at standard conditions = 44.64	$\text{mol m}^{-3}$
$\sigma$	Surface tension	$\text{N m}^{-1}$
$\sigma$	Stress	MPa
$\tau$	Residence time	$\text{s}^{-1}$
$\tau$	Tortuosity of bed	-
$\zeta$	Distribution parameter	-

## Indices

Index	Meaning
298	Reference temperature of enthalpy in K
0	standard pressure $p=1.013 \text{ bar}$
add	added area
ad	adiabatic
red	reduced area
bed	packed bed
boil	boiling
cat	catalyst
char	characteristic
conf	confined
conv	Convective
c	cooling
corru	corrugated
crit	critical
cross	cross-sectional area
CO	related to CO

Index	Meaning
C <sub>n</sub>	Hydrocarbons with n carbon atoms
C <sub>5+</sub>	Hydrocarbons with 5 or more carbon atoms
dev	developing
eff	effective
e	empty
evap	evaporative
f	fins
f	fluid
frit	frit
FGE	related to FGE
g	gaseous
hex	heat exchange area
H <sub>2</sub>	related to H <sub>2</sub>
HP	related to HP
∞	infinitely extended
in	inlet
i	inner
i	species i
LM	Logarithmic mean
lam	laminar
latent	latent heat
l	lattice
l	layer in AM
l	referring to length of overflown object
loss	loss
mod	modified
m	molecular diffusion
md	mono-disperse
N	standard conditions
oil	oil
onb	on-set of nucleate boiling
os	outermost slit
o	outer
out	outlet
PF	partial flow
p	particle
p	pins
pd	poly-disperse
pore	pore
r	reaction
slit	slit
s	solid
strut	strut
total	total
t	tube
turb	turbulent

Index	Meaning
-------	---------

w	wall
---	------

### Non-dimensional Numbers

Abbreviation	Meaning
--------------	---------

Bo	Bodenstein number
Nu	Nusselt number
Pr	Prandtl number
Re	Reynolds number

### Abbreviations

Abbreviation	Meaning
--------------	---------

Al <sub>2</sub> O <sub>3</sub>	aluminium oxide (alumina)
Ar	argon
CH <sub>2</sub>	hydrocarbon repetition unit
CH <sub>4</sub>	methane
CO <sub>2</sub>	carbon dioxide
CO	carbon monoxide
Co	cobalt
Cu	copper
Fe	iron
H <sub>2</sub> O	water
H <sub>2</sub>	hydrogen
He	helium
Hf	hafnium
Li	lithium
Mn	manganese
N <sub>2</sub>	nitrogen
Nd	neodymium
Pt	platinum
Re	rhenium
Rh	rhodium
Ru	ruthenium
Si	silicon
TiO <sub>2</sub>	titanium dioxide (titania)
AG	Aktiengesellschaft
AISI	American Iron and Steel Institute
AM	additive manufacturing
ASF	Anderson-Schulz-Flory
BMBF	German Federal Ministry of Education and Research
CAD	computer aided design

Abbreviation	Meaning
CFD	Computational Fluid Dynamics
CtL	Coal-to-Liquid
DAC	direct air capture
DB	diffusion bonding
DCN	derived cetane number
DfAM	design for additive manufacturing
DIN	Deutsches Institut für Normung
<i>ET</i>	exposure time
EU	European Union
FBR	fixed bed reactor
FEA	finite element analysis
FGE	fluid guiding element
FGU	fluid guiding unit
FTS	Fischer-Tropsch synthesis
GC	gas chromatograph
GmbH	Gesellschaft mit beschränkter Haftung
GtL	Gas-to-Liquid
<i>HD</i>	hatch distance
HM	hybrid manufacturing
HP	heating plate
IMVT	Institute for Micro Process Engineering
ISO	International Standards Organisation
KIT	Karlsruhe Institute of Technology
LASER	light amplification by stimulated emission of radiation
<i>LC</i>	laser current
<i>LCP</i>	longitudinal conduction parameter
LHV	lower heating value
<i>LP</i>	lens position
<i>LV</i>	laser velocity
MSR	micro-structured reactor
<i>MTW</i>	melting trace width
MVM	Institut für Mechanische Verfahrenstechnik und Mechanik
NDT	non-destructive testing
NI	National Instruments
NNPC	Nigerian National Petroleum Corporation
$P_L$	laser power
P2X	Power-to-X
P&ID	piping and instrumentation diagram
PBF-LB/M	laser-based powder bed fusion of metals
PC	personal computer
<i>PD</i>	point distance
PFD	process flow diagram
POCS	periodic open cellular structure
PTFE	poly-tetra fluorine ethylene
PtL	Power-to-Liquid
PtX	Power-to-X

---

Abbreviation	Meaning
SAF	sustainable aviation fuels
SBC	slurry bubble column reactor
<i>SD</i>	spot diameter
SEC	specific energy consumption
SLS	static light scattering
SMDS	Shell middle distillate synthesis
STL	standard tessellation language
<i>STY</i>	space time yield
<i>SV</i>	space velocity
<i>TOS</i>	time on stream
UK	United Kingdom
UNG	Uzbekneft Gas
USA	United States of America
VDI	Verein Deutscher Ingenieure
w/	with
w/o	without
YAG	yttrium aluminium garnet





## A. Sustainable Aviation Fuels (SAF)

### A.1. Chemical Species

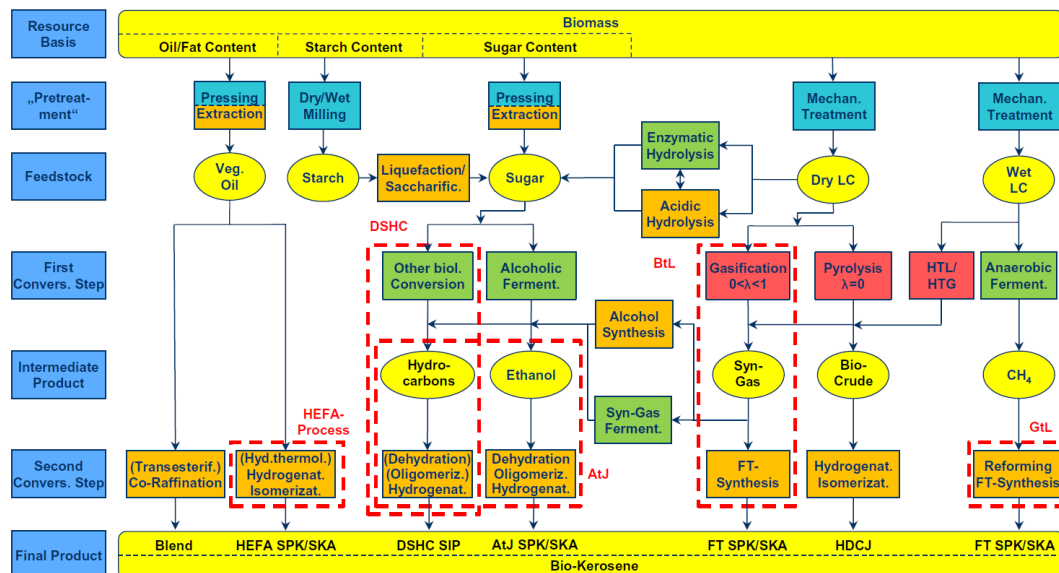
Table A.1 shows some of the short-chained paraffins and olefins present in FTS product.

**Table A.1.:** Paraffins and olefins up to carbon number of four present in Fischer-Tropsch product.

$n_C$	Paraffin	Olefine
1	CH <sub>4</sub>	-
2	C <sub>2</sub> H <sub>6</sub>	C <sub>2</sub> H <sub>4</sub>
3	C <sub>3</sub> H <sub>8</sub>	C <sub>3</sub> H <sub>6</sub>
4	C <sub>4</sub> H <sub>10</sub> , i-C <sub>4</sub> H <sub>10</sub>	1-Butene, 2-Butene, 1,3-Butadiene (cis and trans), Isobutene

### A.2. SAF Production Routes

Biogenic routes towards sustainable aviation fuels (SAF) are given in fig. A.1. The FTS route presented in this thesis as well as the alcohol-to-jet route can also be based on renewable electricity.



**Figure A.1.:** Different biogenic production routes for SAF [303]. Reproduced with permission from Elsevier (©2018).

### A.3. Calculations

The molar density at standard conditions is given in eq. (A.1).

$$\tilde{\rho}_N = \frac{n}{V} = \frac{p}{\tilde{R} \cdot T} = \frac{101,325 \text{ J m}^{-3}}{8.314 \text{ J mol}^{-1} \text{ K}^{-1} \cdot 273.15 \text{ K}} = 44.62 \text{ mol m}^{-3} \quad (\text{A.1})$$

$$V_N = 0.022,41 \text{ m}^3 \text{ mol}^{-1} \quad (\text{A.2})$$

Axial dispersion is insignificant, if eq. (A.3) is fulfilled, the left side of the equation being 380 for reactor and catalyst used in chapter 5. Calculation of Bodenstein number  $Bo$  is given in eq. (A.4)

$$\frac{l_{\text{cat}}}{d_p} > \frac{8}{Bo_i} \cdot n_i \cdot \ln \left( \frac{1}{1 - X_i} \right) \text{ with } i = \text{H}_2, \text{CO} \quad (\text{A.3})$$

$$\frac{1}{Bo_i} = \frac{\epsilon_{\text{bed}} \cdot D_{\text{im}}}{\tau \cdot d_p \cdot u_0} + 0.5 \quad (\text{A.4})$$

$$u_0 = \frac{\dot{V}}{A_{\text{cross}}} \quad (\text{A.5})$$

$$\dot{V} = \dot{V}_N \cdot \frac{p_N}{p} \cdot \frac{T}{T_N} \quad (\text{A.6})$$

$$c_i = \frac{y_i \cdot p}{\tilde{R} \cdot T} \quad (\text{A.7})$$

$$r_{\text{CO}}^V = \frac{\dot{n}_{\text{CO,conv}}}{V_{\text{cat}}} \quad (\text{A.8})$$

$$\dot{n}_{\text{CO,conv}} = \dot{n} \cdot y_{\text{CO,in}} \cdot X_{\text{CO}} \quad (\text{A.9})$$

$$\dot{n} = \dot{V}_N \cdot \tilde{\rho}_N \quad (\text{A.10})$$

Intra-particle and inter-particle mass transfer limitations and intra-particle and inter-particle heat transfer limitations can be neglected, when the inequalities in eqs. (A.11) to (A.14) are fulfilled.

$$\frac{\left( \frac{d_p}{6} \right)^2 \cdot \frac{n_i+1}{2} \cdot r_i^V}{(1 - \epsilon_{\text{bed}}) \cdot D_{\text{ieff}} \cdot c_i} < 0.15 \text{ with } i = \text{H}_2, \text{CO} \quad (\text{A.11})$$

$$\frac{d_p^2 \cdot r_i^V}{12 \cdot (1 - \epsilon_{\text{bed}}) \cdot D_{\text{im}} \cdot c_i} < 1 \text{ with } i = \text{H}_2, \text{CO} \quad (\text{A.12})$$

$$\frac{-\Delta H_R^0 \cdot \left( \frac{d_p}{2} \right)^2 \cdot r_{\text{CO}}^V}{(1 - \epsilon_{\text{bed}}) \cdot \lambda_{\text{bed}} \cdot T} \cdot \frac{E_a}{\tilde{R} \cdot T} < 1 \quad (\text{A.13})$$

$$\frac{-\Delta H_R^0 \cdot \frac{d_p}{2} \cdot r_{\text{CO}}^V}{(1 - \epsilon_{\text{bed}}) \cdot \alpha_{\text{bed}} \cdot T} \cdot \frac{E_a}{\tilde{R} \cdot T} < 0.05 \quad (\text{A.14})$$

**Table A.2.:** Additional values for calculation of reaction criteria.

Parameter	Symbol / unit	Value	Comment
Bed length	$l_{\text{cat}} / \text{m}$	0.055	
Bed porosity	$\epsilon_{\text{bed}} / -$	0.5	
Mixture diffusivity	$D_{\text{H}_2\text{m}} / \text{m}^2 \text{s}^{-1}$	$6.86 \times 10^{-5}$	
Mixture diffusivity	$D_{\text{COm}} / \text{m}^2 \text{s}^{-1}$	$6.05 \times 10^{-5}$	
Bed tortuosity	$\tau / -$	2	$\tau = 1/\epsilon_{\text{bed}}$
Particle diameter	$d_p / \text{m}$	0.00015	
Reaction order	$n_{\text{H}_2}$	0.5	
Reaction order	$n_{\text{CO}}$	1	
Effective pore diffusivity	$D_{\text{H}_2\text{eff}} / \text{m}^2 \text{s}^{-1}$	$5 \times 10^{-9}$	
	$D_{\text{COeff}} / \text{m}^2 \text{s}^{-1}$		
Reaction enthalpy	$\Delta H_{\text{R}}^0 / \text{J mol}_{\text{CO}}^{-1}$	-160,000	
Bed thermal conductivity	$\lambda_{\text{bed}} / \text{W m}^{-1} \text{K}^{-1}$	1	
Activation energy	$E_a / \text{J mol}_{\text{CO}}^{-1}$	100	
Inlet molar fraction	$y_{\text{H}_2,\text{in}} / -$	0.646	
Inlet molar fraction	$y_{\text{CO},\text{in}} / -$	0.323	
Bed gas heat transfer coefficient	$\alpha / \text{W m}^{-2} \text{K}^{-1}$	5267	With $\lambda_g=0.16$ $\text{W m}^{-2} \text{K}^{-1}$ and $\text{Nu}=5$
Cross-sectional area	$A_{\text{cross}} / \text{mm}^2$	80	

Additional values for the calculation of the above mentioned criteria are provided in table A.2.

The evaluated criteria for each set-point can be found in table A.3.

The adiabatic temperature rise can be estimated via eq. (A.15).

$$\dot{n} \cdot \tilde{c}_p \cdot \Delta T_{\text{ad}} = \dot{n} \cdot y_{\text{CO},\text{in}} \cdot (-H_{\text{R}}^0) \quad (\text{A.15})$$

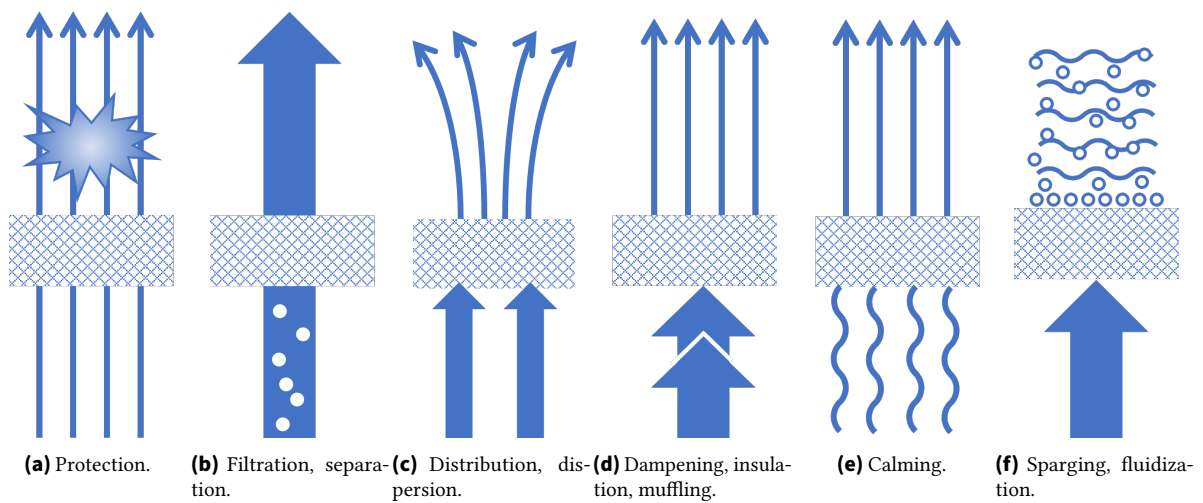
$$\Delta T_{\text{ad}} = \frac{0.323 \cdot 152 \times 10^3 \text{ J mol}^{-1}}{29 \text{ J mol}^{-1} \text{ K}^{-1}} = 1730 \text{ K} \quad (\text{A.16})$$

Table A.3.: Evaluation of criteria.

N.	$T /$ $^{\circ}\text{C}$	$SY_{\text{mod}}$ $/ \text{Ln}$ $\text{g}^{-1}_{\text{cat}}$ $\text{h}^{-1}$	$\dot{V}_N /$ $\text{Ln}$ $\text{h}^{-1}$	$X_{\text{CO}}$ $\%$	$X_{\text{H}_2}$ $\%$	$c_{\text{H}_2} /$ $\text{mol}$ $\text{m}^{-3}$	$c_{\text{CO}} /$ $\text{mol}$ $\text{m}^{-3}$	$r^V_{\text{H}_2} /$ $\text{mol}$ $\text{m}^{-3}$ $\text{s}^{-1}$	$r^V_{\text{CO}} /$ $\text{mol}$ $\text{m}^{-3}$ $\text{s}^{-1}$	$u_0 / \text{m}$ $\text{s}^{-1}$	Eq. A.3 $\text{H}_2$	Eq. A.3 $\text{CO}$	Eq. A.11 $\text{H}_2$	Eq. A.11 $\text{CO}$	Eq. A.12 $\text{H}_2$	Eq. A.12 $\text{CO}$	Eq. A.13	Eq. A.14
1	200	3.59	12	39.3	36.7	329	164	8.57	4.28	3.6	59	114	0	0.01	1.43E-06	1.62E-06	4.14E-04	1.05E-03
2	209	3.59	12	52.6	51.5	322	161	11.45	5.73	3.67	92	167	0.01	0.01	1.94E-06	2.20E-06	5.34E-04	1.35E-03
3	219	3.59	12	70.9	72.4	316	158	15.46	7.73	3.75	160	271	0.01	0.01	2.68E-06	3.03E-06	6.91E-04	1.75E-03
4	219	5.38	17.9	56	55.8	316	158	18.3	9.15	5.61	68	121	0.01	0.01	3.17E-06	3.59E-06	8.18E-04	2.07E-03
5	229	5.38	17.9	79	80.6	310	155	25.8	12.9	5.73	134	226	0.02	0.02	4.56E-06	5.17E-06	1.11E-03	2.81E-03
6	209	5.38	17.9	43.3	41.2	322	161	14.15	7.08	5.5	45	86	0.01	0.01	2.40E-06	2.72E-06	6.59E-04	1.67E-03
7	200	5.38	17.9	27.8	26.5	329	164	9.07	4.54	5.4	27	50	0.01	0.01	1.51E-06	1.71E-06	4.39E-04	1.11E-03
8	209	1.85	6.2	65.1	67.7	322	161	7.31	3.66	1.89	276	453	0	0.01	1.24E-06	1.41E-06	3.41E-04	8.62E-04
9	200	1.85	6.2	53	53.5	329	164	5.96	2.98	1.86	190	331	0	0	9.91E-07	1.12E-06	2.88E-04	7.30E-04
10	190	1.85	6.2	31.4	31.2	336	168	3.52	1.76	1.82	95	169	0	0	5.74E-07	6.51E-07	1.78E-04	4.50E-04
11	209	9	30	16.9	16.6	322	161	9.23	4.62	9.2	9	17	0.01	0.01	1.57E-06	1.78E-06	4.30E-04	1.09E-03
12	229	9	30	48.5	50.5	310	155	26.51	13.25	9.58	35	59	0.02	0.02	4.68E-06	5.31E-06	1.14E-03	2.88E-03
13	219	9	30	38.5	38.4	316	158	21.03	10.52	9.39	25	44	0.01	0.02	3.64E-06	4.13E-06	9.41E-04	2.38E-03
14	234	9	30	69.2	71	307	153	37.82	18.91	9.68	61	103	0.02	0.03	6.75E-06	7.65E-06	1.59E-03	4.03E-03
1R	200	3.59	12	42.3	41.2	329	164	9.22	4.61	3.6	68	125	0.01	0.01	1.53E-06	1.74E-06	4.46E-04	1.13E-03

## B. Fabrication

### B.1. Application of Fluid-Permeable Structures



**Figure B.1.:** Application of porous structures in process engineering [304].

### B.2. Manufacturing of Micro-Structured Reactors

The following steps are part of the fabrication process of micro-structured reactor (MSR) at IMVT [101]. Foils have to be designed in order to withstand compression during diffusion bonding. A rule of thumb is that the remaining foil thickness must be at least half of channel width.

- thermocouple foil: sinker electric discharge machining
- cooling foil: etching
- catalyst foil: laser cutting, deburring, milling
- foils stack: cleaning, measuring, aligning, stacking
- foils stack: diffusion welding
- reactor body: milling of front sides
- reaction connectors: electron beam welding
- cooling connectors: tungsten inert gas welding
- spacers: wire electric discharge machining

### B.3. Realizer SLM125

The laser power in W is related to the laser current in mA via eq. (B.1). Important values of power can be seen in table B.1.

$$LP = (LC - 177.73) / 9.4047 \quad (B.1)$$

**Table B.1.:** Laser power as function of laser current

LC / mA	P / W
178	0
600	45
1000	87
1100	98
1118	100
2059	200
2999	300
3940	400

The spot diameter as a function of the lens position can be seen in table B.2.

**Table B.2.:** Spot diameter as a function of lens position.

LP / mm/100	LP / mm	SD / $\mu\text{m}$
50	0.5	138
0	0	75
-50	-0.5	48
-75	-0.75	44
-100	-1	47
-150	-1.5	57
-175	-1.75	87
-200	-2	112
-250	-2.5	163
-300	-3	317
-400	-4	661

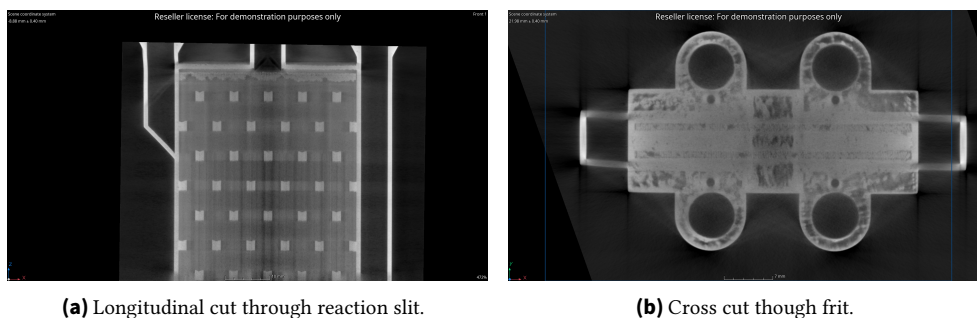
Scan strategy of lattice is shown in table B.3.

### B.4. CT of AM Reactor

At Formnext 2022, employees of Comet Xylon GmbH (Hamburg, Germany) kindly performed a computer tomography scan of a reactor similar to the one used in the experiments in chapter 5. fig. B.2 depicts slices through the reactor.

**Table B.3.:** Scanning strategies used in this work.

Detail	Unit	Value
Process conditions		
Melting trace width ( <i>MTW</i> )	mm	0.16
Heating	°C	130
$h_1$	mm	0.05
Heat function	-	False
Support definition	-	$> 10 \text{ mm}^2$ ; 0-45°
Comment	-	
Lattice		
Exposure time ( <i>ET</i> )	$\mu\text{s}$	180
Point distance ( <i>PD</i> )	$\mu\text{m}$	40
Laser velocity ( <i>LV</i> )	$\text{m s}^{-1}$	0.22
Laser current ( <i>LC</i> )	mA	1800
Laser power ( $P_L$ )	W	172
Lens position ( <i>LP</i> )	mm	0.6

**Figure B.2.:** CT scan of a reactor similar to the one used in chapter 5.

## B.5. TÜV Approval

Additive manufacturing techniques such as PBF-LB/M are not harmonized with Pressure Equipment Directive, although this is in a planning stage. The German mirror committee for the European working group has issued the draft for the prEN 13445-14 as technical specification.

TÜV Süd has a procedure for the approval of AM pressure vessels. This is created as a modular inspection and test plan, where, depending on the part and application, requirements for design, materials, fabrication, and testing are stipulated. The procedure always includes so-called initial material data, being tensile properties, in its simplest form.

Together with a notified body, BASF created guidelines, based on which they produce and approve pressure vessels. It abides by the steps of TÜV Süd's procedure. To streamline the process, BASF establishes the smallest defects they can detect with a reasonable effort via non-destructive testing (NDT). They select a higher margin of safety to reduce the fraction of a part that has to be tested. They identify the space in the build chamber which results in the least good material properties, and this is where they build accompanying test parts for destructive testing.



Draft – Muster / Proposal / Proposta - ITP [Inspection and Test Plan]

**Legende/ legend** W = bestätigter Abnahmepunkt Witness point / punto di accettazione confermato  
**legenda:** R = Dokumentationsprüfung review documents / Revisione della documentazione  
 RI = gleitende Inspektion Random inspection / ispezione di rotolamento  
 H = Haltepunkt hold point / Stop

M = Hersteller Manufacturer / costruttore  
 NoBo = Notified Body  
 C = Kunde/Besteller Client/ cliente

<b>Inspection &amp; test plan (ITP)</b>			Datum: date: data:	Rev.
Hersteller / manufacturer / costruttore:	Benennung / designation / denominazione:	Besteller / orderer / ordinatore:		
Auftrags-Nr. / Order No / N d'ordine.:	Herstell-Nr. / serial no. / N di produzione:			
Positions-Nr. / N di posizione:	Zeichng. Nr. / drawing no / N di disegno.:			

Lfd. Nr. / No.N.	Art und Umfang der Prüfung type and range of check tipo e portata dell'esame	Anzuwendende Dokumente / Kriterien Applicable documents and acceptance criteria documenti/criteri applicabili	Prüfzuständigkeit test competence responsabilità del test								Bemerkungen remark commenti
			M	Signum	C	Signum	NoBo	Signum	xx	Signum	
1.	Prüfung vor Fertigungsbeginn Inspection before manufacturing Ispezione prima dell'inizio della produzione										
1.1	Entwurfsprüfung review of design Revisione del design										
1.2a	Prüfung NDT-Konzept inkl. Bewertungskriterien Review NDT-concept with assessment-criteria Esame del concetto di NDT, compresi i criteri di valutazione										
1.2b	Validierung NDT-Konzept bei komplexen Strukturen Validation NDT concept for complex structures Convalida del concetto di NDT per strutture complesse										

Figure B.3.: First page of inspection and test plan: template for the approval of AM parts by TÜV Süd [305].

## B.6. Realizer SLM 125

### B.6.1. Tensile Tests

With a scanning strategy leading to porous parts, flat tensile test specimens were fabricated. The strength observed at room temperature and at  $T=250\text{ }^{\circ}\text{C}$  was lower, compared to wrought sheet metal fig. B.4. Sample cubes showed porosity in cross-cuts between contour and hatching and within the hatching. The former porosity was also seen in the ruptured tensile samples fig. B.5.

### B.6.2. Thin Walls with Discrete Thicknesses

Decreasing wall thickness is desirable as it leads to lower material demand, print time, and cost with otherwise constant conditions. However, there are the following constraints: depending on the part design, the stability might be insufficient. The risk of fabrication errors increases as the thin walls are compared to thick walls more influenced by the recoater movement and heat. With very low wall thickness, leakage might occur depending on the scanning strategy. Depending on printing parameters, a thin wall below a certain threshold consists of only two or four contours, fig. B.6. It is reasonable to identify the correct discrete values for these cases. Starting from the value where sufficient hatching is included, wall thickness can be chosen arbitrarily.

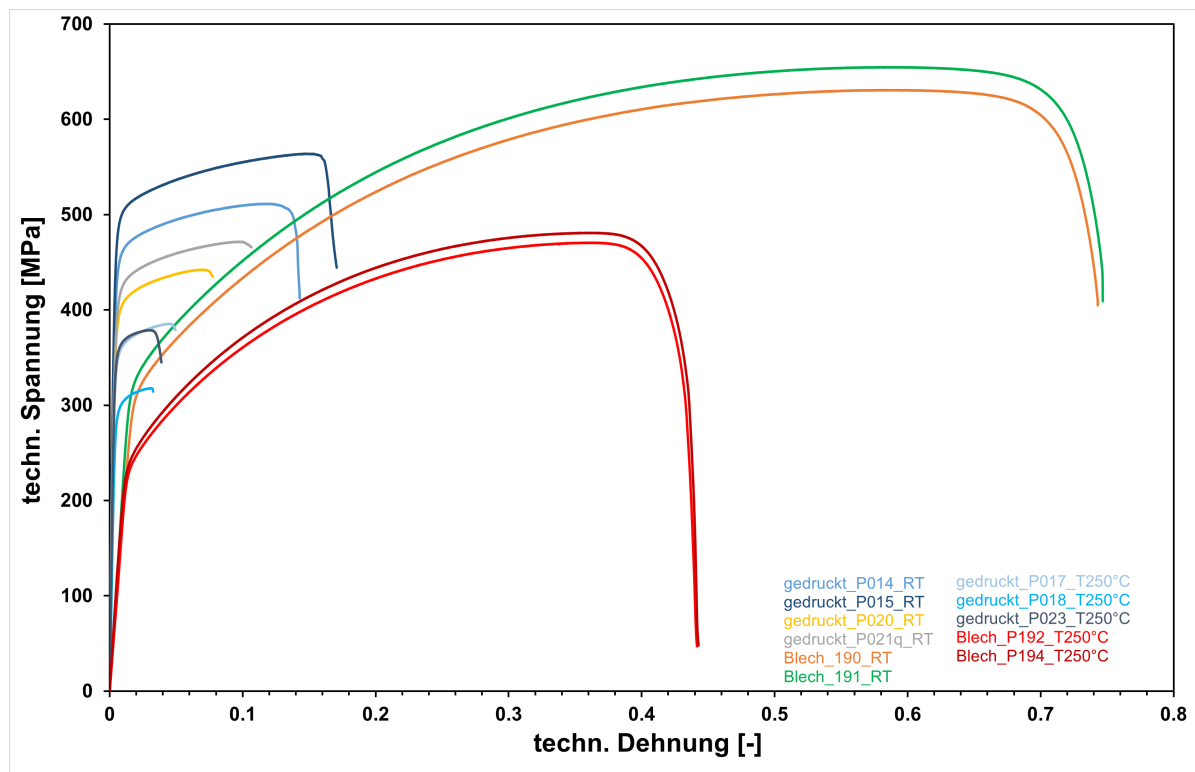


Figure B.4.: Strain-stress diagram.



(a) Rolled sheet metal specimens.



(b) PBF-LB/M specimens.

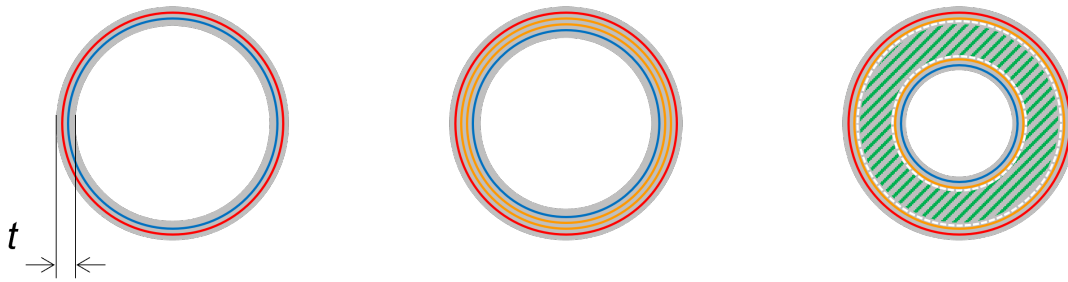


(c) Rolled sheet metal specimens fracture surface. Ductility was clearly visible.



(d) PBF-LB/M specimens fracture surface. Fracture had resemblance to brittle fracture. At the walls seemed to be a gap.

Figure B.5.: Photos of tensile specimens and fracture surface.



**Figure B.6.:** Schematic of part with varying wall thickness and realistic scanning vectors.

## B.7. Reactors

Reactor 'fully additive' cut open is shown in fig. B.7.

Manufacturing drawing of a flange for the hybrid concept is shown in fig. B.8.

Several reactors were designed over the course of the work with gradual improvements (fig. B.9). One of these reactors, shown in fig. B.10, could not be post-processed well at the connections due to vibrating. In addition, the flange was not solid and the sealing and bolt holes were undersized.



**Figure B.7.:** Picture of reactor 'fully additive' cut open.

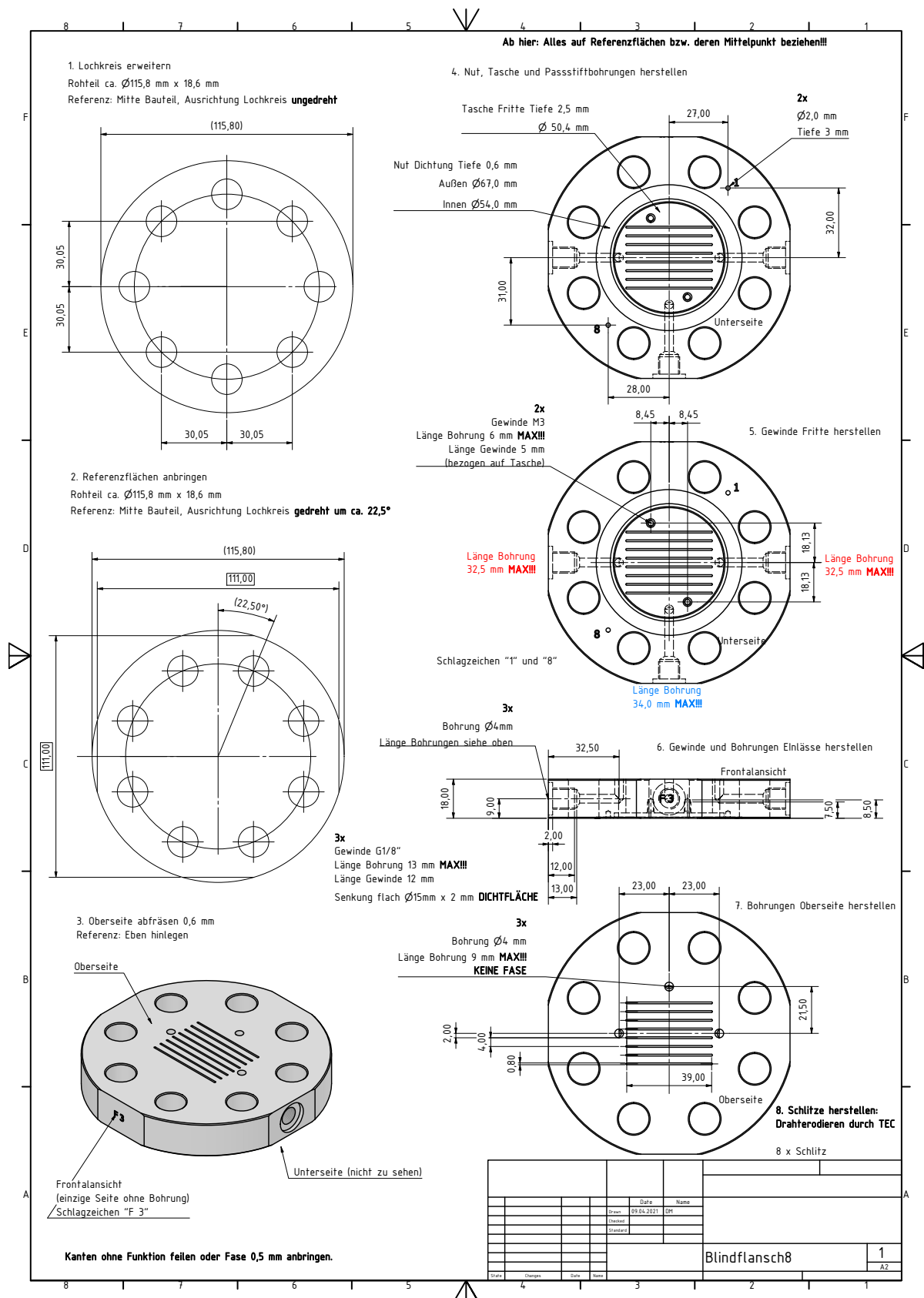
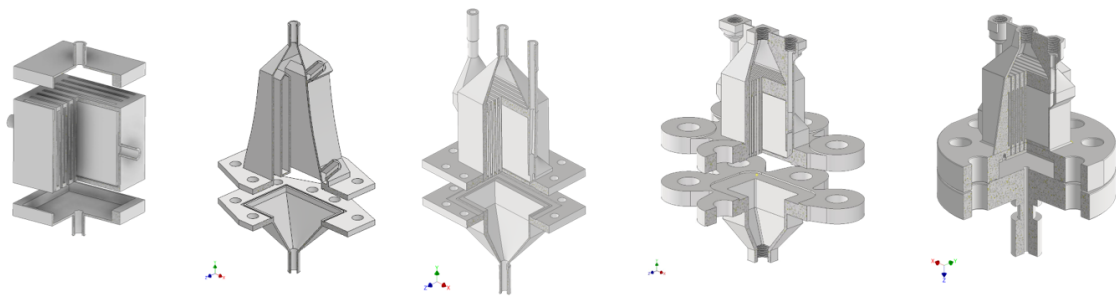
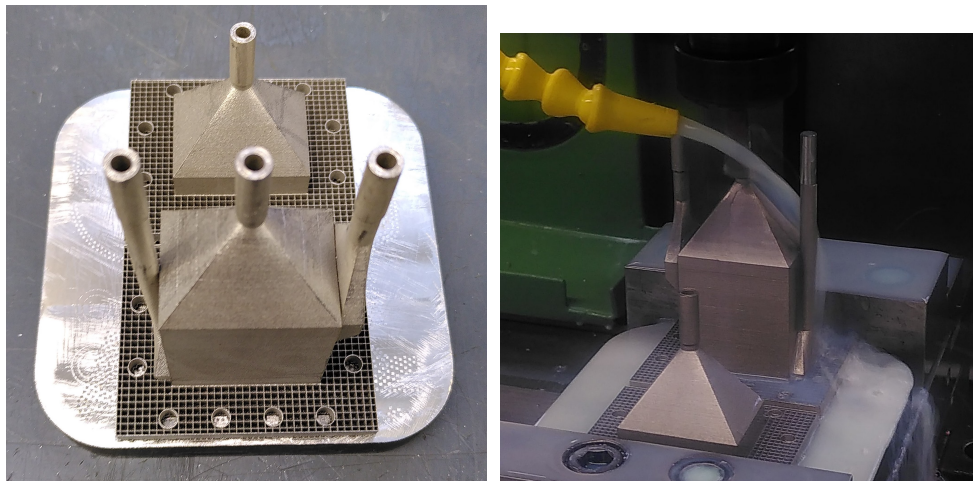


Figure B.8.: Manufacturing drawing of a flange for the hybrid concept.



**Figure B.9.:** Reactor designs having been gradually improved over time.



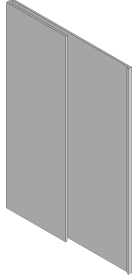
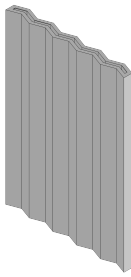
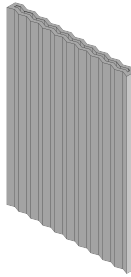
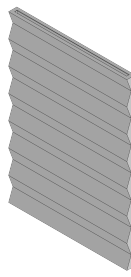
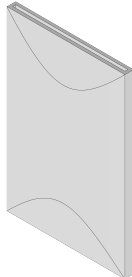
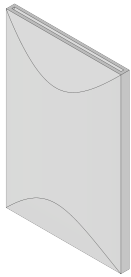
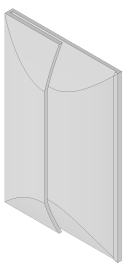
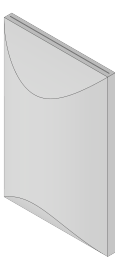
**(a)** Printed reactor still on build-plate facilitating fixation during post-processing. **(b)** Connectors being post-processed vibrated due to high aspect ration. Right connector was already done.

**Figure B.10.:** Pictures of preliminary fully additive reactor.

## B.8. All Modules

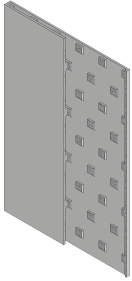
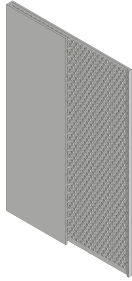
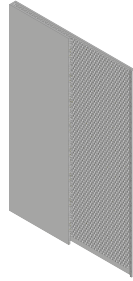
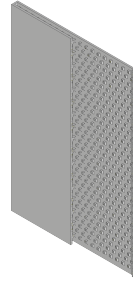
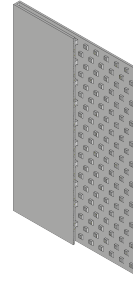
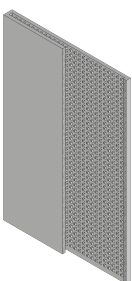
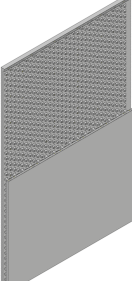
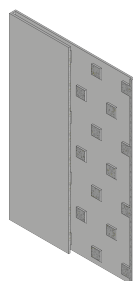


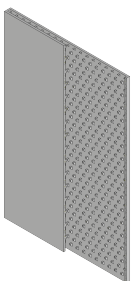
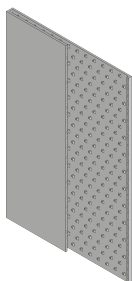
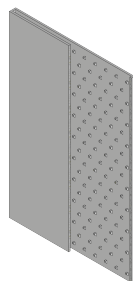
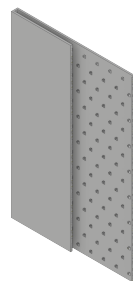
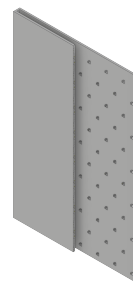
All modules used for testing are shown in tables B.4 to B.10.

**Table B.4.:** Modules without internal structures  $t_w=1$  mm,  $\varphi=0$ .

Planar	Corrugated $n = 5$	Corrugated $n = 10$	Corrugated per- pendicular
			
Arched $\delta=5^\circ$	Arched $\delta=15^\circ$	Arched $\delta=30^\circ$	Arched $\delta=45^\circ$
			

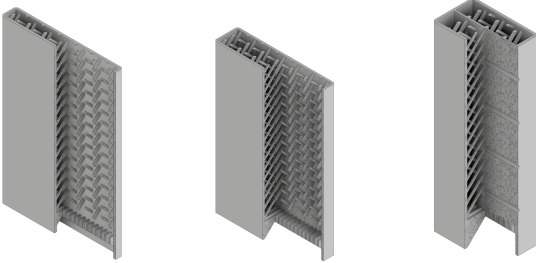


**Table B.5.:** Pin-equipped modules with  $t_w=0.6$  mm.

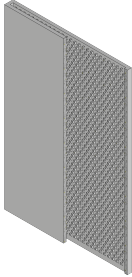
$t_p$ / mm	2	0.42	0.26	0.6	1.0
    					
$\varphi$ / -	0.09	0.15	0.19	0.14	0.12
$t_p$ / mm	0.42 regular.	0.42 trans.	3	4	5
    					
$\varphi$ / -	0.13	0.15	0.12	0.11	0.11
$t_p$ / mm	0.42	0.42	0.42	0.42	0.42
    					
$\varphi$ / -	0.07	0.04	0.02	0.017	0.01



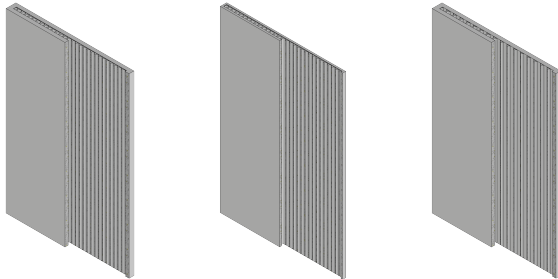
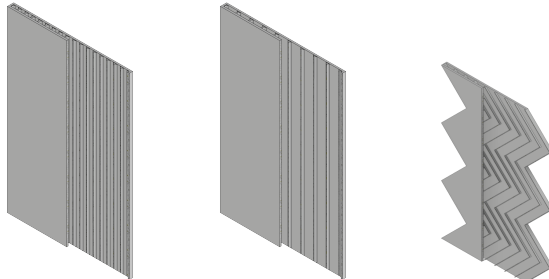
**Table B.6.:** Pin-equipped module with  $t_w=0.8$  mm,  $t_p=1$  mm, and  $a=3.4$  mm.

$d_{\text{slit}}$ / mm	4	8	12
			
$\varphi$ / -	0.15	0.15	0.15

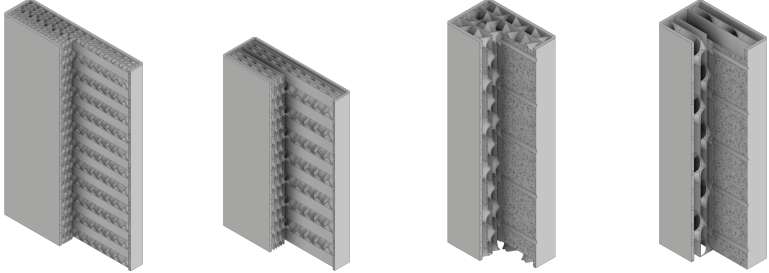
**Table B.7.:** Pin-equipped module with  $t_w=1$  mm.

$t_p$ / mm	0.42
	
$\varphi$ / -	0.15

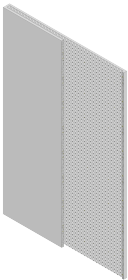
**Table B.8.:** Fin-equipped modules.

$t_w / \text{mm}$	1.0	0.6	1.0
$t_e / \text{mm}$	1	1	2
			
$\varphi / -$	0.33	0.33	0.14
$t_e / \text{mm}$	2	4	4
$t_w / \text{mm}$	0.6		
			
$\varphi / -$	0.14	0.10	

**Table B.9.:** FGE-equipped modules  $t_w=0.8 \text{ mm}$ .

$d_{\text{FGE}} / \text{mm}$	1.333	2	3	4
				
$\varphi / -$				

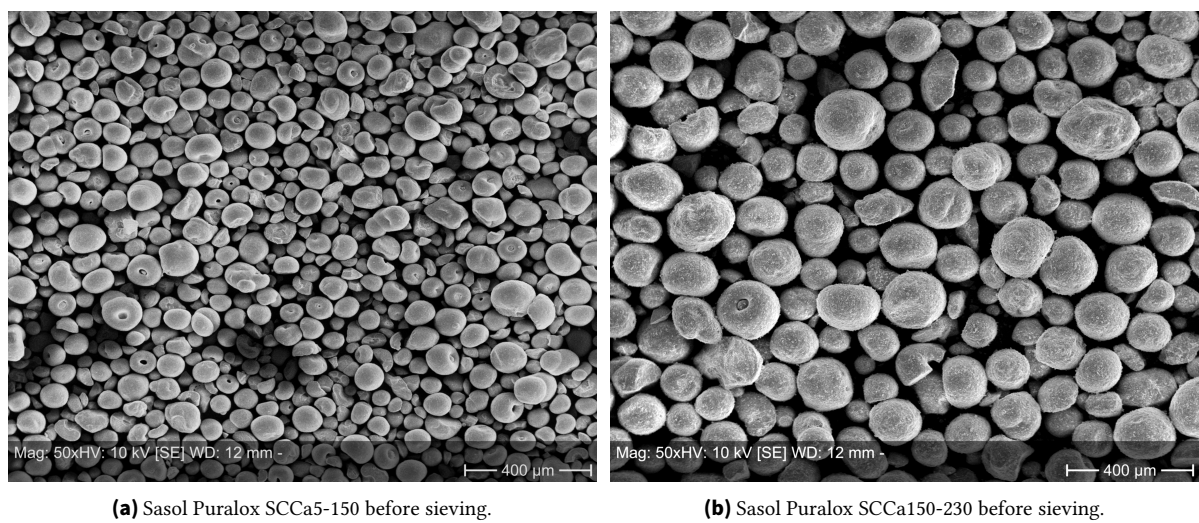
**Table B.10.:** Lattice-equipped module.

6201	
$t_w$ / mm	0.6
$t_e$ / mm	1
	
$\varphi$ / -	0.20

## C. Materials

### C.1. Alumina Powders

Before the powders was sieved to remove the smallest 10 wt-% of each, scanning electron microscope images were captured fig. C.1.



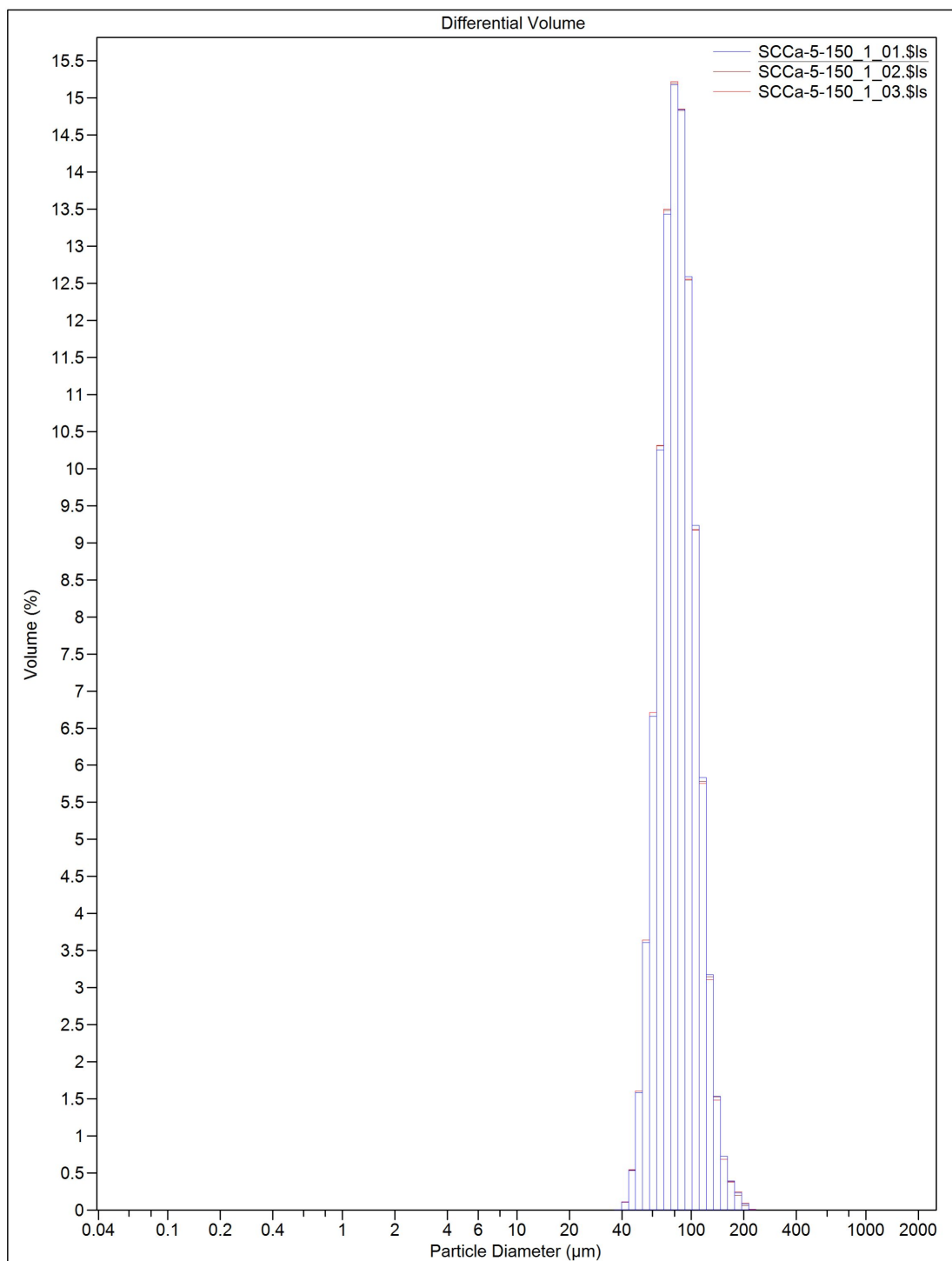
**Figure C.1.:** Scanning electron microscope images of alumina powders.



## LS Particle Size Analyzer

7 Aug 2023 16:57

Beckman Coulter LS 13 320



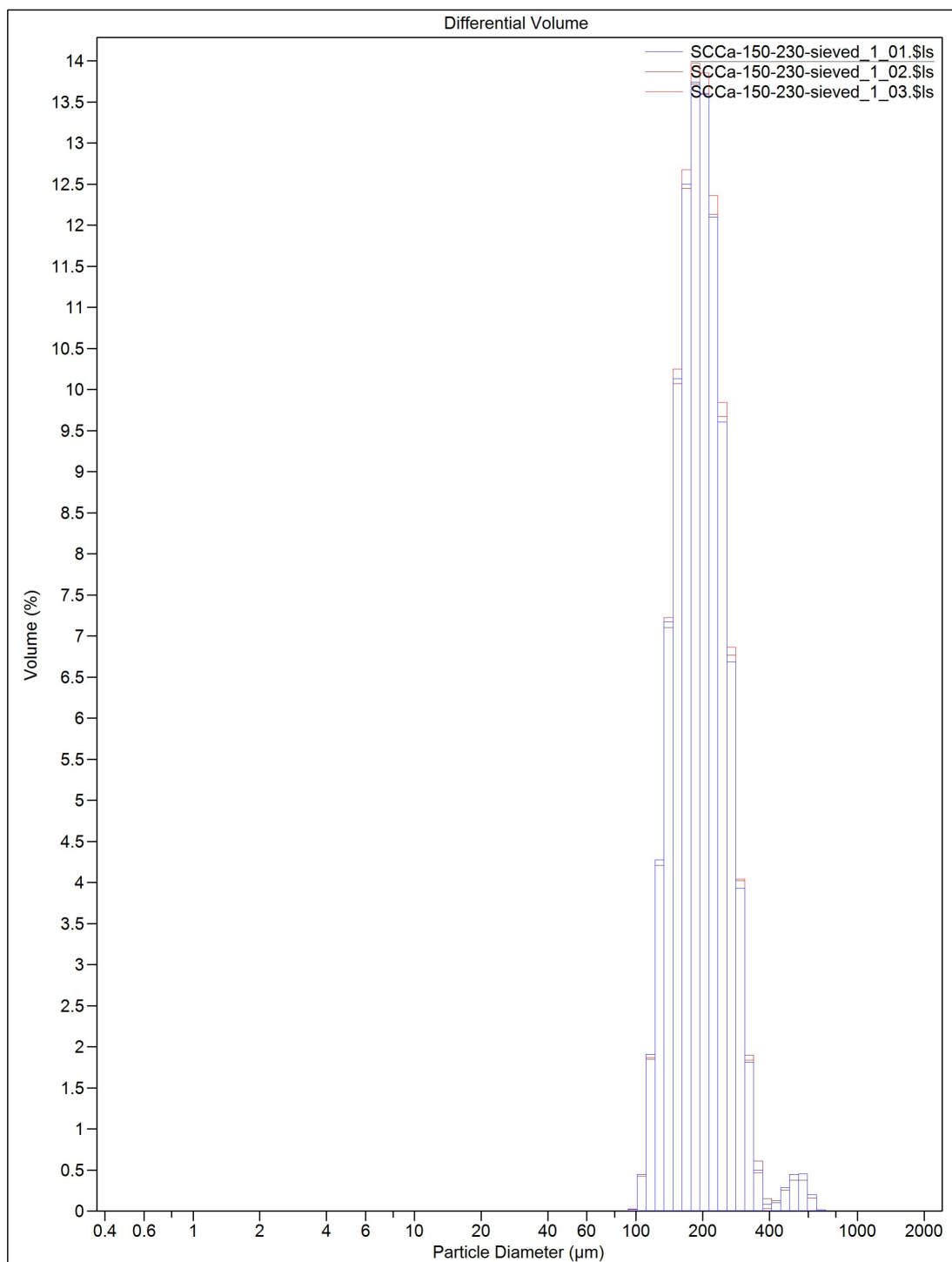
**Figure C.2.:** Report from static light scattering (SLS) analysis of sieved Sasol Puralox SCCa5-150.



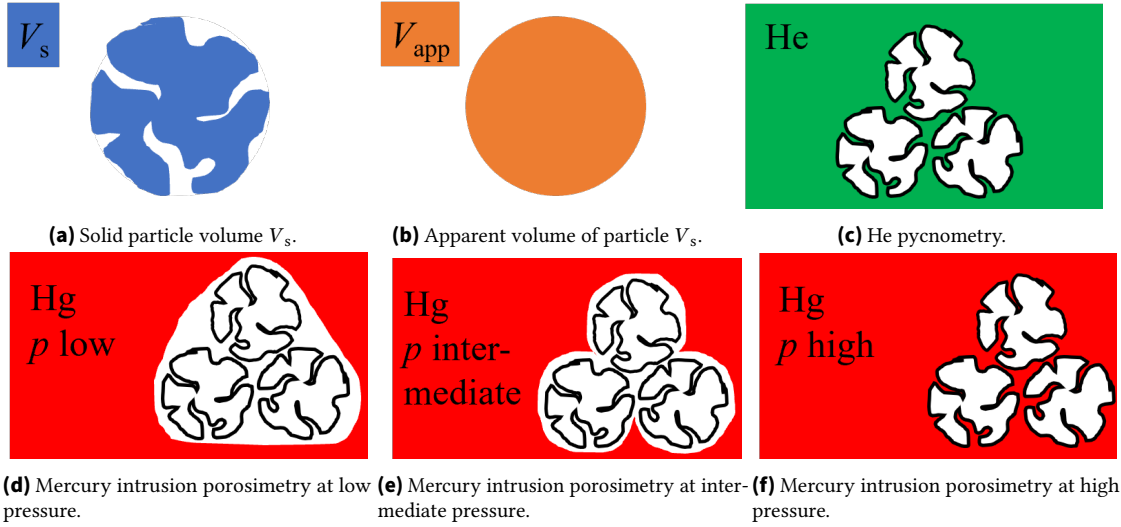
## LS Particle Size Analyzer

8 Aug 2023 12:15

Beckman Coulter LS 13 320

**Figure C.3.:** Report from SLS analysis of sieved Sasol Puralox SCCa150-230.

For calculating porosity of packed beds  $\rho_{\text{bed}}$  in this work the apparent particle density  $\rho_{\text{app}}$  was required. In fig. C.4 necessary definitions and explanations of experiments are given. The solid volume is shown in fig. C.4a and relates to the particle mass  $m_s$ . It can be obtained from He pycnometry (fig. C.4c) or from Hg intrusion porosimetry at high pressure (neglecting micro pores, fig. C.4f). The apparent volume is shown in fig. C.4b and can be obtained from Hg intrusion porosimetry at intermediate pressure (fig. C.4e).



**Figure C.4.:** Schematic representation of porous particle(s) being tested with He pycnometry and Hg intrusion porosimetry.

With the help of Hg intrusion porosimetry both the mass-specific pore volume  $v_{\text{pore}}$  and the solid particle density  $\rho_p$  were obtained. From these the apparent particle density  $\rho_{\text{app}}$  could be calculated according to eqs. (C.1) to (C.3). In table C.1 obtained results and calculated solid densities are given.

$$V_{\text{app}} = V_s + V_{\text{pore}} \quad (\text{C.1})$$

$$\frac{m_s}{\rho_{\text{app}}} = \frac{m_s}{\rho_p} + v_{\text{pore}} \cdot m_s \quad (\text{C.2})$$

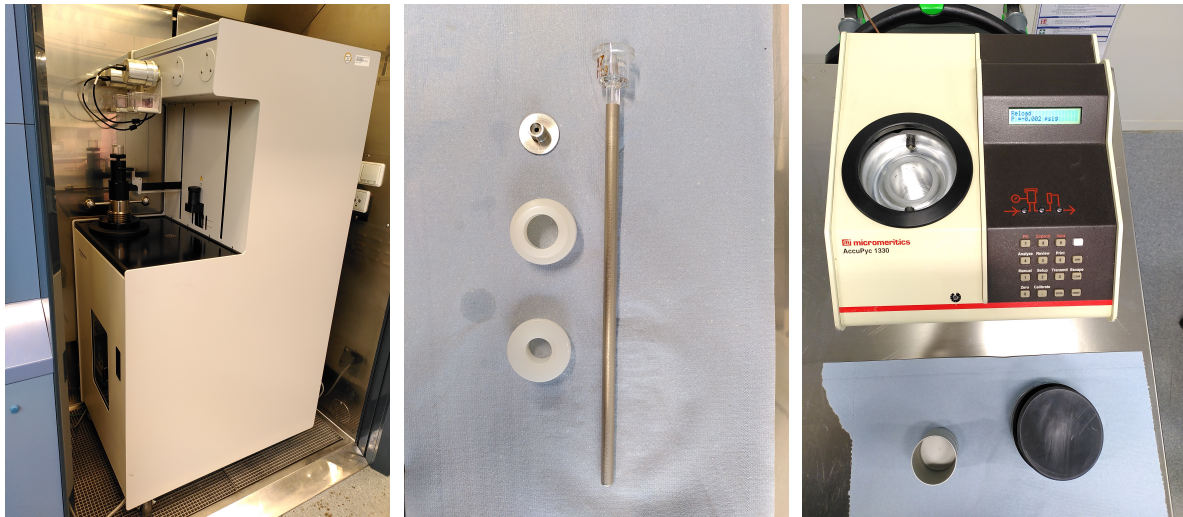
$$\rho_{\text{app}} = \frac{1}{1/\rho_p + v_{\text{pore}}} \quad (\text{C.3})$$

**Table C.1.:** Results from Mercury intrusion porosimetry and calculation of solid density.

$d_p / \mu\text{m}$	$v_{\text{pore}} / \text{ml g}^{-1}$	$\rho_p / \text{g ml}^{-1}$	$\rho_{\text{app}} / \text{g ml}^{-1}$
83	0.4359	3.5151	1.388
194	0.4753	2.9668	1.231

$$\rho_{\text{app}} = (1 - \epsilon_{\text{bed}}) \cdot \rho_s \quad (\text{C.4})$$

Mercury intrusion porosimetry was executed on a AutoPore V Servies (fig. C.5a), He pycnometry was conducted on a AccuPyc 1330 (fig. C.5c) both by Micromeritics GmbH (Unterschleißheim, Germany). For Mercury intrusion porosimetry a penetrometer suitable for fine particles was used. The penetrometer has a sample chamber with a recess for the powder and a hollow shaft (fig. C.5b). With the outside being metal-coated, the level of Hg inside the capillary could be measured via electrical capacitance.



(a) Mercury intrusion porosimetry machine. (b) Mercury intrusion porosimetry penetrometer. (c) He pycnometry device.

**Figure C.5.:** Pictures of mercury intrusion porosimetry and He pycnometry analysis.

## C.2. Controlled Permeability Materials

In a pressurized nutsche, pressure is applied on the liquid-solid mixture above the filter material. A pressurized nutsche was modified, so that the frit module became the filter material. The filtrate was collected and used as feed for a vacuum nutsche.

A vacuum nutsche is a common piece of lab equipment. It is also called a Büchner funnel. A funnel with a perforated plate is placed on a Büchner flask with a rubber gasket. The Büchner flask is a flask with a side arm, where a vacuum pump is attached. A filter paper is placed inside the funnel, and a liquid-solid mixture is added. Pressure difference and gravity pull the liquid through the filter, the solid stays in the filter.

## C.3. Metal Powder

Specific energy consumption (SEC) of gas atomization of  $N_2$  for AM can be calculated with eq. (C.5) according to [282].  $Y$  is the yield of powder suitable for AM.  $q$  is enthalpy per mass. Indices G and M stand for gas production/heating and melting, respectively.



$$c_p \approx 500 \text{ J kg}^{-1} \text{ K}^{-1} \quad (\text{C.5})$$

$$\rho_{\text{N}_2, \text{N}} = 1.2 \text{ kg m}_\text{N}^{-3} \quad (\text{C.6})$$

$$SEC_{\text{N}_2} = 2 \text{ MJ kg}^{-1} \quad (\text{C.7})$$

$$\dot{V}_g / \dot{m}_{\text{metal}} = 4 \quad (\text{C.8})$$

$$Y = 0.45 \quad (\text{C.9})$$

$$q'_G = c_p \cdot \Delta T = 0.113 \text{ MJ kg}^{-1} \quad (\text{C.10})$$

$$q_G = 4 \cdot 1.2 \cdot (q'_G + SEC_{\text{N}_2}) = 10.14 \text{ MJ kg}^{-1} \quad (\text{C.11})$$

$$q_M = 2.25 \text{ MJ kg}^{-1} \quad (\text{C.12})$$

$$SEC_{\text{N}_2, \text{GA}} = (q_G + q_M) / Y = 27 \text{ MJ kg}^{-1} \quad (\text{C.13})$$

The metal powders used had a composition given in table C.2.

**Table C.2.:** Composition of metal powders in wt-%. Both powders conformed both ASTM A276 and DIN EN 10088.

Component	CT 316LF Batch PR100334	POWDERRANGE SLM Solutions 316L Batch 2022000726
C	0.02	0.011
Cr	17.8	16.901
Fe	Bal.	Bal.
Mn	0.91	1.127
Mo	2.34	2.322
Ni	12.6	11.413
N	0.06	0.0987
O	0.02	0.0385
P	0.012	0.012
Si	0.67	0.718
S	0.007	0.02

#### C.4. Experimental Materials

Materials and equipment used in experiments are given in table C.3.

**Table C.3.:** Experimental materials and equipment.

Name	Company	Product
Male threaded connectors	Swagelok	SS-6M0-1-2RS, SS-12M0-1-8RS, SS-6-MTA-1-2RS
Metal gasket	Swagelok	304L-2-RSNB-2, 304L-8-RSNB-2, Cu-2-RP-2
Sinter metal	GKN	SIKA-R 100 AX, t = 2 mm
Graphite sealing	Frenzelit	Novaphit VS, t = 2 mm
Thermocouples	Conatex	Type K (NiCr-Ni) OD 0.5 mm; 1 mm
Heating cartridges	Kleinesdar	OD ¼", 100 W @ 230 VAC
Thermal conductivity paste	IBF Chemotechnik Elektronik GmbH	Ferotherm 4
Mass flow controllers (MFC)	Brooks	Vol flow = 300; 600; 30 NMLPM for CO, H <sub>2</sub> and N <sub>2</sub>
Oil thermostat	Lauda	Proline P12C
Thermal oil	Fragol	Fragoltherm 660
Insulation material	Isover	U Protect Pipe Sect- Alu2
Preprocessing software	DMG MORI	RDesigner (version 1.23.01, Revision 2017)
Printer operating Software	DMG MORI	ROperator (version 1.0.2.376, Revision 943 (2018))
Printer	DMG MORI	Realizer SLM 125
Laser	IPG	YLM-400-AC; Continuous wave (CW); Nd:YAG fibre laser; 1090 nm
Purge gas	Air Liquide	Argon 5.0
Metal powder	Carpenter Additive	CT PowderRange 316LF
NC mill	Deckel	FP5
Laboratory scale	Kern und Sohn	ABS-N ABJ-NM, error 0.2 mg
Pump	Verder	Digit-100
Pump head	Verder	230.0144 V015.12
Pump	Ismatec/Masterflex	MCP-Z
Pump head	Ismatec/Masterflex	1830
Oven 70 °C	Binder	FED 400
Oven 130 °C and vacuum	Heraeus	Vacutherm kelvitron t °C
Vacuum pump	vacuubrand	MZ 2C
Leakage detector	Leybold	
Screw press	SITEC Engineering (Maur, Switzerland)	
Alumina powder	Sasol	Puralox SCCa-5/150 sieving fraction above 50 µm
Alumina powder	Sasol	Puralox SCCa-150/230 sieving fraction above 100 µm
Lab sieving tower	Retsch	Analysette Pro 3
Static light scattering analyzer	Coulter-Beckmann	LS-230
Lab scale	Sartorius	LE225D-0CE, error 0.02 mg
Membrane filter	Ahlstrom-Munksjö	ReliaDisc Non-sterile cellulose acetate, pore size=0.45 µm, d=47 mm (art.-n. 760104)
Optical 3D profilometer	Sensofar	S neox

**Table C.3.:** Experimental materials and equipment. (Continued)

Name	Company	Product
Quartz wool	VWR	Kieselwolle 9 $\mu\text{m}$ (art.-n.24950.152)
External micrometer	Mitutoyo (Neuss, Germany)	25 mm, e=0.001mm
Pressure gauge FT reaction outlet	Swagelok	63 mm, 40 bar, Cl1.6
Pressure gauge FT reaction inlet	Swagelok	63 mm, 100 bar, Cl1.6
Pressure gauge mechanical stability test rig	VDO	80 mm, 40 bar, Cl 1.6 assumed
Water pressure test rig	Konstandin und Partner engineering GmbH (Pfinztal, Germany)	
Measurement and control unit	National Instruments (Austin, TX, USA)	cRIO 9056
Input and output modules	National Instruments (Austin, TX, USA)	NI 9203, 9213, 9266, 9472
Solid state relays	Sensata Technologies (Attleboro, MA, USA)	Crydom DR24D06, CKRD24

## D. Heat Transfer

### D.1. Convective Heat Transfer in the Reaction Zone

Syngas conditions: H<sub>2</sub>/CO=2; N<sub>2</sub>/CO=0.1; p=20 bar; T=200°C.

$$d = 0.5-1.5 \text{ mm} \quad (\text{D.1})$$

$$\text{Re}_0 = \frac{u_0 \cdot 2 \cdot d \cdot \rho}{\eta} \quad (\text{D.2})$$

$$d_p = 100 \text{ }\mu\text{m} \quad (\text{D.3})$$

$$\rho = 9.313 \text{ kg m}^{-3} \quad (\text{D.4})$$

$$\eta = 2.565 \times 10^{-5} \text{ kg m}^{-1} \text{ s} \quad (\text{D.5})$$

$$\lambda_f = 0.0884 \text{ W m}^{-1} \text{ K} \quad (\text{D.6})$$

$$\text{Pr}_{\text{Syngas}} = 0.438 \quad (\text{D.7})$$

$$\lambda_p \approx 1 \text{ W m}^{-1} \text{ K}^{-1} \quad (\text{D.8})$$

$$\text{Nu}_w \approx 5 \quad (\text{D.9})$$

$$\frac{1}{\alpha_w} = 6.67 \times 10^{-4} - 2 \times 10^{-3} \text{ m}^2 \text{ K W}^{-1} \quad (\text{D.10})$$

### D.2. Evaporative Heat Transfer

For calculation of evaporation heat transfer coefficient the boiling portion is only considered, when  $\dot{q}$  is above  $\dot{q}_{\text{onb}}$ , which is calculated according to eq. (D.11). The critical bubble radius is  $r_{\text{cr}} = 0.3 \times 10^{-6} \text{ m}$ . [7]

$$\dot{q}_{\text{onb}} = \frac{2 \cdot \sigma \cdot T_{\text{sat}} \cdot \alpha_{\text{LO}}}{r_{\text{cr}} \cdot \rho_{\text{GO}} \cdot h_{\text{evap}}} \quad (\text{D.11})$$

### D.3. Heat Transfer Coefficient Error Calculation

A measured variable  $x$  has a systematic error  $\Delta x$ . For a derived variable  $f$  the systematic error  $\Delta f$  was calculated via linear error propagation, eq. (D.12). The derived variable could be reported according to eq. (D.13), where  $f^*$  is the derived variable calculated from the initial measurements.

$$\Delta f = \sum_i \left| \frac{\partial f}{\partial x_i} \cdot \Delta x_i \right| \quad (\text{D.12})$$

$$f = f^* \pm \Delta f \quad (\text{D.13})$$

Systematic errors of select measured variables are given in table D.1.

**Table D.1.:** Systematic errors of measured variables.

Variable $x$	Systematic error $\Delta x$
$p$	0.1 bar
$T$	1 K
$\dot{m}$	0.1 % of m.v. <sup>1</sup>
$t$	0.1 mm
$U$	1.25 V
$R$	0.846 $\Omega$
<sup>1</sup> m.v. = measured value	

Systematic errors for most derived variable are trivial and were calculated according to eq. (D.12). For the systematic error of  $\dot{Q}_{\text{loss}}$  the standard deviation of  $\dot{Q}_{\text{loss}}$  from the one-phase experiments of the respective module was taken. The error of electrical power considered the errors of voltage and the error of resistance at room temperature. The error of the logarithmic mean temperature difference was calculated according to eq. (D.14).

$$\Delta\Delta T_{\text{LM}} = [a + b + c] \cdot \Delta T \quad (\text{D.14})$$

$$a = \frac{1}{\ln\left(\frac{T_{\text{HP}} - T_{\text{in}}}{T_{\text{HP}} - T_{\text{out}}}\right)} - \frac{T_{\text{out}} - T_{\text{in}}}{\ln^2\left(\frac{T_{\text{HP}} - T_{\text{in}}}{T_{\text{HP}} - T_{\text{out}}}\right) \cdot (T_{\text{HP}} - T_{\text{out}})} \quad (\text{D.15})$$

$$b = -\frac{1}{\ln\left(\frac{T_{\text{HP}} - T_{\text{in}}}{T_{\text{HP}} - T_{\text{out}}}\right)} + \frac{T_{\text{out}} - T_{\text{in}}}{\ln^2\left(\frac{T_{\text{HP}} - T_{\text{in}}}{T_{\text{HP}} - T_{\text{out}}}\right) \cdot (T_{\text{HP}} - T_{\text{in}})} \quad (\text{D.16})$$

$$c = \frac{(T_{\text{out}} - T_{\text{in}})^2}{\ln^2\left(\frac{T_{\text{HP}} - T_{\text{in}}}{T_{\text{HP}} - T_{\text{out}}}\right) \cdot (T_{\text{HP}} - T_{\text{in}}) \cdot (T_{\text{HP}} - T_{\text{out}})} \quad (\text{D.17})$$

## Vapor Pressure

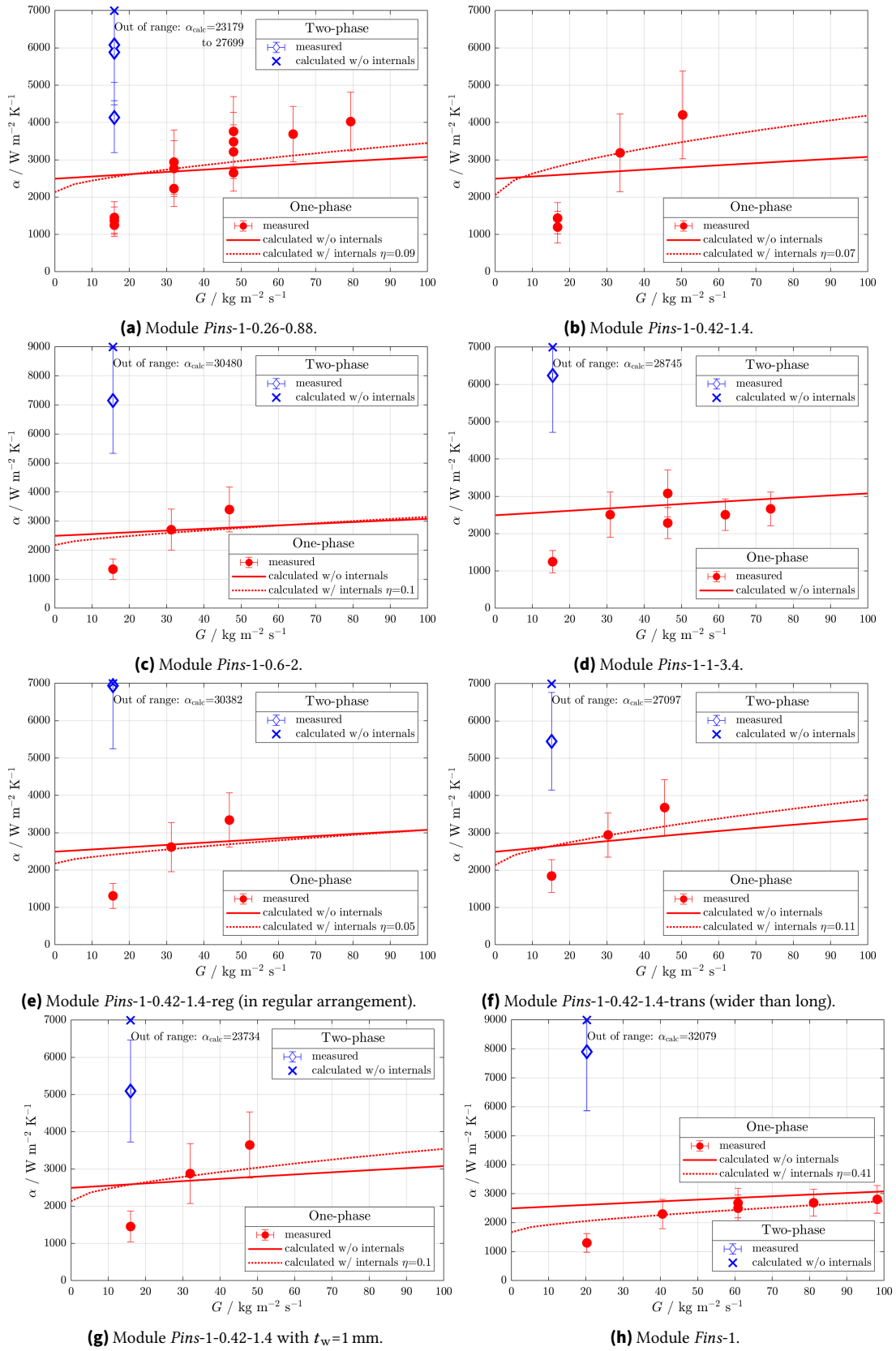
The vapor pressure of water as a function of temperature is given in table D.2.

**Table D.2.:** Vapor pressure as function of boiling temperature according to Antoine equation [306] and Wagner equation in the 2.5-5-form [7].

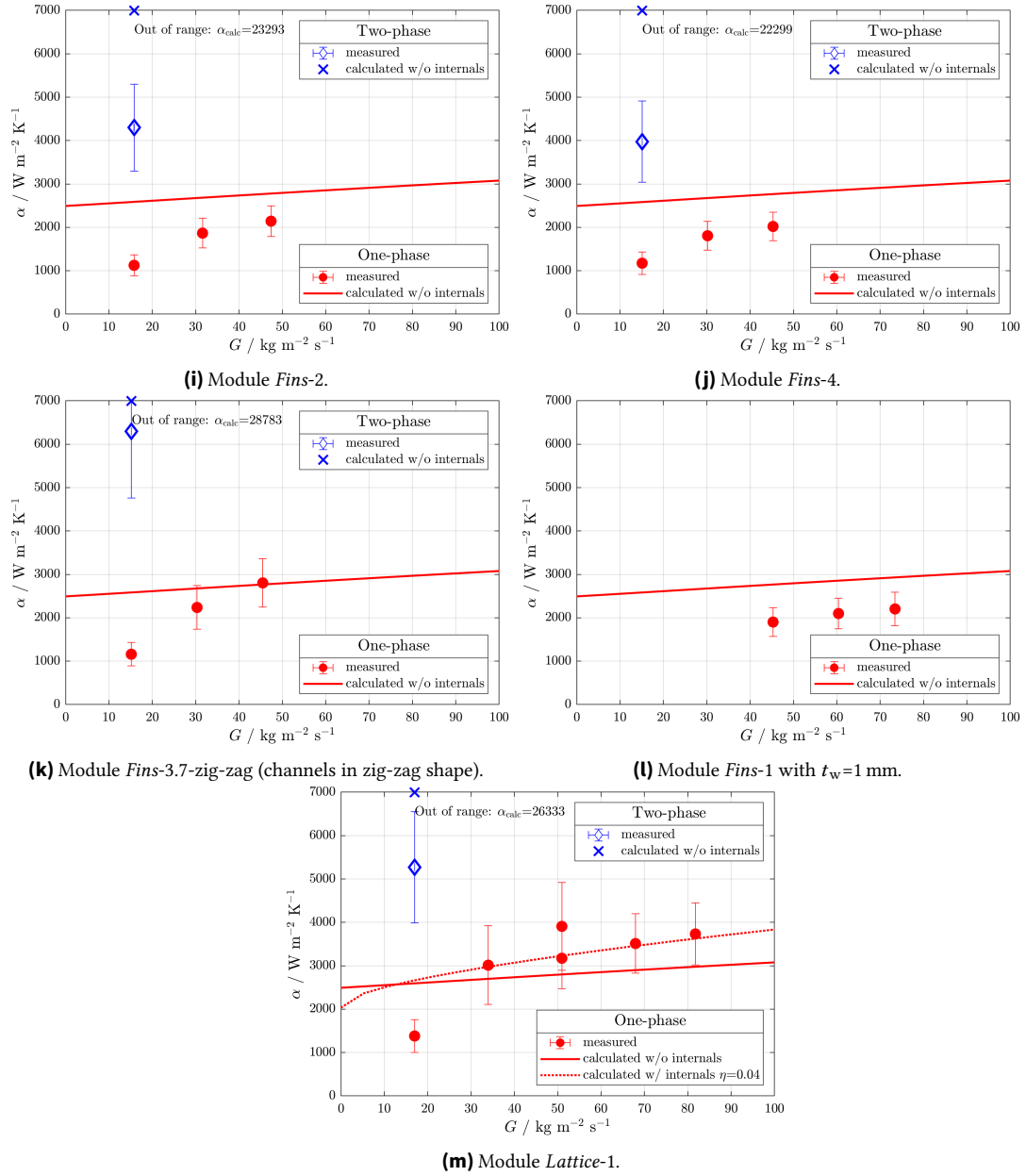
$T / ^\circ\text{C}$	$T / \text{K}$	$p_{\text{boil}} / \text{bar (Antoine)}$	$p_{\text{boil}} / \text{bar (Wagner)}$
0	273.15	0.006	0.006
10	283.15	0.012	0.012
20	293.15	0.023	0.023
30	303.15	0.042	0.043
40	313.15	0.074	0.074
50	323.15	0.123	0.124
60	333.15	0.199	0.200
70	343.15	0.311	0.312
80	353.15	0.473	0.474
90	363.15	0.700	0.702
100	373.15	1.019	1.014
110	383.15	1.434	1.433
120	393.15	1.980	1.986
130	403.15	2.687	2.702
140	413.15	3.590	3.614
150	423.15	4.726	4.760
160	433.15	6.137	6.182
170	443.15	7.870	7.922
180	453.15	9.974	10.03
190	463.15	12.50	12.55
195	468.15	13.95	13.99
200	473.15	15.52	15.55
210	483.15	19.08	19.08
220	493.15	23.24	23.20
230	503.15	28.08	27.98
240	513.15	33.67	33.48
250	523.15	40.07	39.77

#### D.4. Results Heat Transfer Coefficient Water

Additional results for heat-transfer testing with water are given in fig. D.1.



**Figure D.1.:** Results of modules with various internal structures during heat-transfer testing with water.  $T_{\text{in}}=150^\circ\text{C}$  for one-phase and  $170^\circ\text{C}$  for two-phase heat transfer. If not otherwise indicated  $t_w=0.6$  mm. All dimensions are in mm.

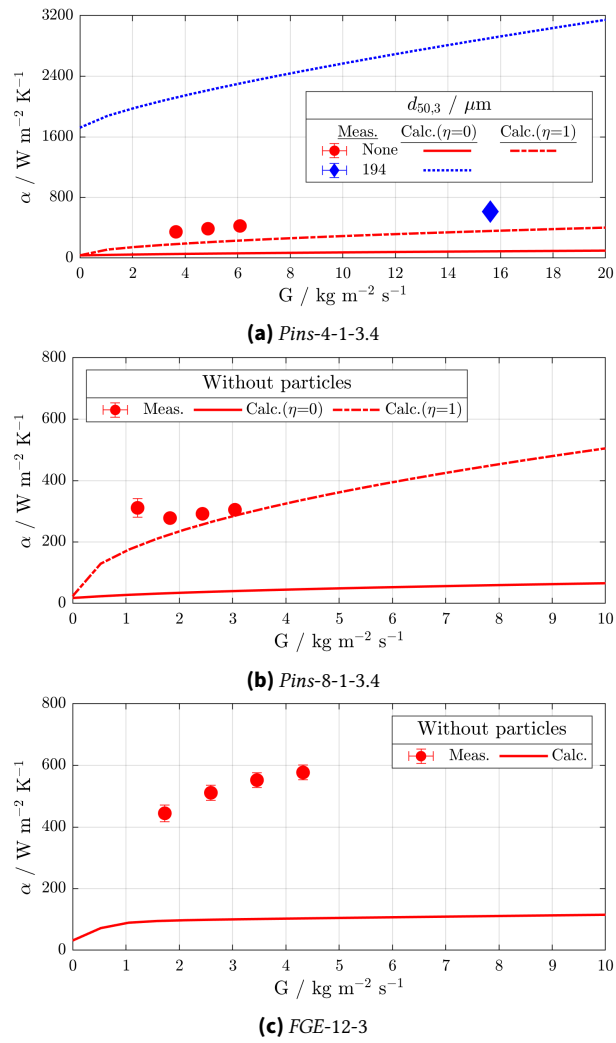


**Figure D.1.:** Results of modules with various internal structures during heat-transfer testing with water.  $T_{in}=150^\circ\text{C}$  for one-phase and  $170^\circ\text{C}$  for two-phase heat transfer. If not otherwise indicated  $t_w=0.6$  mm. All dimensions are in mm. (Continued.)

## D.5. Results Heat Transfer Coefficient Nitrogen

Additional results for heat-transfer testing with  $\text{N}_2$  are given in fig. D.2.





**Figure D.2.:** Experimental results of heat transfer with nitrogen without and with particles.





**Metzger, David (IMVT)**

---

**Von:** Bulsink, Jaap <jbulsink@k3d.nl>  
**Gesendet:** Freitag, 25. Februar 2022 15:28  
**An:** Metzger, David (IMVT)  
**Cc:** Lutikholt, Stijn  
**Betreff:** RE: Request for quotation LPBF

Dear David,

Thank you for the request. We can print this part for [REDACTED] in 316L with optimized settings.  
Startup costs will be 20 euro

We can print the thread and post process it if you like.

**Met vriendelijke groet / With kind regards,**



Mob: +31-(0)6 811 640 28  
E-Mail: [jbulsink@k3d.nl](mailto:jbulsink@k3d.nl)

Varsseveldseweg 20a  
NL7061 GA Terborg  
The Netherlands  
[www.k3d.nl](http://www.k3d.nl)

---

**Van:** Metzger, David (IMVT) <david.metzger@kit.edu>  
**Verzonden:** donderdag 24 februari 2022 16:43  
**Aan:** Bulsink, Jaap <jbulsink@k3d.nl>  
**Onderwerp:** Request for quotation LPBF

Dear Jaap,

we met at Formnext in Frankfurt/Germany last year, where you advertised your 3D printing services.

Could you please send me a quotation for manufacturing of a prototype? The attached prototype should be manufactured by LPBF out of 316L. The design is optimized for LPBF. It is mandatory, that the part has a low porosity/high relative density. Since we are going to use this prototype for chemical reactions we will control the leak tightness with the helium leakage rate.

Should you have any questions, feel free to call me.

Thank you un advance and kind reagrds,  
David

## Metzger, David (IMVT)

**Von:** Anfrage <anfrage@wjw.de>  
**Gesendet:** Freitag, 25. Februar 2022 10:07  
**An:** Metzger, David (IMVT)  
**Betreff:** AN220225LS01 Angebotsanfrage LPBF

**ANGEBOT**



WASSERSTRAHLSCHNEIDEN | LASERSCHMELZEN

Guten Tag Herr Metzger,

vielen Dank für Ihre Anfrage. Nachstehend bieten wir Ihnen gem. unserer AGB's unverbindlich an.

**Laserschmelzen; Support entfernen, Gewinde einbringen und Sandstrahlen  
ohne weitere Folgebearbeitung,**

Toleranzen gem. DIN ISO 2768      Teil1 (m) minimum  $\pm 0,1\text{mm}$ , Teil 2 (K) Qualitätsbauweise  
Teil1 (c) minimum  $\pm 0,25\text{mm}$ , Teil 2 (L) Standardbauweise

**inkl. Material: 1.4404**

**1 STK gem. Zeichn. 21DM1816\_Rev10**      **Bauvolumen: 65,534mm<sup>3</sup>**  
**(Angaben müssen geprüft werden, sind Basis des Angebotes)**

**Schichtdicke 50 µm Standardbauweise**       €/STK

**Schichtdicke 25 µm Qualitätsbauweise**       €/STK  
**Wird aufgrund der Anforderungen empfohlen**

Wir hoffen, dass unser Angebot Ihren Vorstellungen entspricht, sichern Ihnen bereits jetzt einen reibungslosen Ablauf zu.

Lieferzeit: 8-10 AT

Für Rückfragen stehe ich Ihnen jederzeit zur Verfügung.

Mit freundlichen Grüßen

Konrad Andres  
Tel.: 06327 / 97408-50

Preis: netto, ab Werk | Preisbindung: 3 Wochen | Zahlungsbed.: 30 Tage netto  
Die Preise haben nur Gültigkeit bei Bestellung des Gesamtauftrages; Mengenabweichungen führen zu Preisänderungen.

**WJW WATERJET GMBH**  
Im Altenschemel 49 | 67435 Neustadt / Weinstraße  
Tel.: 0 63 27 / 97 408 – 0 | Fax: 0 63 27 / 97 408-99 | E-Mail: [info@wjw.de](mailto:info@wjw.de)

[www.wjw.de](http://www.wjw.de)

Amtsgericht Ludwigshafen HRB 42521



FIT Prototyping GmbH  
 Industriegebiet  
 Am Grohberg 1  
 92331 Lupburg  
 Phone: +49 (0) 9492 94 29 0  
 Fax: +49 (0) 9492 94 29 11  
 Mail: prototyping@pro-fit.de  
 Web: www.fit-prototyping.de

FIT Prototyping GmbH \* Am Grohberg 1 \* 92331 Lupburg

Karlsruher Institut für Technologie - KIT  
 David Metzger  
 Hermann-von-Helmholtz-Platz 1  
 76344 Eggenstein-Leopoldshafen  
 Deutschland

**Angebot: 465753 - 1 - Chemischer Reaktor**  
*(Bitte bei Bestellung angeben)*



Gewinde wird mitgebaut und beim Kunden nachgeschnitten

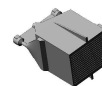
Datum: 08.03.2022

Kontakt: Thomas Geitner  
 Telefon: +49 (0)9492 94 29 61  
 Mail: prototyping@pro-fit.de  
 Projekt: Chemischer Reaktor

Angebotsnummer: 465753-1  
 Lieferantenummer: 10125575  
 Kundennummer: 15835

**1. Bauteilgeometrie: 21dm181610\_100ccm**

Datendatei: 21dm181610\_100ccm.stl  
 Diese Datei ist für die Herstellung von Bauteilen verwendbar  
 Länge: 132 mm, Breite: 101.36 mm, Höhe: 92.81 mm



**1.1 1 x LM (PBF-LB/M) Metallbauteil**

Ergänzung: Laserschmelzen von Metallpulver  
 Lieferzeit : 8 Arbeitstage  
 - Material Edelstahl 1.4404 (316L)  
 - Rohteil, Oberfläche gestrahlt  
 - Das Bauteil wird massiv aufgebaut  
 - Bauteil wird in Schichtstärke 50µm aufgebaut

**Bestehend aus folgenden Einzelleistungen:**

1.1.1	1 x	LM Aufbau	á
1.1.2	1 x	LM Supportentfernung	á

Seite 1/3

USt-IdNr.: DE297000178

Gerichtsstand: Amtsgericht Nürnberg HRB 30932

Geschäftsführer: Carl Fruth, Thomas Geitner

Bankverbindung: Sparkasse Parsberg

BIC (Swift Code): BYLADEM1NMA

DE37 7605 2080 0042 1783 92



**3D LASER BW** GmbH & Co. KG • Wielandstr. 19 • 73230 Kirchheim unter Teck

Karlsruhe Institute of Technology (KIT)  
Institute for Micro Process Engineering (IMVT)  
G. 605, R. 406  
Hermann-von-Helmholtz-Platz 1  
76344 Eggenstein-Leopoldshafen

**3D Laser BW GmbH & Co. KG**  
Wielandstr. 19  
73230 Kirchheim unter Teck

Telefon 07021 73467 20  
Fax 07021 73467 22  
E-Mail info@3-d-laser.de  
Internet www.3-d-laser.de

HRA 733627 Amtsgericht Stuttgart  
USt-IdNr. DE 315 816 579  
Steuernummer: 69026/45908

Geschäftsführer:  
Oliver Wagner  
Silvio Peschke

## ANGEBOT 20103334

Datum 03.03.2022  
Kunden-Nr. 30897  
Ihre Zeichen: David F. Metzger  
Unsere DV-Nr.: 20103032

Seite 1

Sehr geehrter Herr Metzger ,

wir danken für die Anfrage vom 03.03.2022 per Email und bieten wie folgt an:

Pos.	Artikel-Bezeichnung	Menge	ME	Einzelpreis	PE	Rabatt %	Gesamtpreis
10	<b>Metall-Laserschmelzen</b> 21DM1816_Rev10 Material 1.4404 Toleranz nach DIN 2768m Schichtstärke 0,03mm Alles relevanten Flächen/Bohrungen benötigen ein Aufmaß Stützgeometrien entfernt, Sandgestrahlt inklusive Gewinde einbringen	1	Stk				

Bemerkung:  
Bei Auftragsvergabe benötigen wir ein Step-Datensatz

Zwischensumme Nettobetrag	MwSt.	Zwischensumme Bruttobetrag
---------------------------	-------	----------------------------

Pers. haftende Gesellschafterin  
**3D Laser BW Verwaltungs GmbH**  
Sitz: Markgröningen  
Registergericht: Amtsgericht Stuttgart HRB 761904

**Volksbank Kirchheim-Nürtingen eG**  
IBAN: DE92 6129 0120 0453 4850 06  
BIC: GENODES1NUE

**VR-Bank Asperg-Markgröningen eG**  
IBAN: DE49 6046 2808 0681 8860 05  
BIC: GENODES1AMT



Wir sind zertifiziert nach DIN ISO 9001:2015



PROTIQ GmbH - Flachsmarktstr. 54 - 32825 Blomberg - Deutschland

Herr  
David Metzger  
Karlsruher Institut für Technologie  
Herrmann-von-Helmholtz-Platz 1  
76344 Eggenstein-Leopoldshafen  
Deutschland

Benutzerkonto: david.metzger@kit.edu  
Angebotsnummer 2022022412

Blomberg, 24.02.2022

### Angebot

Menge	Art.-Nr.	Beschreibung	Einzelpreis	Gesamtpreis
1	HISIR-55	3D-Print '21DM181610_100ccm.stl' - Material: Werkzeugstahl 1.2709 - Finishing: Strahlen - Gewicht: 2.45 kg		
1	NOXAR-31	3D-Print '21DM1816_Rev10.stl' - Material: Werkzeugstahl 1.2709 - Finishing: Strahlen - Gewicht: 0.51 kg		
1	GOXEV-47	3D-Print '21DM181610_5ccm.stl' - Material: Werkzeugstahl 1.2709 - Finishing: Strahlen - Gewicht: 0.26 kg		
			zzgl. gesetzl. MwSt.	zzgl. gesetzl. MwSt.
			Summe Artikel (netto)	
			Versandkosten (netto)	
			<b>Gesamtsumme (netto)</b>	
			zzgl. 19% MwSt.	
			<b>Gesamtsumme</b>	

Dieses Angebot hat eine Gültigkeit bis zum 10.03.2022.

Zahlungsziel bei Rechnungsbau: 14 Tage

Für Fragen zu diesem Angebot kontaktieren Sie uns gerne per Email: [service@protiq.com](mailto:service@protiq.com)  
oder unter der Telefonnummer: +49 (0) 5235 3-43800

Sitz der Gesellschaft: 32825 Blomberg  
Amtsgericht HRB HRB 8933  
Ust.-ID: DE308331885

Geschäftsführer  
Ralf Gärtner

PROTIQ GmbH  
IBAN: DE80 3607 0050 0220 1051 00  
BIC: DEUTDE33XXX  
SEPA Gläubigernummer: DE63ZZZ00001944946



SCHOELLER - BLECKMANN OILFIELD TECHNOLOGY GmbH  
A-2630 Ternitz, Hauptstraße 2, Austria  
Tel.: +43 / 2630 / 315 - 0, Fax: +43 / 2630 / 315 - 401



## Angebot

Seite: 1 / 2

Firma  
Karlsruher Institut für Technologie  
Institute for Micro Process  
Engineering  
Hermann-von-Helmholtz-Platz 1  
76344 EGGENSTEIN-LEOPOLDSHAFFEN  
GERMANY

Nummer: 20003868  
Datum: 31.03.2022  
gültig bis: 08.04.2022  
Ihre Anfragennummer: Angebot  
vom: 31.03.2022  
Kundennummer: 1630  
Kontakt: Daniel Wutzlhofer

Versandanschrift:

Firma  
Karlsruher Institut für Technologie  
Institute for Micro Process  
Engineering  
Hermann-von-Helmholtz-Platz 1  
76344 EGGENSTEIN-LEOPOLDSHAFFEN  
GERMANY

Wir danken für ihre Anfrage und dürfen Ihnen gemäß unseren allgemeinen Geschäftsbedingungen (letzte Ausgabe) wie folgt anbieten.

Wir möchten Sie darüber informieren, dass im Zusammenhang mit der Auftrags- und Bestellabwicklung ihre personenbezogenen Daten von uns verarbeitet werden. Informationen zur Verarbeitung personenbezogener Daten durch SBOT und den damit verbundenen Rechten finden Sie unter [www.sbo.at/privacypolicy](http://www.sbo.at/privacypolicy)

Zahlungsbedingungen: Sofort zahlbar ohne Abzug

Lieferbedingungen: FCA TERNITZ

\*\*\* Lieferzeit \*\*\*

2-3 Wochen ab Bestelleingang

Pos.	Menge	ME	Beschreibung	KG Netto	Preis/Einheit EUR	Wert
0010	1	ST	D.KIT.PROTO.01 Additive Fertigung Prototype lt. 3D Modell 21DM1816_Rev10.stl  Material: INCONEL 718  Inklusive: - Abtrennung von der Bauplatte  Weitere erforderliche Nachbearbeitungen oder Wärmebehandlungen müssen noch im Detail besprochen werden. Dazu sind Fertigungszeichnungen erforderlich.	1		
0020	12	ST	D.KIT.PROTO.01 Additive Fertigung Prototype	12		

Firmensitz/Reg. Office: 2630 Ternitz/Austria. Firmenbuch/Comm.Reg.No: FN 152516 p Handelsgericht Wr. Neustadt. DVR 0883387 UID/VATNo: ATU64257547  
EUR BankAccount: UniCredit Bank Austria AG, BLZ/Routing Code: 12000, Kto.Nr. 0127-01827/00, IBAN: AT61 1100 0012 7018 2700, BIC: BKAUATWW  
USD BankAccount: UniCredit Bank Austria AG, BLZ/Routing Code: 12000, Kto.Nr. 0127-01827/02, IBAN: AT31 1200 0012 7018 2702, BIC: BKAUATWW



3D-LASERDRUCK

3D-Laserdruck GmbH & Co. KG, Halskestraße 10, 72766 Reutlingen

Karlsruher Institut für Technologie  
David Metzger  
Hermann-von-Helmholtz-Platz 1  
76344 Eggenstein-Leopoldshafen

Angebot			
Belegnummer	Version	Datum	Seite
104669	1	09.01.2023	1 / 2
Kundennummer	UID-Geschäftspartner		
10968	DE266749428		
Ihre Zeichen			
David Metzger +49 721 608-23047 david.metzger@kit.edu +49 721 608-23047			
Referenz			
Ihre Anfrage per E-Mail vom 20.12.2022			
Ihr Ansprechpartner			
Friedrich Fester friedrich.fester@3d-laserdruck.de +49 7121 14789-13			
Gültig bis			
09.02.2023			

Sehr geehrter Herr Metzger,

Es freut uns, dass Sie sich für unsere Produkte und Dienstleistungen entschieden haben. Gerne offerieren wir wie folgt.


Beschreibung	Menge	ME	Preis	Gesamt
1 <b>Metall-Laserschmelzen 1.4404 50µm</b>	1,00	Stk		
<b>DM22209006_Reaktor_Assembly</b>				
CAD Daten vom: 20.12.2022				
Schichtstärke: 50µm; Toleranz: ISO 2768 m				
Oberflächenrauheit: Rz 30 - 40 µm				
Ohne Mechanische Bearbeitung				
Gewinde ist im 3D-Druck nicht anforderungsgerecht herstellbar und muss nach dem Druck mechanisch nachbearbeitet werden. Verzug aufgrund der Teilegeometrie möglich.				
Preisanpassungen bei Maßänderungen sind vorbehalten.				


Übertrag

3D-Laserdruck GmbH & Co. KG  
Halskestraße 10  
72766 Reutlingen  
Germany

Geschäftsführer: Martin Hirlinger & Tobias Wenz  
Tel.: +49 7121 14789 0  
Fax.: +49 7121 14789 89  
E-Mail: info@3d-laserdruck.de  
UID-Nummer: DE296337297


Bankverbindung: Kreissparkasse Reutlingen  
Kontonummer: 0100087057  
Bankleitzahl: 64050000  
Swift/BIC-Code: SOLADES1REU  
IBAN-Nummer: DE20640500000100087057








Edelstahl 1.4404  
316L


Anbieter




































































































































































































































Datum 24.01.23

Seite 1 | 2

toolcraft AG • Handelsstraße 1 • 91166 Georgensgmünd

Karlsruhe Institute of Technology  
David Metzger  
Kaiserstraße 12  
76131 Karlsruhe  
DEUTSCHLAND

**Ansprechpartner**

Oliver Sombrowski  
T +49 9172 6956-515  
F +49 9172 6956-560  
oliversombrowski@toolcraft.de  
www.toolcraft.de

**Angebot VAG2300141**

Anfrage: VAN2300005  
Ihre Anfrage: ANGEBOTSANFRAGE REAKTOR C22  
Lieferbedingung: FCA Georgensgmünd  
Zahlungsbedingung: 14 Tage netto

Ihre Kd.-Nr.: 385595  
Unsere L.-Nr.:  
Ansprechpartner:  
David Metzger

Sehr geehrter Herr David Metzger,

vielen Dank für Ihre Anfrage. Hiermit bieten wir Ihnen wie folgt freibleibend an:

Pos.	Artikelnummer Bezeichnung	Menge	Einheit	E-Preis EUR	+/- %	Gesamtpreis EUR
1.	01030604 DM22209006 Reaktor Hastelloy C22 DMLS-Bauteil: - Material: Hastelloy C 22 - Inklusive Wärmebehandlung (Vakuumofen) - Bauteil mittels Drahschnitt von der Bauplatte getrennt - Support händisch entfernt - Bauteil gestrahlt - Inklusive spanender Bearbeitung - Toleranz auf unbearbeitete Flächen ca. ± 0,3 mm / Rz40 µm (kann in manchen Bereichen abweichen) - optische Vermessung (GOM) "best-fit" - ausführliche Fertigungsdokumentation - Heliumlecktest "gas-dicht" <1*10 <sup>-8</sup> mbar*l/s  - Liefertermin: nach Absprache (~ 30 - 40 AT.n.AE.)	1	Stück			

Bei der Bestellung bitte auf "AA LS 046 material specification Hastelloy® C22 Rev.03" verweißen.

Vorstand | Members of the Executive Board:  
Karlheinz Nüßlein, Christoph Hauck,  
Marc Volkhardt

Vorsitzender des Aufsichtsrats |  
Chairman of the Supervisory Board:  
Bernd Krebs

Sitz der Gesellschaft | company  
headquarters: Georgensgmünd  
Reg.-Gericht | register court:  
Nürnberg HRB 38176  
USt-IdNr. | VAT Ident. No.:  
DE133528187

Sparkasse Mittelfranken-Süd  
IBAN: DE52 7645 0000 0620 0016 77  
BIC: BYLADEM15RS

Raiffeisenbank Roth-Schwabach  
IBAN: DE42 7646 0015 0003 5042 80  
BIC: GENODEF15WR

HypoVereinsbank Schwabach  
IBAN: DE17 7642 0080 0005 6698 04  
BIC: HYVEDEMM065

Commerzbank Nürnberg  
IBAN: DE65 7604 0061 0521 6338 00  
BIC: COBADEFFXXX



FIT Prototyping GmbH \* Am Grohberg 1 \* 92331 Lupburg

Karlsruher Institut für Technologie - KIT  
David Metzger  
Herrmann-von-Helmholtz-Platz 1  
76344 Eggenstein-Leopoldshafen  
Deutschland

FIT Prototyping GmbH  
Industriegebiet  
Am Grohberg 1  
92331 Lupburg  
Phone: +49 (0) 9492 94 29 0  
Fax: +49 (0) 9492 94 29 11  
Mail: prototyping@pro-fit.de  
Web: www.fit-prototyping.de

**Angebot: 488096 - 1 - Anfrage**  
(Bitte bei Bestellung angeben)



**Hinweise:**

- Richtpreisangebot
- die Wandstärken sind stellenweise zu gering konstruiert; Gasdichtheit kann erst ab einer Wandstärke von 1,0 mm garantiert werden
- Gewinde sind gedruckt nicht funktionsfähig

Datum: 22.12.2022

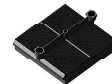
Kontakt:	Johannes Gürtler	Angebotsnummer:	488096-1
Telefon:	+49 (0)9492 94 29 66	Lieferantennummer:	10125575
Mail:	prototyping@pro-fit.de	Kundennummer:	15835
Projekt:	Anfrage		

**1. Bauteilgeometrie: DM22209006\_Reaktor\_Assembly\_Schritt2\_Vereinfach...**

Datendatei: DM22209006\_Reaktor\_Assembly\_Schritt2\_Vereinfachen\_1.stl

Diese Datei ist für die Herstellung von Bauteilen nicht verwendbar

Länge: 237 mm, Breite: 204.8 mm, Höhe: 71 mm



**1.1 1 x LM (PBF-LB/M) Metallbauteil**

Ergänzung: Laserschmelzen von Metallpulver

Lieferzeit : 8 Arbeitstage

- Material Edelstahl 1.4404 (316L)
- Rohteil

**Bestehend aus folgenden Einzelleistungen:**

1.1.1	1 x	LM Aufbau	à
1.1.2	1 x	LM Supportentfernung	à

**Beschreibung:**

Bauteil wird gemäß Anfrage nicht gestrahlt

**Gesamtbetrag Netto :**

**Zahlungsbedingungen: 30 Tage Netto**

**FCA (frei Frachtführer/Free Carrier) Lupburg (Incoterms 2020)**

**Der Mindestbestellwert liegt bei 50,00EUR, die Versandkosten können ggf. für jede Sendung individuell ausgewiesen werden.**

Seite 1/2

USt-IdNr.: DE297000178

Gerichtsstand: Amtsgericht Nürnberg HRB 30932

Geschäftsführer: Carl Fruth, Thomas Geitner

Bankverbindung: Sparkasse Parsberg

BIC (Swift Code): BYLADEM1NMA

DE37 7605 2080 0042 1783 92



Xometry Europe GmbH  
Ada-Lovelace-Str. 9,  
85521 Ottobrunn  
T: +49 89 38 034 818  
F: +49 89 33 960 142  
E: info@xometry.de  
www.xometry.de

UST-id.Nr.: DE318027176  
Steuer-Nr.: 143/194/00231  
Handelsregister: Amtsgericht München  
/ HRB 256172  
Bank: J.P. Morgan AG  
IBAN: DE33 5311 0800 6161 5322 02  
BIC: CHASDEFX

Directors / Geschäftsführer: Albert Belousov, Dmitry Kafidov

## Angebot E-479337-449720

An:	<b>Karlsruher Institut für Technologie - KIT Finanzmanagement</b>	Angebotsnummer:	<b>E-479337-449720</b>
z. Hd:	David Metzger	Angebotsdatum:	<b>21.12.2022</b>
Rechnun	Kaiserstraße 12	Voraussichtliches Versanddatum:	<b>* 11.01.2023</b>
gsadress	76131 , Karlsruhe		
e:	Germany		* (Bei Bestellung bis 22.12.2022)
UST-ID:	DE266749428		

Pos.	Beschreibung	Anzahl	Preis pro Stück	Gesamt
10.	 <b>Teilebezeichnung:</b> DM22209006_Reaktor_Assembly_Schritt2_Ver-einfachen_1.stl <b>Abgrenzung:</b> 237.0mm x 204.8mm x 71.0mm <b>Verfahren:</b> 3D-Druck DMLS - Direktes Metall-Lasersintern <b>Material:</b> Stainless Steel 316L <b>Finish:</b> Standard <b>Einsätze:</b> - <b>Gewinde und Gewindebohrungen:</b> -	1		
	Lieferkosten nach: Kaiserstraße 12 76131 Karlsruhe, Germany. (Delivery terms: DAP)			
	VAT (19.0%)			
	<b>Gesamtbestellwert, netto:</b>			
	<b>Gesamtbestellwert, brutto:</b>			

Angebotsstatus: **Manuell kalkuliert**

[Angebot öffnen](#)

**Wir wollen Ihnen das beste Angebot machen. Wenn Sie ein niedrigeres Angebot erhalten, schicken Sie es uns und wir werden uns bemühen, es zu unterbieten.**

### Bitte überprüfen Sie dieses Angebot vor der Bestellung auf Richtigkeit

- Wir haben für Ihren Auftrag einen Preis und ein Lieferfenster kalkuliert, basierend auf der von Ihnen bereitgestellten Geometrie im 3D-Modell, zusammen mit den Toleranzen, Merkmalen und Nachbearbeitungen, die Sie während des Einreichungsprozesses ausgewählt haben und von uns in diesem Angebot ausdrücklich bestätigt werden. Wir extrahieren Merkmale, Toleranzen und andere nicht-geometrische Informationen nicht automatisch aus dem von Ihnen eingereichten 3D-Modell, auch wenn sie darin vorkommen (z.B. Gewinde, Bohrungen usw.). Auch wenn unsere Preise dynamisch in Echtzeit generiert werden, werden wir den Preis in diesem Angebot für sieben (7) Tage ab Generierung einhalten (das voraussichtliche Lieferfenster wird jedoch zum Zeitpunkt der tatsächlichen Bestellung neu berechnet).

- Auch wenn wir Ihnen Unterstützung beim Design für die Herstellung geben, sind Sie letztendlich für die Tauglichkeit Ihres Designs und die damit verbundene Materialauswahl für jeden beabsichtigten Zweck verantwortlich. Sie können uns eine oder mehrere technische Zeichnungen und/oder Spezifikationsblätter bereitstellen. Wir werden unser Bestes tun, um jegliche Inkonsistenzen oder Konflikte in Ihren Materialien vor der Herstellung Ihres Teils zu identifizieren. Sie sind jedoch allein verantwortlich für jegliche Inkonsistenzen zwischen den Materialien, die Sie uns zur Verfügung stellen, und dem, was in diesem Angebot wiedergegeben ist.

- Sofern nicht anders angegeben, gelten die [Allgemeinen Geschäftsbedingungen](#) der Xometry Europe GmbH

- Teile aus rostanfälligen Materialien können nach unserem Ermessen mit einem Korrosionsschutzmittel auf Ölbasis beschichtet werden. Bitte informieren Sie uns, wenn Sie das Risiko einer möglichen Korrosion während des Transports in Kauf nehmen und Ihre Teile ölfrei erhalten möchten.

Web: [get.xometry.eu](https://get.xometry.eu)  
Kundendienst: [enquiry@xometry.de](mailto:enquiry@xometry.de)  
Telefon: + 49 89 3803 4818

Seite 1 von 1